THE UNIVERSITY OF
MELBOURNE

School of Chemistry

Synthesis and Optical Properties of CdSe Core and Core/Shell Nanocrystals.

Joel Leonard van Embden.

Submitted in total fulfilment of the requirements for the degree of Doctor of Philosophy

July 2008

Abstract

The synthesis of nanocrystals is unique compared to the formation of larger micron-sizes species as the final crystal sizes are not much larger than the primary nuclei. As a consequence the final outcome of a nanocrystal synthesis i.e mean crystal size, concentration and standard deviation is almost solely determined by the end of the nucleation phase. Directing the growth of crystals beginning from aggregates of only tens of atoms into mature monodisperse nanocrystals requires that the governing kinetics are *strictly* controlled at every moment of the reaction. To effect this task various different ligands need to be employed, each performing a particular function during both nucleation and growth.

In this thesis, by means of empirical investigation, the effects of oleic acid and bis-(2,4,4-trimethylpentyl)phosphinic on the nucleation and growth of cadmium selenide (CdSe) nanocrystals was conducted. It was found that these two ligands have remarkably different effects on the nucleation and growth of CdSe, despite the fact that both are basically anionic surfactants, which complex cadmium ions. The major reason for their different behaviour lies in the solubility of their respective complexes. Oleic acid accelerates particle ripening and growth and inhibits nucleation, where as TMPPA catalyses nucleation and drastically impedes growth, enabling smaller nanocrystals to be isolated. The relative amounts of these ligands determines the overall survival probability of the nuclei and the resultant longer-term growth behavior. By combining both ligands, the nucleation and ripening can be controlled systematically, enabling the isolation of high yields of nanocrystals with predictable sizes.

The ultimate success of applications based on nanocrystals requires the increasing ability to control and manipulate both the chemical and electronic behaviour of the crystals. Considering that the phase transfer of these crystals into non-ideal environments is predominantly the first step toward usable nano-devices, the crystals themselves require protection from degradation of their desired properties. Core-shell structures provide a means to isolate the chromophore from its environment.

Despite the fact that core-shell materials are a vital part of impending semiconductor technologies on the nanoscale, to date there has still been little detailed studied on the properties of core-shell materials. This is perhaps due to the fact that methods with which to synthesise core-shell structures with well defined dimensions has emerged only recently. In this thesis detailed studies into the conditions necessary to realise high-quality CdSe based core-shell structures are reported. It was found that while CdSe/CdS heterostructures could be grown with the greatest control of shell thickness, CdSe/CdS/ZnS multishell heterostructures are more resistant to adverse chemical environments. Refining the methods of core-shell synthesis toward the production of high-quality well defined core-shells will act not only to improve the way shell coatings are conducted, but via optical investigations deepen our understanding of how the shell functions.

Declaration

This is to certify that:

(i) The thesis comprises only original work undertaken by the author in the School of Chemistry, The University of Melbourne towards the PhD except where indicated,

(ii) Due acknowledgement has been made in the text to all other material used,

(iii) The thesis is less than 100,000 words in length, exclusive of table, diagrams, bibliographies, appendices and footnotes.

Joel Leonard van Embden

Publications

The work presented in this thesis has been published in the following peer-reviewed journal articles:

- Chon, J. W. M.; Zijlstra, P.; Gu, M.; van Embden, J.; Mulvaney, P. "Two-photon-induced photoenhancement of densely packed CdSe/ZnSe/ZnS nanocrystal solids and its application to multilayer optical data storage". Applied Physics Letters **85**, 5514-5516 (2004).

- van Embden, J.; Mulvaney, P. "Nucleation and Growth of CdSe Nanocrystals in a Binary Ligand System". Langmuir **21**, 10226-10233 (2005).

- Jasieniak, J.; Bullen, C.; van Embden, J.; Mulvaney, P. "Phosphine-Free Synthesis of CdSe Nanocrystals". Journal of Physical Chemistry B Letters **109**, 20665-20668 (2005).

- Gómez, D. E.; van Embden, J.; Mulvaney, P. "Spectral diffusion of single semiconductor nanocrystals: the influence of the dielectric environment". Applied Physics Letters **88**, 154106-1 (2006).

- Gómez, D. E.; van Embden, J.; Jasieniak, J.; Smith, T. A.; Mulvaney, P. "Blinking and surface chemistry of single CdSe nanocrystals". Small **2**, 204-208 (2006).

- van Embden, J.; Jasieniak, J.; Gómez, D. E.; Mulvaney, P.; Giersig, M. "Review of the Synthetic Chemistry Involved in the Production of CdSe Core/Shell Semiconductor Nanocrystals". Australian Journal of Chemistry **60**, 457-471 (2007).

The work presented in Chapters 3 and 6 will form the basis of articles to be published under the following titles:

- van Embden, J.; Mulvaney, P. "The evolution of colloidal nanocrystals: Theory and Modelling". *(in prep 2008).*
- van Embden, J.; Jasieniak, ,J.; Mulvaney, P. "Synthesis and Optical properties of CdSe-CdS Heterostructure Nanocrystals". *(in prep 2008).*

Acknowledgements

There is some people to whom I wish to express my gratitude for their contribution, both direct and indirect, towards the completion of the work presented in this thesis.

Firstly, to Professor Paul Mulvaney for his patience, intellect, constant enthusiasm and for granting me the freedom to extensively explore a very small world.

To my colleagues and friends from the "blue lab" for a thoroughly enjoyable, though at times tumultuous, four years in the lab. Special thanks to Phil, with whom I studied undergraduate chemistry, also to Daniel and finally to my confidant and partner in crime, Jack.

Also, to my brother and sister for keeping me youthful and making me laugh and to my parents for their support and for instilling in me a deep respect for knowledge.

Lastly, to my loving partner and best friend Emma, for her careful proof reading of this manuscript and for her enduring love.

Foreword

The contents of this thesis are based on investigations into the conditions necessary to synthesise high quality core and core-shell nanocrystals. Specific attention has been given to the effect of ligands on the nucleation and growth kinetics of CdSe nanocrystals as well as to the optical properties of CdSe core-shell systems. The information presented in this manuscript is organised as follows:

In Chapter 1 those concepts pertinent to size dependent phenomena and nanocrystyal synthesis are presented. Particular attention has been given to developing an understanding of quantum confinement and the density of states. Finally, the concepts of supersaturation and steric stabilisation, which are necessary to understand colloid formation are presented.

Chapter 2 presents those experimental methods used throughout this thesis. A list of equipment used and their operating conditions is also presented.

In Chapter 3 we present studies on the nucleation and growth kinetics of CdSe nanocrystals. The dependence of the extent of nucleation and final nanocrystal size on the nature and concentration of ligands in solution is discussed.

In Chapter 4 we develop an expression for the nucleation rate and size dependent growth rate of nanocrystals in the liquid phase. In the framework of flux corrected mass transport a population balance equation is used to solve these expressions. The results of numerical simulations using various (simulated) initial reaction conditions are presented.

Chapter 5 reviews the synthesis of CdSe heterostructure nanocrystals (core-shells). The synthetic conditions necessary to realise high quality core-shell materials are presented. The vital role of ligands to direct slow uniform growth of the shell material is emphasised. An effective mass model is implemented to account for the changes to the optical properties during shell deposition.

In Chapter 6 we present results on the synthesis and optical properties of CdSe/CdS and CdSe/CdS/ZnS heterostructure nanocrystals. Epitaxial growth of a shell with a predefined thickness allows reliable tracking of the optical properties as a function of shell thickness to be conducted. Reliable experimental data on such systems provides a valuable reference

point to the accuracy of current models used to describe the wavefunctions in complex semiconductor nanocrystals.

Finally, the thesis is concluded with a short section summarising the key findings and contributions made by the author. Further studies and an outlook toward future investigations are also presented.

Contents

List of Figures

List of Tables

Chapter 1

Introduction

Upon irradiation of a semiconductor nanocrystal with an energy above the band gap an electron is promoted from the valence band (VB) into the conduction band (CB). Due to their mutual Coulombic attraction the electron and hole form a bound state known as an exciton. When the dielectric constant of the semiconductor is small the exciton binding energy is large and as such the electron and hole are localised to an area typically the size of the unit cell (Frenkel exciton). On the contrary, semiconductors with large dielectric constants screen the Coulomb attraction between the electron and hole. As a consequence the exciton may extend over a distance significantly greater than the lattice constant of the semiconductor. These excitons are known as Mott-Wannier excitons and the size of such excitons is termed the "Bohr diameter". Further discussion will be restricted to excitons of this type.

When a semiconductor is reduced in size below its exciton Bohr diameter (typically tens of nanometres) the motion of the charge carriers in the excited state become strongly perturbed by the physical dimensions of the crystal. This perturbation is explained by a phenomenon known as quantum confinement. To gain an appreciation of the effects of confinement on the band structure and hence the allowed transition energies within a nanocrystal we may first consider the simple case of a particle confined to a three dimensional box.

1.1 Quantum confinement

1.1.1 Particle in a three dimensional box

For this analysis a potential, V, is set at zero inside the box and infinite everywhere else. For a particle of mass m moving in three dimensions the time-independent Schrödinger equation is

$$\hat{H}\Psi(x,y,z) = E\Psi(x,y,z)\,, \tag{1.1}$$

with the Hamiltonian operator given by the sum of the kinetic and potential energy terms:

$$\hat{H} = -\frac{\hbar^2}{2m}\nabla^2 + V(x,y,z)\,. \tag{1.2}$$

Here ∇^2 is the Laplacian operator. Upon assigning a potential of zero inside the box we obtain the following partial differential equation:

$$-\frac{\hbar^2}{2m}\left\{\frac{\partial^2}{\partial x^2} + \frac{\partial^2}{\partial y^2} + \frac{\partial^2}{\partial z^2}\right\}\Psi = E\Psi\,. \tag{1.3}$$

To solve this we must first separate the above partial differential equation into a set of ordinary differential equations. This may be accomplished by assuming that the wavefunction is the product of three separate functions, each dependent on a single spatial direction.

$$\Psi(x,y,z) = \mathbf{X}(x)\mathbf{Y}(y)\mathbf{Z}(z)\,. \tag{1.4}$$

Substitution of Equation 1.4 into Equation 1.3 and solving for E gives:

$$-\frac{\hbar^2}{2m}\left\{\frac{1}{\mathbf{X}(x)}\frac{d^2\mathbf{X}(x)}{dx^2}+\frac{1}{\mathbf{Y}(y)}\frac{d^2\mathbf{Y}(y)}{dy^2}+\frac{1}{\mathbf{Z}(z)}\frac{d^2\mathbf{Z}(z)}{dz^2}\right\}=E\,. \tag{1.5}$$

Each of the terms in the brackets is a function of a different independent variable and as such they may be separated. The resulting set of ordinary differential equations are:

$$-\frac{\hbar^2}{2m}\left\{\frac{1}{\mathbf{X}(x)}\frac{d^2\mathbf{X}(x)}{dx^2}\right\}=E_x\,, \tag{1.6}$$

$$-\frac{\hbar^2}{2m}\left\{\frac{1}{\mathbf{Y}(y)}\frac{d^2\mathbf{Y}(y)}{dy^2}\right\}=E_y\,, \tag{1.7}$$

$$-\frac{\hbar^2}{2m}\left\{\frac{1}{\mathbf{Z}(z)}\frac{d^2\mathbf{Z}(z)}{dz^2}\right\}=E_z\,. \tag{1.8}$$

Each of the above functions are similar in form to a particle confined to a one-dimensional potential well, which has general solutions of the form

$$\Psi=A\sin kx+B\cos kx\,. \tag{1.9}$$

Given that we know the potential is zero inside the box and infinite everywhere else and that the wavefunction must be a continuous function at the boundaries, it follows that the wavefunction must also be zero *at* the boundaries themselves. Substituting the boundary condition that $\Psi=0$ at $x=0$ we find

$$\Psi=A\sin kx\,. \tag{1.10}$$

It follows that $\sin kx=0$ since $A=0$ would imply $\Psi=0$ for all values of x, and the wavefunction must have some amplitude somewhere. Hence, kx must be chosen such that $\sin kx=0$, which is satisfied by:

$$kx = n\pi \qquad n = 1, 2, \ldots \tag{1.11}$$

Assigning L_x, L_y, L_z to be the dimensions of the box in the x, y and z directions, the solutions to the set of ordinary differential equations outlined above are

$$\mathbf{X}(x) = A_x \sin \frac{n_x \pi x}{L_x} \,, \tag{1.12}$$

$$\mathbf{Y}(y) = A_y \sin \frac{n_y \pi y}{L_y} \,, \tag{1.13}$$

$$\mathbf{Z}(z) = A_z \sin \frac{n_z \pi z}{L_z} \,. \tag{1.14}$$

Substitution into Equation 1.4 gives

$$\Psi(x, y, z) = A_x A_y A_z \sin \frac{n_x \pi x}{L_x} \sin \frac{n_y \pi y}{L_y} \sin \frac{n_z \pi z}{L_z} \,. \tag{1.15}$$

We must now normalise the wavefunction. To do so we must find values for A_x, A_y and A_z that ensure that the integral of Ψ^2 over all x,y or z respectively is equal to 1, as the probability of finding the particle somewhere in the box must be unity. Thus,

$$1 = \int_{-\infty}^{\infty} \Psi \Psi^* dx = A^2 \int_0^{L_x} \sin^2 kL_x \, dL_x = \frac{A^2 L_x}{2} \,. \tag{1.16}$$

Hence the normalised wavefunction is

$$\Psi(x, y, z) = \sqrt{\frac{8}{L_x L_y L_z}} \sin \frac{n_x \pi x}{L_x} \sin \frac{n_y \pi y}{L_y} \sin \frac{n_z \pi z}{L_z} \,. \tag{1.17}$$

Given that $E = E_x + E_y + E_z$ as well as $k(x) = n\pi/L_x$ and so forth, and that

$$E = \frac{k^2\hbar^2}{2m}\,, \tag{1.18}$$

the energies of the translating particle are quantised such that

$$E = \frac{h^2}{8m}\left\{\frac{n_x^2}{L_x^2} + \frac{n_y^2}{L_y^2} + \frac{n_y^2}{L_y^2}\right\} \qquad n = 1, 2\ldots \tag{1.19}$$

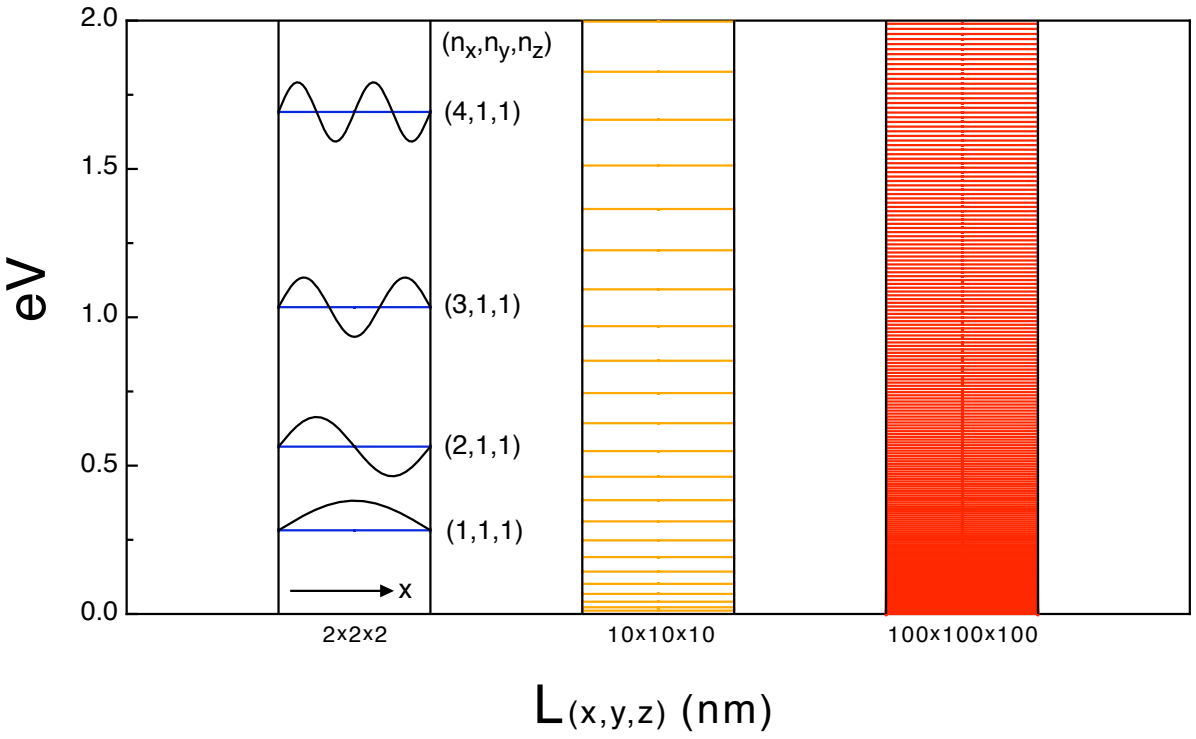

Figure 1.1: From left to right; A plot of the solutions to Equation 1.19 for boxes (crystals) with equal side lengths of 2, 10 and 100 nm respectively. A carrier mass equal to that of a free electron was employed to construct these plots.

Inspection of Equation 1.19 reveals that there is a discrete quantum number, n, associated with each spatial direction. It should be noted that $(n_x, n_y, n_z) = (1, 1, 2)$ is degenerate with levels $(1, 2, 1)$ and $(2, 1, 1)$. Figure 1.1 shows a plot of the solutions to Equation 1.19 for boxes (crystals) of increasing dimensions. For a 2 nm^3 box the energies of the ground state and the first three non-degenerate excited states are plotted along with the correspond-

ing wavefunction in the x-direction. Comparison of the three box sizes reveals that upon increasing the dimensions of the box the energy levels condense, with more energy levels becoming available within a given absolute energy range. For a box of infinite dimensions the separation between the energy levels, ΔE, is zero. However, even for crystals (boxes) with large yet finite dimensions at room temperature, ΔE, is well below kT ($\backsim 25\ meV$) and thus through exciton-phonon coupling[1] all energies are essentially allowed and the particle may be treated as if its translational motion is no longer quantised.

1.1.2 Particle in an infinite uniform spherical potential

We now consider the case where exciton motion is confined by an infinite spherical potential. The following derivation is accomplished within the framework of the effective mass approximation. Converting the Hamiltonian of Equation 1.2 into spherical polar coordinates yields:

$$\hat{H} = -\frac{\hbar^2}{2m}\nabla^2 + V(r,\theta,\phi)\ , \tag{1.20}$$

with the Laplacian operator in spherical polar coordinates expressed as

$$\nabla^2 = \frac{1}{r^2}\frac{\partial}{\partial r}\left\{r^2\frac{\partial}{\partial r}\right\} + \frac{1}{r^2 sin\theta}\frac{\partial}{\partial\theta}\left\{sin\theta\frac{\partial}{\partial\theta}\right\} + \frac{1}{r^2 sin^2\theta}\frac{\partial^2}{\partial\phi^2}\ . \tag{1.21}$$

Separating the wavefunction into its radial and angular components we seek a solution of the form

$$\Psi(r,\theta\psi) = R_{n,l}(r)Y_{l,m}(\theta,\phi)\ . \tag{1.22}$$

Here $R(r)_{n,l}$ is the radial component and $Y_{l,m}(\theta,\phi)$ is the angular component whose solutions

are *spherical harmonics*. The subscripts n, l and m are the principle, orbital and magnetic quantum numbers respectively. With the use of Equations 1.20 and 1.22 the separation of Equation 1.21 gives the radial Schrödinger equation.

$$-\frac{\hbar^2}{2m}\left\{\frac{\partial^2}{\partial r^2}+\frac{2}{r}\frac{\partial}{\partial r}\right\}R_{n,l}(r)+\left\{\frac{\hat{L}^2}{2mr^2}+V(r)\right\}R_{n,l}(r)=ER_{n,l}(r)\,, \tag{1.23}$$

where the angular momentum is expressed as:

$$\hat{L}^2=-\hbar^2\left[\frac{1}{sin\theta}\frac{\partial}{\partial\theta}\left\{sin\theta\frac{\partial}{\partial\theta}\right\}+\frac{1}{sin^2\theta}\left\{\frac{\partial^2}{\partial\phi^2}\right\}\right]\,. \tag{1.24}$$

The term $\hat{L}^2$ is dependent only on θ and ϕ and as such is purely angular. The solutions to the radial part for the function $R_{n,l}(r)$ are combinations of the spherical Bessel and Neumann functions.

As appropriate to nanocrystals in the strong confinement regime, we now restrict this analysis to evaluate the eigenvalues of the lowest order spherically symmetric excited state. For this specific case the quantum numbers are $n = 1$, $l = 0$ and $m = 0$. We also impose the boundary condition that there is an infinite confining potential outside the radius given by a:

$$V_{\text{conf}}(\mathbf{r})=\begin{cases}0 & \text{if } r<a\,,\\ \infty & \text{if } r>a\,.\end{cases} \tag{1.25}$$

Evaluation of Equation 1.23 under these conditions yields the confinement energy for a particle of mass m.

$$E_{1\,0\,0}=\frac{h^2}{8ma^2}\,. \tag{1.26}$$

We may now express the energy of the lowest excited (spherically symmetric) state for a semiconductor nanocrystal with a bulk band gap E_g and a radius a as

$$E_{1S_e\,1S_h} = E_g + \frac{h^2}{8m_e a^2} + \frac{h^2}{8m_h a^2}\,. \tag{1.27}$$

The inclusion of perturbation terms, which account for the Coulomb interactions between the electron and hole as well as the solvation energies of the charge-carriers was derived by Brus[2, 3] and is given by

$$E_{1S_e\,1S_h} = E_g + \frac{h^2}{8a^2}\left\{\frac{1}{m_e} + \frac{1}{m_h}\right\} - 1.786\frac{e^2}{\epsilon a} - 0.248\left\{\frac{4\pi e^4 m_0}{2(4\pi\epsilon)^2 h^2(\frac{1}{m_e}+\frac{1}{m_h})}\right\}\,. \tag{1.28}$$

Figure 1.2 is a plot of Equations 1.27 and 1.28 appropriate to cadmium selenide (CdSe) nanocrystals. Experimental data obtained for CdSe nanocrystals in the size range 2-9 nm is also shown*. Inspection of Figure 1.2 reveals that with the inclusion of coulomb interactions (and solvation energies) there is good agreement between the calculated and observed energies for CdSe nanocrystals with diameters above $\sim$7 nm. However, Equation 1.28 overestimates the confinement energies for smaller nanocrystals. We may attribute this overestimation to the imposed restriction that the wavefunction vanishes at the nanocrystal surface. Inclusion of a finite potential at the surface would lower the estimated energies, especially for smaller nanocrystals where the increasing kinetic energy of the charge-carriers at the surface results in larger tunnelling coefficients into the surrounding environment.

*This data was acquired from CdSe nanocrystals produced using the methods outlined in Chapter 3. The sizes were gathered from high-resolution transmission electron micrographs of no less than 100 crystals.

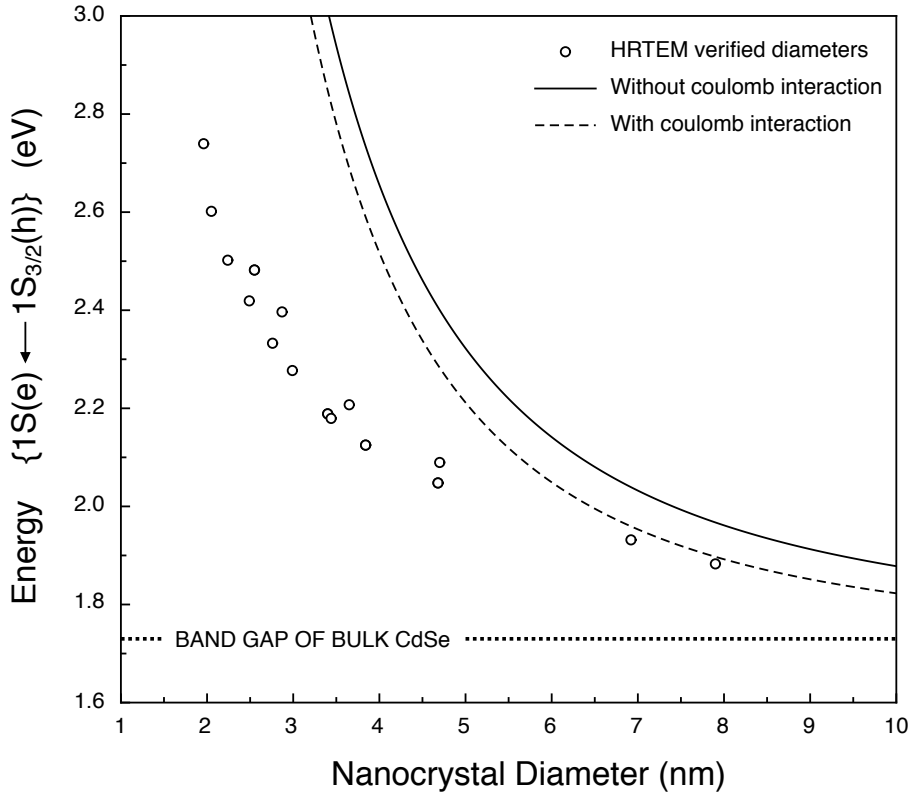

Figure 1.2: Predicted eigenvalues for the first excited state in CdSe nanocrystals without e-h interactions (solid line - Equation 1.27). Predicted eigenvalues for the first excited state in CdSe nanocrystals with the inclusion of coulomb interactions and solvation energies (dashed line - Equation 1.28). A bulk band gap of 1.73 eV, with $m_e = 0.14$ and $m_h = 0.37$ and $\epsilon = 8.23 \times 10^{-11}$ was used to construct the plot. Experimental data obtained for CdSe nanocrystals in the size range 2-9 nm (open circles).

1.1.3 Density of states

To determine the density of states (DOS), $g(E)$, we must find the number of solutions to Schrödinger's equation per unit volume and energy. Operating in k-space we limit our analysis to only positive values of k_x, k_y and k_z, which avoids counting identical solutions in $\pm n_x$, $\pm n_y$ and $\pm n_z$. This restricts the volume in k-space to one eighth of a sphere. The number of solutions, N, is given by dividing this volume by the volume for a *single* solution $(\pi/L)^3$, which yields

$$N = 2\left\{\frac{1}{8}\left\{\frac{L}{\pi}\right\}^3 \frac{4}{3}\pi k^3\right\}, \tag{1.29}$$

where L is the length of the sides of the single state cube in k-space. A multiplicative factor of two is introduced to account for the spin-up and spin-down configurations of each solution. Through use of the chain rule the number of states, N, in a given energy range may be expressed as

$$\frac{dN}{dE} = \frac{dN}{dk}\frac{dk}{dE} \,. \tag{1.30}$$

Firstly we find the derivative of k in Equation 1.29 with respect to N, which gives

$$\frac{dN_{3D}}{dk} = \frac{L^3 k^2}{\pi^2} \,. \tag{1.31}$$

We must now find an expression for the change of k with respect to E. Using the relation between k and E from Equation 1.18 and taking the derivative of k with respect to E we obtain

$$\frac{dk}{dE} = \frac{m}{\hbar^2 k} \,. \tag{1.32}$$

Substitution of Equations 1.31 and 1.32 into Equation 1.30 gives the DOS for a three dimensional (bulk) material.

$$g(E)_{3D} = \frac{8\pi L^3 \sqrt{2} m^{3/2}}{h^3} \sqrt{E} \,. \tag{1.33}$$

The expression for the DOS in the conduction band of a semiconductor makes use of the effective mass of the electron, m_e, and the potential of the conduction band minimum, E_c. Thus the DOS in the conduction band of a semiconductor of defined dimensions is given by

$$\frac{1}{L^3} g(E)_{3D} = \frac{8\pi \sqrt{2} m_e^{3/2}}{h^3} \sqrt{E - E_c} \,. \tag{1.34}$$

A similar rationale may be used to modify Equation 1.33 for holes in the valence band. To find the DOS for materials with fewer degrees of freedom i.e.: 2D (quantum well) and 1D (quantum wire) structures we must use different relations for dN/dk.

$$\frac{dN_{2D}}{dk} = \frac{L^2 k}{\pi} \,, \tag{1.35}$$

$$\frac{dN_{1D}}{dk} = \frac{L}{\pi} \,. \tag{1.36}$$

Thus the resulting DOS in 2D and 1D are

$$g(E)_{2D} = \frac{4\pi m}{h^2} \,, \tag{1.37}$$

$$g(E)_{1D} = \frac{1}{h}\sqrt{\frac{2m}{E}} \,. \tag{1.38}$$

For a zero-dimensional structure, such as a quantum dot, there is no k-space to be filled and all states are present *only* at discrete energies. As such we describe the 0D DOS with the Dirac delta function δ. Hence,

$$g(E)_{0D} = 2\delta E \,. \tag{1.39}$$

Figure 1.3 A-D show the DOS in three, two, one and zero dimensions as given by Equations 1.33, 1.37, 1.38 and 1.39 respectively. A particle mass of $9.109 \times 10^{-31}\ kg$ and a band minimum of 1 eV was arbitrarily chosen to construct these plots. We note that for the bulk (unconfined) material the DOS increases rapidly above the band minimum. In sharp contrast, highly confined (0D) structures possess excited states with appreciable densities only at discrete energies as outlined in Section 1.1.1.

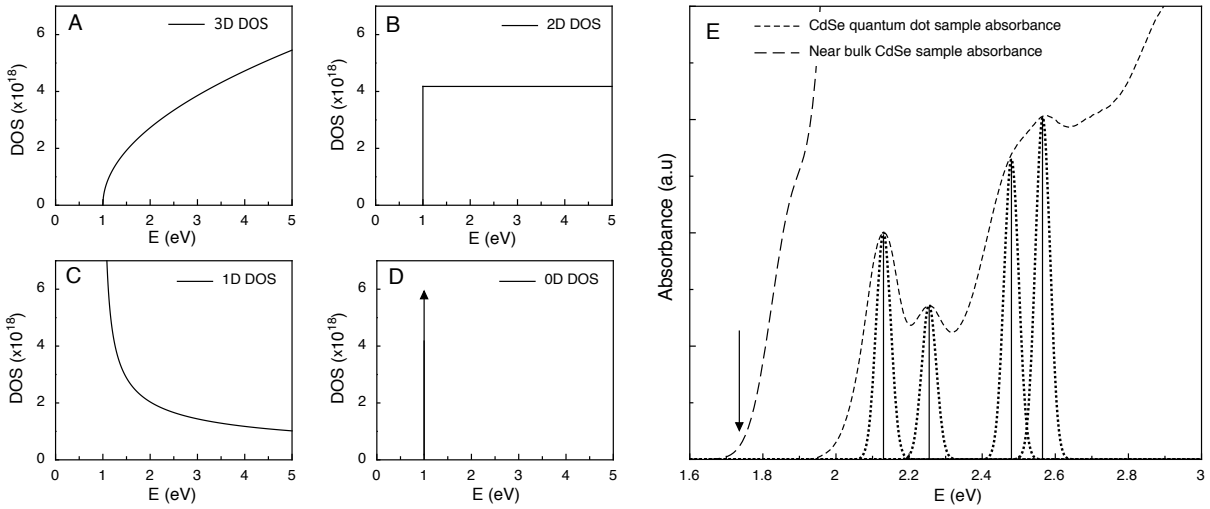

Figure 1.3: Density of states in the conduction band of (**A**) 3D, (**B**) 2D, (**C**)1D and (**D**) 0D structures. (**E**) A plot of near bulk 9.2 nm CdSe nanocrystals in chloroform and 3.9 nm CdSe nanocrystals in chloroform. The Dirac delta function describes the hypothetical transitions of a single nanocrystal at zero Kelvin (solid lines). Thermally broadened transitions (dotted lines).

To gain an appreciation of how these phenomena manifest experimentally Figure 1.3 E shows an absorption spectrum of near bulk cadmium selenide (long dashes)[†] and an absorbance spectrum obtained from an ensemble of $sim3.9\ nm$ cadmium selenide nanocrystals (short dashes). The spectrum obtained from the near bulk sample is almost featureless, as expected from the rapid increase in the DOS immediately above the band minima, while the spectrum from the nanocrystals exhibit several well resolved excited states. For simplicity only the first four transitions are shown. Beginning from the lowest energy transition, these excited states correspond to the $1S(e) - 1S_{3/2}(h)$, $1S(e) - 2S_{3/2}(h)$, $1P(e) - 1P_{3/2}(h)$, $1S(e) - 3S_{1/2}(h)$ transitions respectively[4]. Although for a single nanocrystal at zero Kelvin these transitions would appear like a series of delta functions (solid lines), at room temperature these transitions are thermally broadened (homogeneous broadening) as depicted by the dotted lines. These transitions are further broadened, inhomogeneously, through the size distribution of the nanocrystal ensemble. It may be foreseen that the sum of the result-

[†]This spectrum was obtained from CdSe nanocrystals with an average size of 9.2 nm as verified from HRTEM measurements. This value is close to the Bohr diameter of CdSe ($\backsim 10\ nm$) and as such is representative of the absorption spectrum of the bulk crystal.

ing series of homogeneously and inhomogeneously broadened transitions would then appear similar to the experimentally observed absorbance spectra for an ensemble of nanocrystal quantum dots (short dashed line).

1.2 Band Structure and surface states

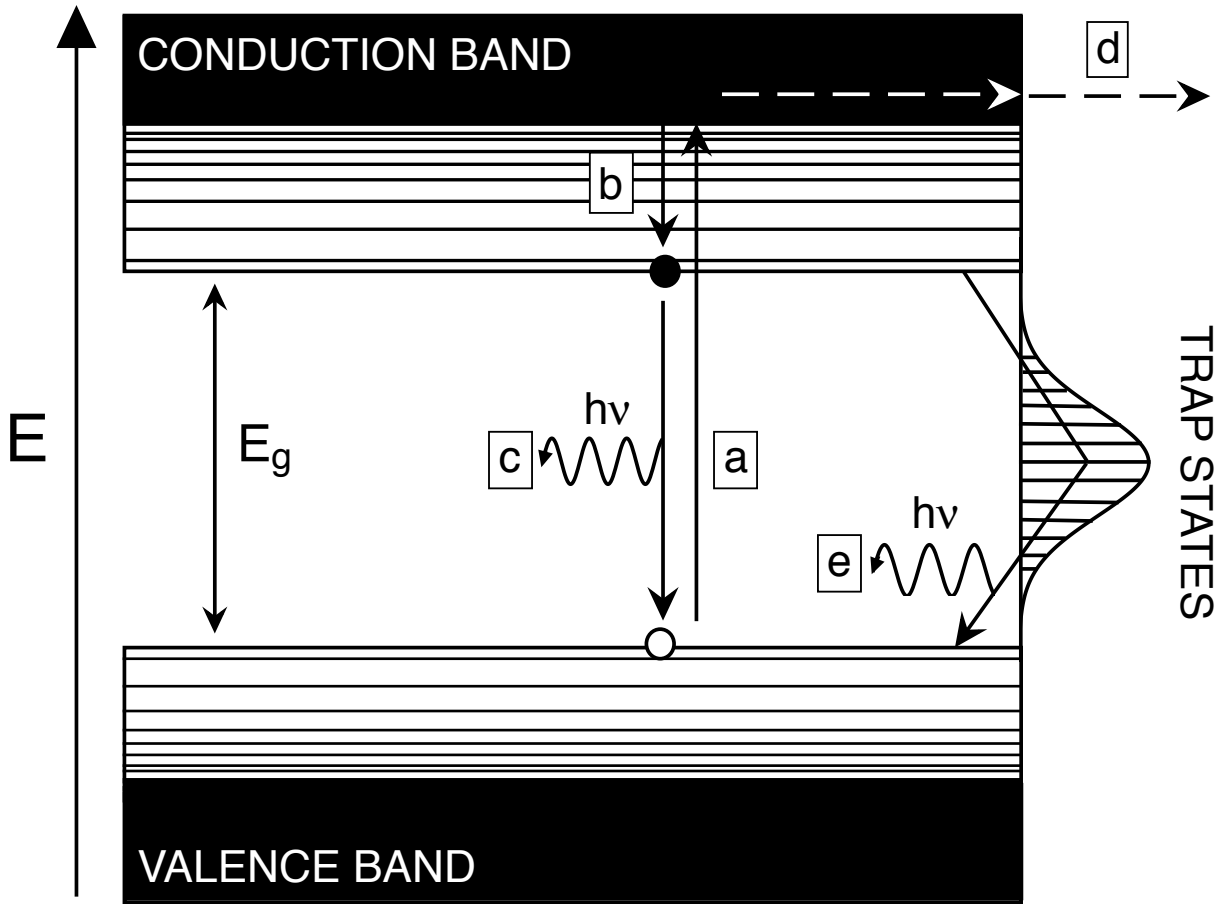

Figure 1.4: Schematic of the band profile of a typical semiconductor nanocrystal. The electron and hole are depicted by a filled circle and an open circle respectively. The processes (a)-(e) are outlined in the text.

Figure 1.4 shows a schematic of the band profile of a typical semiconductor nanocrystal. The valence band and the conduction band are separated by a bandgap of an energy denoted E_g. The levels in the VB and CB of nanocrystals are known to spread out close to the band edges due to fine-structure splitting[4, 5], giving rise to the discrete transitions observed in

Figure 1.3 E. Upon excitation with radiation of an energy greater than E_g an electron is promoted to an arbitrary empty level in the CB, leaving behind an empty level in the VB (a hole). Process (a) depicts the generation of an exciton upon illumination of the nanocrystal with UV light. After thermalisation of the charge-carriers to the band edge (Process (b)[‡]) they recombine and emit a photon whose energy is characteristic of the band gap energy, E_g (Process (c)). After excitation there are many other processes that directly compete with radiative recombination via the band edge. In cases where a nanocrystal is excited with a high intensity laser beam, multiple excitons may be generated inside the nanocrystal[6]. One of these excitons may then annihilate and transfer its energy to a third particle (typically the electron) and eject it from the nanocrystal. This process is referred to as Auger ionisation (Process (d))[7]. Thermalised or "hot" electrons may also be scavenged by oxidants in solution such as organic radicals, oxygen and water (Process (d)). In addition to these processes the electron may recombine through trap states at the nanocrystal surface (Process (e)). These trap states derive from either the orbitals of unpassivated atoms at the nanocrystal surface or from ligands that, when binding to the surface atoms, generate orbitals inside the band gap.

Photoluminescence is an ideal tool to measure the surface quality of nanocrystals. Figure 1.5 displays three steady-state photoluminescence (PL) traces taken at different stages during the overcoating of CdSe core nanocrystals with a zinc selenide (ZnSe) shell. The as-prepared core nanocrystals (solid line) have a band edge PL peak at $sim485\ nm$ as well as a broad distribution of emissive states extending from the band edge peak to lower energies. This broad luminescence profile is indicative of a broad distribution of trap states at the nanocrystal surface[8]. Heating the nanocrystals in a mixture of "activating" ligands[§] was found to be able to remove most of the surface traps resulting in reduced trap emission and an increase in the PL from the band edge (dotted line). Epitaxial passivation of the

[‡]For simplicity only the thermalisation of the electron is depicted.

[§]Here the nanocrystals were heated in a octadecylamine/trioctylphosphine mixture, which has been shown to enhance (activate) the band edge luminescence in CdSe nanocrystals[9]

surface of the nanocrystals with a layer of zine selenide completely removed the remaining trap states, further increasing the band edge PL.¶

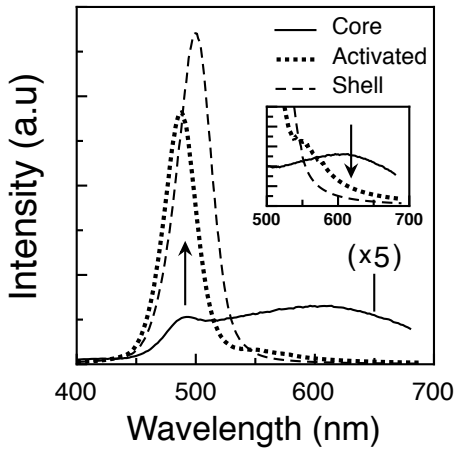

Figure 1.5: Photoluminescene spectra of as-prepared (solid line) , octadecylamine/trioctylphosphine (dotted line), and ZnSe (dashed line) passivated CdSe nanocrystals. All samples were normalised to an optical density of 0.1 at the excitation wavelength (350 nm). The inset highlights the reduction to the trap emission, which occurs concurrently with an enhancement of the band edge luminescence.

1.3 Nanocrystal formation

1.3.1 Monomer saturation

The precipitation of monomer from solution may be divided into two catagories: Precipitation from a solution of homogeneously dissolved monomer (*homogeneous nucleation*) and precipitation from solution onto an existing surface (*heterogeneous nucleation*). The barrier to homogeneous nucleation is always higher than that of heterogeneous nucleation as it requires the formation of a new phase. The magnitude of these barriers are dependent on the intrinsic properties of the monomer employed, the solution temperature as well as the nature and concentration of surfactants in solution.

¶An in-depth discussion of the effects of epitaxial shell growth are presented in Chapters 5 and 6. At this juncture it is enough that the reader understand that epitaxial passivation (with an appropriate material) leads to the greatest reduction in surface traps.

Figure 1.6 shows a schematic of the monomer concentration as a function of time for a typical precipitation reaction in a closed system[‖] as first outlined by LaMer [10]. In order for precipitation (homogeneous nucleation) to be thermodynamically facile the concentration of monomer must first be raised above a critical concentration, $[C]_s$ (dashed line). As monomer is consumed during nucleation the concentration of free monomer, $[C]_f$, will eventually drop below $[C]_s$ and nucleation will cease. The time for which $[C]_f > [C]_s$ is dependent largely on the nucleation rate of the system. Upon the cessation of nucleation, $[C]_f$ is still well above the equilibrium monomer concentration, $[C]_{eq}(r = a)$, (barrier to heterogeneous nucleation for a particle of radius a -dotted line) and as such the particles grow through the accretion of monomer. Although C_f is still well above $[C]_{eq}(r = \infty)$, eventually $[C]_f$ will drop below $[C]_{eq}(r = a)$ and coarsening (Ostwald ripening) will ensue. Coarsening involves the dissolution of the smaller particles within the distribution to support the growth of the larger ones and is typically characterised by a broadening of the particle size distribution[11].

1.3.2 Ligand stabilisation

The role of ligands during the nucleation and growth of nanocrystals is twofold. They must precipitate strongly on the surface to physically limit the rate of growth and in addition they must provide a steric barrier to aggregation. To synthesise and isolate nano-sized crystals it is necessary to nucleate crystallites with diameters around 1 nm. Given the extremely high surface energy of such small nuclei, dissolution and aggregation are highly favoured processes. Ligands must be chosen such that they limit these processes but still allow growth to proceed at a reasonable rate.

Figure 1.7 shows a $sim3$ nm CdSe nanocrystal capped with a typical ligand (octadecylamine) used during its formation (only the {002} surface capping is shown for clarity). It

[‖] A *closed system* is one where the monomer is introduced at a specific juncture in time, after which the reaction is allowed to proceed without the introduction of additional chemical reagents or monomers. Contrary to this, *open systems* define those reactions conducted with the continuous introduction of monomer.

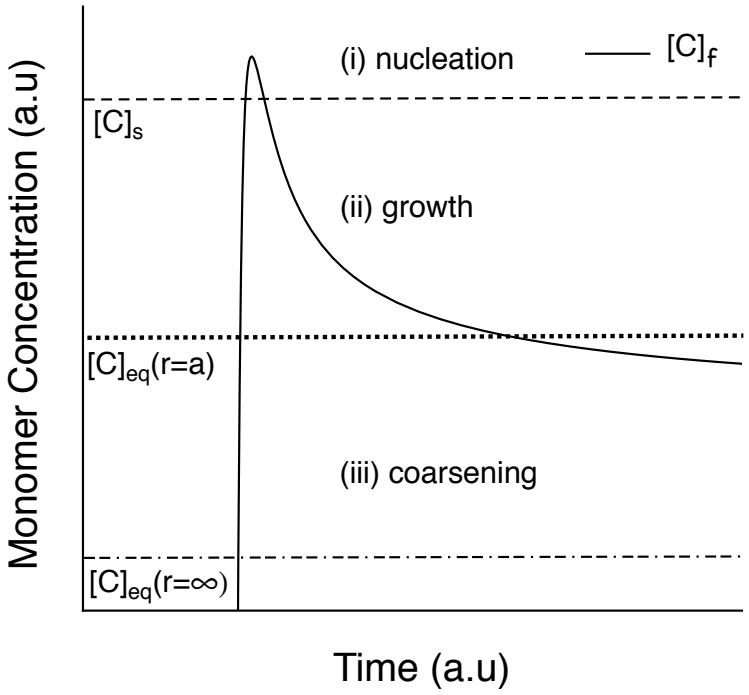

Figure 1.6: Monomer concentration profile during a typical reaction scheme. The critical ($[C]_s$ - dashed line) and equilibrium ($[C]_{eq}(r = a)$ - dotted line) monomer concentrations separate the nucleation/growth phase and the growth/coarsening phase respectively. The concentration of monomer in equilibrium with an infinitely flat surface, $[C]_{eq}(r = \infty)$ (dot-dash line), is plotted for reference

can be seen that the length of the ligands is approximately the same as the radius of the nanocrystal, providing a significant steric barrier to the close approach of other nanocrystals. A prevalent theme throughout this thesis is the effect these ligands have on the nucleation and growth kinetics of nanocrystals and on monomer deposition in general.

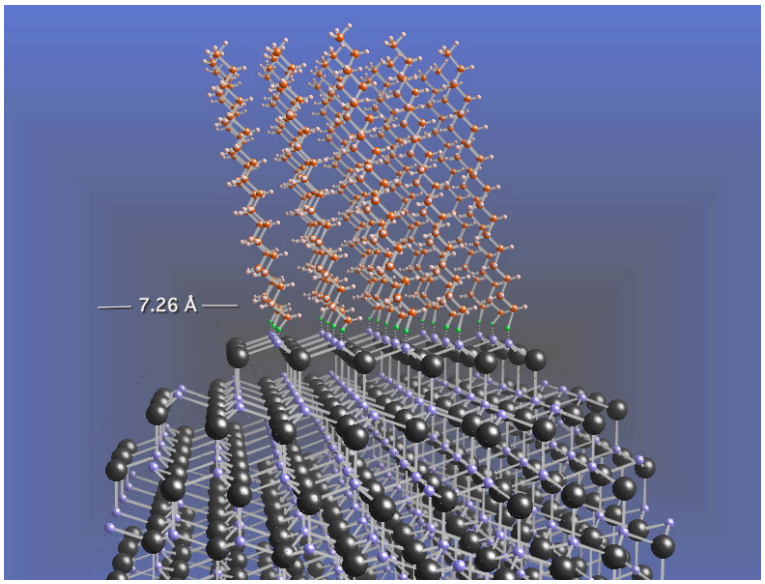

Figure 1.7: Model of a *sim*3 *nm* CdSe nanocrystal with octadecylamine ligands occupying the |002| face. Notably, the ligand length is approximately the same as the radius of the nanocrystal.

Bibliography

[1] V. I. Klimov, A. A. Mikhailovsky, D. W. McBranch, C. A. Leatherdale and M. G. Bawendi. Physical Review B: Condensed Matter and Materials Physics **61**, R13349 (2000).

[2] L. E. Brus. J. Chem. Phys. **79**, 5566 (1983).

[3] L. E. Brus. J. Chem. Phys. **80**, 4403 (1984).

[4] V. I. Klimov, D. W. McBranch, C. A. Leatherdale and M. G. Bawendi. Phys. Rev. B **60**, 13740 (1999).

[5] P. Guyot-Sionnest, M. Shim, C. Matranga and M. Hines. Phys. Rev. B **60**, R2181 (1999).

[6] V. I. Klimov, A. A. Mikhailovsky, D. W. McBranch, C. A. Leatherdale and M. G. Bawendi. Science **287**, 1011 (2000).

[7] V. I. Klimov, A. A. Mikhailovsky, D. W. McBranch, C. A. Leatherdale and M. G. Bawendi. Science (Washington, D. C.) **287**, 1011 (2000).

[8] D. E. Gomez, J. L. van Embden, J. Jasieniak, T. A. Smith and P. Mulvaney. Small **2**, 204 (2006).

[9] C. Bullen and P. Mulvaney. Langmuir **22**, 3007 (2006).

[10] V. K. LaMer, and R. Dinegar. Journal of the American Chemical Society **72**, 4847 (1950).

[11] W. Ostwald. Z. Phys. Chem **34**, 495 (1900).

Chapter 2

Materials, methods and apparatus

The synthesis and characterisation of nanocrystals is multidisciplinary. Knowledge of the chemistry used to synthesise nanocrystals and modify their surfaces as well as the skills to use the instruments that characterise them have been prerequisite to the compilation of this thesis. The aim of this brief chapter is to provide the reader with a reference of those materials, methods and apparatus used throughout this thesis. Further experimental particulars are provided where necessary in the subsequent chapters.

2.1 Materials

Cadmium oxide, (99.99%), zinc acetate dihydrate (99.99%), trioctylphosphine (TOP) (90%), 1-octadecene (ODE) (90%), oleic acid (OA) (90%), tributyl phosphite (90%), sulfur (99.999%) and selenium powder 99.99% were purchased from Aldrich, bis (2,2,4-trimethylpentyl) phosphinic acid (TMPPA) was obtained from Cytec Specialty Chemicals. Octadecylamine (ODA) $\backsim$95% was procured from Merck. Unless otherwise stated, Acetone, chloroform, methanol, ethanol and hexane were all of AR grade and purchased from either Univar or BDH Pty. Ltd. All chemicals and solvents were used without further purification.

2.2 Methods

2.2.1 Reaction set-up

Figure 2.1 shows the typical set-up employed to synthesise nanocrystals. All reactions were accomplished under a positive pressure of nitrogen in a three neck round-bottom flask. The three-neck configuration of the reaction vessel allows for atmospheric control (1), temperature control (4) and precursor injection/aliquot removal (2) respectively.

2.2.2 Washing and Storage

Post synthesis, the as-prepared nanocrystals were purified from their reaction by-products with the aid of a separation funnel (Ref: Figure 2.2). Contrary to precipitation, extraction of the nanocrystals is a less invasive way to remove reaction by-products and has been shown to help prevent aggregation of the nanocrystals. The separation technique involves extracting the product phase* containing the as-prepared nanocrystals using a chloroform-

*The solvent of the product phase consisted predominantly of 1-octadecene in the case of core preparations or a 1-octadecene/octadecylamine mixture in the case of core/shell preparations. Both types of nanocrystals

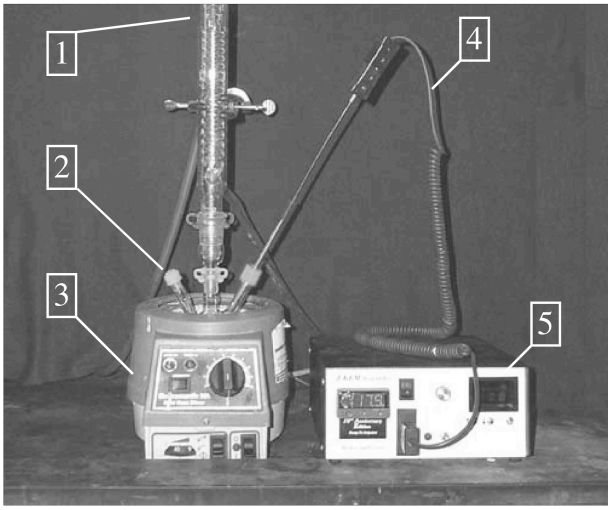

Figure 2.1: Reaction set-up used to synthesise nanocrystals: (1) N_2/vacuum inlet from Schlenk line (not shown); (2) Reaction vesel injection port; (3) Heating mantle;, (4) Themocouple; (5) Themostat.

methanol-acetone mixture ($\backsim$ 2:2:1). After separation the lower phase containing unreacted monomers, ligands and growth solvent is discarded. For each extraction additional amounts of fresh ODE (equal to the amount of remaining reaction mixture) were added along with the other solvents to facilitate separation. Typically three to four separations were necessary to remove most of the unreacted monomer and ligands. At this point the washed nanocrystals in ODE were diluted in a minimum amount of n-hexane and stored in a concentrated state under air in the dark.

2.2.3 Transmission electron microscope grid preparation

The typical methodology employed to prepare a sample of nanocrystals for HRTEM analysis is as follows. The as-prepared colloid was first washed according to the procedure outlined above. Next, a small aliquot ($\backsim$200-300 μL) of the nanocrystals in the ODE/n-hexane mixture was added to an Eppendorff tube and diluted with acetone ($\backsim$1 mL). The resulting cloudy dispersion was then centrifuged at 10000 rpm for several minutes. This process was repeated until a clean dry *plug* was obtained. The *plug* of nanocrystals was then dispersed in

were washed in the same manner.

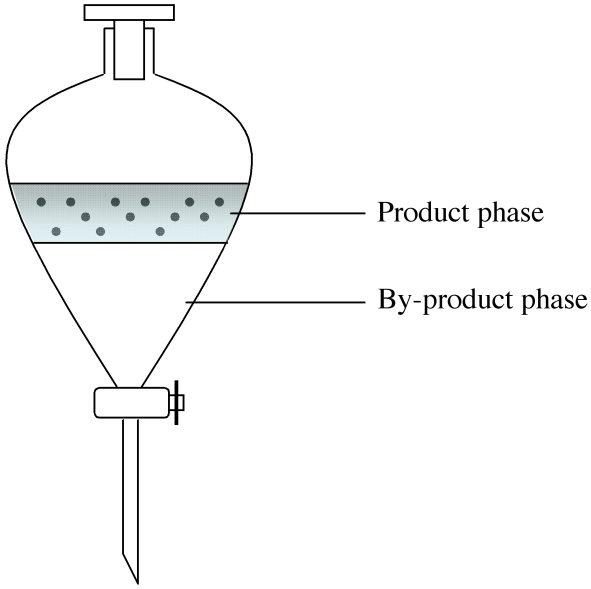

Figure 2.2: The *upper* product phase containing the as-prepared nanocrystals is extracted several times using a chloroform-methanol-acetone mixture. The unreacted monomers, excess ligands and reaction solvent are extracted into the *lower* by-product phase and are discarded.

spectroscopic grade chloroform and diluted to obtain an optical density of $\backsim$0.15-0.2 at the first absorption maximum. 50 μL of this solution was then drop-cast onto a strong carbon coated copper TEM grid (300 mesh). After approximately 5 s the solution was removed by gently touching the side of the grid with the edge of a lint-free tissue. The grid was then placed on a fresh piece of tissue and air dried for 2-3 minutes after which time it was placed into storage for later use. Provided the sample is highly monodisperse, preparation of grids in this manner allows for the creation of 2D arrays of nanocrystals.

2.3 Apparatus

- Absorbance measurements were performed using a Cary 5 UV-vis-NIR spectrometer operated in dual beam reference mode.

- Steady state photoluminescence measurements were conducted using a Varian Eclipse.

- High Resolution Transmission Electron Microscopy was accomplished using either a LEO 922A instrument equipped with a LaB6 emitter or a JEOL 2010. Both instruments were operated at 200 keV. Images were acquired by a slow-scan 2048×2048 pixel CCD on both instruments.

- X-ray diffraction (XRD) was performed using a Bruker D8 ADVANCE powder diffractometer with a graphite-monochromated copper tube source and scintillation counter detector. Spectra were acquired from 15-60 degrees 2θ with a step size of 0.02° and a count rate of 4 seconds using the following settings: Generator Setting: 40 kV @ 35 mA, Wavelength: 1.5406 Å, Antiscatter slit: 1°, Divergence slit: 1°, Receiving slit: 1 mm.

- In-situ time resolved absorbance measurements were aquired using a custom built high temperature resistant absorbance probe from Ocean Optics. The nanocrystals were illuminated in-situ from a Mikropak DH-200-BAL dueterium/halogen UV-VIS-NIR light source. The spectra were collected by a HR-2000 High-resolution Miniature Fibre Optic Spectrometer in 0.1 s intervals with a 10 ms integration time. Before beginning each experiment a reference spectra was acquired from a solution consisting of the growth solvent and the precise concentrations of ligands used in the synthetic procedure.

- Time resolved photoluminescence measurements were aquired on a Horiba Jobin Yvon Fluorolog-3, pulse duration ≤200 ps. Excitation slit widths of 5 nm and an emission band-pass of 5 nm with 0.1 s integration times were employed.

Chapter 3

Nucleation and Growth Kinetics of CdSe cores *

The pioneering work of Henglein [2–5] and Brus [6] on the photochemistry of cadmium sulfide in the early 1980's incited rigorous investigation into the synthesis and optical properties of colloidal semiconductors. A material that has gained particular interest over the past decade is cadmium selenide (CdSe). Early synthetic methods used for the synthesis of CdSe nanocrystals (NCs) employed dimethyl cadmium (DMC) and trioctylphosphine selenide (TOPSe) as the reactive precursors [7]. Owing to its highly volatile nature, DMC is both difficult to work with and permits only limited control of the nucleation and growth kinetics to be achieved. Replacing DMC with acid complexed cadmium precursors [8, 9] allowed for the reactivity of the cadmium source to be altered in dependence upon the type of acid to which it is complexed. The use of such precursors in conjunction with a non-coordinating solvent, such as 1-octadecene, provides a controlled environment for monitoring ligand induced changes to nucleation and growth kinetics [1, 10–12]. In this chapter the competing effects of two ligands, oleic acid (OA) and bis-(2,2,4-trimethylpentyl) phosphinic acid (TMPPA), on the nucleation rate and growth of CdSe nanocrystals in ODE are reported.

*The material presented in the following sections was published in reference [1].

3.1 Introduction

The chemical synthesis of nanocrystals by arrested precipitation depends heavily on the ability of capping agents to prevent particle-particle aggregation in the moments following nucleation. The most efficacious capping agents appear to be small ligands or surfactants which adsorb rapidly to the nascent particle surface and act to minimize the van der Waals interactions between crystallites through a combination of (electro)steric repulsion and solvation forces. These adsorbates usually have a high chemical affinity for the particle surface and a variety of amines, phosphines, carboxylic acids and mercaptans have all been shown to cap semiconducting [7, 8, 13–18], metallic [19–21] and magnetic nanocrystals [22–24].

It is unlikely that these ligands only begin to function after nucleation is complete. Inevitably, such molecules will bind to the monomers and will therefore directly influence the rate of nucleation as well as subsequent growth processes. Prior work conducted in ODE has shown that the capping agent oleic acid can be used to tune the activity of the dissolved metal during synthesis of colloidal CdS [9], CdSe [1, 11], InAs and InP [25]. Alkylamines employed in the synthesis of ZnSe and ZnS nanocrystals in ODE/tetracosane have been shown to improve the activity of the zinc salt precursor [26], resulting in higher particle yields. The effect these ligands exert varies in dependence upon the bond strength between the ligand and the monomer unit and its solubility. A strong bond between the ligand and monomer unit reduces the availability of the free monomer, which in turn reduces the number of monomer collisions that lead to nucleation. However, the more complicated issue is the solubility of the ligand-monomer complex. There will be a tendency for ligands that form soluble complexes with the monomer to leach lattice atoms out of nascent crystallites and dissolve the newly formed embryos. Under certain conditions such ligands actually hinder the formation of the particles they are designed to passivate and stabilize. Thus, ligands that form highly soluble complexes with the monomers will retard nucleation and also enhance the rate of Ostwald ripening. We term these ligands *ripening agents* or *growth promoters*.

Conversely, ligands may bind strongly to the particle surface and form insoluble surface precipitates, kinetically hindering both the dissolution and growth of the embryos. These types of ligands, which we term *nucleating agents*, increase the stability of the evolving embryos and thus actively lower the barrier to nucleation. To optimize particle synthesis it would appear to be useful to have both of these classes of ligands present to effect control over the critical nucleus size, the concentration of embryos formed and their subsequent survival probability.

To test this concept of ligand controlled reaction kinetics, we have examined the nucleation and growth of CdSe nanocrystals in the non-coordinating solvent ODE in the presence of both a *nucleating agent*, TMPPA, and a *ripening agent*, OA. Cadmium selenide has been chosen as a case study based on the recent work of Yu *et al* [27], which correlates the mean particle size of CdSe nanocrystals to the position of the first exciton peak in the ensemble absorption spectrum. The size versus extinction coefficients outlined therein also enable us to calculate the concentration of nanocrystals at any time during the reaction[†]. The values the authors obtained for CdSe are consistent with those obtained from Leatherdale *et al* [28]. The ability to spectroscopically track particle number and size with time permits an in-depth investigation into the factors that modify the nucleation and growth kinetics of CdSe nanocrystals to be conducted.

3.2 Experimental

All reactions were performed in a 25 mL three-neck round-bottom flask under a nitrogen atmosphere. The mother solutions were degassed at 80 °C for $\backsim$ 10 min, then pump/purged several times and subsequently heated to 300 °C for 2 hrs in order to form a homogeneous

[†]The extinction values determined by Yu *et al* (and hence the extrapolated NC concentrations) are accurate to ±10%. The extent of this error may be attributed to a combination of errors associated with HRTEM and AAS measurements. It is important to note that for clarity in viewing the trends, error bars are not displayed in some of the figures presented here, where particle concentrations over time are plotted. In these cases the error is assumed to be ±10%.

mixture containing the precursor. The injection solutions were all freshly prepared prior to injection. The investigations into the effect of varying both the amount and type of each acid were carried out while maintaining a constant reaction volume (accomplished by altering the amount of ODE in the injection or mother solutions). This allows the effect of differing acid concentrations to be accurately contrasted while maintaining comparable temperature profiles during the reactions (Appendix A).

For all reactions the injection temperature was set at 300 °C, and the growth temperature was set at 230 °C. The sampling scheme involved taking aliquots from the stirring nanocrystal batch at the desired time intervals. To obtain quantitative absorbance measurements, 0.100 g of each aliquot were carefully weighed into quartz cuvettes and diluted with 2.00 g of chloroform. These same samples were also used to perform photoluminescence (PL) measurements in order to extract the full width at the half maximum (FWHM), which correlates to the size distribution of the evolving ensemble.

3.2.1 Bis-(2,2,4-trimethylpentyl) phosphinic acid Studies

These reactions employed the method as outlined for the production of "orange" CdSe (Epilogue). All other conditions were maintained constant and only the amount of TMPPA in the injection solution was varied. Specifically, the amounts injected were 0.0 g (0 mM), 0.250 g (37 mM), 0.385 g (56 mM), 0.618 g (90 mM), 0.767 g (112 mM), 1.539 g (225 mM), and 3.079 g (448 mM). Concentrations in brackets indicate the final concentration of TMPPA in the system after injection.

3.2.2 Oleic acid Studies

CdO (0.0603 g, 0.47 $mmol$) was heated with varying amounts of oleic acid; 0.601 g (90 mM), 0.902 g (135 mM), 1.203 g (180 mM), 1.500 g (225 mM), and 2.105 g (315 mM), and made

up to a total volume of 23.66 mL with varying amounts of ODE. It should be noted that for this series of reactions the injection solution was of a constant composition: Se (0.0372 g, 0.47 *mmol*), TOP (1.160 g), TMPPA (0.618 g), and ODE (3.682 g).

3.3 Results

We begin by separately comparing the effects of the two additives, TMPPA and OA on the nucleation and growth of CdSe in ODE. The important parameters are the number of particles formed and surviving as a function of time, their initial size, and the average particle radius, and polydispersity of the ensemble of surviving nuclei over longer times. The data obtained from the investigation will be presented first. Analysis of the data will follow in the discussion section.

3.3.1 Effect of TMPPA on a Typical Reaction Scheme

Figure 3.1A shows the temporal evolution of the absorbance profile as per the synthesis of "orange" CdSe outlined in the Epilogue without the use of TMPPA. Figure 3.1B shows the same reaction under otherwise identical conditions except for the addition of 0.250 g of TMPPA. In spite of the small amount of TMPPA added relative to the OA content (6:1 molar excess of OA) a striking effect on the reaction kinetics is observed. The incorporation of TMPPA alters the reaction in three distinct ways. First, the nucleation begins at much smaller particle sizes, (below 2 nm; $\lambda\text{max} < 500\ nm$ being commonly observed after 5-10 s in reactions with TMPPA). Second, it can also be seen that the size distribution at 5 s is already extremely narrow. Considering the extinction coefficient scales with r^3, comparison of the absorbance spectra at 5 s in Figures 3.1A and 3.1B reveal that the nuclei concentration at this time is much higher in the presence of TMPPA. Finally, from the time scale of the reaction, it is clear that TMPPA retards the overall kinetics of particle growth.

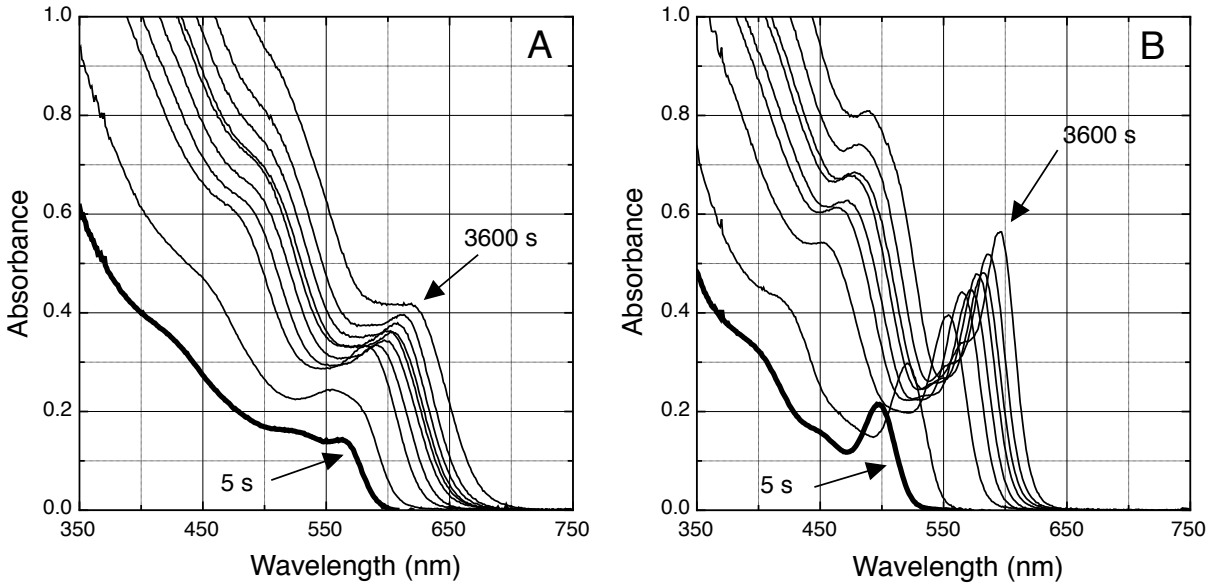

Figure 3.1: Effect of TMPPA concentration on the absorbance profiles obtained during the growth of CdSe; **A**: 0 mM TMPPA; **B**: 37 mM TMPPA. [Cd] = [Se] = 20 mM, [OA] = 225 mM, injection at 300 °C growth at 230 °C. The time intervals for the spectra are; 5, 10, 30, 60, 120, 300, 600, 1200 and 3600 seconds respectively.

3.3.2 Effect of TMPPA on Particle Number and Size

Figure 3.2A shows the CdSe particle concentration as a function of time for reactions performed with [TMPPA] between 0 and 90 mM. The reactions were performed at a fixed concentration of OA (225 mM, $\backsim$10:1 OA:Cd). The temperature profiles were identical in each experiment performed (Appendix A). In all of these reactions, an initial increase in CdSe nanocrystal concentration was observed, which peaked at a maximum concentration, $[\text{CdSe}]_{max}$. This period will be defined as the *nucleation phase*, and typically lasted between 10 and 20 s. It is important to note that particle nucleation extended for a long time after the initial fast injection of monomers.

After the *nucleation phase*, the particle concentration declined rapidly over the following 400 s during which time the majority of particle growth was completed. As can be seen in Figure 3.2A, in the absence of TMPPA, the dissolution of particles in the 60 min after the *nucleation phase* resulted in the annihilation of almost 45% of the initial population from $\backsim$27 μM down to $\backsim$15 μM. By comparison, in the presence of 90 mM TMPPA, the

concentration of nuclei decreased from ∽75 to ∽47 μM, which is only a 37% decrease. It is important to note that this rapid decline in [CdSe] is not due to particle coagulation. Since coagulation rates scale with the square of the particle concentration, one would expect a higher fraction to disappear in the more concentrated nanocrystal solution, contrary to what is observed. The reasons for this rapid decline in particle numbers will be made clear in the forthcoming section. The next regime, which typically runs from around 400 s reaction time up to 3600 s, will be defined as the *growth phase*. This phase is characterized by a monotonic decrease in particle concentration, and concomitant slow growth of the residual particles.

When the concentration of TMPPA was raised from 0 to 90 mM, a three-fold increase in $[CdSe]_{max}$ was observed. Although particle dissolution was seen to occur in all systems, [CdSe] after 60 min growth was still 3 times larger in the reaction incorporating 90 mM TMPPA. The final particle size, after 60 min growth, dropped systematically from 5.5 to 3.6 nm (Figure 3.2B). The FWHM versus time data for these reactions are presented in Table

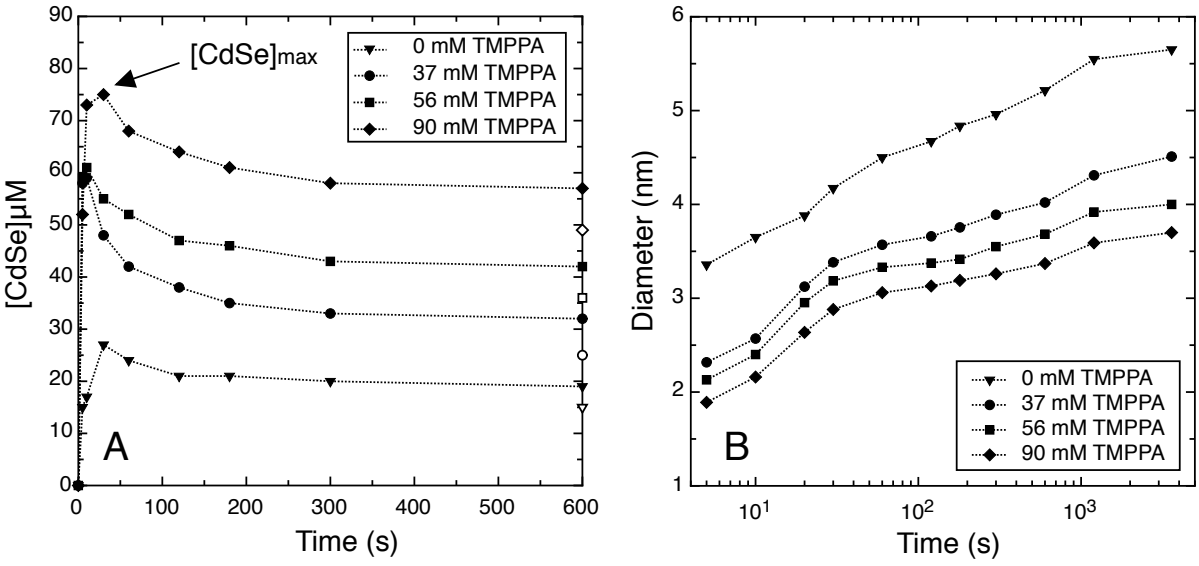

Figure 3.2: **A**: Concentration of CdSe as a function of time. [Cd]=[Se]= 20 mM, [OA] = 225 mM, [TMPPA] varied from 0-90 mM. Only the first 600 seconds of the reaction profile are shown here for clarity, the open symbols correspond to the final CdSe concentration after 60 min growth; **B**: Change in particle diameter as a function of time for the reactions depicted in panel **A**.

Table 3.1: FWHM obtained from the PL spectra taken during the reactions incorporating [TMPPA] between 0 mM and 90 mM. The values listed are in nanometres

Time (sec)	0 mM TMPPA	37 mM TMPPA	56 mM TMPPA	90 mM TMPPA
5	30.6	31.0	31.9	36.5
10	32.3	29.5	27.8	31.4
30	36.2	30.0	28.6	28.9
60	38.5	29.5	28.8	29.4
120	41.2	29.6	28.8	29.6
180	43.2	29.5	28.9	29.7
300	44.2	29.5	28.5	29.3
600	43.2	29.5	28.4	29.4
1200	42.0	29.4	28.4	29.6
3600	41.0	27.7	28.7	29.8

*Corresponding PL spectra in Appendix B

3.3.2. It should be noted that in all cases (except 0 mM TMPPA) the FWHM obtained from the photoluminescence of the particles isolated at the end of the reaction was less than 30 nm. These data highlight that TMPPA prevents dephasing of the size distribution during ripening and growth. From the results in Figure 3.2B, it is clear that the rate of growth of the CdSe particles is highest during the early stages of the reaction when the particle concentrations were in rapid decline.

Figure 3.3A summarizes the major effects of TMPPA on the final concentration of nanocrystals, $[CdSe]_\infty$, and the mean final diameter, D_∞, (60 min growth) for the entire concentration range investigated. The final concentration of nanocrystals was found to increase almost linearly with an increase in [TMPPA] between 0 and 90 mM, which was accompanied by a concomitant reduction of the mean particle size. At 90 mM, a critical point was reached, $[TMPPA]_{crit}$, above which concentration the addition of TMPPA caused a reduction in $[CdSe]_\infty$. At concentrations between 90 and 450 mM $[CdSe]_\infty$ declined from $\backsim$47 to $\backsim$9 μM, whereas D_∞ increased from 3.6 to 5 nm. To gain an appreciation of the extent and rate of ripening we measured the decay in particle concentration, Δ[CdSe], from the peak

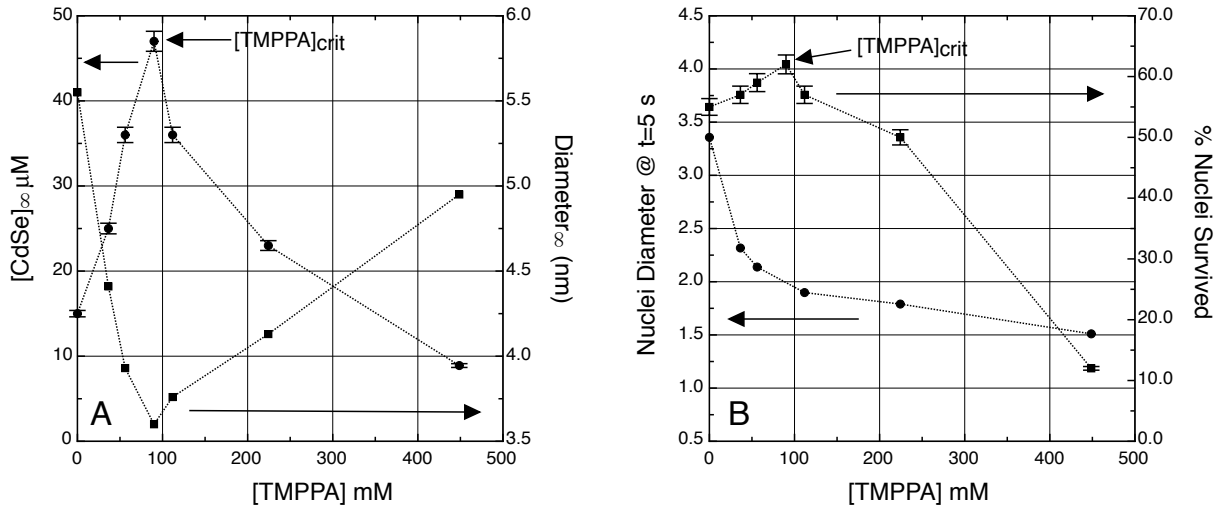

Figure 3.3: **A**: Changes in final particle concentration (60 *min* growth) as a function of [TMPPA] (left axis) and the corresponding changes in final diameter (right axis). [Cd] = [Se] = 20 mM, [OA] = 225 mM, [TMPPA] varied from $0 \rightarrow 450$ mM; **B**: Changes in nuclei size at t = 5 s (left axis) and the % nuclei survived after the end of nucleation up to 60 *min* growth (right axis) as a function of [TMPPA]. In both graphs the critical point, $[\text{TMPPA}]_{crit}$, can be clearly seen.

concentration to the final particle concentration. Figure 3.3B is a plot of the percent nuclei survived, defined as $[\text{CdSe}]_\infty/[\text{CdSe}]_{max}\times 100$, as a function of [TMPPA]. From Figure 3.3, panels A and B, we see that below $[\text{TMPPA}]_{crit}$ both nuclei concentration and the fraction of surviving nuclei increase with increasing [TMPPA], which is ideal for the isolation of smaller particles. This trend is then reversed at concentrations above the critical point. At [TMPPA]=225 mM only sim50% of the original number of nuclei survive and at 450 mM only sim12% of the initial particles are present after 60 *min* growth.

To demonstrate that TMPPA directly affects the nucleation process, it is useful to consider the effect of TMPPA on the size of the primary nuclei (embryos) at the earliest times. Figure 3.3B shows a plot of the mean nuclei diameter at t=5 s as a function of [TMPPA]. A dramatic decrease in initial nuclei diameter is evident as the concentration of TMPPA in the system is increased. A sharp decline in the mean nucleus diameter from 3.3 to 2 nm is seen for concentrations below the critical point, consistent with improved nucleation. Most striking is the fact that adding TMPPA reduces the rate of nuclei dissolution in spite of the fact that the mean size of the nuclei at any time is smaller as the TMPPA concentration

is increased, provided [TMPPA]<[TMPPA]$_{crit}$. Only a slight further reduction in nucleus size ($\backsim$0.5 nm) is apparent above 90 mM despite the fact that the acid concentration is increased five-fold.

3.3.3 Effect of Oleic Acid on Particle Number

For this set of reactions concentrations of OA between 90 mM and 315 mM were employed. It was found that the minimum ratio of oleic acid molecules to cadmium atoms needed to form a stable, homogeneous dispersion of precursor is $\backsim$4:1, thus data from reactions with [Cd]= 20 mM and [OA] < 90 mM are not reliable. The following experiments were therefore conducted while maintaining [TMPPA]= [TMPPA]$_{crit}$= 90 mM, with [OA] being varied from 90 to 315 mM. Contrary to the effects observed with TMPPA, increasing [OA] was found to result in a reduction in the maximum number of particles observed. This is seen in Figure 3.4, which shows a 45 % decline in [CdSe]$_{max}$ as the concentration of OA is increased from 90 to 315 mM. Intriguingly almost the same 45% decrease is seen in final particle concentrations as a function of [OA], revealing that the number of particles that dissolve $\Delta[CdSe] = [CdSe]_{max} - [CdSe]_{\infty}$, remains almost constant within the range investigated. This establishes a clear link between the total number of particles that can form during the *nucleation phase* and the extent of their dissolution. Increasing the oleic acid concentration from 90 to 315 mM resulted in an increase in the size of the nuclei observed 5 s after injection from 1.6 to 2.2 nm (Figure 3.4; inset).

3.3.4 Effect of Oleic Acid on Particle Dissolution

Plotted in Figure 3.5 are the concentration vs time curves for five different reactions where [OA] was varied from 90 to 315 mM. Once again, an initial rise in particle number to a maximum concentration is observed, followed by particle dissolution. As previously determined

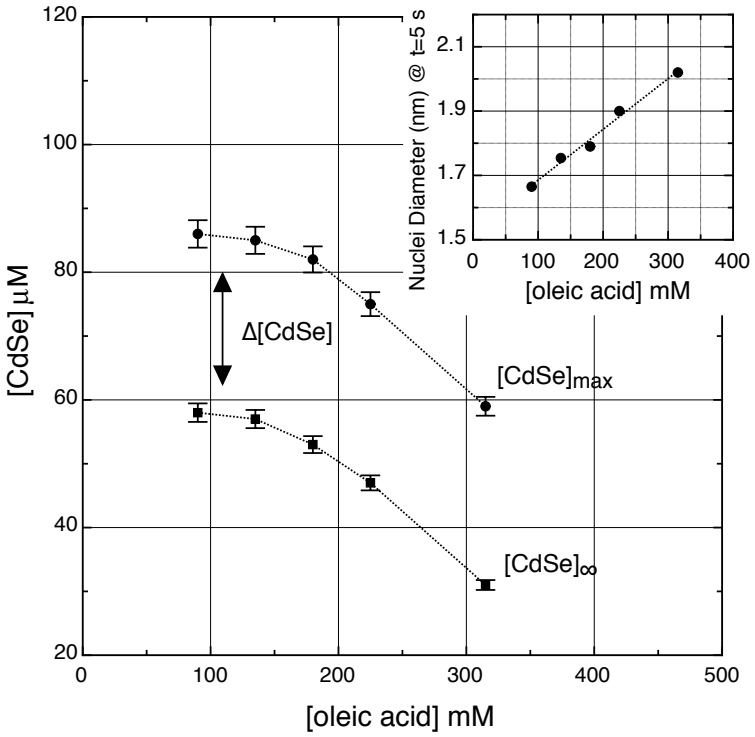

Figure 3.4: Values for the [CdSe] at the maximum particle concentration and at the final particle concentration (60 *min* growth) as a function of [OA] between 90 and 315 mM; **Inset**: Nuclei size at t =5 s for the range of OA concentrations investigated.

Δ[CdSe] for all of the reactions is constant with the [OA] determining the final particle concentration, $[CdSe]_\infty$ (open symbols). However, close examination of the early time data for these reactions reveals steeper declines in particle numbers within the first 300 s in the reactions where more oleic acid was used. One might consider the particle loss to be some sort of back-reaction with unstable nuclei simply redissolving in the solvent, a phenomenon called denucleation [29]. However, by plotting the total volume of the nanocrystal population over time, it was found that there was a constant decrease in free monomer concentration, proving that monomer that leached into the solution from dissolving particles was contributing to a net increase in particle size. We may term this *Early Time Ripening* (ETR). Although ETR is analogous to Ostwald ripening (OR) in its mechanism, it may be distinguished from classical OR as it occurs under conditions where the supersaturation is high enough to promote rapid particle growth through monomer accretion. Because increasing the oleic acid

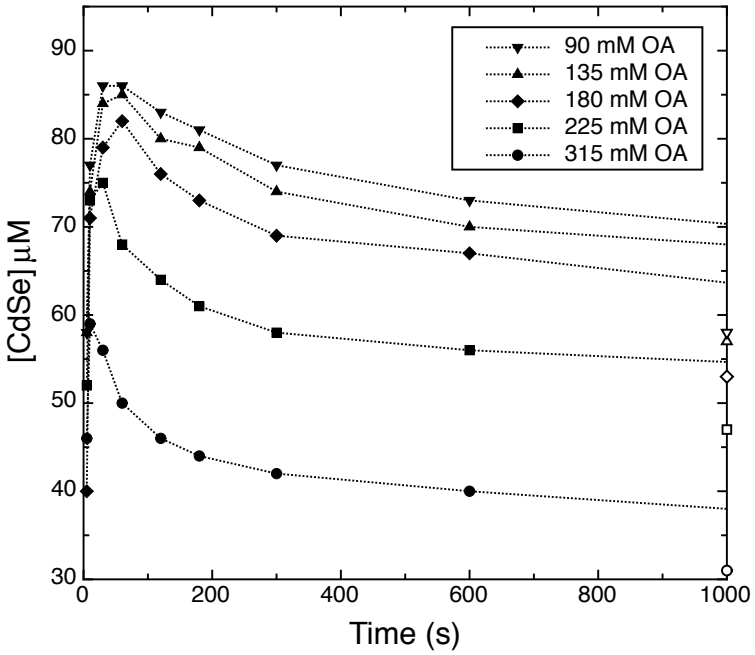

Figure 3.5: CdSe concentration as a function of time for five different oleic acid concentrations. Only the first 1000 seconds are displayed to enhance the effects observed at early times. Note the steeper decline in [CdSe] in the first 300 s for reactions with higher [OA].

concentration reduces the maximum number of particles nucleated and also promotes ETR, an overall faster growth rate is expected for systems with higher OA content. Figure 3.6 is a plot of the rate of change in volume per particle as a function of time. This figure clearly shows faster rates of monomer conversion in systems with higher concentrations of oleic acid. The rates are seen to converge at around 600 s, signifying the end of the fast growth stage (ETR dominant regime). Figure 3.6 (inset) shows the particle diameter as a function of time for the five OA concentrations studied. It is seen that decreasing the amount of OA results in smaller particle sizes after 60 min growth, ranging from 3.3 nm (90 mM OA) to 4.0 nm (315 mM OA). The corresponding FWHM are presented in Table 3.3.4. Analysis of this table reveals that although the FWHM are initially large a quick narrowing of the spectra is seen within the first 30 s, after which time the FWHM remain relatively constant 29.5$\pm$0.5 nm. The narrow FWHM adds validity to the data obtained for these reactions as it proves that growth of the nanocrystals proceeded in a controlled manner, reducing the

error associated with calculating particle numbers due to extensive broadening [27].

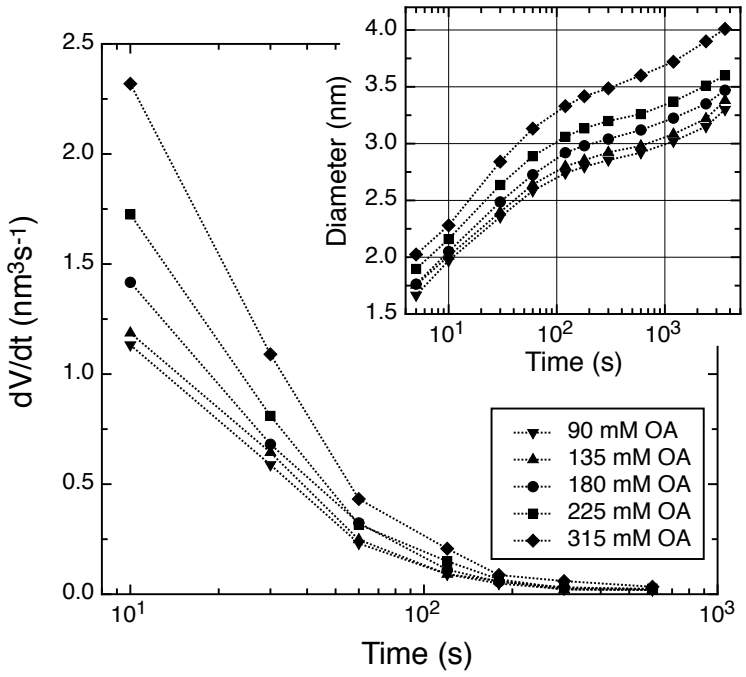

Figure 3.6: The rate of change in the volume per particle is plotted against log time (sec). We see faster particle growth rates in systems with increased [OA] due to both a reduction in the number of growing particles in addition to more pronounced ETR. The growth rates of the different reactions are seen to converge at t = 600 sec signifying the end of ETR and the fast growth stage; **Inset**: The corresponding changes in particle diameter with time are seen for the same reactions.

3.3.5 Effect of TMPPA on Particle Growth

To fully understand the effects of TMPPA, its roles in nucleation and growth must be decoupled. To accomplish this, 0.5 g of TMPPA, [TMPPA]=107 mM, was added 70 s after nucleation of CdSe nanocrystals containing 1.5 g of OA, [OA]=225 mM. Figure 3.7 shows the concentration of particles as a function of time for the full 60 min growth period. As expected both reactions have the same growth profile at times preceding 70 s. This also demonstrates the reproducibility of the synthesis. The introduction of TMPPA (at 70 s) caused particle dissolution to cease almost instantly. An 8% drop in particle number is observed after the injection of TMPPA compared to a 47% drop seen for the control reaction

Table 3.2: FWHM obtained from the PL spectra taken during the reactions incorporating [OA] between 90 mM and 315 mM.

Time (sec)	90 mM OA	135 mM OA	180 mM OA	225 mM OA	315 mM OA
5	N/A	N/A	N/A	36.5	32.1
10	38.0	30.8	31.4	31.4	30.4
30	28.8	28.1	27.2	28.9	29.8
60	28.2	29.4	29.9	29.4	29.0
120	29.6	29.8	29.7	29.6	29.2
180	29.7	29.7	29.9	29.7	29.2
300	29	29.7	29.8	29.3	29.0
600	29	29.5	29.6	29.4	29.0
1200	28.8	29.6	29.4	29.6	29.0
3600	29	29.7	29.9	29.8	29.1

*Corresponding PL spectra in Appendix C

(injection of the same volume of ODE). The size of the particles isolated after 60 min growth time were 4.4 and 4.0 nm for the control and TMPPA samples, respectively.

3.4 Discussion

The results presented demonstrate that nanocrystal nucleation and growth follow different kinetic patterns dependent upon the type and concentration of ligand employed. We have also shown conclusively that ligands may play two completely opposing roles in nanocrystal synthesis, as either *growth promoters* or *nucleating agents*. We will now consider the mechanisms involved in conventional colloid formation, followed by an examination of how ligands modify these mechanisms.

3.4.1 Colloid Formation

In classical colloid chemistry, particles are grown by increasing the monomer concentration first above the equilibrium level and then further above the nucleation threshold. The

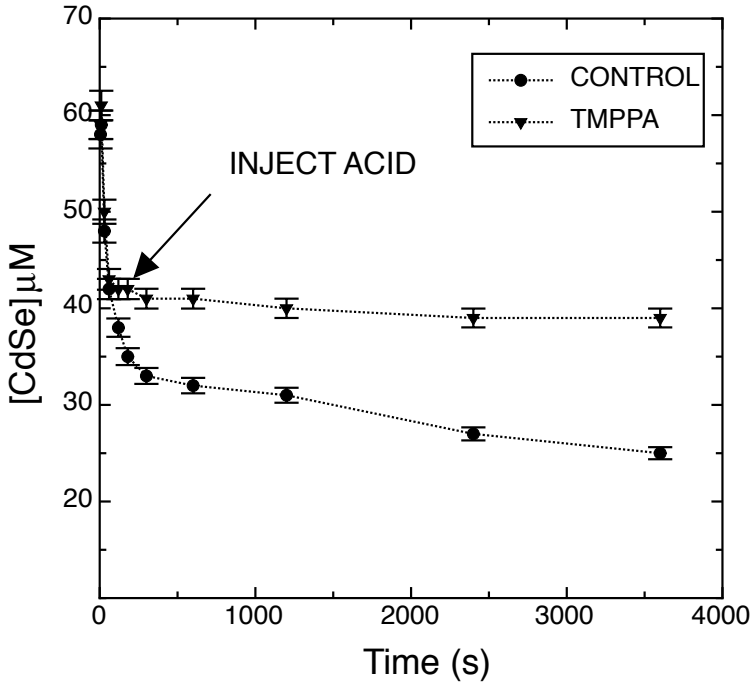

Figure 3.7: Particle concentration as a function of time curves for two reactions: The control (circles) and 0.5 g of injected TMPPA at t=70 s (triangles). Note the almost complete preservation of particle numbers after the injection of TMPPA.

nucleation threshold defines a concentration at which the nucleation of particles becomes kinetically facile. The brief burst of nucleation that ensues serves to reduce the monomer concentration to a level below the nucleation threshold but above the equilibrium level. Subsequently, these primary nuclei grow to form larger particles. Several observations demonstrate that this picture is inadequate to describe the processes that occur during nanocrystal syntheses involving "hot injection" protocols. First, there is an extended *nucleation phase* where the formation of extremely small crystals continues for up to 30 s after injection of the monomer. Secondly, we observe annihilation of many of the initial nuclei in the minutes immediately following nucleation. Thirdly, the number of nuclei formed and their survival probability are intrinsically linked. Finally, we have observed that the early time kinetics are *highly* sensitive to the nature and concentration of the ligands in the reaction medium. The importance of these phenomena are accentuated on the nanoscale where, in sharp contrast

to "classical" colloid formation, the final size of the particles is not much larger than the primary nuclei.

To rationalize these effects we must first understand the factors that control nucleation. The production of a viable nucleus at any given moment requires that it overcome the activation barrier, ΔG_{max}. We relate the radius of the nucleus to the number of monomer units it contains, n, as

$$r_n = r_m n^{1/3} \,, \tag{3.1}$$

where r_n is the radius of a nucleus with n monomers and r_m is the equivalent spherical radius of the monomer as deduced from the molar volume, V_m. In this way we can express ΔG_{max}, a combination of surface and volume free energies, as a function of the number of individual monomer units added as

$$\Delta G_{max} = \sum_{n=1}^{n_{crit}-1} \left| \left\{ 4\pi r_m^2 \gamma [(n+1)^{(2/3)} - n^{2/3}] \right\} - \left\{ k_b T ln S \right\} \right| \,, \tag{3.2}$$

where γ is the surface free energy of the cluster per unit area, S is the supersaturation and k_B and T are the Boltzmann constant and temperature respectively. Monomer units will condense at time intervals given by their instantaneous macroscopic growth rate, to form a nucleus. This process is summarised in Figure 3.8, which shows the energy changes associated with the step-wise formation of a nucleus.

Examination of Figure 3.8 reveals that the barrier to the incorporation of a single monomer unit is largest for the smallest n and that it decreases to zero as $n \rightarrow n_{crit}$. This implies that at early times in the *nucleation phase* the reaction solution will contain extremely high concentrations of monomer, few dimers, even fewer trimers and so on. The sequence of monomer addition increases the total free energy of the embryo until it reaches a critical size, n_{crit}, at which time it traverses from the metastable to the stable regime. The

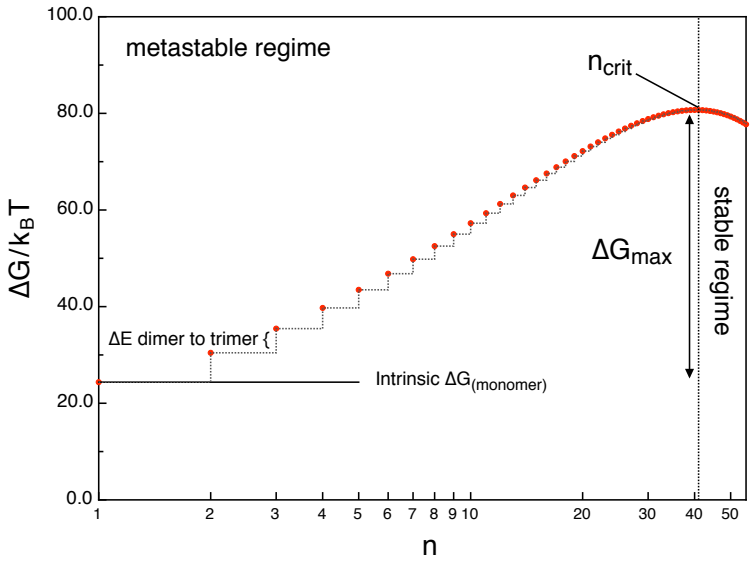

Figure 3.8: Change in the free energy of the embryo as a function of monomer units, n. Data evaluated for a supersaturation of 100 and $\gamma = 0.2 Jm^{-2}$.

barrier to the formation of n_{crit} is indicated by ΔG_{max}, which in the case evaluated here is $\sim$ 57 k_BT for the formation of a cluster containing 42 monomer units. Figure 3.8 gives a holistic view of the free energy changes as monomers form dimers then trimers etc. Although this picture is a highly accurate one, to proceed it is convenient to evaluate the free energy changes in terms of radius, r, as opposed to monomer units, n. The activation barrier to successful collision is therefore given by $\Delta G_{max} = 16\pi\gamma^3/3\Delta G_v^2$, where ΔG_v = -(RT/V_m)lnS is the free energy per unit volume for the condensation of monomer. We note the classical rate constant for nucleation may be written as:

$$R_{nuc} = Aexp\frac{-\Delta G_{max}}{k_B T} , \tag{3.3}$$

where A is a constant related to the frequency of encounters between monomers. Substituting the radius-dependent activation barrier (ΔG_{max}) into Equation 3.3 yields

$$R_{nuc} = Aexp\frac{-16\pi\gamma^3}{3k_B T\Delta G_v^2} . \tag{3.4}$$

For any combination of S, T, and γ, there is a critical radius, r_{crit} (analogous to n_{crit}). In principle, the minimum size of particles at any time in solution should be about $2r_{crit}$, since smaller ones should rapidly dissolve. The value of r_{crit} changes during the reaction, being very low at the moment of injection, but rising at a rate dependent on changes in S and T (with the assumption that γ is independent of cluster size). At any moment, the critical radius of the nuclei is given by

$$r_{crit} = \frac{2\gamma V_m}{RT \ln S} , \tag{3.5}$$

which enables the nucleation rate to be written in terms of the critical radius as

$$R_{nuc} = Aexp\frac{-4\pi r_{crit}^2 \gamma}{3k_B T} . \tag{3.6}$$

As mentioned previously the parameters that determine r_{crit} and thus the rate of nucleation are T, S, and γ. Kinetically, higher temperatures favour nucleation as there is an increased number of monomers with an energy in excess of ΔG_{max}. Thermodynamically, crystal growth from a given solution of monomers is favoured by lower temperatures since the solubility of most crystals increases rapidly at higher temperatures, lowering S drastically. Hot injection synthesis optimizes nanocrystal formation by combining these two effects: Injection of cool reagents into the hot solvent leads to high initial nucleation rates that rapidly decrease due to the fast consumption of monomer and temperature drop resulting from the injection.[‡]

We first consider the long nucleation time. In the systems studied here nucleation is seen to continue for up to 30 s. The sudden temperature drop after injection rapidly acts to decrease the solubility of the monomer. It has been shown that the nucleation rate of crystals is strongly dependent on the extent of temperature quenching, with higher initial nucleation rates observed with increasing quench depths [30]. As the reaction continues to

[‡]A more detailed analysis of the nucleation kinetics is presented in the Chapter 4.

cool, the solubility of the free monomer will decrease likewise, which keeps S high enough to maintain nucleation for some 20-30 s, while the temperature falls from 300 to 250 °C. In the systems investigated here, at around 250 °C, the nucleation rate becomes negligible.

It might be expected that this extended *nucleation phase* would produce very polydisperse nanocrystals, which is not observed in the binary ligand systems investigated here. One reason for this is *nucleation tuning*. The value of r_{crit} will increase over the 30 s that nucleation occurs because S is decreasing. If we assume that at any moment only particles with a radius r$\backsim$ r_{crit} can be nucleated, then both the newly formed nuclei and the existing nuclei will tend to have a similar radius, r_{crit}, throughout the *nucleation phase*.

As calculated from Figures 3.2A and 3.5, and inferred from the temperature profiles, at the end of the *nucleation phase*, temperatures are still high (sim250 °C) and on average $\backsim$40% of the monomer has been consumed. These reaction conditions have a drastic consequence for nanocrystal growth following nucleation. Having significantly depleted the monomer concentration during nucleation, the nanocrystal ensemble begins to ripen immediately after nucleation is complete. In the cases investigated here where S drops extremely rapidly, r_{crit} will be pushed to large sizes (Equation 3.5) by the end of the *nucleation phase*. As r_{crit} is increasing at a rate faster than the smallest nuclei within the ensemble can grow, many of the newly formed nuclei cross back over from the stable into the metastable regions and begin to dissolve (Figure 3.8). Thus, we see distribution kinetics take effect earlier than one would expect in cases of classical Ostwald ripening [31, 32]. It should be noted that a decline in particle number after nucleation has been observed before in nanocrystal systems [10], however, no analysis of this phenomenon was presented. The collective results observed here prove that nucleation, ripening, and growth in nanocrystal hot injection systems occur simultaneously, with the definition of these three phases reliant only on the observation of the dominant process. Classical models of colloid formation such as the LaMer model are inadequate to describe colloid formation on the nanoscale, since they assume that the nucleation burst does not alter the value of S significantly and that all of the seeds created grow

for extended times into much larger particles, in the absence of competing reactions such as fresh nucleation or Ostwald ripening.

3.4.2 Effect of the Ligands OA and TMPPA

The effects of ligands on the early time processes (t $< 300\ s$) are both dramatic and complex. Oleic acid and TMPPA have essentially opposing roles in the growth of CdSe nanocrystals, though both are complexing agents present in the solvent prior to nucleation. We write the basic reactions occurring in the presence of these two additives as

$$Cd(OA)_2 \underset{k_{-1}}{\overset{k_1}{\rightleftharpoons}} Cd^{2+} + 2OA^- \tag{3.7}$$

$$Cd^{2+} + 2OA^- \underset{k_{-2}}{\overset{Se \quad k_2}{\rightleftharpoons}} CdSe \multimap OA + OA^- \tag{3.8}$$

$$Cd(TMPPA)_2 \underset{k_{-3}}{\overset{k_3}{\rightleftharpoons}} Cd^{2+} + 2TMPPA^- \tag{3.9}$$

$$Cd^{2+} + 2TMPPA^- \underset{k_{-4}}{\overset{Se \quad k_4}{\rightleftharpoons}} CdSe \multimap TMPPA + TMPPA^- \tag{3.10}$$

The above reactions have the equilibrium constants, K_1, K_2, K_3 and K_4 respectively. It should be noted that the equilibria responsible for particle formation (Reactions 3.8 and 3.10) involve the introduction of TOPSe. Discussion of the additional equilibrium reactions invoked by this precursor are omitted as all reactions conducted in this investigation contained equal concentrations of TOPSe. As such, any observed perturbation to the reaction kinetics are a direct consequence of the metal binding ligands. For an analysis of the effects of TOP on CdSe formation the reader is referred to reference [12].

Both OA and TMPPA complex the cadmium monomer through Reactions 3.7 and 3.9, lowering the effective supersaturation at all times in solution. The consequence of this is poorer nucleation (Equation 3.6). Another parameter that affects nucleation is the binding strength of the ligand at the particle surface (implicit in the equilibrium of Reactions 3.8 and 3.10). Figure 3.9 displays the free energy changes of a surface site associated with the chemisorption of a ligand. At the ligands equilibrium distance from the surface the free energy (potential energy of the reactive site) is at a minimum. For simplicity we assume that the barrier to adsorption, ΔG_{ads} (energies D and E), which is associated with conformational changes at the surface upon the arrival of the ligand is negligible for the temperatures at which nucleation and growth are conducted [33]. In order for the ligand to desorb from the surface and allow for the incorporation of a monomer unit it must overcome a barrier to desorption, ΔG_{des}, as indicated by energies B and C in Figure 3.9. The height of this barrier will be controlled by a convolution of binding strength of the ligand and its solubility in solution. Any difference in energy at the base of the potential well (surface free energy in the adsorbed state) for particles coated with different ligands is directly related to changes in γ. Strongly bound ligands will tend to reduce γ to a larger extent than weakly adsorbed ligands. The thermodynamic effect is that the stronger the bond between the ligand and the surface the lower the surface free energy and the higher the barrier to desorption, ΔG_{des}. Furthermore, if the solubility product of the ligand monomer complex is particularly large, then driven by the inherent high surface energy of the particle, the system will achieve a lower total free energy through a process where the ligand desorbs from the surface taking a lattice atom into solution (Reaction 3.8 and 3.10).

Drawing from the ideas presented in Sections 1.4.1 and 1.4.2 we now begin to discuss the specific effects of OA and TMPPA on particle formation and growth. It can be seen in Figure 3.5 that $[\mathrm{CdSe}]_{max}$ is reduced as the concentration of OA is increased, and that the particle sizes at all times in Figure 3.6 (inset) are larger for higher OA concentrations,

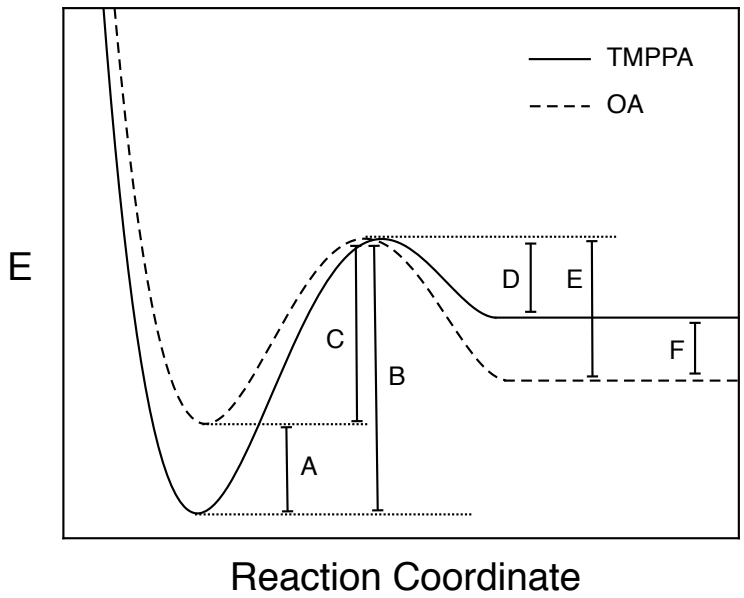

Figure 3.9: A proposed depiction of the energy changes associated with the chemisorption of TMPPA and OA at the surface of a CdSe nanocrystal. **A**; Difference in free energy of the reactive site, in the adsorbed state, between an OA and a TMPPA coated particle. **B** and **C**; Barrier to desorption, ΔG_{des}, for TMPPA and OA respectively. **D** and **E**; Barrier to adsorption, ΔG_{ads}, for TMPPA and OA respectively. **F**; Difference in the free energy of the reactive site, in the desorbed state between an OA and a TMPPA coated particle.

both of which indicate a lowering of S. The consequence of this is that r_{crit} is always higher in the presence of greater OA concentrations. This causes an increase in the annihilation rate of nascent particles, as seen in the data of Figure 3.5, where the ripening rate increases steadily as the concentration of OA is increased. These trends are consistent with a ligand that binds with only a moderate strength to the particle surface and forms a complex that is highly soluble in the reaction medium, resulting in a overall low value for K_2.

The effects of TMPPA can be understood as follows. The data in Figure 3.2 show that TMPPA dramatically increases particle numbers and results in smaller particle sizes at all reaction times. Thus, it may be inferred that the size-dependent solubility of the particles in the reaction solution is being decreased. This dramatic improvement in nucleation conditions appears to be due to the fact that TMPPA forms a strong insoluble surface complex (high K_4). In this manner, TMPPA will aid the precipitation of embryos by reducing their solubility, through a significant lowering of γ upon adsorption. Further proof of this mechanism

is seen in Figure 3.7 wherein addition of excess TMPPA caused an almost complete halt to particle dissolution, such that it was possible to maintain the final nanocrystal concentration at a level $\sim 40\%$ higher than in the absence of the injection.

Finally, from Figure 3.3, panels A and B, we note that as we add more TMPPA, the nuclei size decreases rapidly to about 1.9 nm. Further additions lower this value only slightly, but Ostwald ripening accelerates, and the final particle size increases due to the lower survival probability of the nuclei. The precise reasons for this optimal concentration are not clear, but presumably, as more TMPPA is added, the crystals are nucleating at such small sizes that the crystallites dissolve and ripen onto more stable crystallites before they can grow. Since the nuclei size is still decreasing in systems with higher concentrations of TMPPA, its effects as a *nucleating agent* are still increasing, but the resultant nuclei are becoming less viable. Even with the extra stability provided by TMPPA, particles nucleated with diameters below 2 nm are highly unstable with respect to dissolution and ripening. This places a lower limit on the particle size that can be stably isolated in hybrid TMPPA/OA systems.

3.4.3 Combining OA and TMPPA

At first sight, the beneficial effects of TMPPA would lead one to suppose that for nanocrystal synthesis zero OA and controlled addition of TMPPA would provide the optimal control over the particle size and growth kinetics. In fact, we believe that a mixture of both *nucleating agents* and *ripening agents* are necessary to provide the optimal conditions for nanocrystal synthesis in solution. To synthesise large CdSe nanoparticles, with close to bulk optical properties, high [OA] are required to retard the nucleation rate and ensure maximum ripening of the nuclei. However, this leads to the formation of particles with a broad size distribution. The introduction of excess monomer can be used to counter this effect such that focusing of the size distribution occurs at intermediate reaction times [34]. However, this process is often time consuming and difficult to control. By adding TMPPA a narrow initial size

distribution can be achieved and maintained even at high [OA]. Then by exploiting ETR using oleic acid, monodisperse populations of intermediate sizes or near bulk particles can be obtained in a single step reaction.

Furthermore, even at $[\text{TMPPA}]_{crit}$ and the lowest OA concentrations, the smallest isolatable particles were $sim3\ nm$ in diameter. Attempts to circumvent this bottleneck by reducing the overall monomer concentrations meet with difficulty due to the reduction in supersaturation needed for good nucleation. The production of the smallest CdSe nanocrystals requires both extensive nucleation and very slow growth rates. In TMPPA only systems, green or even blue emitting CdSe can be isolated at long reaction times.

3.5 Concluding Remarks

We have found that the two ligands, oleic acid and bis-(2,4,4-trimethylpentyl)phosphinic acid have remarkably different effects on the nucleation and growth of CdSe, despite the fact that both are basically anionic surfactants, which complex cadmium ions. The major reason for their different behaviour lies in the solubility of their respective complexes. Oleic acid accelerates particle ripening and growth and inhibits nucleation, where as TMPPA catalyses nucleation and drastically impedes growth, enabling smaller nanocrystals to be isolated.

It is found that ETR determines the overall survival probability of the nuclei and the resultant longer-term growth behaviour. By combining both ligands, the nucleation and ripening can be controlled systematically, enabling the isolation of high yields of nanocrystals with predictable sizes.

3.6 *Epilogue*

Optimised Synthesis of CdSe Nanocrystal Batches

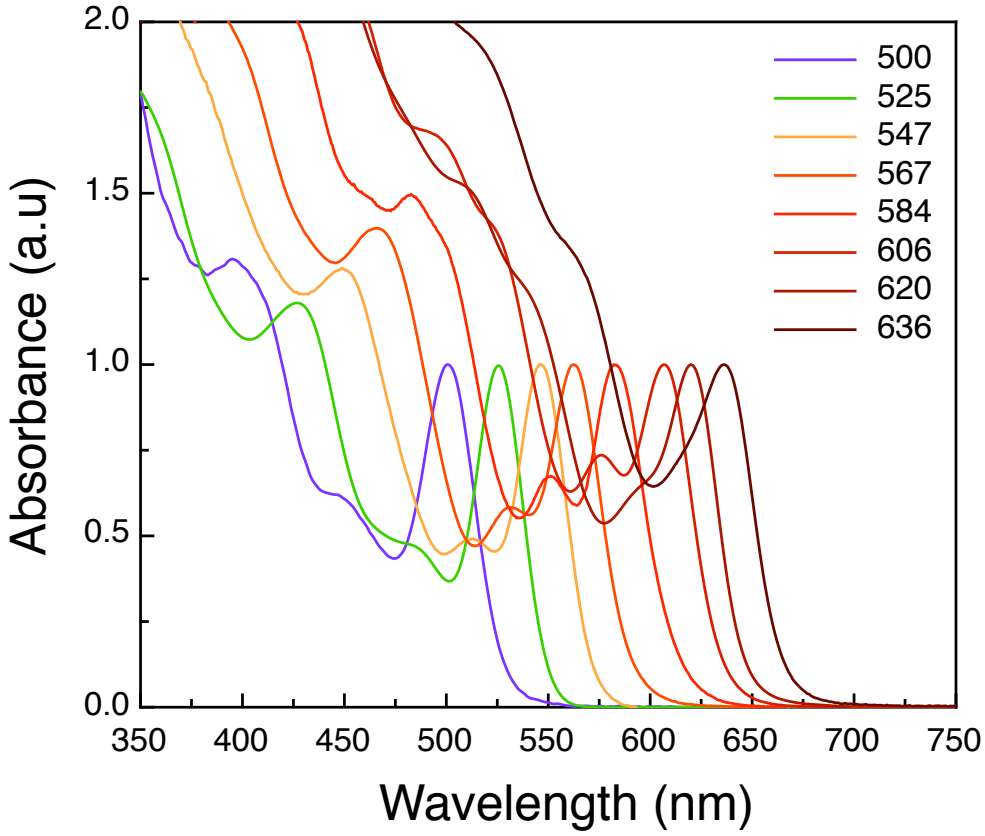

Figure 3.10: Absorption spectra of six nanocrystal batches with sizes ranging from 2.3 *nm* to 6.7 *nm* as outlined below

The following optimised procedures generate CdSe nanocrystals with mean diameters between $\sim$ 2.4 *nm* and $\sim$ 6.8 *nm*, corresponding to first exciton absorption maxima in the range *sim*500-640 *nm*.

2.4 *nm* CdSe (Green PL)

0.03 *g* of CdO, 0.600 *g* of TMPPA, and 10 *g* of ODE were heated at 300 °C for 6 *hrs*, then heated to 315 °C at which time 0.158 *g* of selenium in 1.16 *g* of TOP mixed with 6.0 *g* of ODE was swiftly injected. The temperature was then allowed to drop to 190 °C for the growth of the nanocrystals (20 *min* growth, λmax at 510 *nm*, FWHM 29 *nm*). Maintaining the same conditions as above but transferring 2.00 *g* of ODE from the mother solution into the injection solution, to ensure a faster cooling rate, and allowing the batch to cool to room temperature after injection resulted in the reliable production of 2.2 *nm* CdSe (λmax at 490 *nm*, FWHM 30 *nm*).

2.9 *nm* CdSe (Yellow PL)

0.03 *g* of CdO, 0.300 *g* of TMPPA, and 12 *g* of ODE were heated at 300 °C for 6 *hrs*, at which time 0.158 *g* of selenium in 1.16 *g* of TOP mixed with 4.0 *g* of ODE and 0.300 *g* of TMPPA was swiftly injected. The temperature was then allowed to drop to 200 °C for the growth of the NCs (60 *min* growth, λmax at 545 *nm*, FWHM 30 *nm*).

3.5 *nm* CdSe (Tangerine PL)

0.06 *g* of CdO, 1.500 *g* of OA, and 12 *g* of ODE were heated at 300 °C for 2 *hrs*, at which time 0.0372 *g* of selenium in 1.16 *g* of TOP mixed with 3.55 *g* of ODE and 0.767 *g* of TMPPA was swiftly injected. The temperature was then allowed to drop to 230 °C for the growth of the NCs (60 *min* growth, λmax at 570 *nm*, FWHM 29 *nm*).

4.4 *nm* CdSe (Orange PL)

0.06 *g* of CdO, 1.500 *g* of OA, and 12 *g* of ODE were heated at 300 °C for 2 *hrs*, at which time 0.0372 *g* of selenium in 1.16 *g* of TOP mixed with 4.00 *g* of ODE and 0.250 *g* of TMPPA

was swiftly injected. The temperature was then allowed to drop to 230 °C for the growth of the nanocrystals (60 *min* growth, λmax at 595 *nm*, FWHM 31 *nm*).

5.6 → 6.8 *nm* CdSe (Red → Deep Red PL)

Using identical conditions as outlines for the production of 4.4 *nm* CdSe nanocrystals but increasing the initial amount of oleic acid from 1.5 to 1.7 *g* allows 5.6 *nm* CdSe (red PL), λmax at 620 *nm*, FWHM 29 *nm* to be isolated after 60 *min* reaction time. A further increase to 1.8 *g* OA, results in 6.72 *nm* CdSe nanocrystals (deep red PL), λmax at 638 *nm*, FWHM 32 *nm* after 80 *min* reaction time (near bulk CdSe).

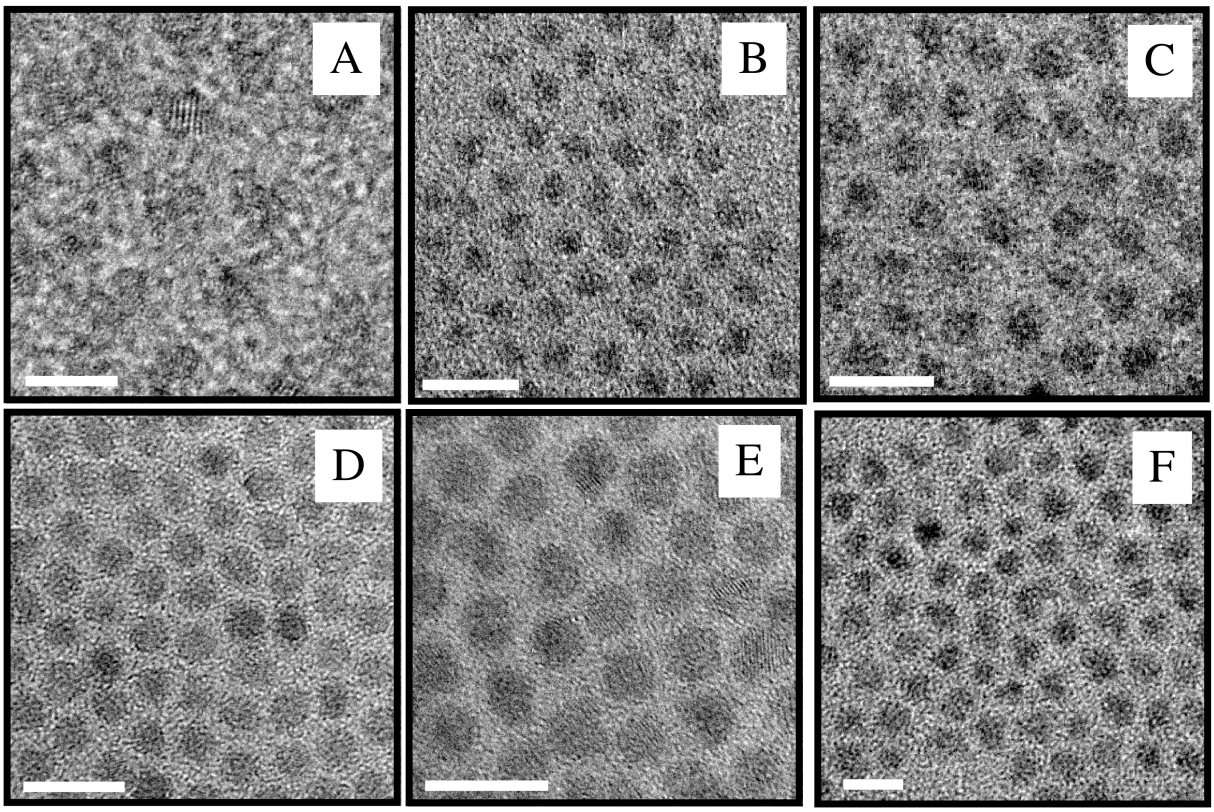

Figure 3.11: Randomly selected HRTEM images of spherical CdSe cores with sizes in the range 2.4 *nm* to 6.1 *nm*. The mean diameter established from measurements of no less than 200 particles are **(A)** 2.5 *nm*; **(B)** 3.0 *nm*; **(C)** 3.4 *nm* and **(D)** 4.0 *nm*. **(E)** 4.9 *nm*. **(F)** 6.1 *nm*

Bibliography

[1] J. L. van Embden and P. Mulvaney. Langmuir **21**, 10226 (2005).

[2] A. Henglein. Journal of Physical Chemistry **86**, 2291 (1982).

[3] L. Spanhel, M. Haase, H. Weller and A. Henglein. J. Am. Chem. Soc. **109**, 5649 (1987).

[4] L. Spanhel, H. Weller, A. Fotjik and A. Henglein. Ber. Bunsenges. Phys. Chem. **91**, 88 (1987).

[5] M. Hasse, H. Weller and A. Henglein. Journal of Physical Chemistry **92**, 4706 (1988).

[6] R. Rossetti and L. E. Brus. J. Phys. Chem. **86**, 4470 (1982).

[7] C. B. Murray, D. J. Norris and M. G. Bawendi. J. Am. Chem. Soc. **115**, 8706 (1993).

[8] Z. A. Peng and X. Peng. J. Am. Chem. Soc. **123**, 183 (2001).

[9] W. W. Yu and X. Peng. Angewandte Chemie, International Edition **41**, 2368 (2002).

[10] L. Qu, W. W. Yu and X. Peng. Nano Letters **4**, 465 (2004).

[11] C. R. Bullen and P. Mulvaney. Nano Letters **4**, 2303 (2004).

[12] J. Jasieniak, C. Bullen, J. L. van Embden and P. Mulvaney. The Journal of Physical Chemistry B **109**, 20665 (2005).

[13] L. Qu, Z. A. Peng and X. Peng. Nano Letters **1**, 333 (2001).

[14] L. Balogh, C. Zhang, S. O'Brien, N. J. Turro and L. Brus. Chimica Oggi **20**, 45 (2002).

[15] J. Aldana, Y. A. Wang and X. Peng. Journal of the American Chemical Society **123**, 8844 (2001).

[16] D. V. Talapin, A. L. Rogach, I. Mekis, S. Haubold, A. Kornowski, M. Haase and H. Weller. Colloids & Surfaces A Physicochemical & Engineering Aspects—Colloids & Surfaces A: Physicochemical & Engineering Aspects **202**, 145 (2002).

[17] A. Rogach, S. Kershaw, M. Burt, M. Harrison, A. Kornowski, A. Eychmuller and H. Weller. Advanced Materials **11**, 552 (1999).

[18] C. B. Murray, S. H. Sun, W. Gaschler, H. Doyle, T. A. Betley and C. R. Kagan. IBM Journal of Research & Development **45**, 47 (2001).

[19] A. Fojtik, P. Mulvaney, T. Linnert, M. Giersig and A. Henglein. Berichte der Bunsen-Gesellschaft **95**, 770 (1991).

[20] A. Henglein. Journal of Physical Chemistry **97**, 5457 (1993).

[21] G. Schmid. *Nanoparticles-From Theory to Application* (WileyVHC: Weinheim, Germany, 2004).

[22] S. H. Sun, C. B. Murray, D. Weller, L. Folks and A. Moser. Science **287**, 1989 (2000).

[23] D. V. Talapin, E. V. Shevchenko and H. Weller. Nanoparticles 199–238 (2004).

[24] M. Hilgendorff. *Encyclopedia of Nanoscience and Nanotechnology*, vol. 10 (American Science Publications: Stevenson Ranch, CA, 2003).

[25] D. Battaglia and X. Peng. Nano Letters **2**, 1027 (2002).

[26] L. S. Li, N. Pradhan, Y. Wang and X. Peng. Nano Letters **4**, 2261 (2004).

[27] W. W. Yu, L. Qu, W. Guo and X. Peng. Chemistry of Materials **15**, 2854 (2003).

[28] C. A. Leatherdale, W. K. Woo, F. V. Mikulec and M. G. Bawendi. J. Phys. Chem. B **106**, 7619 (2002).

[29] G. Madras and B. J. McCoy. Chem. Eng. Sci. **58**, 2903 (2003).

[30] H. Wennerstrom, J. Morris and U. Olsson. Langmuir; **13**, 6972 (1997).

[31] G. Madras and B. J. McCoy. Chemical Eng. Sci. **57**, 3809 (2002).

[32] D. V. Talapin, A. L. Rogach, M. Haase and H. Weller. J. Phys. Chem. B **105**, 12278 (2001).

[33] P. W. Atkins. *Physical Chemistry*. 5th ed. (Oxford University Press, Oxford, 1994).

[34] X. Peng, J. Wickham and A. P. Alivisatos. Journal of the American Chemical Society **120**, 5343 (1998).

Chapter 4

The evolution of colloidal nanocrystals: Theory and Modelling

In this chapter, through the use of a population balance equation (PBE), the nucleation and growth of nanocrystals evolving under various initial reaction conditions are simulated. The evolution of a distribution of nanocrystals is distinct from the evolution of larger micron-sizes species as the final crystal sizes are not much larger than the primary nuclei. As a consequence the final outcome of a nanocrystal synthesis i.e. mean crystal size, concentration and standard deviation is almost solely determined by the end of the nucleation phase. As concluded from the results presented in Chapter 3, the early stages of NC synthesis involves simultaneous nucleation, growth and coarsening. The simulations performed here are able to replicate these conditions, providing insight into the factors that govern these early time processes as well as the consequences they have at longer reaction times.

4.1 Introduction

Experimental investigations designed to reveal the underlying mechanisms of colloid nucleation and growth have spanned many decades [1–8]. Scientific curiosity as well as the increasing number of technologies that use colloid particles continues to fuel this interest. Complementary to these experimental investigations, mathematical investigations on colloid formation have also been conducted [9–11]. In addition, numerical models describing the nucleation and growth of near-micrometer-sized colloids [12] and binary alloys [13–15] as well as Ostwald ripening [16, 17] have been reported. Other studies have focused solely on the numerical issues involved in effectively modelling mass transport [18–21].

Despite the plethora of literature on the numerical modelling of colloid formation, to date there exists few reports that contain simulations of nanoparticle nucleation and growth [22–27], presumably due to the fact that reliable experimental data on such systems has emerged only recently. Although valuable information can be gleaned from such reports, most of the current models on nanoparticle evolution suffer from a failure to accurately simulate nucleation and growth under experimentally realistic conditions. These inaccuracies typically arise from assigning inappropriate values to the diffusion coefficient as well as employing unrealistic monomer concentrations. As such, in order to gain the greatest insight into the mechanisms that govern nanocrystal nucleation and growth (wherever feasible) care was taken to ensure the simulation conditions were as close to realistic experimental conditions as possible.

In this chapter we focus on simulating the nucleation and growth of nanocrystals from a homogeneous solution of monomer in the liquid phase. We begin with a discussion of monomer diffusion in general and present expressions for the particle growth rates in both the diffusion limit and the reaction limit. Using steady state assumptions we then progress and derive a more flexible expression for the growth rate that is tuneable between these limits. In the framework of equilibrium theory the derivation of the nucleation rate is then

presented. To ensure mass balance, a governing equation that keeps track of the movement of monomer is then outlined. Next, the details of the numerical scheme employed to solve the relevant rate equations is presented along with test simulations that highlight the stability and accuracy of the scheme. Finally, simulations on NC growth only, NC growth via the sequential injection of monomer and simultaneous nucleation and growth are presented. It should be noted that although the simulations performed here have focused on the formation of nanocrystals in the liquid phase via the "hot injection" method, the governing equations and numerical scheme may be directly applied to the formation of micron-sized particles as well as to different reaction strategies.

4.2 Monomer diffusion

The diffusion of monomer occurs in the presence of a difference in chemical potentials between two given regions of space. Specifically it occurs from a region where its chemical potential is high to one where it is low. As stated by Fick′s first law the flux, J ($molm^{-2}s^{-1}$), of monomer toward a given surface is proportional to the product of the concentration gradient, $d[C]/da$, surrounding the surface and the diffusion coefficient, D (m^2s^{-1}). Given this information we express the total flux (I) of molecules through a diffusion sphere of radius a as

$$\mathrm{I_{dif}} = 4\pi a^2 J = 4\pi a^2 D \left.\frac{d[C]}{da}\right|_{a \geqslant r} . \tag{4.1}$$

We now calculate the concentration of monomer at any distance from the surface by integrating this equation. To do so we must first establish some boundary conditions. For a diffusion sphere of radius, δ, $[C]_a$=$[C]_{(r+\delta)}$. The boundary conditions are that at $(r+\delta)$ the concentration of monomer is equal to the value in the bulk solution ([C]=$[C]_b$), and that at $a = r$ the concentration of monomer is equal to the interfacial concentration ([C]=$[C]_i$). Also under steady state conditions I_{dif} is a constant independent of a, thus:

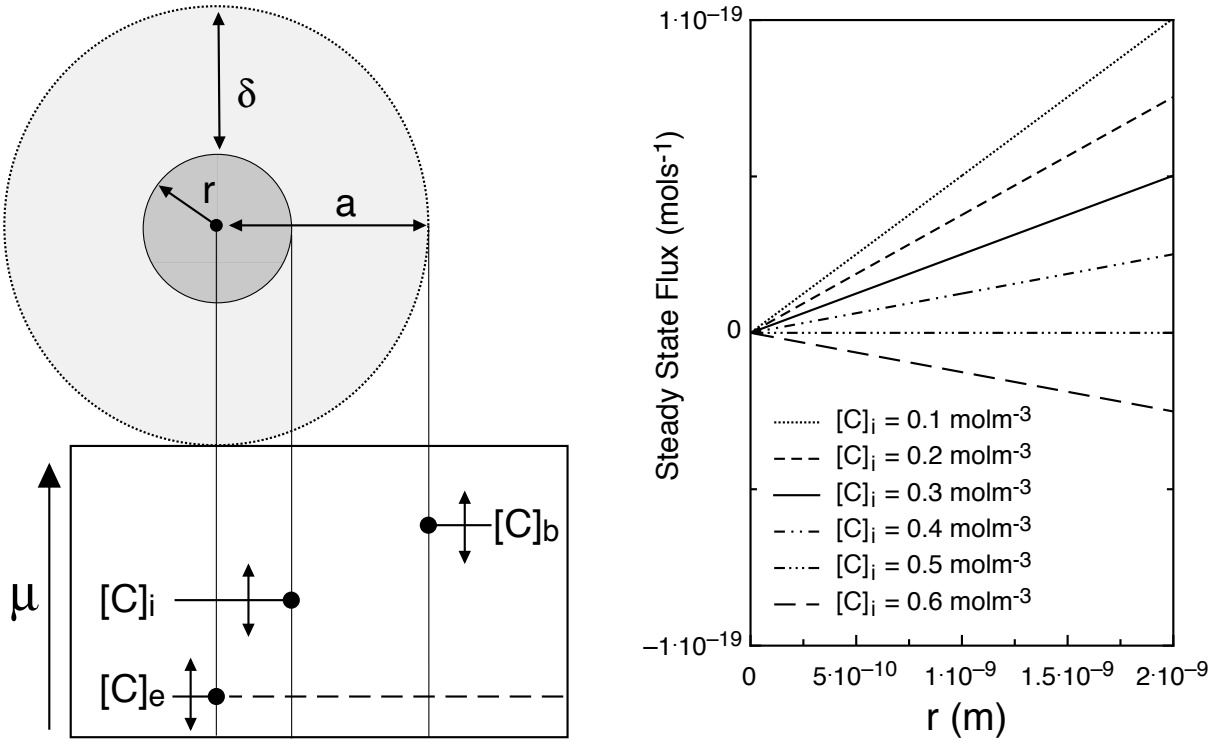

Figure 4.1: **(left)** An isolated particle of radius r surrounded by a diffusion layer of radius δ. $[C]_b$ and $[C]_i$ are the bulk and interfacial monomer concentrations respectively. These concentrations and the chemical potential they exert will change as monomer is consumed during the growth of a particle (indicated by the arrows). When these concentrations become equal at some $[C]_e$, there is no flux of monomer either into or out of the diffusion sphere. **(right)** A plot of the steady-state flux as a function of particle radius for varying interfacial concentrations at a fixed $[C]_b$ of 0.5 $molm^{-3}$. The flux is seen to vary linearly as a function of particle size (given the diffusion limited condition). All fluxes are positive (*toward* the surface) when $[C]_i < [C]_b$, become zero at $[C]_i = [C]_b$, denoted the equilibrium condition $[C]_e$, and become negative (*away* from the surface) for $[C]_i > [C]_b$. In this way the condition that flux always occurs down a concentration gradient is satisfied.

$$\int_{[C]_i}^{[C]_b} d[C] = \frac{I_{dif}^{SS}}{4\pi D} \int_{a=r}^{r+\delta} \frac{da}{a^2} \, . \tag{4.2}$$

After some minor algebraic manipulation we obtain the total steady-state flux of momomer (in $mols^{-1}$) toward the surface of the particle:

$$I_{dif}^{SS} = \frac{4\pi D r(r+\delta)}{\delta}([C]_b - [C]_i) \, . \tag{4.3}$$

With the assumption that $r \lll \delta$ for nanoscale systems [12, 28], then the total flux of

molecules incident at the particle surface may be expressed as:

$$I_{dif}^{SS} = 4\pi r D\left([C]_b - [C]_i\right) \ . \tag{4.4}$$

Similarly, for a first order surface reaction, the flux of monomer incorporated into a spherical particle is given by the difference in interfacial, $[C]_i$, and equilibrium, $[C]_e$, monomer concentrations:

$$I_{react}^{SS} = 4\pi r^2 k_r([C]_i - [C]_e) \ , \tag{4.5}$$

where k_r is the rate constant for surface reaction. Given that I^{SS} scales with volume over time, it can be expressed through the growth rate as:

$$I^{SS} = \frac{d}{dt}\frac{4\pi r^3}{3V_m} = \frac{4\pi r^2}{V_m}\frac{dr}{dt} \ , \tag{4.6}$$

where V_m is the molar volume of the monomer. To proceed, we must make certain assumptions concerning the limiting rates of the reaction. In the pure diffusion limit, monomer reacts instantly *at* the surface, hence $[C]_i \cong [C]_e$. Combining Equations 4.4 and 4.6 after some algebraic manipulation, we obtain:

$$\frac{dr}{dt} = \frac{DV_m}{r}([C]_b - [C]_e) \ . \tag{4.7}$$

In the pure reaction limit, monomer diffuses to the particle surface but reacts at a rate dependent upon the nature and concentration of adsorbates in solution, hence $[C]_i \cong [C]_b$. Combining Equations 4.5 and 4.6 we obtain:

$$\frac{dr}{dt} = k_r V_m([C]_b - [C]_e) \ . \tag{4.8}$$

The equilibrium concentration, $[C]_e$, is given by the Gibbs-Thomson equation:

$$[C]_e = [C]^0_\infty \exp\left\{\frac{2\gamma V_m}{rRT}\right\} , \tag{4.9}$$

where $[C]^0_\infty$ is the concentration of monomer in equilibrium with an infinitely flat surface. Defining $S = [C]_b/[C]^0_\infty$, where S is the supersaturation, we may recast this simple expression into a similar form to Equation 4.9 by assuming a critical radius, r_{crit}, that is dependent on S:

$$[C]_b = [C]^0_\infty \exp\left\{\frac{2\gamma V_m}{r_{crit}RT}\right\} , \tag{4.10}$$

where r_{crit}=$[2\gamma V_m/RTIn(S)]$. Retaining only the first term in the Taylor expansion of Equations 4.9 and 4.10 followed by substitution into Equations 4.7 and 4.8 respectively we obtain expressions for the growth rate in both the diffusion and reaction limits:

$$\frac{dr}{dt} = \frac{2\gamma D V_m^2 [C]^0_\infty}{rRT}\left[\frac{1}{r_{crit}} - \frac{1}{r}\right] , \tag{4.11}$$

$$\frac{dr}{dt} = \frac{2\gamma k_r V_m^2 [C]^0_\infty}{RT}\left[\frac{1}{r_{crit}} - \frac{1}{r}\right] . \tag{4.12}$$

The form of these equations was first outlined by Sugimoto *et al* [12].

Tracing these two equations back to their origins (Equations 4.7 and 4.8) we find that in both cases if the equilibrium concentration, $[C]_e$, is greater than the bulk concentration, $[C]_b$, the net flux will be *away* from the particle surface and particle dissolution will occur. However, if $[C]_e$<$[C]_b$ the net flux will be *toward* the particle surface and the particle will grow.

Figure 4.2 shows the normalised radial dependence of the growth rate under diffusion and

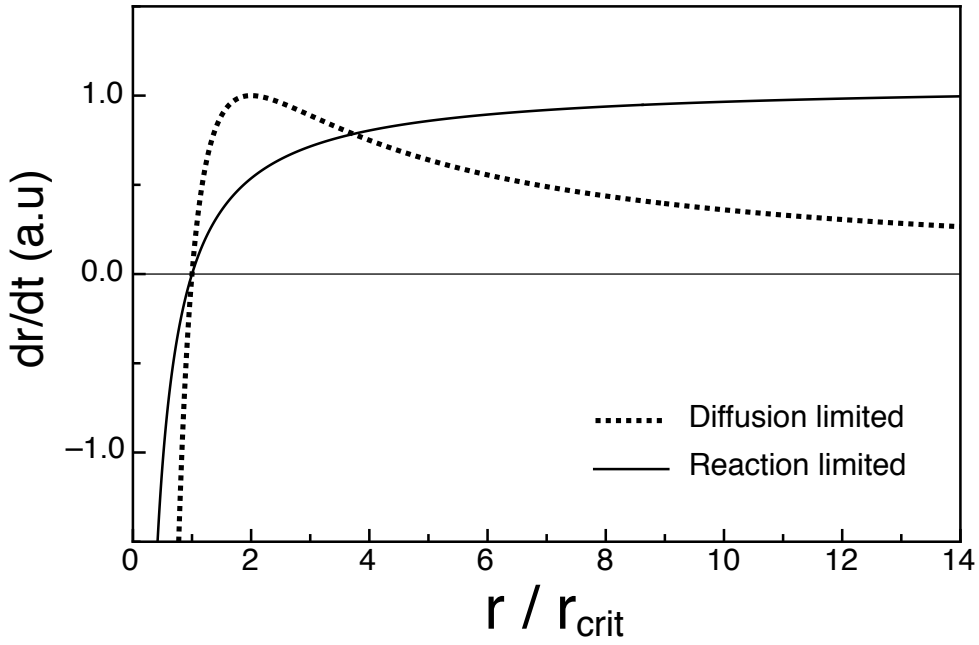

Figure 4.2: Growth rate as a function of particle radius in the diffusion limit (dotted line; Equation 4.11) and the reaction limit (solid line; Equation 4.12).

reaction control. Immediately we see that in both limits the growth rate varies strongly with size for radii close to the critical radius and that the zero growth rate (ZGR) occurs when $r = r_{crit}$. Given an ensemble distribution of particle sizes, we expect vastly different growth kinetics in these two regimes. In the case of diffusion limited growth, provided that the mean radius $\hat{r} \gtrsim 2r_{crit}$, we expect focusing of the particle size distribution (PSD) to occur throughout the growth process. In the reaction limit larger particles will always grow at a rate faster than the smaller ones. Thus we expect defocusing of the PSD will always occur due to the self-accelerating growth of the larger particles. However, focusing of the PSD in the reaction limit may occur provided the particle distribution surrounds r_{crit} due to the extremely fast dissolution of the smallest particles. Given the complex nature of nanocrystal growth, a convolution of purely diffusion limited and purely reaction limited growth is the likely mechanism by which the PSD evolves.

4.3 Evaluation of the nanocrystal growth rate

To effectively model nanoparticle growth it is useful to establish a form of the growth rate that is able to be tuned between the reaction and diffusion limits. The derivation will be accomplished assuming first order reaction kinetics.

In the steady state, the flux of monomer *at* the surface is equal to the surface reaction rate. Thus combining Equations 4.4 and 4.5 we get:

$$\frac{D}{k_r r}([C]_b - [C]_i) = ([C]_i - [C]_e) \, . \tag{4.13}$$

We then solve for the interfacial concentration to obtain:

$$[C]_i = \frac{D[C]_b + k_r r[C]_e}{k_r r + D} \, . \tag{4.14}$$

The limiting condition is that monomer may not react at a rate faster than it may diffuse to the surface, which in turn is governed by the slope of the concentration gradient. At an instant in time (steady state) the concentration gradient will be established by the difference in interfacial and bulk monomer concentrations. Thus the total flux of monomers *at* the particle surface at that moment is given by combining Equations 4.4 and 4.14:

$$I^{SS} = 4\pi r D \left[[C]_b - \left(\frac{D[C]_b + k_r r[C]_e}{k_r r + D} \right) \right] \, . \tag{4.15}$$

From Equation 4.6 we know that I^{SS} is related to the particle growth rate. Thus a combination of Equations 4.6, 4.9 and 4.15 give:

$$\frac{dr}{dt} = \frac{V_m D k_r \left([C]_b - [C]_\infty \exp\left\{ \frac{2\gamma V_m}{rRT} \right\} \right)}{(D + k_r r)} \, . \tag{4.16}$$

After some algebraic manipulation we may express the instantaneous growth rate as:

$$\frac{dr}{dt} = \frac{DV_m\left([C]_b - [C]_\infty \exp\left\{\frac{2\gamma V_m}{rRT}\right\}\right)}{\left(r + \frac{D}{k_r}\right)} \,. \tag{4.17}$$

The form of the growth rate is similar to that obtained by other authors [13, 22, 25]. To calculate the growth rate it is convenient to convert Equation 4.17 into dimensionless units. The growth rate then becomes

$$\frac{d\beta}{d\tau} = \frac{\left(S - \exp\left\{\frac{1}{\beta}\right\}\right)}{(\beta + \xi)} \,, \tag{4.18}$$

where we have introduced the following dimensionless radius, supersaturation and time:

$$\beta = r\phi \qquad \text{Dimensionless radius} \,, \tag{4.19}$$

$$S = \frac{[C]_b}{[C]_\infty^0} \qquad \text{Supersaturation} \,, \tag{4.20}$$

$$\tau = t\psi \qquad \text{Dimensionless time} \,, \tag{4.21}$$

with:

$$\phi = \frac{RT}{2\gamma V_m} \,, \tag{4.22}$$

$$\psi = \phi^2 D V_m [C]_\infty^0 \,. \tag{4.23}$$

We also define the dimensionless Damköhler number, which gives the ratio of diffusion to reaction control as:

$$\xi = \frac{D\phi}{k_r} \,. \tag{4.24}$$

We note here that as the Damköhler number is increased the growth rate asymptotes to zero and when decreased asymptotes to the diffusion limit as governed by the value of the diffusion constant.

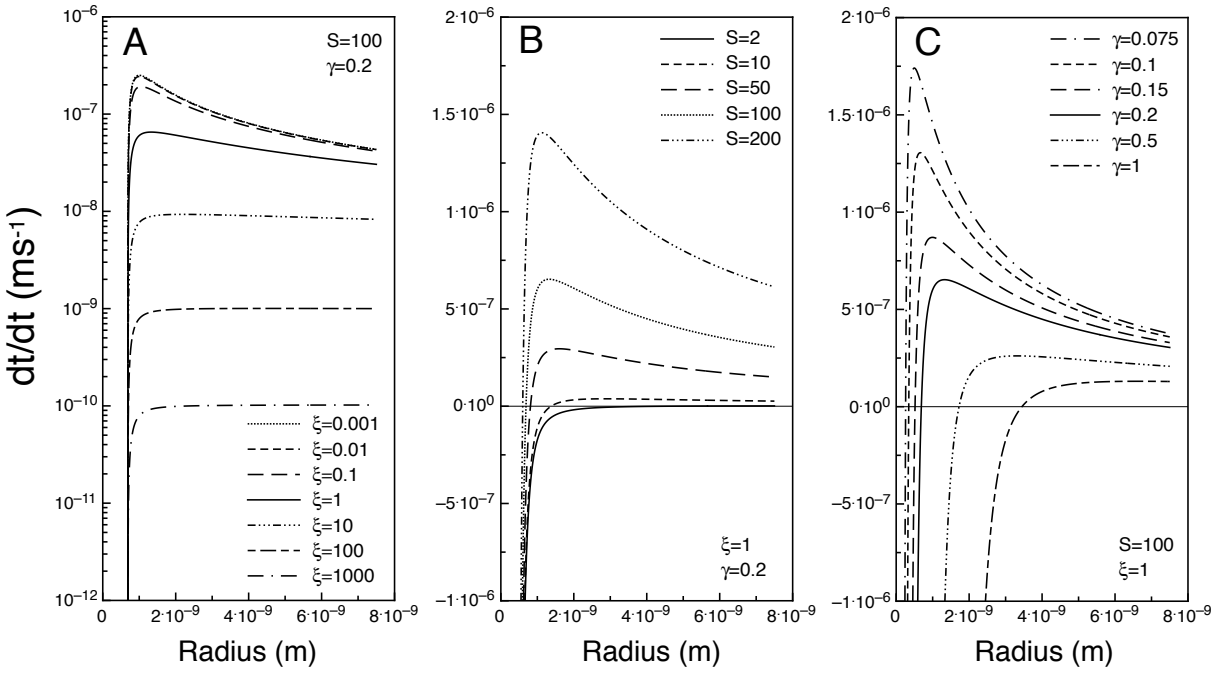

Figure 4.3: Effects of ξ **(A)**, S **(B)** and γ **(C)** on the instantaneous growth rate. The above growth rates were simulated using the following constants: $V_m = 3.29 \times 10^{-5} m^3 mol^{-1}$, $D = 1 \times 10^{-11} m^2 s^{-1}$, $T = 500K$, $[C]^0_\infty = 0.1 mol m^{-3}$.

Figure 4.3 shows three plots of the dimensional instantaneous growth rate (GR) as a function of crystal radius. Panel A displays the growth rate calculated for different values of the Damköhler number ranging from 0.001 to 1000 with S=100 and $\gamma = 0.2 Jm^{-2}$. We see that as ξ is decreased within this range, the GR increases over several orders of magnitude. At $\xi = 1000$, growth is reaction limited and the GR varies with radius only for the smallest

crystal sizes. Within the framework of the imposed conditions at $\xi = 0.01$ the GR has reached the diffusion limit. Further decreases to ξ have little effect on the magnitude of the rate. At low values of ξ the rate of crystal growth is highly sensitive to its radius. It should be noted that changing the ratio of diffusion to reaction limited growth has no effect on the size of the crystals with a zero growth rate.

In Panel B we set $\gamma = 0.2Jm^{-2}$ and $\xi = 1$ and varied the supersaturation, S, from 2 to 200. As expected, increasing S increases the GR. By increasing S we increase the flux of monomer toward the particle surface. Hence, for intermediate values of ξ, where the GR is still reasonably sensitive to changes in the concentration gradient across the diffusion sphere, we see a change in the functional form of the GR from a reaction to a diffusion limited type profile, upon increasing S. Furthermore, increasing S increases the range of crystals with a positive GR.

In Panel C we vary γ for a constant value of S and ξ. Increasing γ from 0.075 Jm^{-2} to 1 Jm^{-2} the radius of the crystals with a ZGR increases from c.a 0.25 nm to 2.2 nm, which defines the smallest achievable NCs. Through the exponential term, γ has a massive effect on the instantaneous $[C]_e$ for the crystals. Similar to the trends observed for increasing S a drastic reduction to $[C]_e$ at low γ materialises by increasing the driving force for growth across all crystal sizes. It is important to note that the sensitivity of the functional form of the GR to changes in either S or γ is evident only at intermediate values of ξ, with this sensitivity diminishing in either the reaction or diffusion limit.

4.4 Derivation of the source term - Nucleation

The above section is concerned with the rate of growth of an existing ensemble of NCs. However, we have not yet considered the mechanisms involved in the formation of the ensemble. In this section a source term is developed, which accounts for the formation of particles. The

source term has been derived within the framework of Equilibrium Theory. Firstly let us consider the simple case for the reaction of a monomer unit, C, with a cluster of n units:

$$C + C_n \underset{k_{-1,n}}{\overset{k_{1,n}}{\rightleftharpoons}} C_{n+1} \, . \tag{4.25}$$

The above reaction has the equilibrium constant:

$$K_{1,n} = k_{1,n}/k_{-1,n} = \frac{[C_{n+1}]}{[C][C_n]} \, . \tag{4.26}$$

The Gibbs free energy change at standard states for $C + C_n \rightarrow C_{n+1}$ may be expressed as:

$$\Delta G^0_{1,n} = -k_B T \ln K_{1,n} \, , \tag{4.27}$$

and for the condensation reaction of monomer onto an infinitely large particle, C_∞, as:

$$\Delta G^0_{1,\infty} = -k_B T \ln K_{1,\infty} \, . \tag{4.28}$$

The difference in the Gibbs energy between adding a monomer unit to an infinitely large particle and that of a particle with a finite number of units, n, is given by the sum of the surface and volume free energy changes for the cluster upon addition of the monomer unit:

$$\Delta G^0_{1,n} - \Delta G^0_{1,\infty} = \Delta G^{vol}_{1,n} + \Delta G^{surf}_{1,n} \, . \tag{4.29}$$

Combining Equations 4.27, 4.28 and 4.29 we obtain:

$$-k_B T \ln \left(K_{1,n}/K_{1,\infty} \right) = \Delta G^{vol}_{1,n} + \Delta G^{surf}_{1,n} \, . \tag{4.30}$$

We define $K_{1,\infty}$ to be the reciprocal of the monomer concentration in equilibrium with a flat surface, $[C]^0_\infty$. This allows us to write an expression for the equilibrium constant between the monomer, C, and a particle, C_n as:

$$K_{1,n} = \frac{1}{[C]^0_\infty} \exp\left\{ \frac{-\left(\Delta G^{vol}_{1,n} + \Delta G^{surf}_{1,n}\right)}{k_B T} \right\} . \tag{4.31}$$

In the framework of equilibrium theory we assume all particles with fewer monomer units than a particle with p monomer units have condensation reactions that are in equilibrium, however, for $n > p$; $[C_n] = 0$. Now we consider all the reactions that occur simultaneously at equilibrium:

$$\begin{aligned} C + C &\rightleftharpoons C_2 \\ C_2 + C &\rightleftharpoons C_3 \\ C_{p-1} + C &\rightleftharpoons C_p \end{aligned} \tag{4.32}$$

The sum of these reactions is:

$$pC \rightleftharpoons C_p \tag{4.33}$$

where p units condense to form a critical nucleus. The equilibrium constant for nucleation (Reaction 4.33) is simply the product of the equilibrium constants for all the sequential reactions that result in the production of a critical nucleus:

$$K_{nuc} = \prod_{n=1}^{p-1} K_{1,n} . \tag{4.34}$$

As such we may express Equation 4.31 as:

$$K_{nuc} = \frac{1}{[C]_{\infty}^{p-1}} \exp\left\{ \frac{-\left(\Delta G_{1,p}^{vol} + \Delta G_{1,p}^{surf}\right)}{k_B T} \right\} . \tag{4.35}$$

Given that $[C_p] = K_{nuc}[C]^p$ from Reaction 4.33, we may form an expression for the concentration of critical clusters, $[C_p]$, as:

$$[C_p] = \frac{[C]^p}{[C]_{\infty}^{p-1}} \exp\left\{ \frac{-\left(\Delta G_{1,p}^{vol} + \Delta G_{1,p}^{surf}\right)}{k_B T} \right\} . \tag{4.36}$$

The rate of nucleation is given by the rate of formation of the first stable particle, C_{p+1}:

$$R_{nuc} = k_{1,p}[C][C_p] . \tag{4.37}$$

Thus the nucleation rate becomes:

$$R_{nuc} = k_{1,p} \frac{[C]^{p+1}}{[C]_{\infty}^{p-1}} \exp\left\{ \frac{-\left(\Delta G_{1,p}^{vol} + \Delta G_{1,p}^{surf}\right)}{k_B T} \right\} . \tag{4.38}$$

As all reactions are at equilibrium $k_{1,p}$ is equal to the diffusional collision frequency, $z_{1,p}$, which is given by:

$$z_{1,p} = 8\pi r_m D N_A , \tag{4.39}$$

where N_A is the Avogadro constant and r_m is the effective radius of the monomer as extracted from the molar volume V_m. Employing this relation and using the expression for the supersaturation, Equation 4.20, we obtain:

$$R_{nuc} = z_{1,p} S^{p+1} ([C]^0_\infty)^2 \exp\left\{ \frac{-\left(\Delta G^{vol}_{1,p} + \Delta G^{surf}_{1,p}\right)}{k_B T} \right\} . \tag{4.40}$$

To evaluate the barrier (activation energy) we sum the first derivative of the surface and volume terms and set the change in free energy as a function of size to zero. Evaluation of this gives the free energy activation barrier to the formation of a critical particle, C_p. For consistency with the instantaneous growth rate we firstly evaluate the barrier as a function of the critical radius. Remembering that C_p is equivalent to r_{crit} the critical barrier is evaluated as:

$$\Delta G^{vol}_{1,p} + \Delta G^{surf}_{1,p} = \Delta G^{\dagger}_{1,p} = \frac{16\pi\gamma^3}{3(\Delta G_v)^2} , \tag{4.41}$$

where

$$\Delta G_v = \frac{2\gamma}{r_{crit}} . \tag{4.42}$$

We may now combine Equations 4.40, 4.39, 4.41 and 4.42 to obtain:

$$R_{nuc} = 8\pi r_m D N_A S^{p+1} ([C]^0_\infty)^2 \exp\left\{ \frac{-\left(4\pi r^2_{crit}\gamma\right)}{3 k_B T} \right\} . \tag{4.43}$$

Given that the reaction scheme outlined by Equation 4.33 does not account for coagulation during nucleation, which may be considered significant given the extremely small sizes of the nanocrystals, we introduce a coagulation coefficient, u. Noting that $p = (r_{crit}/r_m)^3$ we may write the final expression for the nucleation rate, determining the mole of critical clusters per unit volume per unit time ($molm^{-3}s^{-1}$):

$$R_{nuc} = 8\pi r_m D N_A S^{pu+1} ([C]^0_\infty)^2 \exp\left\{ \frac{-\left(4\pi r_m^2 p^{2/3}\gamma\right)}{3k_B T} \right\} . \tag{4.44}$$

Here, u may take values between 0 and 1 and acts as a scaling factor, which balances the kinetic and thermodynamic aspects of the nucleation rate. Loosely it accounts for the probability that in addition to the stepwise addition of monomer units, nucleation may proceed via the coagulation of dimers and trimers etc. with each other and with the monomer. For example, a decrease in the value of u from 1 to 0.5 assumes that on average only half the number of processes are involved in the formation of the critical nucleus C_p. Thus Equation 4.33 becomes:

$$pu(C_{1/u}) \rightleftharpoons C_p \, . \tag{4.45}$$

The boundary condition is that $\frac{1}{u} \leq p$. At equilibrium the concentration of monomers and dimers ($n = 1, 2$) etc is extremely high compared to cluster species with higher p values. Given that the probability of coagulation decreases with both decreasing concentration and increasing size of the coagulants, the coagulation rate decreases rapidly as n is increased from $1 \rightarrow p$. As such, an implicit assumption is that coagulation does not significantly modify the thermodynamic barrier to nucleation.

Figure 4.4A is plot of the number of monomer units in the critical cluster and the corresponding nucleation rate as a function of S. We see that at low supersaturations a small increase in S results in a dramatic reduction to p. As S is further increased p decreases monotonically and at $S \cong 100$ the nucleation rate begins to increase in magnitude. The arrows indicate a nucleation rate of 5 $\mu M s^{-1}$, which corresponds to a supersaturation of $\backsim$8300 (8.3 $molm^{-3*}$) and a p value of $\backsim$32. The sensitivity of R_{nuc} to S and γ is best viewed in Panel B, which shows the nucleation rate as a function of S for different values

*Typical monomer concentrations in the range 20-60 $molm^{-3}$ are employed for nanocrystal synthesis.

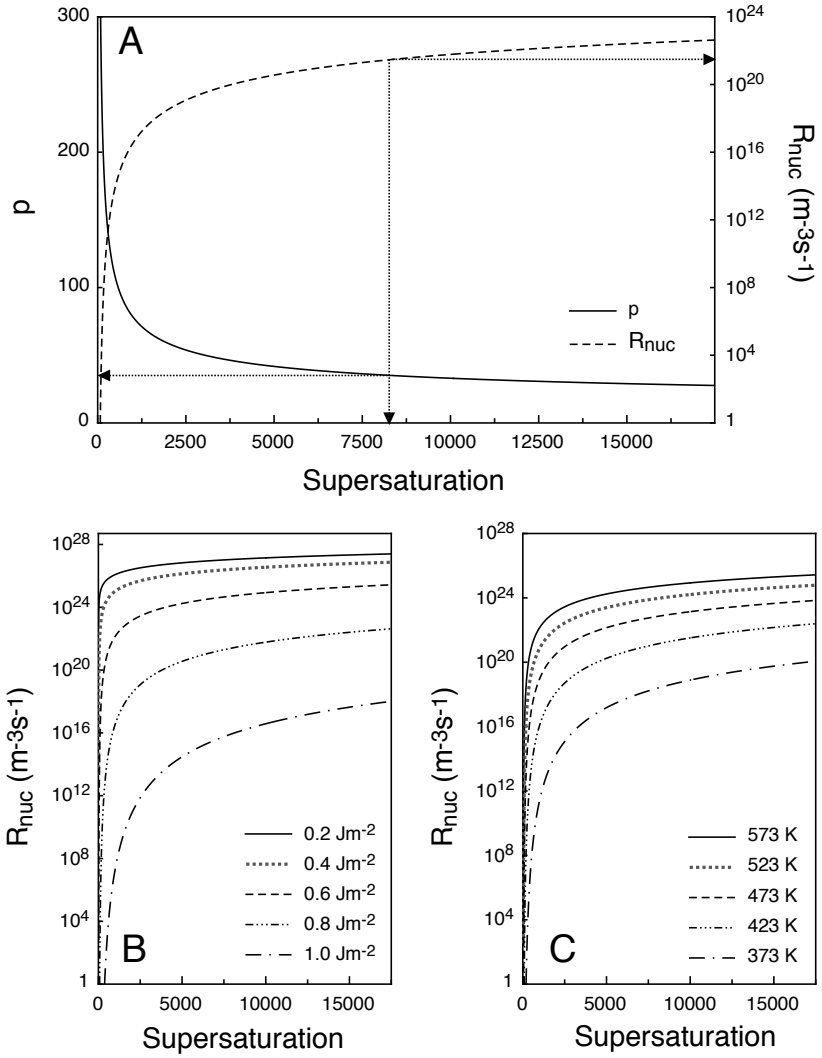

Figure 4.4: **(A)** Nucleation rate and the corresponding p value in solution as a function of supersaturation with $T = 573K$, $u = 0.46$, $r_m = 1.87 \times 10^{-10}m$, $D = 1 \times 10^{-10}m^{-2}s^{-1}$, $[C]^0_\infty = 1 \times 10^{-3}molm^{-3}$ and $\gamma = 0.6Jm^{-2}$. **(B)** and **(C)** Nucleation rates as a function of supersaturation for varying values of γ ($T = 573K$) and T ($\gamma = 0.6Jm^{-2}$) respectively.

of γ. For a surface energy of 0.2 Jm^{-2} increasing S from 2 to 200 results in an increase in the number of nucleated particles per cubic metre per second from 3×10^8 to 2×10^{25}. The responsiveness of R_{nuc} to S drops as γ is increased. By raising γ from 0.2 Jm^{-2} to 1 Jm^{-2} the onset of nucleation requires an S value of c.a 418 compared to 1.7. Panel C displays a plot of the nucleation rate as a function of S at different reaction temperatures (γ=0.6 Jm^{-2}). As T is decreased from 573 K to 373 K R_{nuc} drops off significantly. A solution

with an S value of 215 at 373 K will nucleate $\backsim$10 particles per metre cubed per second compared with 6×10^{18} at 573 K. Under standard laboratory conditions a supersaturation of 2000 would be required to nucleate just one single particle per second per cubic metre.

The only remaining variable to evaluate is the nucleation distribution function $g(r)$. Here we have assumed a thermalised distribution (Gaussian) around the critical radius with a FWHM $\backsim k_B T$. Although we would expect many more monomers and dimers than critical nuclei, we will see later this is a reasonable assumption given the large negative growth rates of particles with radii below the critical radius.

4.5 Supersaturation Dynamics

To correctly model nucleation and growth it is necessary to keep constant track of the movement of monomer in solution. We now derive the expression necessary to evaluate the supersaturation in solution at any time, t, during the course of the reaction. Upon the growth or dissolution of a population, i, containing N particles with radius r_i after a time Δt, we obtain a volume change:

$$\Delta V_i = \frac{4\pi(N_i^{t+\Delta t} - N_i^t)(r_i^3)}{3} \,. \tag{4.46}$$

The number of monomer units added to or removed from the solution by this population is given by:

$$\Delta C_i = \frac{\Delta V_i \rho}{M_W} \,. \tag{4.47}$$

where, ρ, is the density of the bulk material and M_W its monomeric molecular weight. Inside the simulated reaction volume, V_{tot}, the bulk monomer concentration after the growth or dissolution of population i is given by:

$$[C]_b^{t+\Delta t} = [C]_b^t - \left\{ \frac{\Delta C_i}{V_{tot}} \right\} . \tag{4.48}$$

Given Equation 4.20 and taking out the constant Q we may evaluate the change in the supersaturation, ΔS_i, after the partial growth or dissolution of a single finite population as:

$$\Delta S_i = Q \left\{ (N_i^{t+\Delta t} - N_i^t)(r_i^3) \right\} , \tag{4.49}$$

with

$$Q = \frac{4\pi\rho}{3M_W V_{tot} C_\infty^0} . \tag{4.50}$$

Given a total of P populations the final supersaturation after a time, Δt, is given by subtracting the sum of the supersaturation changes, ΔS_i, across all of the populations from the value of S at t. Thus the governing equation controlling the supersaturation is:

$$S^{t+\Delta t} = S^t - \left[\sum_{i=1}^{P} Q r_i^3 (N_i^{t+\Delta t} - N_i^t) \right] . \tag{4.51}$$

4.6 Population Balance Model: Finite differencing

To calculate and implement the actual growth and nucleation rates we use a standard population balance model (PBM). Firstly we decide on a grid configuration that divides the otherwise continuous distribution function into small volumes each with a radius spanning Δr. In principle, the grid design must suit its application. A typical grid is composed of a series of populations (grid points) and a series of corresponding boundaries separating these populations. A one-dimensional staggered linear grid, as implemented here, separates individual populations by a constant value. The author notes that more complex non-linear

[18] and time evolving grids [25] have been previously employed in the modelling of particle growth. Figure 4.5 displays a schematic of the grid configuration used in this work.

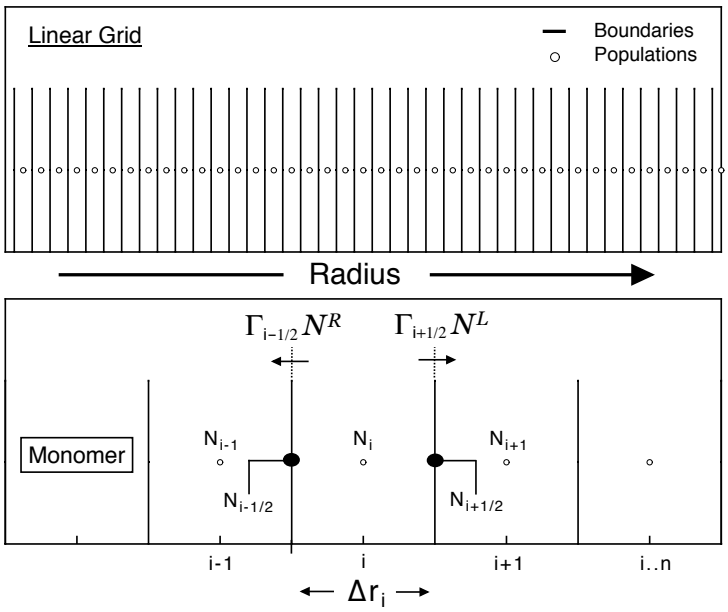

Figure 4.5: Staggered linear grid configuration, where i denotes the radius of the i^{th} population. Using a mass transfer approach matter flows into or out of the discrete volume described by Δr_i through rates $\Gamma_{i-1/2}$ and $\Gamma_{i+1/2}$.

The continuity equation giving mass balance is:

$$\frac{\partial N}{\partial t} = -\frac{\partial f}{\partial r} + R_{nuc} g(r) \, . \tag{4.52}$$

Here, f is the flux through the volume elements on the grid and $R_{nuc}g(r)$ is the source term for new nuclei given by the nucleation rate, R_{nuc}, and its distribution function $g(r)$. The vectorial flux $f^{\pm}$ through each element may be expressed as, $N\Gamma^{\pm}$, where N is the frequency of the population and $\Gamma^{\pm}$ is the velocity as given by the instantaneous growth rate. As such, the governing evolution equation is:

$$\frac{\partial N}{\partial t} = -\frac{\partial N\Gamma^{\pm}}{\partial r} + R_{nuc} g(r) \, . \tag{4.53}$$

For the purposes of growth only, we may ignore the source term. This term may be introduced again later and operated on by the appropriate flux rates to give the final distribution function under the conditions of simultaneous formation and growth, without compromising the mass balance. Having integrated over Δt, we arrive at the integral form of the conservation law with spatial variables a and b:

$$\int_a^b N_{(r)}^{t+\Delta t} dr - \int_a^b N_{(r)}^{t} dr = -\Delta t \left\{ \hat{f}(N_{(a)}) - \hat{f}(N_{(b)}) \right\} . \tag{4.54}$$

Here, $\hat{f}$ is the time average of the physical flux between levels t and Δt. The spatial variables surrounding, i, as given at the cell faces (boundaries) are $a = i - 1/2$ and $b = i + 1/2$. The approximate density in the i^{th} population is:

$$N_i = \frac{1}{\Delta r} \int_{i-1/2}^{i+1/2} N(r,t) dr , \tag{4.55}$$

and hence the integral conservation law becomes

$$\overline{N_i^{t+\Delta t}} - \overline{N_i^t} = -\frac{\Delta t}{\Delta r} \left\{ \hat{f}(N_{(i+1/2)}^t) - \hat{f}(N_{(i-1/2)}^t) \right\} . \tag{4.56}$$

$\overline{N_i^t}$ can be evaluated directly. However, we need to correctly define the quantity to be transported, $N_{i\pm1/2}$, in order to arrive at an accurate value for $\hat{f}$. To accomplish this we use a finite difference method of second-order accuracy in space. Second order spatial accuracy can be achieved by introducing more points upstream from where the flux needs to be evaluated. In doing so we gather more information about the density of the function surrounding the flux point. In such high-order schemes, the values at the cell faces are extrapolated from neighbouring cell averages. This method of variable extrapolation is often referred to as

the MUSCL approach (Monotone Upstream-centred Schemes for Conservation Laws) as developed by Van Leer *et al* [29].

The MUSCL reconstruction provides a powerful high-order solution to the problem of interpolating the values of $N_{i\pm1/2}$. MUSCL is a higher order scheme with flux limiting to ensure the solution is bounded. Higher order schemes without flux limiting can develop oscillations even though they are formally more accurate when assessed by Taylor series expansion. Flux limiters prevent non-physical oscillations from occurring near the region of the "shock" (sharp or sudden changes to the independent variables) as well as diffusivity of the solution[†]. These limiters act to find the most accurate value for the quantity to be transported by evaluating the solution in a non-linear manner. Schemes using these limiters are called Total Variation Diminishing (TVD) schemes. TVD is a mathematical property that ensures the variation, or differences, between adjacent grid points must remain the same or decrease. In this way the system may not generate any false maxima or minima. We write the general expression for the fully upstream MUSCL scheme with the inclusion of the flux limiters as [30]:

$$N^R_{i-1/2} = \left\{ N_i - \frac{\phi}{4} \left[(1+\kappa)\Psi\left(\frac{\Delta_i^+}{\nabla_i^-}\right)\nabla_i^- + (1-\kappa)\Psi\left(\frac{\nabla_i^-}{\Delta_i^+}\right)\Delta_i^+ \right] \right\} , \tag{4.57}$$

$$N^L_{i+1/2} = \left\{ N_i + \frac{\phi}{4} \left[(1-\kappa)\Psi\left(\frac{\Delta_i^+}{\nabla_i^-}\right)\nabla_i^- + (1+\kappa)\Psi\left(\frac{\nabla_i^-}{\Delta_i^+}\right)\Delta_i^+ \right] \right\} . \tag{4.58}$$

The L and R superscripts indicate the upstream direction from which the mass is transported are not associative properties of the evaluated differences. The subscripts denote the boundary at which the fluxes are calculated. As is typical in upstream schemes, positive (L) fluxes are calculated at the upstream cell boundary and negative (R) fluxes at the down-

[†]Here diffusivity refers to artificial results caused by numerical errors that propagate between iterations and should not be confused with the physical diffusion of monomer.

stream cell boundary (Ref: Figure 4.5). We also note that the limiter function, Ψ, depends on the gradient operators, Δ_i and ∇_i. We define these operators for the specific case of a second-order fully upstream scheme as:

$$\Delta_i^+ = (N_{i+1} - N_i) \tag{4.59}$$
$$\nabla_i^- = (N_i - N_{i-1}) \, .$$

For a second order upstream reconstruction, $\phi = 1$ and $\kappa = -1$ and the Equations 4.57 and 4.58 reduce to:

$$N_{i-1/2}^R = \left\{ N_i - \frac{1}{2} \left[\Psi \left(\frac{\nabla_i^-}{\Delta_i^+} \right) \Delta_i^+ \right] \right\} \, , \tag{4.60}$$

$$N_{i+1/2}^L = \left\{ N_i + \frac{1}{2} \left[\Psi \left(\frac{\Delta_i^+}{\nabla_i^-} \right) \nabla_i^- \right] \right\} \, . \tag{4.61}$$

We see that for mass transport from the right we invoke a forward extrapolation and for mass transport from the left we invoke a backward extrapolation. These values may be substituted back into Equation 4.56 to yield the new array of N_i at $t + \Delta t$. Finally, to calculate the value for, Ψ, we must choose its functional form. There are many types of limiters, perhaps the most common are the MinMod, Van Leer, Van Albada and Superbee limiters as outlined below. With q equal to the appropriate construction of the gradient operators (curved brackets in Equations 4.60 and 4.61):

$$Min\left\{1, \frac{(3-\kappa)}{(1-\kappa)}q\right\} \qquad \text{MinMod}(q)\ . \tag{4.62}$$

$$\frac{2q}{(1+q)} \qquad \text{VanLeer}(q)\ . \tag{4.63}$$

$$\frac{(q+q^2)}{(1+q^2)} \qquad \text{VanAlbada}(q)\ . \tag{4.64}$$

$$Max\left\{0, Min[2q,1], Min[q,2]\right\} \qquad \text{Superbee}(q)\ . \tag{4.65}$$

All the limiters return zero if the gradient ratio is negative. In cases where $q < 0$, $\Psi = 0$, such that in the region of the shock the local reconstruction is reduced to first-order.

4.6.1 Stability and accuracy of the numerical scheme

Prior to the implementation of a numerical scheme it is vital to test its stability and accuracy. This not only ensures that the written code is stable but also gives valuable information regarding the extent of total error associated with the implemented scheme due to *round-off* and *truncation errors*.[‡] In order to test these properties we apply the flux limiting scheme to the linear convection of a square wave with the velocity component (growth rate) constant over all space. The sharp edges of the square wave test how well the scheme deals with sudden gradient changes. Figure 4.6 shows the results of the linear convection of a square wave after 1×10^5 iterations using the different flux limiters outlined above. For reference the top left panel shows the extent of convection. We see that the first-order and second-order schemes

[‡]*Round-off error* is introduced through the omission of significant figures and is associated with the computer numbering system. *Truncation error* is caused by the omission of higher order terms in the Taylor expansion of the integrals that are approximated by finite differencing.

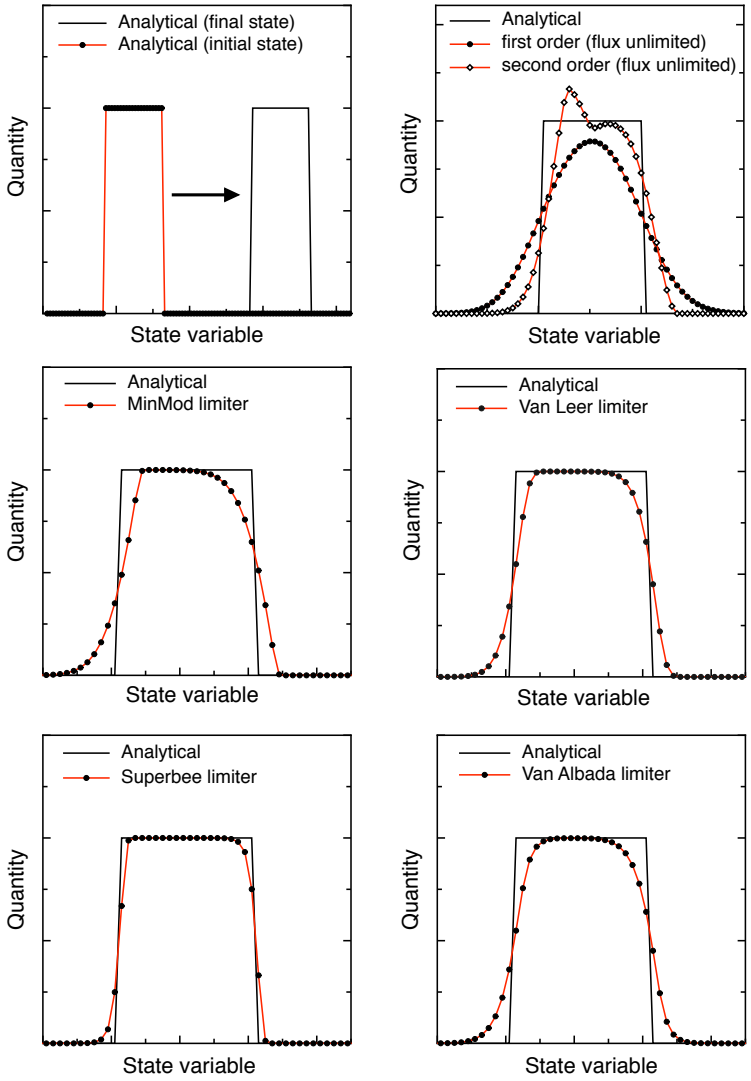

Figure 4.6: Translation of a step function using various flux limiters. For reference the first-order and second-order upstream scheme with no limiter is shown (top right). 200 points 100000 time steps

result in either a large amount of numerical diffusion or the creation of unreal oscillations respectively. Such diffusivity and oscillations are typical of low order and flux unlimited schemes and highlight their inability to cope with sudden gradient changes. Fortunately, through the use of limiters this problem is quickly corrected. In all the cases where the limiters were used the results show excellent preservation of the functional form of the square wave. However, as each limiter functions slightly differently some limiters are better than others at preserving the form of the wave. Figure 4.7 shows the same test simulations where

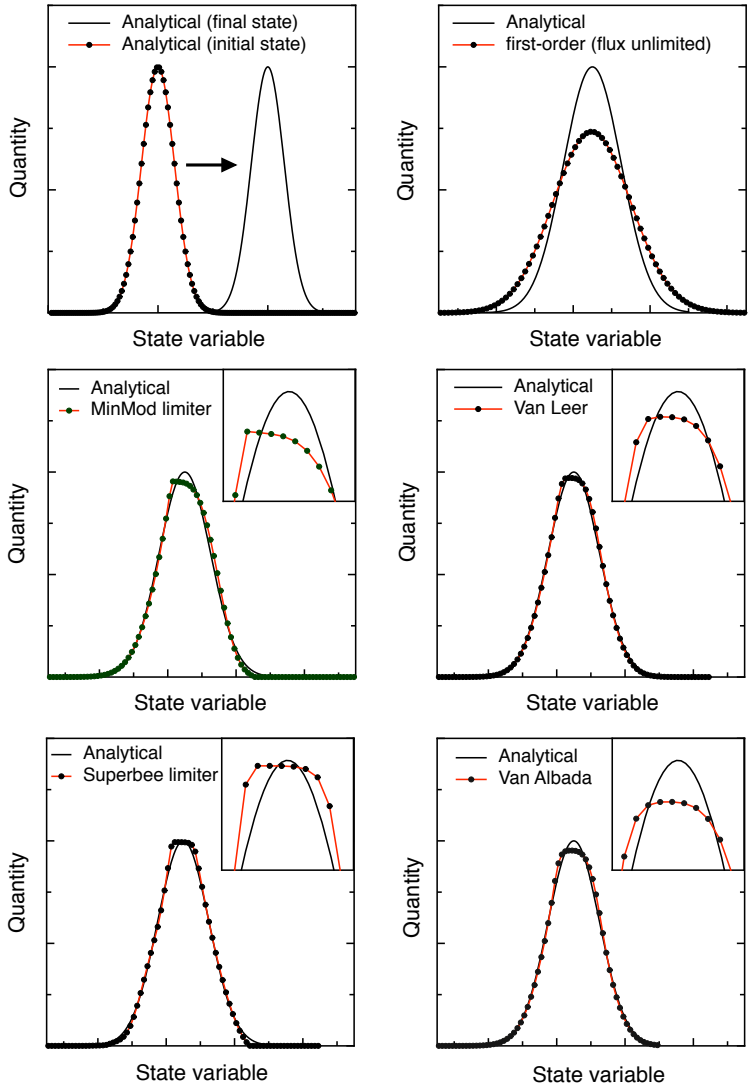

Figure 4.7: Translation of a Gaussian function using various flux limiters. For reference the first-order upstream scheme with no limiter is shown (top right). 200 points 100000 time steps.

the square wave is replaced by a Gaussian, which is more appropriate for the case of modelling nanocrystal growth. From the results obtained by first-order upstreaming (top right) we see that although the analytical and numerical positions of the maxima are almost identical the final profile has *artificially* broadened. This is important to avoid in the modelling of nanocrystals where interpretation of the results of a given simulation relies heavily on the FWHM of the distribution. The remaining four panels show the results obtained from the four limiters. Both the Van Leer and Van Albada limiters return much the same result. The

MinMod limiter acts strongly on the scheme when the gradient drops below a certain value. Thus the data is seen to quickly flatten out around the peak of the Gaussian where $2r < 1$. Although the Superbee limiter copes excellently with sharp gradients, as seen in Figure 4.6, it perhaps deals *too* well when operating on smoother profiles. Through the use of all the limiters (except perhaps for the MinMod limiter), the position of the maximum value of the Gaussian is preserved as is its FWHM and amplitude. From analysis of the information presented in Figures 4.6 and 4.7 we may now implement the scheme with confidence in the obtained values. Given its low diffusivity and ability to cope well with smooth profiles the Van Leer limiter has been chosen for the simulations of NC formation and growth.

The numerical scheme implemented here has the following inherent stability criterion, referred to as the *Courant condition* [31].

$$\frac{|\Gamma^{\pm}|\Delta t}{\Delta r} \leqslant 1 \,. \tag{4.66}$$

The physical meaning of this condition is that stability (and indeed accuracy) is achieved only when *all* finite volumes (populations) do not traverse multiple boundaries in a single iteration. Thus, it becomes necessary to vary Δt in dependence upon the magnitude of the growth rate.

4.7 Growth Simulations

4.7.1 Growth in the Diffusion and Reaction limits

We begin by examining only the growth of nanocrystals (NCs). To accomplish this the source term is removed from the simulation and an artificial distribution of NCs is inserted at t=0. Throughout the following simulations a Gaussian with a mean radius of 1×10^{-9} m and a standard deviation (SD) of $\backsim$10% was employed. Both the mean size and the SD of the initial PSD are approximate to known values obtained at the end of the nucleation phase in the case of CdSe NCs (Ref: Chapter 3).

The following simulations, outlined in Figures 4.8 and 4.9, were designed to uncover the effects of surface energy (γ) on the evolution of a series of PSDs in both the diffusion and reaction limits. These simulations were accomplished with $S = 500$, $D = 1 \times 10^{-12} m^{-2} s^{-1}$, $[C]^0_\infty = 1 \times 10^{-2} mol m^{-3}$, $T = 503K$ and 60 μM nanocrystals.

Figure 4.8 shows the concentration of NCs (A), %SD (B), mean radius (C) and supersaturation (D) as a function of time for increasing values of γ in the range 0.05-0.3 Jm^{-2} under diffusion limited conditions ($\xi = 1 \times 10^{-3}$). For clarity and brevity in the explanation of these results the discussion is firstly restricted to the growth dynamics of those NCs with $\gamma = 0.2 Jm^{-2}$, followed by a discussion of the dynamics of those NCs with differing surface energies. For the case where $\gamma = 0.2 Jm^{-2}$ NC evolution has been divided into three regimes relative to the supersaturation dynamics as indicated by the vertical dotted lines in each of the plots. Specifically, these lines separate the reaction into times when S is in rapid decline, in quasi-equilibrium and finally in slow decline. It is important to note that these three regimes are seen for all NC systems investigated here. For clarity, dividing lines have only been drawn for the system where $\gamma = 0.2 Jm^{-2}$. Inspection of Panel C reveals that between 100 μs and 300 ms the NCs grow at an approximate rate of 40 nms^{-1} to reach a size of sim3.22 nm. During this time S is in rapid decline, the concentration of NCs remains

constant and the PSD narrows from a SD of $\backsim$10% to a minimum of $\backsim$5%. Between 300 ms and 800 ms the mean radius remains constant as does the [NCs] and S. Herein, this time period will be referred to as the *equilibrium phase* of the reaction. Notably, during this time the PSD is rapidly broadening. At around 800 ms a substantial number of NCs have dropped well below the critical radius and the Ostwald ripening phase of the reaction commences. This is signified by a decrease in the NC concentration and an increase in the mean size of the NCs. During the final stage (800 ms to 60 s) growth of the NCs is governed by monomer provided by the dissolution of the smallest crystallites within the evolving PSD. The extremely low S at the onset of the final stage dictates a form of the growth rate where larger particles grow at a rate faster than smaller ones (similar to a reaction limited profile). Thus, as the NCs become larger via Ostwald ripening they also begin to consume monomer from the solution at an increasing rate. This is indicated by the slow decline in S during the late stages of growth. It should be noted that as the NCs begin to ripen the SD begins to plateau. Further rapid broadening of the PSD is prevented by the fast dissolution of small NCs and as such the SD increases only slowly between $\backsim$1 and 60 s.

Upon comparing simulations with surface energies between 0.05 and 0.3 Jm^{-2} some interesting trends are revealed. Firstly, from inspection of the data for $t \lesssim 0.1$ s in Panel C it can be seen that, independent of their initial γ, the NCs grow at the same rate and to the same final size. These results are indicative of diffusion limited growth (at constant [NCs]) where the growth rate is determined solely by the rate at which monomer can reach the surface and independent of those factors that alter the surface reactivity of the particle, such as their surface energy. Inspection of Panel D reveals that the concentration of monomers present in solution once the reaction has reached equilibrium increases with increasing surface energy, with an order of magnitude more monomer required to prevent the dissolution of particles with $\gamma = 0.3Jm^{-2}$ compared to NCs whose $\gamma = 0.05Jm^{-2}$.

During the final stage the NCs grow at a rate determined by the rate at which monomer

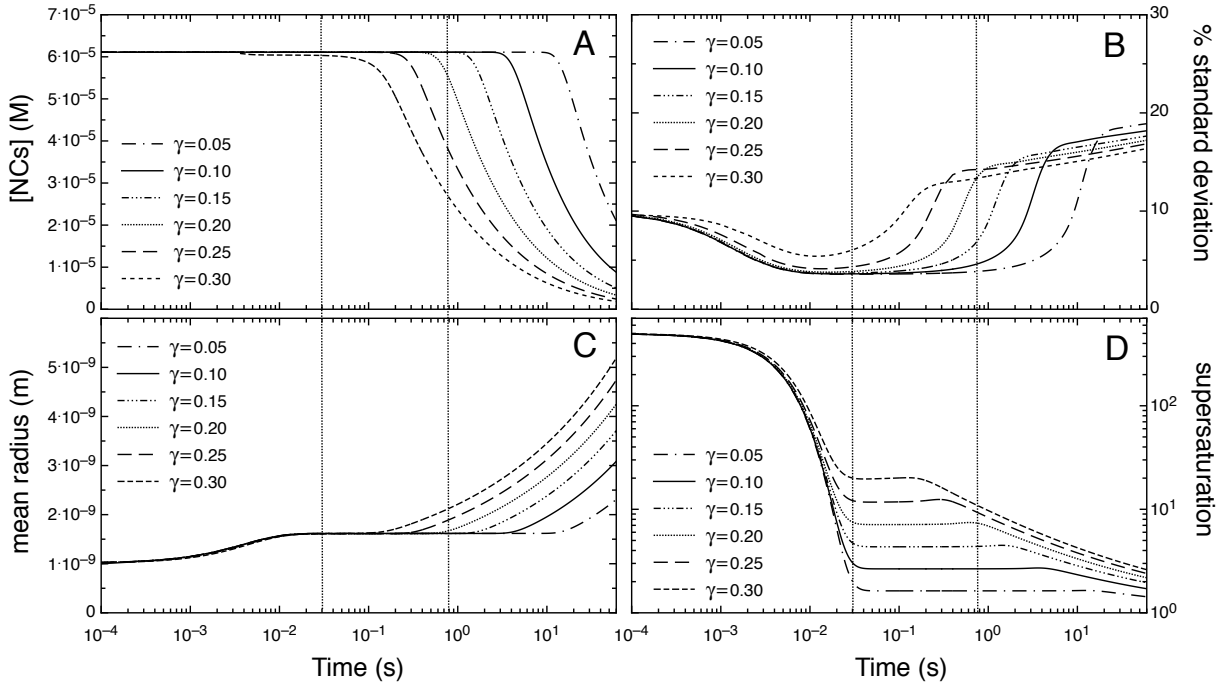

Figure 4.8: Nanocrystal concentration (**A**), standard deviation (**B**), mean radius (**C**) and supersaturation (**D**) as a function of time for NC growth under diffusion limited conditions ($\xi = 1 \times 10^{-3}$) with increasing surface energies. The vertical lines in each of the plots divide the reaction where $\gamma = 0.2 Jm^{-2}$ into three phases in accordance with its supersaturation dynamics; Specifically, these are the growth phase, the equilibrium phase and the Ostwald ripening phase.

is provided to the solution via Ostwald ripening. The time at which the NCs enter the final phase and begin to grow again is determined by their surface energy, as the surface energy governs the time scale on which broadening (and ripening) of the PSD occurs. Comparison of Panels A and B reveals that once the PSDs have reached a SD of sim12.5% they begin to ripen. As distributions with higher surface energies undergo less narrowing during the first stage they possess a higher SD at equilibrium and thus begin to ripen first. As a consequence, the time scale of the *equilibrium phase* is shortened from 10 s to 90 ms upon increasing γ from 0.05 to 0.3 Jm^{-2}. Finally, from Panels A, B and C it can be seen that increasing γ results in less NCs of larger sizes and with narrower distributions at the end of the reaction.

Figure 4.9 depicts results using the same parameters as those used for simulation under diffusion control. However, ξ was raised by simsix orders of magnitude to a value of $\xi = 2000$. Similar trends are observed in the SD and [NCs] over time as those seen for the diffusion

limited simulations, although the time scale of these trends is vastly slower. The differences in reaction kinetics between the diffusion and reaction limited regimes is seen by analysis of the mean radius and S as a function of time; Panels C and D respectively. Contrary to the diffusion limited case the initial rate of growth (when [NCs] is constant) depends strongly on the surface energy of the NCs. The fastest growth rates are seen for NCs with the lowest γ, which decreases as γ is increased. As strongly binding ligands will lower γ to a greater extent than weaker binding ligands, we expect slower rates of growth for lower values of γ, contrary to what is observed. This is understood as in addition to lowering γ, the presence of strong binding ligands in solution will also slow the surface reaction rate (decrease ξ). The surface half-life of strong binding ligands is much greater than weaker binding species and as a consequence they are able to physically inhibit monomer adsorption to a greater extent. It must therefore be realised that γ and ξ are intrinsically linked and that when modelling the evolution of a PSD simulating different types and concentrations of adsorbates in solution, appropriate *concomitant* modifications to *both* γ and ξ need to be made.

Compared to diffusion limited growth the standard deviations of the PSDs under reaction control were seen to broaden to a greater extent during their *equilibrium phase*. On average the final distributions had standard deviations $sim5\%$ greater than those grown under diffusion control. Finally, from the overall time scale of the reactions we may conclude that NC growth **must** proceed under highly reaction controlled kinetics. To reinforce this point it should be noted that the diffusion coefficient used during these simulations was a lower limit for the diffusion of a small precursor species at $\backsim 500K$. Despite the low diffusion coefficient, normal NC growth (during the first phase) still took place on a time scale of milliseconds. Simulations performed using a diffusion coefficient of $1 \times 10^{-10}\ m^2 s^{-1}$ under the same extent of diffusion control ($\xi = 1 \times 10^{-3}$) resulted in the growth of NCs from 1-3 nm in under 1 ms, which is several orders of magnitude too fast compared to the experimentally observed growth rates outlined in Chapter 2.

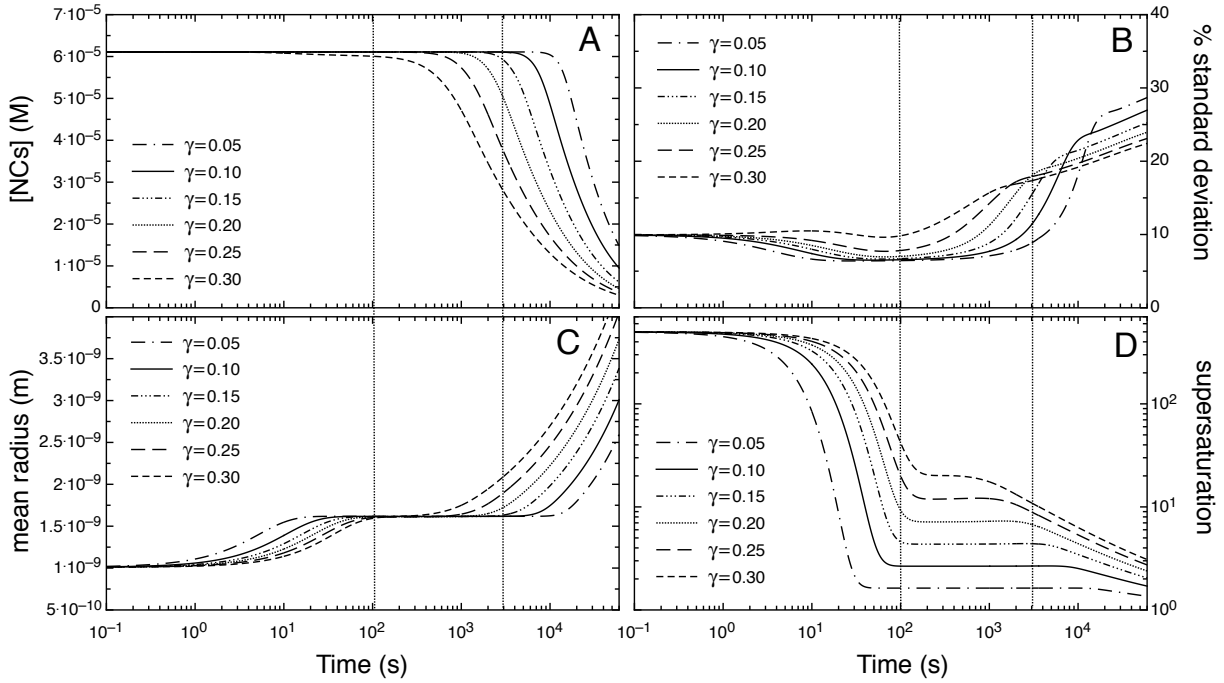

Figure 4.9: Nanocrystal concentration (**A**), standard deviation (**B**), mean radius (**C**) and supersaturation (**D**) as a function of time for NC growth under reaction limited conditions ($\xi = 2000$) with increasing surface energies. The vertical lines in each of the plots divide the reaction where $\gamma = 0.2Jm^{-2}$ into three phases in accordance with its supersaturation dynamics; Specifically, these are the growth phase, the equilibrium phase and the Ostwald ripening phase.

Figure 4.10 shows the evolution of the PSDs in both the reaction (A) and diffusion (B) limits with γ=0.2 Jm^{-2}. The white dots on each of the curves indicates the critical radius (ZGR) of the system at that moment. Panel A shows that under reaction control the FWHM of the distribution remains constant for the first 90 s. During this time the NCs grow from 2-3 nm, and as a result of the drop in S, the critical radius (r_{crit}) increases to approach the mean radius ($\hat{r}$) of the PSD (Ref: Panel C). Inspection of Panel C reveals that r_{crit} remains in equilibrium with $\hat{r}$ between sim200 and 600 s. As previously mentioned the beginning of this stage is characterised by the onset of broadening. During this time period dissolution of the smallest NCs provides monomer to the solution. However, not enough monomer is provided to reinstate net NC growth. As such S gradually increases (only by fractions of a unit) and a concomitant decrease in r_{crit} is observed. At t=1000 s the equilibrium between r_{crit} and $\hat{r}$ is broken as a result of S having increased to a value that allows for net growth

of the PSD. At times between 1000 and 3600 s traditional Ostwald ripening ensues, which is exemplified by an increase in the mean radius and SD of the PSD.

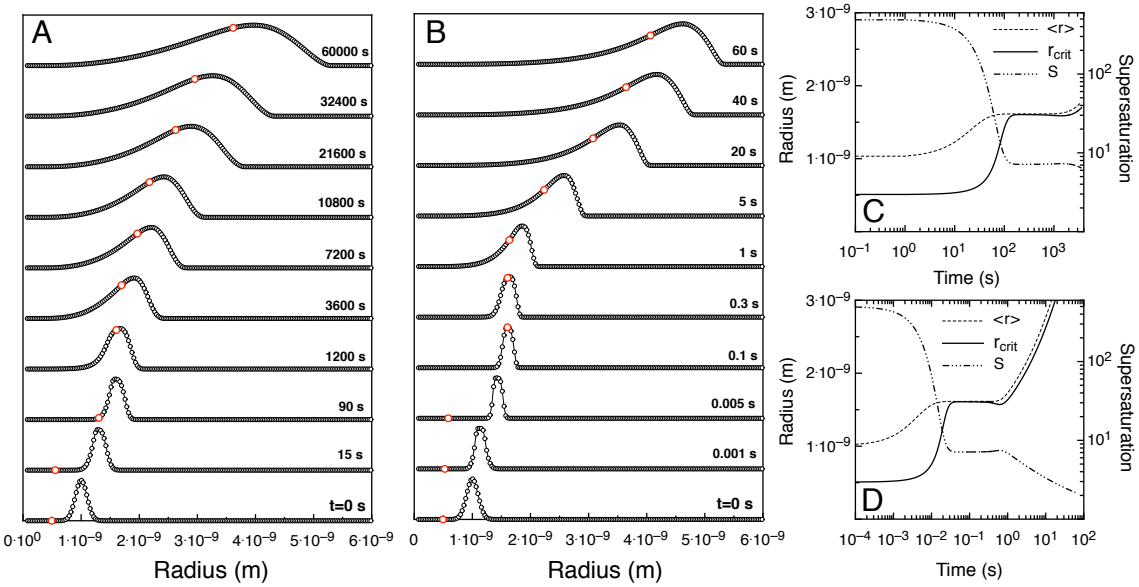

Figure 4.10: PSD as a finction of reaction time in both the Reaction (**A**) and Diffusion (**B**) regimes. Panels (**C**) and (**D**) show the corresponding temporal dynamics of the critical radius, mean radius and supersaturation for both the reaction and diffusion limited simulations respectively.

Panel B displays various snapshots of the PSD under diffusion control. Contrary to the reaction limited case the FWHM of the distribution narrows during the early stages of NC growth. Again we note that the sudden drop in S rapidly increases r_{crit} to the mean value of the distribution, which triggers the onset of broadening and eventual ripening of the PSD. Interestingly, the value of the supersaturation during the time period where $\hat{r}$ and $r - crit$ of the ensembles are in quasi-equilibrium is the same in both limits. As the size of the NCs are the same during this *equilibrium phase* in each of the limits we may infer that the value of S corresponds to the NC solubility. In support of this interpretation Figures 4.8 and 4.9 show that the value of S at equilibrium increases with increasing γ, as NCs with high surface energies will require more monomer to prevent their dissolution. Finally, comparison of the distributions at the termination of the simulations (Panel A- 60000 s and Panel B -60 s) reveals the PSD to be narrower when it has evolved under diffusion limited conditions.

4.7.2 The effect of initial supersaturation

The simulations above clearly prove that NC growth occurs under reaction limited conditions. Consequently, further simulations have been directed solely toward a deeper understanding of NC growth in the reaction limit.

The following simulations were designed to expose the effects of the initial supersaturation on the evolution of a PSD. The same parameters were used as those outlined in the previous section with γ=0.2 Jm^{-2}. Panel C shows that between 0 and 100 s the growth rate is strongly dependent on the supersaturation in solution, with faster growth rates occurring in solutions with higher initial oversaturations. Panel A shows that the onset of ripening occurs at earlier times in systems with a lower initial S. Panel B indicates that, similar to lowering γ, increasing S results in greater initial reductions to the SD and a lower minimum at the onet of equilibrium. By sim10000 s all the SD have converged to a value of $\backsim$24%.

Inspection of Panel C and D reveals convergence of $\hat{r}$ and S at times longer than 10000 s. However, the [NCs] do not converge with higher NC concentrations evident in systems with higher initial S values. This confirms that, at longer times, the evolution of the PSD is no longer governed by the supersaturation in solution but rather by the extent of ripening. Finally, it is of great importance to note that at equilibrium, S adopts larger values for systems with smaller average crystal sizes. As discussed in the previous section the value of S at equilibrium is directly related to the NC solubility. From Panels C and D it may therefore be calculated that NCs with sizes 3.8, 3.2 and 2.4 nm (with surface energies of 0.2 Jm^{-2}) are in equilibrium with monomer concentrations of 51 μM, 72 μM and 162 μM respectively. These numbers are in reasonable agreement with those found experimentally by Qu *et al* [4].

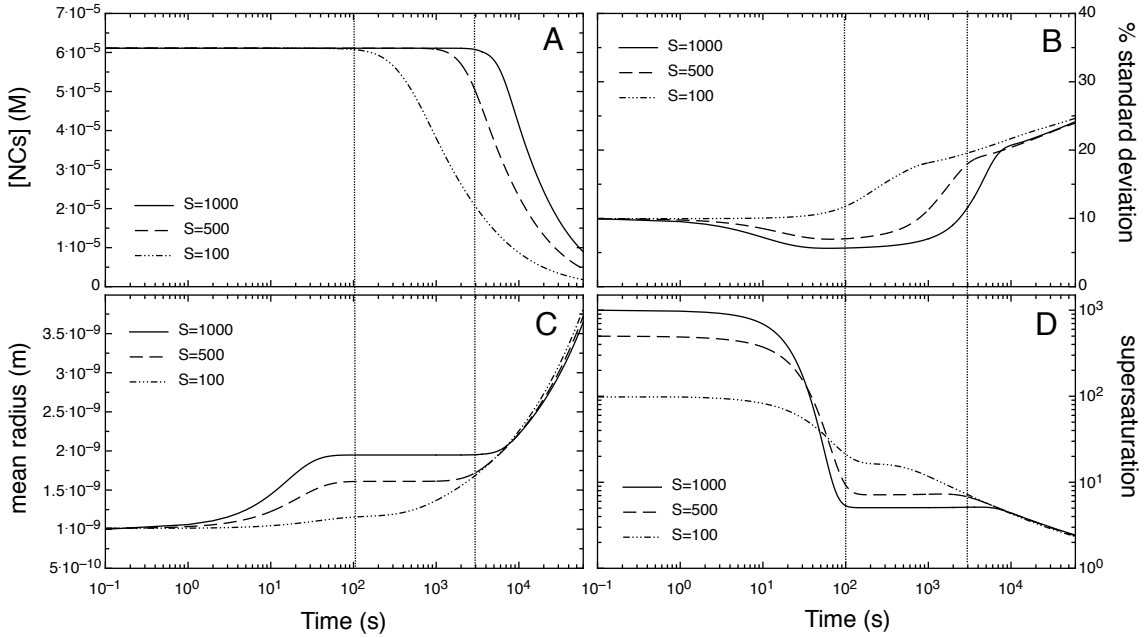

Figure 4.11: Nanocrystal concentration (**A**), standard deviation (**B**), mean radius (**C**) and supersaturation (**D**) as a function of time for NC growth under reaction limited conditions ($\xi = 2000$) with increasing initial supersaturations. The vertical lines in each of the plots divide the reaction where $S = 500$ into three phases in accordance with its supersaturation dynamics. Specifically, the growth phase, the equilibrium phase and the Ostwald ripening phase.

4.7.3 The effect of initial standard deviation

To examine the effect of the initial SD on the evolution of NCs we again assume the same values for the variables and constants outlined in the previous sections (γ=0.2 Jm^{-2} and S=500) and vary the initial SD from 5-30%. Figure 4.12 is a plot of the SD as a function of $\hat{r}$. Plotting the SD as a function of $\hat{r}$ highlights changes to the SD as a direct consequence of NC growth independent of the timescale of either broadening or narrowing. The data shows that regardless of their initial standard deviations, which span 25%, the standard deviations at the termination of the simulation span a range of only $\backsim$3%. However, the dynamics of these changes alter in dependence upon the initial SD. For growth between 2 and 3.2 nm the [NCs] remains constant and greater extents of narrowing are observed for higher initial SDs. During the ripening phase (whose onset is denoted by the arrows in Panels A and B) NCs with an initial SD of 30% broaden by only $\backsim$7% while those distributions with initial SD

values of 5% broaden by 19%. The initially narrow distributions must broaden to a greater extent before a significant number of NC reach the left boundary (dimers) and disappear, subsequently providing the monomer necessary to resume NC growth. Panel B shows that, independent of their initial SDs, when the mean size reaches $sim3.2\ nm$ ($\hat{r} = 1.6nm$) the rapid decline in supersaturation ceases. Further growth decreases S only by a factor of 4 despite the fact that it requires orders of magnitude more monomer to grow a given number of NCs from $sim3.2$-8 nm compared to 2-3.2 nm. These data are in direct support of the conclusion that after the *equilibrium phase* NC growth is dominated by the rate of Ostwald ripening.

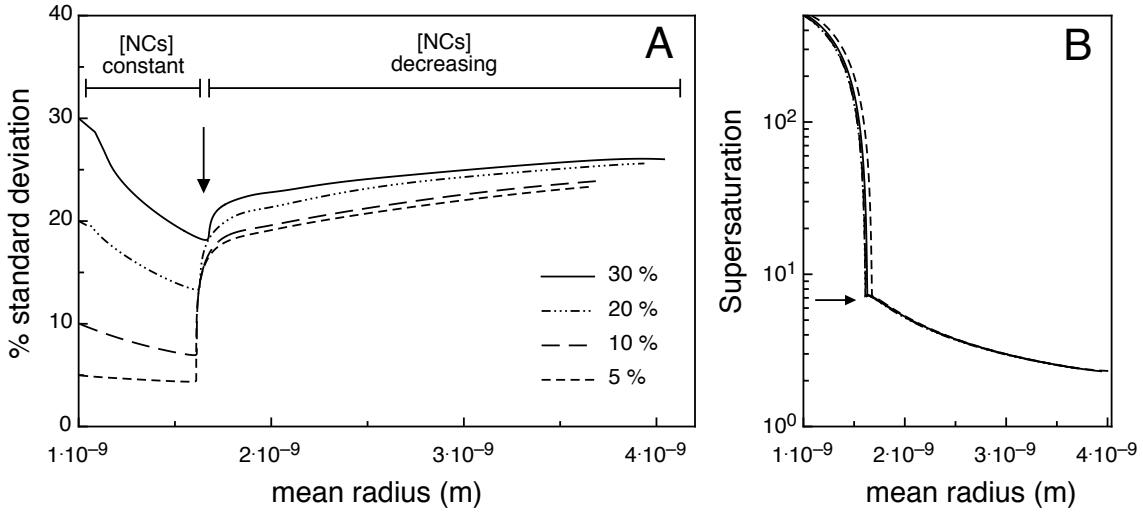

Figure 4.12: (**A**) A plot of the % standard deviation as a function of mean radius. (**B**) The supersaturation in solution as a function of mean radius. The arrows in both panels signify the change in growth dynamics from growth governed by monomer accretion to growth dominated by the rate of ripening within the system.

4.7.4 Comparisons with LSW and Wagner theories

For diffusion and reaction controlled coarsening, stationary size distributions have been predicted by Liftshitz, Slyosov, and Wagner (LSW) [10] and Wagner [32] respectively. For diffusion limited coarsening the stationary distribution function ($W(u)$), where $u = r/r_{crit}$, is given by:

$$W(u) = \begin{cases} \frac{(3^4 e/2^{5/3}) u^2 exp[-1/(1-2u/3]}{[(u+3)^{7/3}(1.5-u)^{11/3}]} & \text{if } 0 < u < 1.5 \\ 0 & \text{otherwise} \end{cases} \tag{4.67}$$

For reaction limited coarsening:

$$W(u) = \begin{cases} 2^7 3u(2-u)^{-5} exp[\frac{-3u}{(2-u)}] & \text{if } 0 < u < 2 \\ 0 & \text{otherwise} \end{cases} \tag{4.68}$$

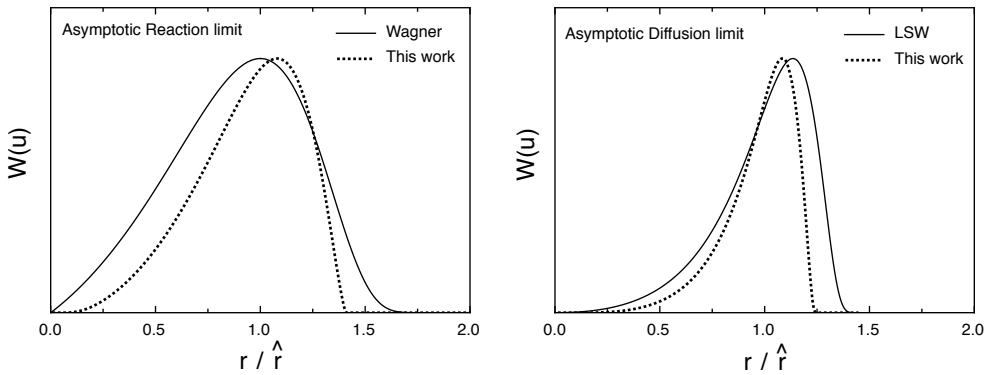

Figure 4.13: (**Left**) Stationary size distribution as predicted by Wagner (solid line) and the asymptotic numerical distribution obtained from simulation (dotted line). (**Right**) Stationary size distribution as predicted by LSW theory (solid line) and the asymptotic numerical distribution obtained from simulation (dotted line).

Figure 4.13 shows the results of the numerical simulations performed in the reaction (ξ=2000) and diffusion limits ($\xi = 1 \times 10^{-3}$). These results are plotted alongside their corresponding stationary distributions as predicted by the LSW and Wagner models; Equations 4.67 and 4.68 respectively. Both numerical simulations were conducted with the following parameters; $T = 503K$, $V_m = 3.2996 \times 10^{-5} m^3 mol^{-1}$, $D = 1 \times 10^{-12} m^{-2} s^{-1}$, $[C]^0_\infty = 1 \times 10^{-2} molm^{-3}$ and $\gamma = 0.3 Jm^{-2}$. At the termination of each simulation changes to the supersaturation were less than 0.001 s^{-1} in the diffusion limit and less than $1 \times 10^{-8} s^{-1}$ in the reaction limit. These correspond to monomer consumption rates of less than 10 nMs^{-1} and 100 fMs^{-1} respectively, indicating that in each case the distribution is close

to its asymptotic limit. Figure 4.13 shows that in both limits the PSDs are narrower than their respective stationary distributions. This is understood as only first order terms in the expansion of the Gibbs-Thomson equation were used to derive each of the stationary distributions outlined by Equations 4.67 and 4.68. Retaining the full exponential term contributes to rapid dissolution of those NCs whose $\hat{r} < r_{crit}$, which is accentuated for nanosized particles. Accounting for this rapid dissolution results in final PSDs with lower SDs than predicted by the LSW and Wagner models. This finding is consistent with other reports that have modelled the long time behaviour of nanoscale colloids [15, 22]. It is important to note that better agreement with the stationary distributions of both limits have been found for simulations describing the evolution of micron-sized particles [17].

4.8 Growth via the sequential injection of monomer

The growth of small NC seeds through the sequential injection of monomer provides a means to achieve particles of a desired size following normal nucleation and growth processes. This technique has been used to grow semiconductor nanocrystals of various types [28, 33–35]. In this section we model the growth of CdSe NCs with an initial radius of 1.5 nm. The following variables and constants were employed to simulate growth: $D = 1 \times 10^{-10} m^{-2} s^{-1}$, $[C]^0_\infty = 0.1 mol m^{-3}$, $T = 503K$, $V_m = 1.65 \times 10^{-5}$ (half the molar volume of a CdSe unit), $\gamma = 0.25 Jm^{-2}$, initial SD=10% and with 10 μM nanocrystals. An initial S value of 3 was also assumed to avoid instantaneous particle dissolution. Five different simulations were performed with ξ in the range 5×10^5 to 5×10^7. As seen in Chapter 2 ligands can vastly alter the growth rates of NCs. Increasing ξ over two orders of magnitude simulates the growth of NCs in the presence of increasing concentrations of strong binding ligands[§].

Figure 4.14A shows the mean radius as a function of time for all five simulations with

[§]For simplicity in the interpretation of the results a constant γ was employed, although as discussed previously concomitant changes to both γ and ξ are more realistic.

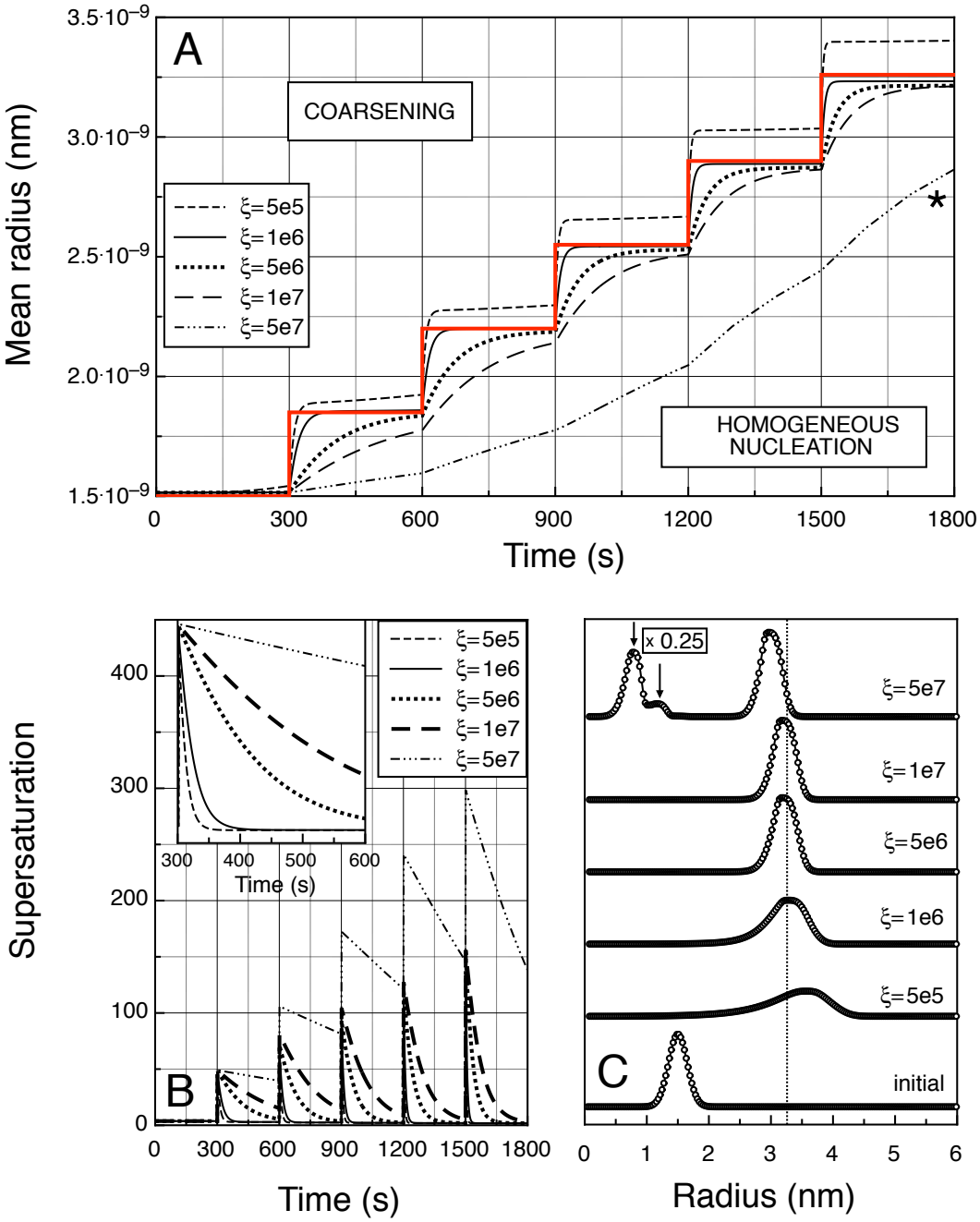

Figure 4.14: (**A**) Mean radius as a function of time for NCs grown via the sequential injection of monomer in reactions with ξ in the range 5×10^5 to 5×10^7. The thick red line indicates the expected NC sizes after each injection of monomer assuming instantaneous growth. (**B**) Supersaturation profiles throughout the reaction. (**C**) The final distributions at $t = 1800s$ for each of the simulations performed.

ξ in the range 5×10^5 to 5×10^7. These results are plotted together with the expected mean radius assuming *instantaneous* NC growth upon monomer injection. Each subsequent injection is separated by 300 s. Panel B shows the supersaturation dynamics throughout the simulation. After each injection S is seen to spike followed by a gradual decrease due to NC growth. Two important features are notable. Firstly, upon increasing ξ from 5×10^5 to 5×10^7 the rate at which S drops after a given injection decreases with the profiles of the decline in S becoming more linear as ξ is increased (see inset). At ξ=5×10^7 the supersaturation decrease is perfectly linear after each injection, typical of highly reaction limited growth, which proceeds at a rate largely independent of the monomer saturation. Secondly, examination of each supersaturation profile individually reveals faster decreases in S after each subsequent injection. This is due to the reaction limited growth profile, which dictates that larger NCs always grow at a rate faster than smaller NCs and as such consume monomer at increasing rates at late times in the reaction when the NCs are larger. Increasing ξ above 1×10^6 results in incomplete consumption of the monomer after the first injection. For the reasons discussed above this process is seen to correct itself for later injections, with the exception of those NCs with ξ=5×10^7.

Panel C displays the final PSDs for each of the simulations. The initial size distribution and the final expected size (vertical dotted line) are also plotted as a reference. At ξ=5×10^5 ripening was seen to accompany NC growth. This results in a broad final distribution and greater than expected increases to the mean radius during growth (Panel A). Clearly, values of ξ=5×10^5 are too low for uniform NC growth and are suggestive of conditions where the ligands in solution are only weakly binding or where not enough strong binding ligands are present to prevent dissolution. At ξ=1×10^6 there is good agreement between the mean radius and the expected mean radius (EMR) at each point throughout the simulation, although the PSD is seen to broaden slightly. The best results were obtained using ξ=5×10^6. Under these conditions the PSD evolved with no significant broadening and the mean radius and the EMR came into almost complete agreement in the moments before subsequent injections.

Further increases to ξ limit the rate of growth too much. At ξ=5 $\times$ 10^7 the mean radius is consistently well below its expected radius. As a consequence, monomer builds up in solution and eventually triggers nucleation. A prodigious number of new nuclei are evident in the final distribution where ξ=5 $\times$ 10^7 as indicated by the arrows.

From the results of these simulations it is clear that to realise the narrowest distributions, with good agreement between the mean and expected sizes, the highest possible values for ξ (slowest reaction rate) must be adopted. However if ξ is very large, as would be the case if the concentration of strong binding ligands in solution was too high, the oversaturation of monomer in solution is relieved via the homogeneous nucleation of the precursor (monomeric) species. Therefore a careful balance of the NC reactivity is required to avoid the extremes of Ostwald ripening and homogeneous nucleation¶.

Figure 4.15 shows detailed results for ideal NC growth where ξ=5 $\times$ 10^6. We can see the SD drops after each injection, verifying the optimal conditions for growth [28, 36]. The changes to the NC concentration throughout the reaction simulation were less than 0.01%, although a minor nucleation event is seen to occur after the injection of monomer at t=1500 s as indicated by the arrow. The bottom panel shows snapshots of the PSD at 300 second intervals beginning from t=0. It can be clearly seen that the distributions maintain their FWHM during the growth process. At the termination of the simulation, mondisperse NC with an average size of 6.5 nm were obtained.

4.9 Nucleation and growth simulations

Having established the effects of various parameters on the growth of NCs we now focus on the more complex dynamics of simultaneous nucleation and growth. Great care was taken to ensure the simulation conditions were as close to realistic experimental conditions as possible.

¶Similar simulations were performed to simulate growth via the continuous injection of monomer (syringe pump method). The results of which are shown in Appendix H. Similar to sequential injections, the best results were found at the slowest surface reaction rates that did not induce nucleation.

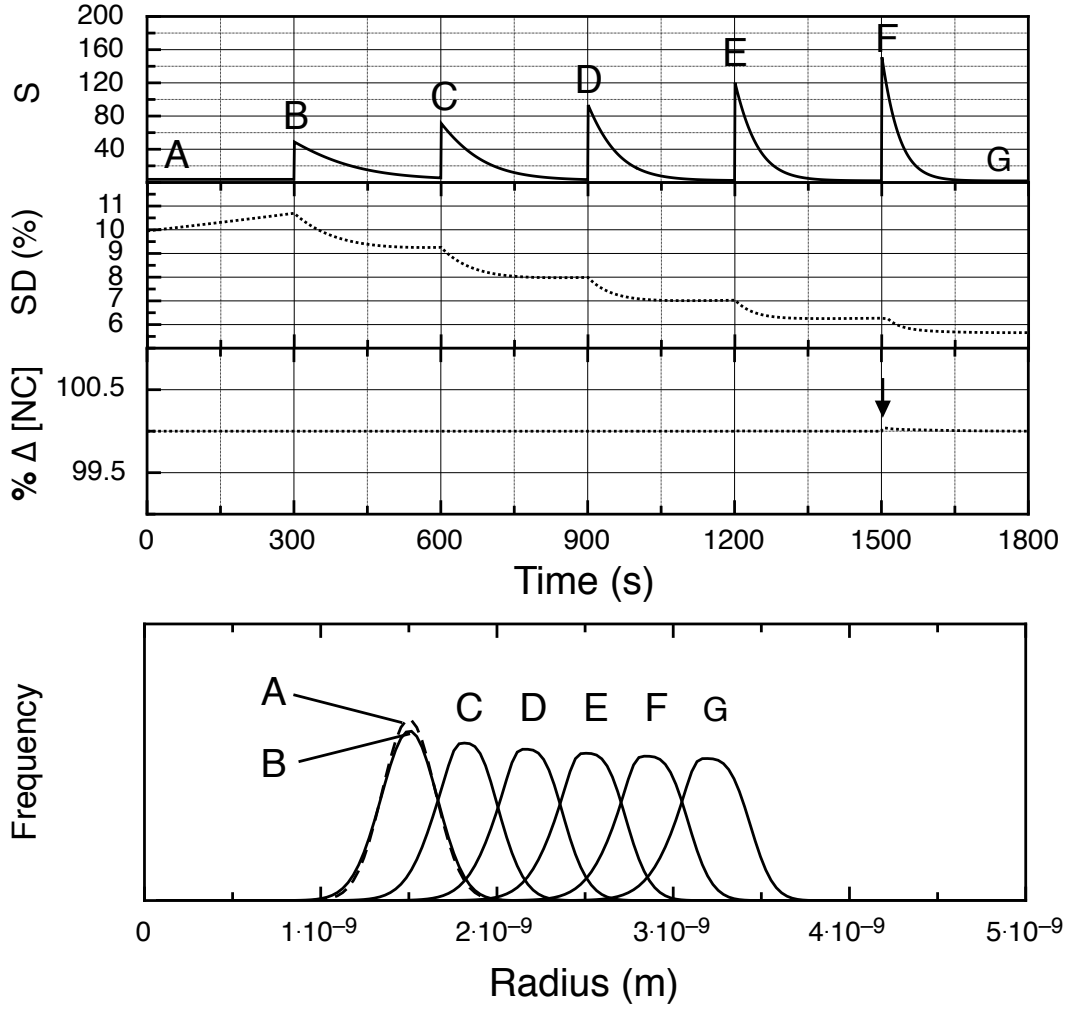

Figure 4.15: From top to bottom: Supersaturation profiles, standard deviation, %Δ[NC] and final PSDs. The letters A-G in the top panel indicate reaction times, which correspond to the PSDs in the bottom panel. The arrow indicates a minor nucleation event. The optimal conditions for NC growth are signified by the absence of either homogeneous nucleation or NC dissolution as well as preservation of the FWHM of the PSD throughout growth.

Typical preparations of NCs employ between 10-50 $molm^{-3}$ of monomer[‖]. Assuming $[C]^0_\infty$ to be on the order of 0.001 $molm^{-3}$ (1 μM monomer in equilibrium with an infinitely flat surface) then initial supersaturations of sim40,000 are reasonable. However, for the following simulations $[C]^0_\infty$ was set to 0.004 $molm^{-3}$ and consequently S was varied between 8000 and 14000 (32-56 $molm^{-3}$ monomer). The temperature during the simulation was adjusted according to a mathematical fit of the temperature drop profiles recorded during the synthesis of CdSe outlined in Chapter 3. For reference, the experimental and modelled temperature drop profiles are displayed in Figure 4.18 in the following section. Estimations of γ using the assumptions of equations outlined by Sugimoto [12] and Bullen *et al.*[37] under the reaction conditions described here yield values for gamma $\backsim$ 0.5 Jm^{-2}. Given that the nucleation and growth of NCs typically occurs in the presence of ligands that form highly soluble complexes with the monomer the value assigned to γ must be somewhat higher than 0.5 Jm^{-2}. As such γ was set at 1.1 Jm^{-2}. To ensure growth on a time scale appropriate to normal NC synthesis ξ was set at 1×10^5. A diffusion coefficient of 5×10^{-11} $m^2 s^{-1}$ was used, which is similar to measurements of other small molecules [38]. The remaining constants were assigned values specific to CdSe. Namely, V_m= 1.65 $molm^{-3}$ (half the molar volume of a CdSe dimer), T_{inj} = 573 K, T_{gr} = 503 K, the radius of the monomer $a = 1.87 \times 10^{-10}$ m. A coagulation coefficient of 0.482 was also employed. Unless otherwise stated the above list of parameters are assumed.

4.9.1 Effect of initial supersaturation

In this section the effect of the initial supersaturation (S_{init}) on the nucleation and growth of nanocrystals is addressed. Figure 4.16A displays the nucleation rate as a function of time on a log-log scale. It can be seen that lower initial supersaturations lead to lower initial nucleation rates. S_{init}=8000 cedes initial rates of 1.4×10^{-3} $molm^{-3}$ (1.4 $\mu M s^{-1}$) while

[‖]Preparation of the CdSe NCs outlined in Chapter 3 employed a total of 42 $molm^{-3}$ of monomer.

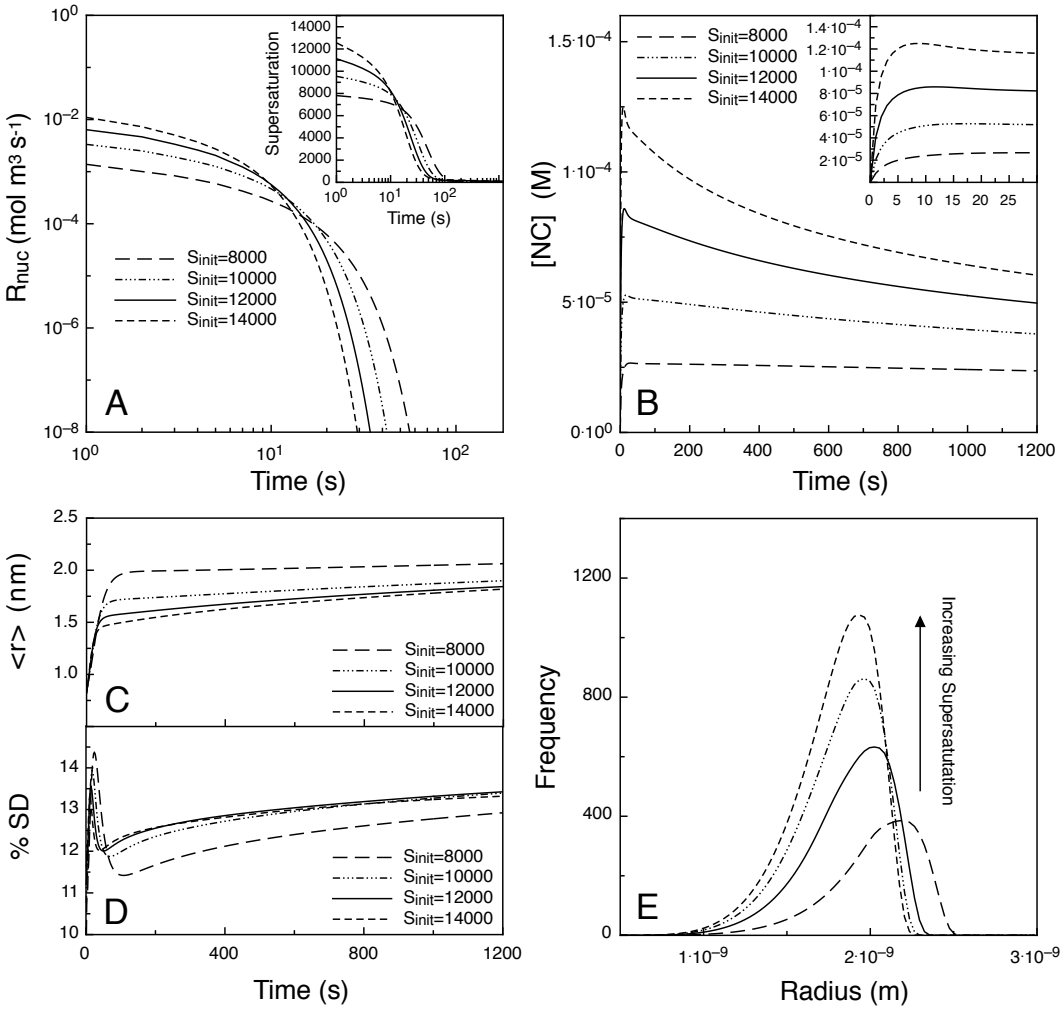

Figure 4.16: (**A**) R_{nuc} as a function of time (the inset shows the supersaturation dynamics). The remaining panels display the [NC] (**B**), mean radius, $\hat{r}$ (**C**) and SD (**D**) as a function of time. Panel (**E**) is a plot of the unscaled PSDs at the termination of the reaction.

S_{init}=14000 imparts initial rates approximately eight times higher at 1.1×10^{-2} $molm^{-3}$ (11 μMs^{-1}). Inspection of Panel B reveals that, in accordance with increasing initial nucleation rates, higher values of S_{init} result in the formation of increasing numbers of NCs. Upon raising S_{init} from 8000-14000 the maximum concentration of nuclei at the end of the nucleation phase increases from 26 μM to 125 μM. Clearly, the rate of monomer depletion is proportional to the number of nuclei formed with an increased number of growth centres containing and removing larger amounts of monomer from the solution per unit of time. As such, having nucleated fewer NCs the nucleation rate for the simulation with S_{init}= 8000 is seen to remain higher for longer periods of time compared to systems with larger values of S_{init}. Specifically, the nucleation phase lasts around twice as long for S_{init}=8000 compared to S_{init}=14000. It should be noted that once R_{nuc} dropped below 1×10^{-8} $molm^{-3}s^{-1}$ (10 pMs^{-1}) the nucleation phase was considered complete.

Upon raising S_{init} from 8000 to 14000 the mean size of the nuclei formed in the first nucleation event decreased from 8.54 $\mathring{A}$ to 8.15 $\mathring{A}$. A decrease in initial nuclei size arises due to the increased thermodynamic stability of smaller NCs in the presence of higher initial oversaturations. Analysis of Panel B highlights the competing kinetic and thermodynamic processes that occur during the early stages of NC formation and growth. Although high S_{init} values kinetically favour nucleation, by increasing the number of collisions, the nuclei that are formed are not thermodynamically stable. As such, ripening is seen to begin directly following the end of the nucleation phase despite the higher monomer saturation levels at the end of nucleation (see insets Panels A and B). Close inspection of the early times in Panel B reveal that once the [NCs] has reached its maximum, $[NC]_{max}$, extremely fast ripening begins, which is more pronounced in systems with larger numbers of NCs.

A direct correlation between the nucleation and growth rates is observed by comparing the data of Panels B and C respectively. Although all the growth rates are similar during the nucleation phase, having nucleated fewer NCs, the growth rate of NCs in systems with lower S_{init} values remains higher for longer periods. Due to the fast continual growth of the

nuclei to larger sizes, they significantly distance themselves from the critical radius of the system. Thus almost no ripening is observed for the case where S_{init}=8000. At longer times the ripening rate is seen to plateau in all systems. The combined data of Panels A, B and C show that the initial supersaturation determines the number of nuclei formed, the early time growth and ripening kinetics as well as the final NC size at $t = 1200s$. The high degree of control the nucleation phase exerts over the subsequent growth kinetics is emphasised by the fact that we observe higher ripening rates and slower growth rates in systems with higher initial supersaturations.

Panel D shows the (percent) standard deviation as a function of time throughout the reaction. It can be seen that the SD increases rapidly at early times to a maximum. Careful analysis of the data presented in Panels D, A and C indicate that broadening of the PSD occurs throughout the nucleation phase. This is a consequence of the disparity between the mean radius of the fast growing PSD and the smaller size of the newly formed nuclei (r_{crit}). Following nucleation, the SD then rapidly decreases due to a combination of NC dissolution and the faster growth of the smaller NCs within the evolving PSD. Interestingly, simultaneous ripening and sharpening is observed contrary to the notion that ripening is always accompanied by broadening of the PSD. At longer times all the standard deviations converge to similar values except for the system with S_{init}=8000, which has a 0.6% lower SD, likely a result of reduced long term ripening and low growth rates.

Finally Panel E displays the final PSDs at $t = 1200s$ for the four systems investigated here. All the PSDs are seen to possess a tail extending to smaller NC sizes. The combined data of Panels A-E demonstrate that the best strategy to achieve smaller NC sizes is to increase the initial monomer concentration to ensure high nucleation rates. Using the simulated conditions outlined here reasonable distributions of NCs with appreciable concentrations in the size range 3.5-4 nm have been achieved. The small resulting size range suggests that altering γ, through the use of appropriate ligands, is a necessary modification to the reaction conditions in order to obtain NCs with sizes tuneable over a wider range.

4.9.2 Effect of injection temperature

In this section the effect of injection temperature, T_{inj}, on nucleation and growth is explored. In order to optimise the batch synthesis of NCs it is common to alter the initial reaction temperature such that a favourable balance between the kinetics and thermodynamics of nucleation and growth is achieved. High initial temperatures ensure high collision rates and successful reaction between the precursor molecules while lower growth temperatures provide thermodynamic stability to the evolving PSD. This methodology is referred to as the "hot injection" method. For the simulations outlined here the injection temperatures were set between 553 K and 593 K as typical synthetic methods used for the production of cadmium selenide NCs are accomplished using these initial temperatures [3, 39]. The growth temperature in all systems was set at 503 K. $[C]_{\infty}^{0}$ was set at 0.004 $molm^{-3}$ and S at 10664, which is appropriate to the total molar amount of monomer employed for the synthesis of CdSe outlined in Chapter 3.

Figure 4.17 Panel A shows a plot of the simulated reaction temperatures as a function of time for T_{inj}=553 K (dashed line), T_{inj}=573 K (solid line) and T_{inj}=593 K (dot-dash line). The reaction temperatures in all systems are seen to converge at the growth temperature at around 600 s. The open circles are digitally recorded reaction temperatures obtained from a typical "hot injection" synthesis. Figure 4.17 Panel B displays R_{nuc} as a function of time. Upon increasing the injection temperature 553 K to 593 K the initial nucleation rate (t= 1s) is seen to increase by around an order of magnitude from $\backsim$0.7 μMs^{-1} to $\backsim$10 μMs^{-1}. As the reaction progresses R_{nuc} is observed to decrease faster in systems with higher initial temperatures. At sim10 s the nucleation rates converge to similar values. For reaction times longer than sim10 s higher values of R_{nuc} are observed in systems with lower temperatures. The crossover at 10 s indicates a switch in nucleation kinetics from temperature dominated nucleation rates to nucleation rates that are governed largely by the number of monomers remaining in solution. Specifically, the system with T_{inj}=553 K has 94% unreacted monomer

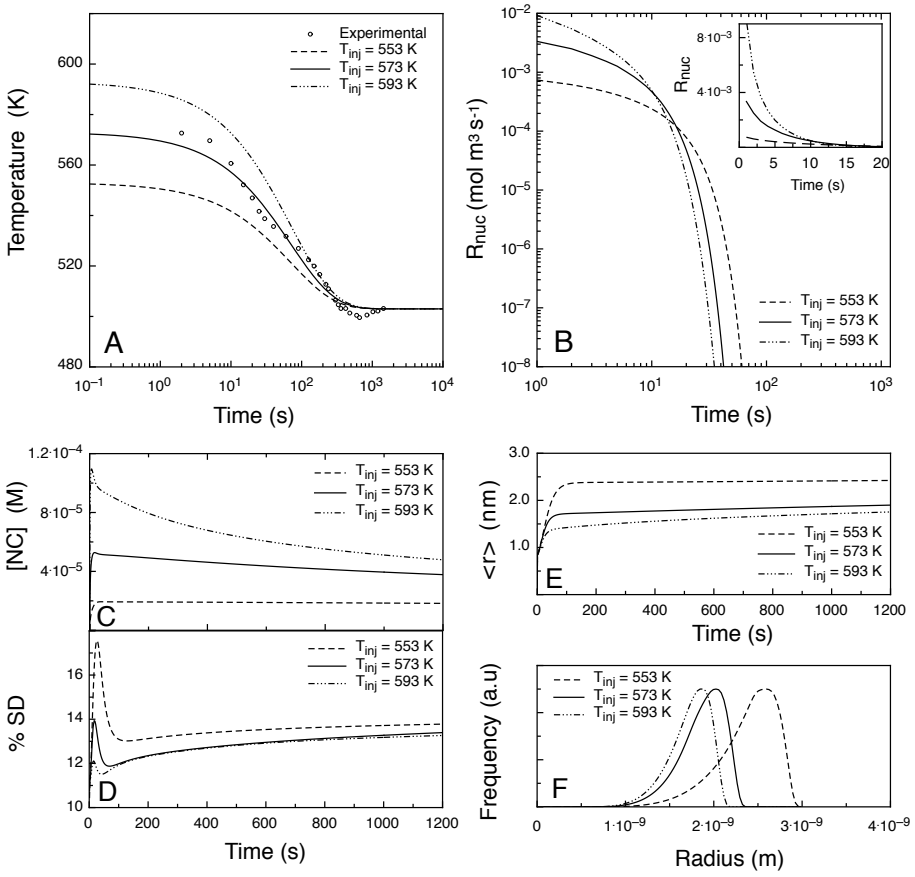

Figure 4.17: Temperature (**A**), R_{nuc} (**B**), [NC] (**C**), SD (**D**) and mean radius, $\hat{r}$ (**E**) as a function of time. Panel (**F**) is a plot of the scaled PSDs at the termination of the reaction.

in solution at t=10 s compared to 62% for the reaction conducted with T_{inj}=593 K. As a direct consequence nucleation continues for around 60 s in the system with T_{inj}=553 K and only 35 s for nucleation at 593 K. Comparison of the data in Panels B and D reveal a direct link between the initial rates and duration of nucleation and the SD of the PSDs. In each individual system the SD is seen to reach a maximum close to the end of nucleation, which is higher for systems evolving at lower temperatures. The fact that nucleation lasts around twice as long upon decreasing the injection temperature from 593 K to 553 K (coupled with faster initial growth rates) culminates in a SD 2.5 % greater at the end of nucleation.

Panel C shows the concentration of NCs as a function of time throughout the reaction. As observed in Figure 4.16 we see that the concentration of NCs reaches a maximum and

then declines more rapidly in systems that have nucleated more NCs. Examination of the early times in Panels D and E reveals that narrowing of the PSD following nucleation occurs only during the fast growth of the NCs. Once the growth rate falls below some critical value narrowing of the PSD no longer occurs. At longer times NC growth slows down and a slow broadening of the PSD is observed.

Collectively the data of Figure 4.17 shows that lower injection temperatures result in poorer nucleation as evidenced by reduced concentrations of nanocrystals and broader distributions at the end of the nucleation phase. It is clear that varying the injection temperature allows tunability of the final NC size, with T_{inj}=553 K resulting in 5 nm NCs after 20 min growth compared to 3.2 nm NCs for T_{inj}=593 K. The final PSDs are plotted in Panel F for reference. Unfortunately there exists an apparent trade off between NC size and concentration. To achieve high yields of larger NCs, it is therefore necessary to employ high temperatures of injection in order to nucleate large numbers of particles and then supplement the reaction with additional monomer, which will allay ripening and promote extended growth and narrowing of the PSD.

4.9.3 Effect of temperature drop

In this section the effects of various rates of undercooling on nucleation and growth are explored. For comparison NC nucleation and growth were also simulated under isothermal conditions**. For "hot injection" methods the rate at which the temperature drops after injection is dependent upon the temperature and volume of both the mother and injection solutions. Various rates of undercooling are experimentally achieved by altering the volume of the injection solution. Figure 4.18A displays the four temperature profiles adopted for the following simulations on a log-linear scale. Systems evolving with these temperature profiles will here in be referred to as T_{iso} (isothermal conditions) and $TP-1$ to $TP-3$ in order of

**For these simulations the following parameters were used: $D = 1\times10^{-10}m^{-2}s^{-1}$, $[C]^0_\infty = 0.004molm^{-3}$, $\gamma = 1.2Jm^{-2}$, $S = 10664$ and $\xi = 2\times10^6$.

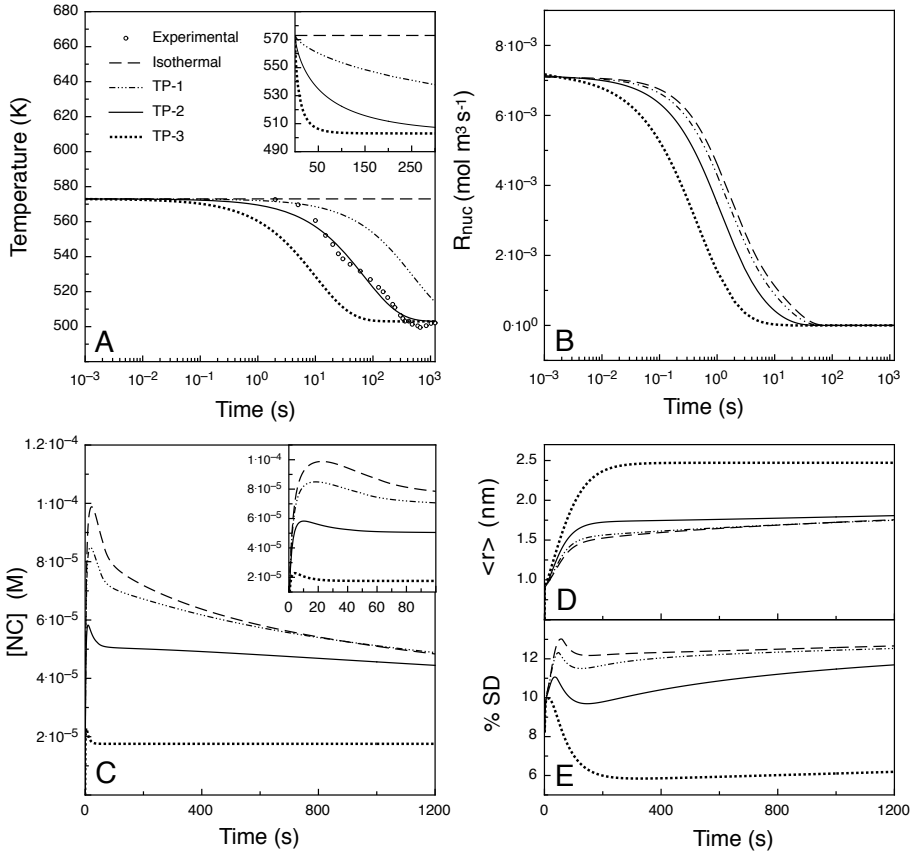

Figure 4.18: Temperature profiles (**A**), R_{nuc} (**B**), [NC] (**C**), mean radius, $\hat{r}$ (**D**) and SD (**E**) as a function of time for various rates of undercooling.

increasing rates of undercooling. For clarity the temperatures during the first few minutes of each reaction are plotted on a linear time scale in the inset of Panel A. The reaction with the fastest rate of undercooling (dotted lines) reaches its growth temperature at $sim100\ s$ while at experimentally determines rates (solid line/open symbols) the growth temperature is reached after $sim600\ s$. It is important to realise that as the duration of the nucleation phase varies between 5-25 s in all the systems investigated here, nucleation is completed while the temperatures are still in rapid decline.

Figure 4.18B shows the nucleation rate as a function of time. As expected at $t = 0$ all the nucleation rates are the same with a value of $7.1 \times 10^{-3} molm^{-3}s^{-1}$ ($7\mu Ms^{-1}$). After the first second of reaction R_{nuc} for $TP-3$ has dropped to 22% of its initial rate to a value of

$1.55 \times 10^{-3} molm^{-3}s^{-1}$ while R_{nuc} for T_{iso} has decreased to only 65% to $4.6 \times 10^{-3} molm^{-3}s^{-1}$. As the temperature difference between T_{iso} and $TP-3$ is only 13 K at $t = 1s$ the data of Panel B highlights the sensitivity of R_{nuc} to the rate of undercooling. Given that we observe consistently lower nucleation rates for systems with increased rates of undercooling the time period during which nucleation is dominant is extended in such systems. Specifically, the time at which $[NC]_{max}$ occurs is delayed from $\backsim 3s$ in system $TP-3$ to $\backsim 20s$ for system T_{iso} (see inset Panel C). Furthermore, it is seen that consistently higher reaction temperatures result in increased numbers of NCs at the end of nucleation, which increases by a factor of five between system $TP-3$ and T_{iso}. If undercooling is fast the nucleation phase is stunted and the increased number of remaining monomers are distributed among fewer nuclei causing faster growth of the PSD (ref: Panel D). As observed for all systems, regardless of the initial conditions, the PSD sharpens following nucleation only during the fast growth of the NCs. The data of Panel E reveals that faster rates of underooling favour narrower final distributions. However, if undercooling is severe the NC yield is compromised.

The true effect of undercooling is best understood by considering that both longer nucleation periods as well as increased rates and extents of ripening are observed for decreasing rates of undercooling. Higher temperatures kinetically drive nucleation in spite of the fact that the system may not be capable of supporting the survival of these nuclei. As such, it may be concluded that the dominant effect of undercooling is kinetic in origin, with the rate of undercooling determining the number of nuclei formed, which in turn governs all subsequent reaction dynamics. Interestingly, at the end of the reaction [NC], $\hat{r}$ and SD are similar for $TP-1$, $TP-2$ and T_{iso}. This suggests that differences in reaction kinetics, and thus tunability of the properties of the final NCs may only be realised in the regime of fast undercooling.

4.10 Concluding remarks

In this chpater we have developed a robust numerical scheme to accurately solve the dynamic rate expressions relevant to simultaneous nucleation and growth. It has been shown that, in addition to higher order upwinding, flux limiters are a necessary inclusion in order to avoid both numerical diffusion and the generation of non-physical oscillations in the data sets. From the simulations performed on NC nucleation and growth it may be concluded that the evolution of NC in the liquid-phase must proceed via highly reaction limited kinetics. This finding is consistent with the experimental results presented in Chapter 3, which showed NC nucleation and growth to be extremely sensitive to the nature and concentration of the adsorbates in solution. The simulations performed here were able to sucessfully replicate the three main aspects of NC evolution observed experimentally. Firstly, the long nucleation time (up to 30 seconds). Secondly, the strong overlap between nucleation, growth and coarsening at early reaction times and finally the presence of a meta-stable (quasi-equilibrium) state, which exists prior to the classical Ostwald ripening of the ensemble. Furthermore, the simulations employed realistic reaction parameters and were conducted over time-scales directly applicable to experimentally observed results on NC evolution.

The inclusion of a particle aggregation mechanism as well as a time and temperature dependent rate expression for the conversion of precursor to monomer constitute further impovements to the current model. Additionally, particle-particle interactions operating through a mean diffusion field may also be included. Although it is expected that interactions of this type would not significantly alter the growth of the NCs given that under reaction limited conditions the interfacial concentrations of the particles are quite similar.

List of Symbols

a= Distance from center of a particle to $[C]_b$

C= Monomer

C_n= Cluster with n units

C_∞= Infinitely large particle (flat surface)

$[C]_e$= Concentration of monomer in equilibrium with particle of radius r

$[C]_i$= Concentration of monomer at the particle interface

$[C]_b$= Concentration of monomer in the bulk of solution

$[C]^0_\infty$= Concentration of monomer in equilibrium with an infinitely flat surface

D= Diffusion coefficient

δ= Radius of the diffusion sphere

I_{react}= Total reaction driven flux

I^{SS}= Total steady state flux

J= Molar flux

k_r= Surface reaction rate

$k_{1,n}$= Forward reaction rate between monomer and a cluster of n units

$k_{-1,n}$= Backward reaction rate between monomer and a cluster of n units

$K_{1,n}$= Equilibrium constant for the reaction $C + C_n \rightarrow C_{n+1}$

$K_{1,\infty}$= Equilibrium constant for the condensation of C onto C_∞

γ= Surface energy

Γ= Instantaneous growth rate

$\Gamma_{i+1/2}$= Convective velocity at the east boundary of i

$\Gamma_{i-1/2}$= Convective velocity at the west boundary of i

$g(r)$= Nuclei distribution function

$\Delta G^0_{1,n}$= Total free energy change at standard states for $C + C_n \rightarrow C_{n+1}$

$\Delta G^0_{1,\infty}$= Total free energy change at standard states for the condensation of C onto C_∞

$\Delta G_{1,n}^{vol}$= Volume free energy change for $C + C_n \rightarrow C_{n+1}$

$\Delta G_{1,n}^{surf}$= Surface free energy change for $C + C_n \rightarrow C_{n+1}$

$\Delta G_{1,p}^{\dagger}$= Activation barrier to the formation of a cluster of p units

ΔG_v= Volume normalised free energy

M_W= Molecular weight

μ= Chemical potential

N_i= Frequency in the i^{th} population N_A= Avagadro constant

N_v= Number of viable nucleation sites

p= Number of units in a cluster of critical size

Ψ= Flux limer operator

r= Particle radius

$\hat{r}$= Mean radius of the distribution

r_{crit}= Critical radius

ρ= Macroscopic density

R= Universal gas constant

S^t= Supersaturation at time t

$S^{t+\Delta t}$= Supersaturation at time $t + \Delta t$

T= Temperature

u= Coagulation coefficient

V_m= Molar volume

V_{tot}= Simulated reaction volume

$z_{1,p}$= Collision frequency between monomer and a critical cluster

Δ^+ and ∇^-= Gradient operators, denoting the direction of the upstream flux

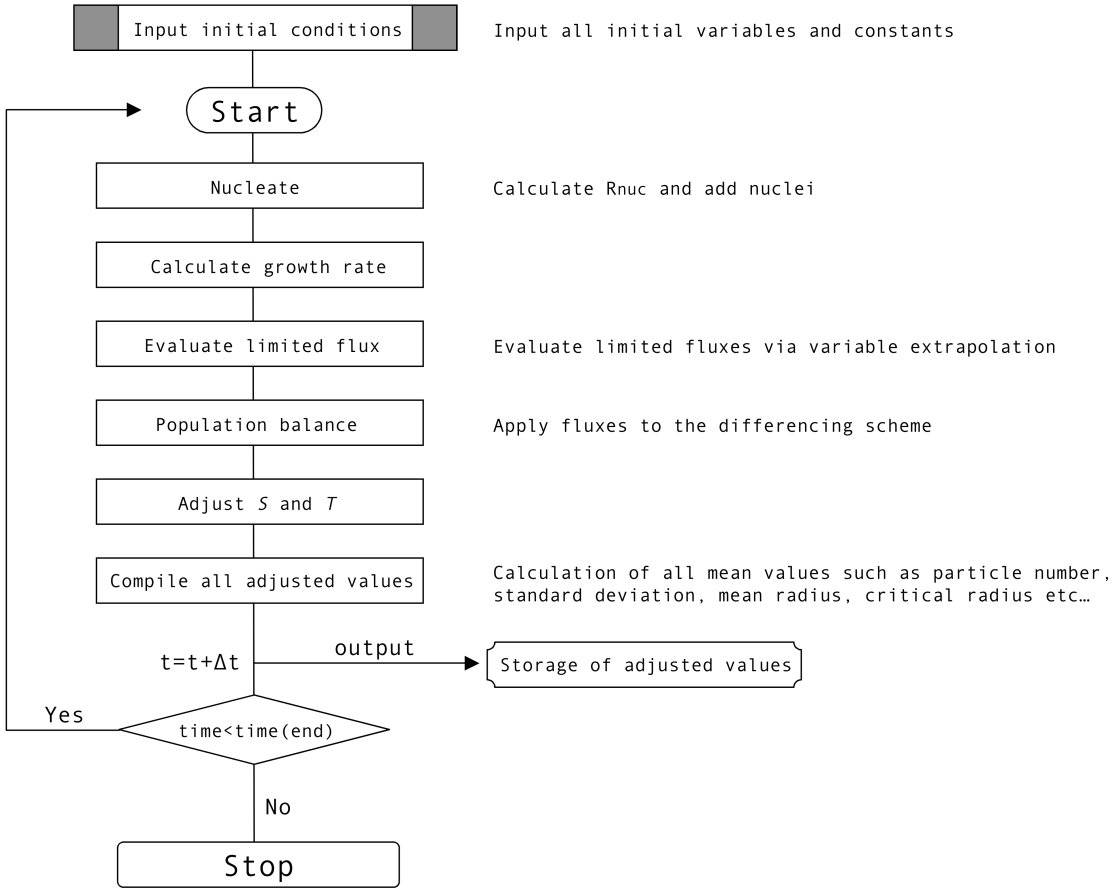

Figure 4.19: Flow-chart showing the basic order of the computer program written in Pascal to solve the population balance equation.

```
program PBE_NUC_GROWTH;

const

{REACTION CONSTANTS}
NN=100;             {Number of populations in simulation}
TI=1e2;             {Time between exportations in units of dt}
RS=3e-11;           {Separation between radii}
dt=1e-2;            {Time step sec}
tau=1200;           {Time of simulation in seconds}
Da=1e5;             {Damkohler number-Diffusion/Reaction control}
g=1.0;              {surface energy: J/m2}
D=1e-10;            {Diffusion coefficient: m2/s}
Cf=0.004;           {Infinity concentration: mol/m3}
VV=5.45e-19;        {Simulated vessel volume: m-3}
TB=1;               {Extent of thermal broadening in nucleated distribution: kT}
y=0.5;              {scaling factor for R_nuc}

{UNIVERSAL CONSTANTS}
Av=6.023e23;        {Avagadros number: mol-1}
kb=1.3806505e-23;   {Boltzmann constant: J/K}
RR=8.314;           {Gas constant: J/K/mol}

{MATERIAL CONSTANTS}
Vm=1.64524e-5;      {Molar volume of monomer: m3/mol}
roe=5816000;        {Bulk material density: g/m3}
MW=95.6874;         {Molecular weight of monomer: g/mol}
a=1.87e-10;         {Radius of a monomer unit: m}

{TEMPERATURE PROFILE CONSTANTS}
TG=503;           {Growth temperature}
TN=573;           {Nucleation temperature}
tau2=70;          {Profile constant}
Beta=0.7;         {Profile constant}
slp=-1;           {degrees per second T drop}
DH=0;             {H: If zero exerts no effect on SS}

{VARIABLES AND ARRAYS}
var i,j,t,p,raw_data,SS,Q,RC,TC,AA,PNC,TNP,SSp,SDc,SSa,TV,TNP1,PPP,SD,u,w;
IV,TQ,TQo,SSc,SSav,pnl,AS,r_crit,k_nuc,p_nuc,knl,psi,gl,rdr;
r: array[1..NN];
pp: array[1..NN];
ff: array[1..NN];
ffo: array[1..NN];
ds: array[1..NN];
nd: array[1..NN];
flr: array[1..NN];

{**************************  BEGIN SIMULATION  ****************************}

begin
j:=12;      {This NEVER changes}
t:=0;       {This NEVER changes}
u:=0;       {This NEVER changes}
```

```
w:=1;       {This NEVER changes}

{DIMENSIONAL CONVERSIONS}
RC:=(RR*TN)/(2*g*Vm);         {Converter of r into r_crit}
TC:=(D*Vm*Cf)*RC^2;           {Converter of tau into time}
Q:=(roe/(MW*VV*Cf));          {Converter of supersaturation}
rdr:=(1/RS);

{SET INITIAL SUPERSATURATION}
SS:=10000;

{GENERATE DATA WINDOW WITH COLUMN NAMES}
Newdatawindow;
raw_data:= Frontwindow;
setcurrentwindow(raw_data);
SetDataWindowProperties(window FrontmostWindow(dataType),
nrrows (tau/(dt*TI))+j, nrcols (tau/(dt*TI))+j);
SelectWindow(raw_data);
SetColumnProperties(col 1,  name 'Time');
SetColumnProperties(col 2,  name 'Supersaturation');
SetColumnProperties(col 3,  name '[NCs]');
SetColumnProperties(col 4,  name 'Rcrit');
SetColumnProperties(col 5,  name 'Boundary');
SetColumnProperties(col 6,  name 'Radius NC');
SetColumnProperties(col 7,  name 'Volume NC');
SetColumnProperties(col 8,  name 'mean radius');
SetColumnProperties(col 9,  name 'max radius');
SetColumnProperties(col 10, name 'SD');
SetColumnProperties(col 11, name 'R_nuc');
SetColumnProperties(col 12, name 'Export parameter');
SetColumnProperties(col 13, name 'Begin data');

{*************************  EXPORT INITIAL VALUES  *************************}

{SET INITIAL SS AND ZERO TIME}
data[1,1]:=t;
data[1,2]:=SS;
{SET INITIAL DIMENSIONLESS DISTRIBUTION - BOUNDARIES}
for i:=1 to NN do
begin;
r[i]:=(i*RS*RC);
end;
{TABULATE INITIAL BOUNDARIES}
for i:=1 to NN do
begin;
data[i,5]:=r[i]/RC;
end;
{TABULATE INITIAL RADII}
for i:=1 to NN do
begin;
data[i,6]:=data[i,5]+(RS/2);
end;
{GENERATE INITIAL DISTRIBUTION}
for i:=1 to NN do
begin;
```

```
ds[i]:=0;
end;
{TABULATE INITIAL DISTRIBUTION}
for i:=1 to NN do
begin;
data[i,11]:=ds[i];
end;
{CALCULATE VOLUME OF NCs}
for i:=1 to NN do
begin;
data[i,7]:=(4/3)*Pi*(data[i,6]^3);
end;
{INITIAL PARTICLE NUMBER}
data[1,3]:=0;
{SET INITIAL Rcrit}
r_crit:=(2*g)/(((RR*TN)/Vm)*Ln(SS));
data[1,4]:=r_crit;
{EXPORT INITIAL MEAN RADIUS}
data[1,8]:=0;
{EXPORT INITIAL MAX RADIUS}
data[1,9]:=0;
{EXPORT STANDARD DEVIATION}
data[1,10]:=INF;
{EXPORT INITIAL TIME}
data[1,1]:=0;
{EXPORT INITIAL NUC RATE}
data[1,11]:=INF;
{EXPORTS TIME INTERVAL FOR EXPORTATION}
for i:=1 to nrrows do
begin
data[i,12]:=i*TI;
end;
{STORES INITIAL TEMPERATURE}
TQ:=TN;
{ZERO STORAGE ARRAY}
for i:=1 to NN do
begin
ffo[i]:=i*0;
end;

repeat

{*************** TEMPERATURE AND DIMENSIONLESS CONVERSIONS  ******************}

{STORE LAST TEMPERATURE AND ADJUST FOR NEW TEMPERATURE}
TQo:=TQ;
TQ:=(TN-TG)*exp(-((t/tau2)^beta))+TG;

{ADJUST TEMP CORRECTED SUPERSATURATION}
SSc:=0;
SSc:=exp(-(DH/RR)*((1/TQo)-(1/TQ)));
SS:=SS*SSc;

{UPDATE DIMENSIONLESS CONVERSIONS}
RC:=(RR*TQ)/(2*g*Vm);
```

```
TC:=(D*Vm*Cf)*RC^2;

{*******************************  NUCLEATION  *******************************}

{CALCULATE NUCLEATION RATE}
if data[j-11,11]>1e-12 then begin
r_crit:=(2*g)/(((RR*TQ)/Vm)*Ln((SS)));
p:=(((4/3)*pi*r_crit^3)/((4/3)*pi*a^3));
p:=p*y;
k_nuc:=(8*Pi*D*a*Av*SS^(p+1)*Cf^2)*(exp(-(4*Pi*r_crit^2*g)/(3*kb*TQ)));
end;

{ENSURES VALID NUMBERS FOR THE NUCLEATION RATE}
data[j-10,11]:=k_nuc;
if data[j-10,11]=INF then k_nuc:=1;
if data[j-10,11]=invalidNum then k_nuc:=1;
if invalid(data[j-10,11]) then k_nuc:=1;
if k_nuc<1e-12 then k_nuc:=0;

{GENERATE NEW NUCLEI}
p_nuc:=k_nuc*Av*VV*dt;
for i:=1 to NN do
begin;
ds[i]:=p_nuc*exp(-(data[i,6]-r_crit)^2/(TB*kb*TQ));
end;

{SUM OLD AND NEW NUCLEI}
for i:=1 to NN do
begin;
nd[i]:=ds[i]+ffo[i];
end;

{*********************************  GROWTH  *********************************}

{GROWTH FUNCTION}
for i:=1 to NN do
begin
pp[i]:=(SS-exp(1/r[i]))/((r[i]+Da))*(TC/RC);
end;

{LIMIT NON PHYSICAL NEGATIVES IN GROWTH RATE:-COURANT CONDITION}
for i:=1 to NN do
if pp[i]<-2.9e-9 then
begin
pp[i]:=-2.9e-9;
end;

{*********************************  PBE  *********************************}

{CALCULATE ALL LIMITED FLUXES}
for i:=2 to NN-1 do
begin

{NEGATIVE FLUX LIMITER}
if pp[i]<0 then
```

```
begin
psi:=0;
if (nd[i+1]-nd[i])<>0 then
gl:=(nd[i]-nd[i-1])/(nd[i+1]-nd[i]);
{Van Leer}
if gl>0 then
psi:=((2*gl)/(1+gl));
flr[i]:=pp[i]*(nd[i]-(0.5*psi*(nd[i+1]-nd[i])));
end;

{POSITIVE FLUX LIMITER}
if pp[i+1]>0 then
begin
psi:=0;
if  (nd[i]-nd[i-1])<>0 then
gl:=(nd[i+1]-nd[i])/(nd[i]-nd[i-1]);
{Van Leer}
if gl>0 then
psi:=((2*gl)/(1+gl));
flr[i+1]:=pp[i+1]*(nd[i]+(0.5*psi*(nd[i]-nd[i-1])));
end;
end;

{POPULATION BALANCE}
for i:=1 to NN-1 do
begin
ff[i]:=nd[i]-(dt*rdr*(flr[i+1]-flr[i]));
if ff[i]<1e-50 then ff[i]:=0;
end;

{*************************  SUPERSATURATION ADJUSTMENTS  *********************}

{RESET "MONOMER"}
for i:=1 to 5 do
begin
ff[i]:=0;
end;

{ADJUST SUPERSATURATION}
for i:=1 to NN-1 do
begin
SSa:=ff[i]-ffo[i];
SSp:=(Q*data[i,7]*SSa);
SS:=SS-SSp;
end;

{**************************  PREPARE NEXT ITTERATION  **************************}

{TIME UPDATE}
t:=t+dt;

{PRESERVES LAST ITTERATION}
for i:=2 to NN do
begin
ffo[i]:=ff[i];
```

```
end;

{*****************  DATA EXPORT AT CERTAIN TIME INTERVALS ONLY  ***************}

if u+1=data[w,12] then begin
{EXPORT SUPERSATURATION}
data[j-10,2]:=SS;
{EXPORTS DATA}
for i:=2 to NN-1 do
begin
data[i,j+1]:=ff[i];
end;
{EXPORTS [NC] IN SIMULATION}
data[j-10,3]:=0;
for i:=1 to NN do
begin;
data[j-10,3]:=data[j-10,3]+ff[i];
end;
TNP:=data[j-10,3];
data[j-10,3]:=TNP/(VV*1000*Av);
{EXPORTS r_crit}
data[j-10,4]:=r_crit;
{EXPORT TIME}
data[j-10,1]:=t;
{EXPORT Rnuc}
data[j-10,11]:=k_nuc;
{EXPORT MEAN RADIUS - RADIUS OF AVERAGE VOLUME}
TV:=0;
for i:=2 to NN do
begin
TV:=TV+(data[i,7]*ff[i]);
end;
IV:=TV/((data[j-10,3])*VV*1000*Av);
data[j-10,8]:=((3*IV)/(4*Pi))^(1/3);
{EXPORT RADIUS WITH GREATEST POPULATION}
for i:=5 to NN-5 do
if  (ff[i] > ff[i-3])
and (ff[i] > ff[i-1])
and (ff[i] > ff[i+1])
and (ff[i] > ff[i+3])
then
begin
data[j-10,9]:=data[i,6];
end;
{EXPORT NUMERICAL STANDARD DEVIATION}
SD:=0;
for i:=2 to NN do
begin
SDc:=ff[i]*((data[i,6]-data[j-10,8])^2);
SD:=SD+SDc;
end;
data[j-10,10]:=Sqrt(SD/TNP);
data[j-10,10]:=(data[j-10,10]/data[j-10,8])*100;
j:=j+1;
w:=w+1;
```

```
end;
u:=u+1;
until
t>=tau;
beep;
SpeakString('Simulation complete');
end; {TERMINATES SIMULATION}
```

Bibliography

[1] Y. Chen, E. Johnson and X. Peng. Journal of the American Chemical Society **129**, 10937 (2007).

[2] E. M. Wong, J. E. Bonevich and P. C. Searson. J. Phys. Chem. B **102**, 7770 (1998).

[3] J. L. van Embden and P. Mulvaney. Langmuir **21**, 10226 (2005).

[4] L. Qu, W. W. Yu and X. Peng. Nano Letters **4**, 465 (2004).

[5] E. V. Shevchenko, D. V. Talapin, H. Schnablegger, A. Kornowski, O. Festin, P. Svedlindh, M. Haase and H. Weller. J. Am. Chem. Soc. **125**, 9090 (2003).

[6] T. Sugimoto, S. Chen and A. Muramatsu. *In Colloids and Surfaces A*, vol. 135, 207–226 (1998).

[7] A. Henglein. Chem. Rev. **89**, 1861 (1989).

[8] A. Henglein and M. Giersig. Journal of Physical Chemistry **98**, 6931 (1994).

[9] J. Langer and A. Schwartz. Physical Review A **21**, 948 (1979).

[10] I. M. Lifshitz and V. V. Slyozov. J. Phys. Chem. Solids **19**, 35 (1961).

[11] P. E. Wagner and G. P. Franz. Journal of Colloid and Interface Science **53**, 429 (1975).

[12] T. Sugimoto. Adv. Colloid Interface Science **28**, 65 (1987).

[13] J. Robson. Acta Materialia **52**, 4669 (2004).

[14] J. Robson. Materials Science and Technology **20**, 441 (2004).

[15] O. Myhr and O. Grong. Acta Materialia **48**, 1605 (2000).

[16] G. Madras and B. J. McCoy. Chem. Eng. Sci. **58**, 2903 (2003).

[17] J. Yao, K. Elder, G. Hong and M. Grant. Physical Review B **45**, 8173 (1991).

[18] S. Kumar and D. Ramkrishna. Chemical Engineering Science **51**, 1311 (1996).

[19] A. Alexopoulos, A. Roussos and C. Kiparissides. Chemical Engineering Science **59**, 5751 (2004).

[20] J. Boris and D. Book. Journal of Computational Physics 38–69 (1973).

[21] S. Zalesak. Journal of Computational Physics **31**, 335 (1979).

[22] D. V. Talapin, A. L. Rogach, M. Haase and H. Weller. J. Phys. Chem. B **105**, 12278 (2001).

[23] J. Thessing, Q. Jianghong, C. Haiyan, N. Pradhan and X. Peng. Journal of the Americal Chemical Society **129**, 2736 (2007).

[24] D. Robb and V. Privman. Langmuir **24**, 26 (2007).

[25] N. Mantzaris. Chemical Engineering Science **60**, 4749 (2005).

[26] S. Kwon, Y. Piao, J. Park, Y. Angappane, S. andJo, N. Hwang, J.-G. Park and T. Hyeon. Journal of the American Chemical Society **129**, 12571 (2007).

[27] C. Riberio, E. Lee, E. Longo and E. Leite. ChemPhysChem **6**, 690 (2005).

[28] X. Peng, J. Wickham and A. P. Alivisatos. Journal of the American Chemical Society **120**, 5343 (1998).

[29] B. van Leer. Journal of Computational Physics **32**, 101 (1979).

[30] C. Hirch. *Numerical Computation of Internal and External Flows*, vol. 2 (John Wiley & Sons Ltd., 2000).

[31] W. Press, B. Flannery, S. Teukolsky and W. Vetterling. *Numerical Recipes: The Art of Scientific Computing* (Cambridge University Press, 1986).

[32] C. Wagner. Z. Elecktrochem. **65**, 581 (1961).

[33] S. Haubold, M. Haase, A. Kornowski and H. Weller. Chemphyschem **2**, 331 (2001).

[34] R. Xie, U. Kolb, J. Li, T. Basch and A. Mews. Journal of the American Chemical Society **127**, 7480 (2005).

[35] S. Kim, B. Fisher, H.-J. Eisler and M. Bawendi. J. Am. Chem. Soc. **125**, 11466 (2003).

[36] J. van Embden, J. Jasieniak, D. Gomez, P. Mulvaney and M. Giersig. Australian Journal of Chemistry **60**, 457 (2007).

[37] C. R. Bullen and P. Mulvaney. Nano Letters **4**, 2303 (2004).

[38] P. W. Atkins. *Physical Chemistry*. 5th ed. (Oxford University Press, Oxford, 1994).

[39] C. B. Murray, D. J. Norris and M. G. Bawendi. J. Am. Chem. Soc. **115**, 8706 (1993).

Chapter 5

A Review of the Synthetic Chemistry Involved in the Synthesis of CdSe Core/Shell Nanocrystals *

It is well known that as-prepared semiconductor nanocrystals exhibit low quantum yields (QY) and that their photoluminescence (PL) is extremely sensitive to the local environment. Although the QY can be increased through passivation of the surface with carefully chosen organic molecules (ligands)[2], these molecules are labile and thus provide no long-term stability. Ligands may desorb from the surface and be replaced by other, less favourable species and they may also undergo side reactions in the solvent [3]. In order to combat these shortcomings, recent efforts have focused on the development of inorganic surface passivation techniques [4–10]. Epitaxial coating of as-prepared core crystals with a "shell" of a wider band gap semiconductor provides a means to permanently passivate the core. Shell deposition can, in principle, enable all surface atoms to be passivated, both physically and electronically insulating the core from its environment. Compared to organically passivated cores, core/shell structures can tolerate harsher processing conditions[11], opening up a much wider array of applications.

*The material presented in the following sections was published in reference [1].

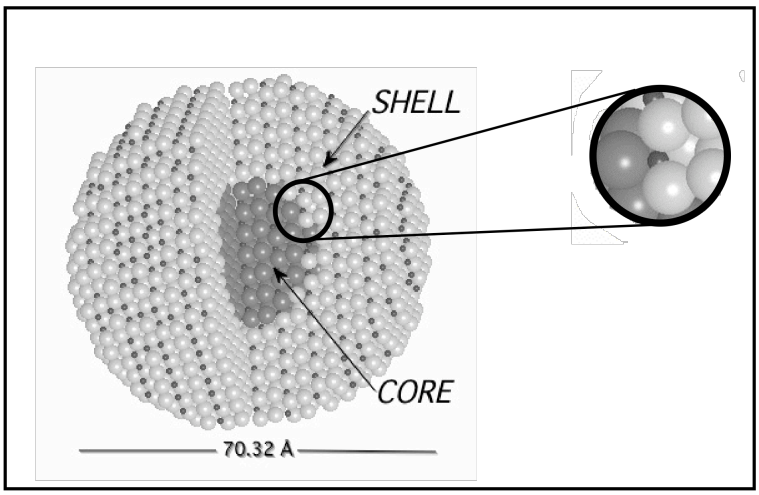

Figure 5.1: Model of a CdSe/CdS nanocrystal with 5 monolayers of CdS shell. The model shows the smaller cadmium atoms occupying the tetrahedral interstitial sites between the larger anions. The expanded region serves to highlight the epitaxial nature of the CdS shell showing both selenium and sulfur coordinating about an interfacial cadmium.

5.1 Introduction

Over the past decade numerous studies of the synthesis and characterisation of high quality colloidal semiconductor nanocrystals have been reported [12–21]. Their narrow size distribution, tuneable emission and photo-stability have made them an attractive alternative to conventional dyes for use as biological fluorescent probes [22–25]. The sensitivity of their fluorescence levels to surface bound adsorbates has opened up the possibility for their use as fluorescence based chemical sensors [26]. Doping these materials into glasses and polymers creates platforms from which more complex structures may be fabricated. QD-based lasers [27–29], LED's [30–32], electroluminescent (EL) devices [33] and solar cells [34] are all being actively developed at present.

Despite the scope of possible uses for these crystals, the production of core/shell semiconductor nanocrystals is still very much in its infancy, and in fact, most of the current research is fuelled by the desire for a more comprehensive understanding of the quantum

size effects in these materials. As research questions become more specific, the necessity to produce structures with well defined dimensionalities becomes more critical. Therefore, achieving greater control over the synthetic procedure of shell deposition is essential not only for the production of more chemically stable luminophores but in providing accurate insights into the complex properties of semiconductor nanocrystal heterostructures.

Figure 5.1 depicts a core/shell nanocrystal highlighting the epitaxial nature of the shell coating. Several methods are currently used to synthesise core/shell nanocrystals, each with its own advantages and disadvantages. As it is unlikely that one type of core/shell will fulfill the needs of all potential applications it is necessary to tailor the particles to suit each purpose. As such, success in the synthetic procedure of shell deposition is subjective. For example, some applications such as biolabelling require high QY and good PL stability, but the actual, final particle morphology is less important. On the other hand, photovoltatic devices do not require particles with a high QY but do require structures that facilitate extremely efficient charge separation. At present, there exist enough experimental procedures for the production of CdSe core/shell particles with the luminescence stability and QY necessary to cater for most of the existing applications. However, there still exists the absence of data which precisely links the physical dimensions of core/shell particles to their optical properties. In light of this, the current challenge is to synthesise heterostructures with well defined physical parameters and to characterise these particles by high resolution transmission electron microscopy, with the goal of establishing a clear link between core size, shell type and shell thickness, and the optical properties of core/shells.

This goal can only be realised through careful optimisation of the reaction conditions. The temperature of the reaction, the growth solvent, the precursor type and concentration and the ligand chemistry must all be optimised to suit both the core and shell materials. The ultimate aims are to be able to tune particle morphology, achieve a high QY, obtain a close agreement between predicted and measured shell thickness, and avoid homogeneous nucleation.

In this chapter we focus on the methodologies involved in the production of CdSe core/shell heterostructures. In fact, the majority of advances in core/shell synthesis were first achieved in CdSe based systems [35, 36]. We will begin by presenting the motivation behind the development of CdSe core/shell nanocrystals. We will then move on to discuss the synthetic challenges involved in the creation of highly defined core/shell structures. The effects of lattice mismatch as well as the types of solvents, precursors and ligands necessary for controlled shell deposition will be discussed. Through the use of an effective mass model we will then comment on the expected changes to the optical properties of core/shells during shell deposition. In the subsequent section, calculations that illustrate how to determine the amount of monomer required to grow a shell of a predetermined thickness will be presented. Finally, in order to place all these issues into context, we will then present the reader with the evolution of CdSe core/shell structures, with reference to significant breakthroughs in the synthetic method of their production. While the focus will be on CdSe core/shell particles, the general principles are directly applicable to other core/shell types.

5.2 General Principles

5.2.1 Physical and electronic isolation of the core

The necessity to synthesise core/shell structures can only be appreciated in conjunction with an understanding of the photo-physics of bare cores. In semiconductor nanocrystals, high QY and PL stability are achieved by maximising the probability that charge recombination will occur via the band edge. This is made difficult by the multitude of competing processes that may occur upon excitation of a nanocrystal. After the generation of an exciton inside a core nanocrystal, one or both of the charge carriers may become "trapped" in surface states whose energies lie within the band gap. These surface states arise as surface atoms are not completely incorporated into the lattice and as such possess orbitals capable of either

accepting or donating electrons. These orbitals (or dangling bonds) are inherent to the nanocrystal and exhibit a range of energy levels that begin in the valence band and extend across the band gap into the conduction band [37, 38]. However, it is only those levels lying within the band gap that provide non-radiative recombination pathways that compete with band edge luminescence. Passivation of these traps with appropriate ligands (those that generate orbitals outside the band gap) has been shown to greatly enhance the luminescence quantum yields of core nanocrystals [2]. Unfortunately, due to steric considerations even the least bulky ligands have packing densities lower than those of the surface atoms [39, 40]. For example, in a moderately sized CdSe nanocrystal (c.a 3 nm) linear alkyl amines can at best passivate only 80% of the total number of cadmuim surface sites [2]. Passivation of the surface chalcogenides (selenium) is even more problematic as in this case the most effective stabilisers are tertiary phosphines such as trioctylphosphine, which have extremely low packing densities. In principle to completely eradicate surface traps an epitaxially grown inorganic shell must be employed.

Surface trapping is only one of many processes that may occur upon excitation of a nanocrystal. The charge carriers may also be scavenged by redox species in solution [41], or (if dispersed in a solid state material) become trapped on local defect sites in the matrix [42]. In addition, the electron may undergo either direct [43] or Auger assisted ionisation, leading to non-radiative recombination or permanent oxidation of the nanocrystal [44, 45].

The epitaxial nature of shell growth, as well as the physical and potential barrier created by the shell, act to reduce the probability of all such processes. This is evidenced by the fact the emission exhibits close to single exponential dynamics and the luminescence lifetime can be up to an order of magnitude longer than cores under the same conditions [46]. Core/shell particles also exhibit vastly improved QY and PL stability compared to bare cores as indicated by both ensemble [47–50] and single particle investigations [5, 51, 52].

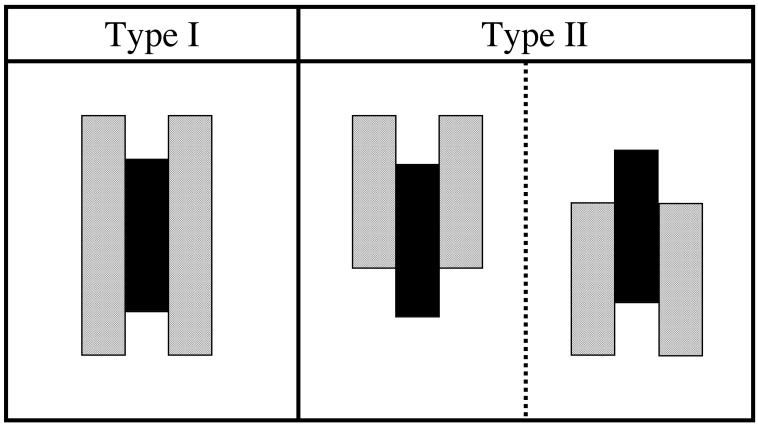

Figure 5.2: Schematics of the different heterostructure types. The core is represented by the dark boxes and the shell with the lighter boxes. In Type I heterostructures both the electron and hole are confined by a potential barrier created by the shell. Type II heterostructures are further split into two classes: Left; conduction band (electron) confinement only, Right; valence band (hole) confinement only.

5.2.2 Shell type, concentration and temperature

The most important consideration prior to embarking on the production of core/shell semiconductor nanocrystals is choosing a shell material with the desired band positions relative to the core. All possible combinations of compatible core and shell materials result in heterostructures that fall within three, main classes. In structures where both the electron and hole are confined to a potential well created by the shell, the structure is classified as Type I. Conversely, if only one carrier is confined by the shell, the structure is classed Type II. In Type III heterostructures neither carrier is confined by the shell as both the valence and conduction band edges of one material lie either above the conduction band or below the valence band of the other. To the best of our knowledge there have been no reports of colloidal Type III semiconductor nanocrystals. As a consequence, no further discussion of these structures will be presented.

Figure 5.2 shows a schematic of the band positions in Type I and Type II core/shell heterostructures. For high QY and luminescence stability Type I nanocrystals are the obvious choice as they provide the greatest probability that charge recombination will occur via the band edge (Ref: Section 2.3). In Type II nanocrystals, one carrier is mostly confined to

the core while the other is mostly confined to the shell. The spatial separation of the charge carriers upon their relaxation to the band edge reduces the overlap of the electron and hole wavefunctions. The resulting depletion in the oscillator strength of the radiative transition lengthens the lifetime of the excited state [53]. In turn this increases the probability that the unconfined charge carrier will be either trapped or scavenged (Ref: Section 2.1). As such, Type II nanocrystals typically exhibit low QY ($\leqslant$10%) [54] and are extremely sensitive to the local environment [53]. Given that they are not stable emitters, Type II nanocrystals may be more beneficial in applications where charge separation is desired, such as photovoltaics.

It should be noted that the choice of shell material is not only limited by the shell band positions. To achieve epitaxial growth the lattice parameters of the core and the shell must be closely matched (Ref: Section 2.2.4). In the case of CdSe this limits the viable "Type I" shell materials to CdS, ZnSe and ZnS.

Once the shell material has been chosen, there are a number of fundamental reaction conditions that must be established. Particle concentration and reaction temperature are among the most important preliminary decisions. In principle shell growth can occur over a wide range of core concentrations. However, it is best to choose a concentration that agrees well with those concentrations found during the later stages of core synthesis (for CdSe between 20 and 60 μM is considered typical).

The temperature of the reaction must be high enough to allow for the decomposition of the shell precursors and the growth of the shell, without inducing Ostwald ripening of the cores (resulting in a defocusing of the size distribution). Temperatures in the range 200-260°C are commonly used to effect the growth of semiconductor core/shells. Given that the rate of ripening depends strongly on particle size [55–57], the temperature at which shell deposition is conducted must be altered to suit the specific particle size, with the smallest particles requiring the lowest temperature. In addition, to anneal defects and achieve high QY, it is best to use the highest temperature possible to impart maximum crystallinity to the shell.

5.2.3 Ligand chemistry in shell deposition

After the synthesis of the core nanocrystals it is customary to remove the unreacted monomer and excess ligand by washing the particles. The concentration of the clean dispersion of particles is then calculated (assuming the extinction coefficient is known), and then the desired amount redispersed in fresh solvent to begin the shelling procedure. Removal of the remaining monomer prevents the growth of a composite shell upon the introduction of shell monomer. As the ligands used to generate the cores may not be favourable for shell growth, washing out the excess ligand allows the synthetic chemistry of core and core/shell production to be independent.

The first synthetic consideration is selecting a growth solvent suitable for shell deposition. The high temperatures required for shell growth necessitate the use of a growth solvent comprised largely of ligands that are able to stabilise the particles at these temperatures, while preventing dissolution or Ostwald ripening. To achieve this it is best to choose ligands that form sparingly soluble complexes with the core and shell constituents. In the case of CdSe, weakly coordinating ligands such as trioctylphosphine oxide (TOPO) and long chain alkyl amines have proved to be successful in this regard.

It is unlikely that the growth solvent alone is capable of controlling shell growth to the degree necessary to realise high quality core/shell nanocrystals. Hence, additional ligands are commonly employed to effect this task. The role of these additional ligands is to control the many linked equilibria that exist in solution during shell deposition. Figure 5.3 illustrates the nature of these competing equilibria. To make this schematic easier to follow, the corresponding equilibria are also outlined below, where "NC" represents the growing nanocrystal, "M" represents the free monomer and "L" the free ligand. The rate constants in parentheses directly relate to those depicted in Figure 5.3, with the rate constants of the forward and back reactions expressed as k_x and k_{-x} respectively.

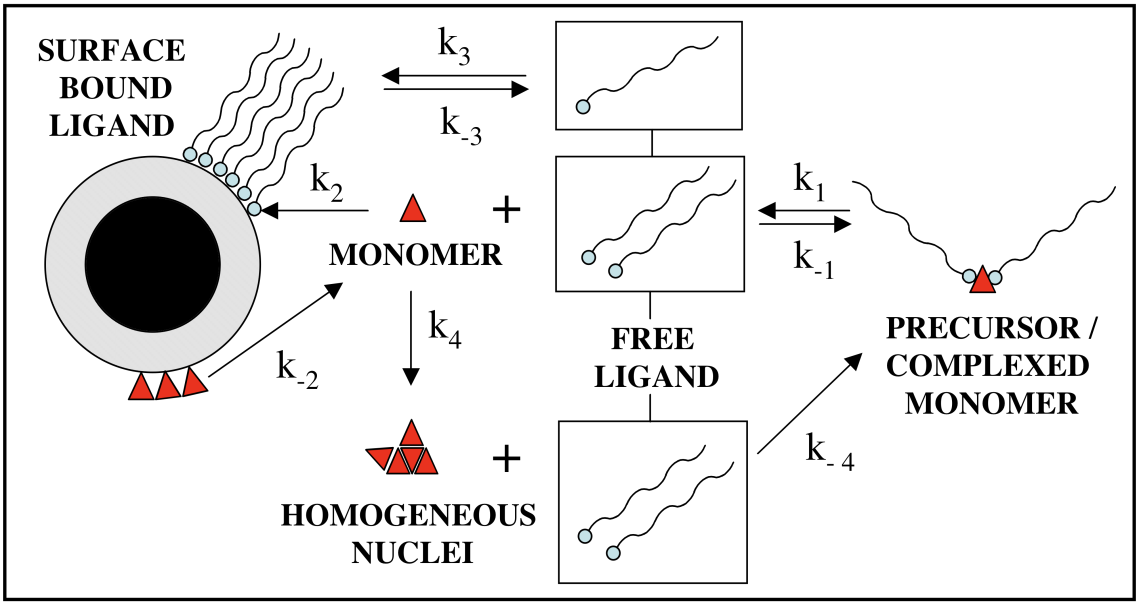

Figure 5.3: The multiple equilibria ($k_1 \rightarrow k_4$) that exist in the growth medium during the production of core/shell nanocrystals. Note that all of the equilibria are controlled by the amount (also type) of "free ligand" present in the reaction solvent.

Equilibrium 1. $\mathrm{M(L)}_x \underset{k_{-1}}{\overset{k_1}{\rightleftharpoons}} \mathrm{M} + \mathrm{xL}$

Equilibrium 2. $\mathrm{NC} + \mathrm{M} \underset{k_{-2}}{\overset{k_2}{\rightleftharpoons}} \mathrm{NC\text{-}M}$

Equilibrium 3. $\mathrm{NC\text{-}L}_x \underset{k_{-3}}{\overset{k_3}{\rightleftharpoons}} \mathrm{NC} + \mathrm{xL}$

Equilibrium 4. $\mathrm{M} + \mathrm{M} \underset{k_{-4}}{\overset{k_4}{\rightleftharpoons}} 2\mathrm{M} \ldots$

In equilibria 1→4 the processes of the forward reactions are: 1. Precursor/complexed monomer dissociation, 2. Shell growth, 3. Ligand desorption from the nanocrystal surface and 4. Homogeneous nucleation. After close inspection of these reactions it becomes clear that the magnitude and direction of all the equilibria are determined by the type and concentration of free ligand (L). The ultimate goal is to achieve uniform shell growth (forward reaction of Equilibrium 2) by using ligands to manipulate the reactivity of both the monomer

(M) and the nanocrystal (NC). There are three main obstacles to achieving this goal: (A) The *Monomer solubility* is too high, (B) *Surface binding* of the ligands is too strong and (C) *Homogeneous nucleation*. With reference to the rate constants outlined in Equilibria 1→4 and Figure 5.3, we will now discuss each of these obstacles in detail.

(A) *Monomer solubility*: The ligands that control the monomer solubility are derived from two sources: Those present in the initial growth solvent; and those liberated from the breakdown of the precursor. As a consequence, Equilibrium 1 may be influenced by more than one ligand type within the growth medium. The function of the ligands, which comprise the initial growth solvent is perhaps most vital when organometallic type precursors are used, as no other ligands are introduced during shell growth. Organometallic precursors, such as dimethyl cadmium and diethyl zinc, are extremely reactive at room temperature. These precursors decompose instantly in solution to form zero valence metal and a mixture of highly volatile gases that are incapable of binding to the surface. Interestingly, even with the use of such highly reactive precursors, shell growth occurs on a timescale slower than expected (typically several minutes). This indicates that speciation (recomplexation) of the precursor is a likely intermediate step prior to deposition. Thus, even when using organometallics, the kinetics of shell growth are not limited by the decomposition rate of the precursors but rather, are controlled by the intervention of the ligands in the solvent [47, 48].

Collectively, the function of all these ligands is to raise the solubility of the monomer to a level that ensures slow, uniform growth of the shell. However, if too much of these ligands are used they may increase the monomer solubility to a point where shell deposition is no longer favourable ($k_2 \ll k_{-2}$). High monomer solubility may also induce Ostwald ripening of the cores or cause dissolution of any existing shell material on the particle surface by enhancing the rate constant, k_{-2}.

(B) *Surface binding*: The ligands used must not bind too strongly to the surface of the nanocrystal, as this will inhibit shell growth by physically blocking the reactive sites

($k_3 < k_{-3}$). To avoid this it is best to use ligands that are labile at the particle surface. It is of importance to note that ligands will bind with different strengths to the core and shell materials [58]. For instance, a ligand that is highly labile at the surface of the core does not dictate that it will behave in the same way at the surface of the growing core/shell. Therefore, it is necessary that the chosen ligands are labile on both the core and shell surfaces.

(C) *Homogeneous nucleation*: A common problem during shell deposition is the homogeneous nucleation of the shell material. This arises from an oversaturation of monomers after the injection of the precursors. Slow introduction of the monomer may stunt but not necessarily allay nucleation, as the rate at which monomers are consumed is reaction controlled by the ligands. Two of the most common scenarios that lead to a build up of monomer in solution and to homogeneous nucleation of the shell material in the solution are:

Surface limited growth - The precursor decomposes rapidly ($k_1 >>> k_{-1}$), as is the case for organometallic precursors, but has a slow deposition rate i.e due to strongly bound surface adsorbates ($k_{-3} >> k_3$).

Solubility limited growth - The precursor has a moderate reactivity ($k_1 > k_{-1}$), common to salt precursors. However, the type and concentration of "free ligand" (L) has not been optimised to suit the system such that rate k_4 is competitive with or faster than k_2. This scenario will be accentuated if the solubility of the shell materials in the growth medium is lower than those of the core.

In context with the rationale presented above, we will now proceed to discuss the ligand chemistry specific to the production of high quality CdSe/CdS core/shell nanocrystals. To begin, we chose a growth solvent comprised of a 2.5:1 ratio by mass of 1-octadecene (ODE) and octadecylamine (ODA). ODE is a high boiling point non-coordinating molecule, which when substituted with ODA allows the particles to reach the shell growth temperature (240°C) without undergoing dissolution or ripening. Furthermore, ODA does not adversely affect the QY of the cores and is labile at the surface of the particle, ensuring Equilibrium

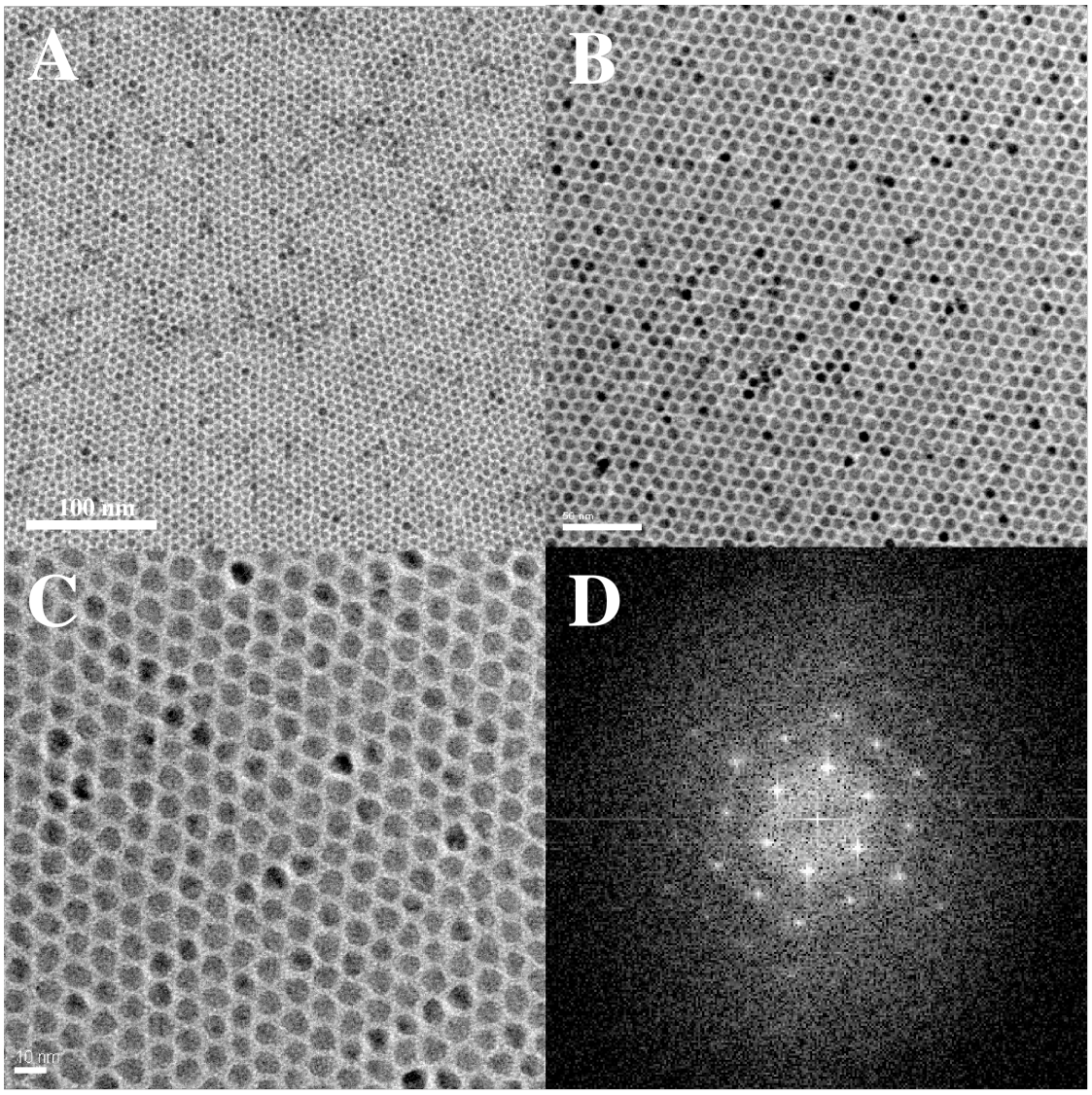

Figure 5.4: **A-C**; Increasing magnifications of a 2D array of CdSe/CdS core/shells. The scale bars from images **A-C** are 100, 50, 10 *nm* respectively. Image **D** shows the reduced FFT of **A**. The multilayered hexagonal pattern arises from the hexagonal packing of the 2D array of particles (colloidal crystal)

3 is dynamic. The cadmium precursor was prepared by dissolving cadmium oxide in bis-(2,2,4-trimethylpentyl) phosphinic acid (TMPPA) in a 1:4 molar ratio to obtain a 0.1 M solution in ODE. To create the sulfur precursor, sulfur powder was dissolved in ODE to a concentration of 0.1 M. We chose these precursors as the resulting Cd-TMPPA [59] and ODE-S [4] complexes are known to be highly reactive. Preliminary experiments using these precursors to grow a CdS shell on CdSe cores resulted in large quantities of homogeneous nuclei. This is likely a result of *Surface limited growth*, effected by TMPPA, as described above. To avoid this outcome we substituted the growth medium with oleic acid (OA). The role of this ligand is to complex cadmium monomer, enhancing the rate k_{-1}, and to aid the displacement of TMPPA at the particle surface, in order to increase particle reactivity. By varying the OA:TMPPA molar ratio, the reactivity of the free cadmium monomer (k_1/k_{-1}) can be adjusted to complement the reactivity at the particle surface (k_3/k_{-3}). Using this binary acid approach we were able to achieve slow, uniform shell growth in the absence of homogeneous nucleation. Controlling the reactivity of the metal cation, by employing two complementary acids has previously proven effective at controlling the nucleation and growth of CdSe cores, as outlined in Chapter 2. Figure 5.4 shows TEM images of a two dimensional array of CdSe/CdS core/shell nanocrystals produced using this methodology. The highly ordered packing in these arrays is only made possible when the particles exhibit extremely narrow size distributions and there is an absence of homogeneous nuclei. †

A vital yet largely neglected aspect of shell growth concerns Equilibrium 1. High monomer conversion into shell material is a prerequisite to obtaining good agreement between calculated and observed shell thicknesses. Clearly, the highest degree of conversion should occur in media with little or no ligand capable of solubilising the monomer. However, as previously mentioned, solubilising ligands are required in the growth medium to establish equilibria conducive to slow, uniform shell growth. Although Equilibrium 1 can be pushed

†The characterisation and optical properties of the CdSe/CdS heterostructures displayed in Figure 5.4 are presented in Chapter 6.

to favour shell growth by refining the reaction conditions, it is highly unlikely that monomer conversion is capable of reaching unity. This is evidenced in the production of semiconductor cores, which even after extended growth periods, are unable to consume more than ∽90% of the monomer in solution [48, 60]. This aspect will undoubtedly compromise even the most accurate calculations of shell thickness. It would therefore be prudent to account for such equilibria by adding excess of the monomer(s) most strongly complexed in solution to ensure the complete growth of each monolayer (ML). ‡

5.2.4 Effect of Lattice mismatch

Figure 5.5A shows the lattice parameters and bulk band offsets for the three compatible Type I shell materials, which can be used to coat CdSe. The lattice mismatch of the shell materials relative to CdSe is 3.86% for CdS, 6.98% for ZnSe and 11.2% for ZnS. Lattice mismatch arises primarily due to the differences in bond lengths between the atoms in the core and in the shell. Although the differences in the lattice mismatch between these materials may only be a few percent it is enough to alter both the kinetics of shell deposition and particle morphology as well as the QY of the resultant particles. Firstly we begin by discussing the effects of the lattice parameters on the QY.

In order to realise high quantum yields it is necessary to minimise the lattice mismatch between the core and shell. In the case of epitaxial shell growth on a perfect crystallite, even the smallest difference in lattice parameters will result in lattice strain at the interface between the two materials. As shell deposition progresses this strain increases and is eventually relieved by the creation of misfit dislocations (defects) within the shell. These defects introduce non-radiative recombination pathways that reduce the QY of the particle.

It is commonly observed that the QY passes through a maximum during the course of

‡For the synthesis of CdSe/CdS core/shells (presented in Chapter 6) we have found that in some cases up to 30% excess cadmium monomer was required to realise the predicted shell thickness.

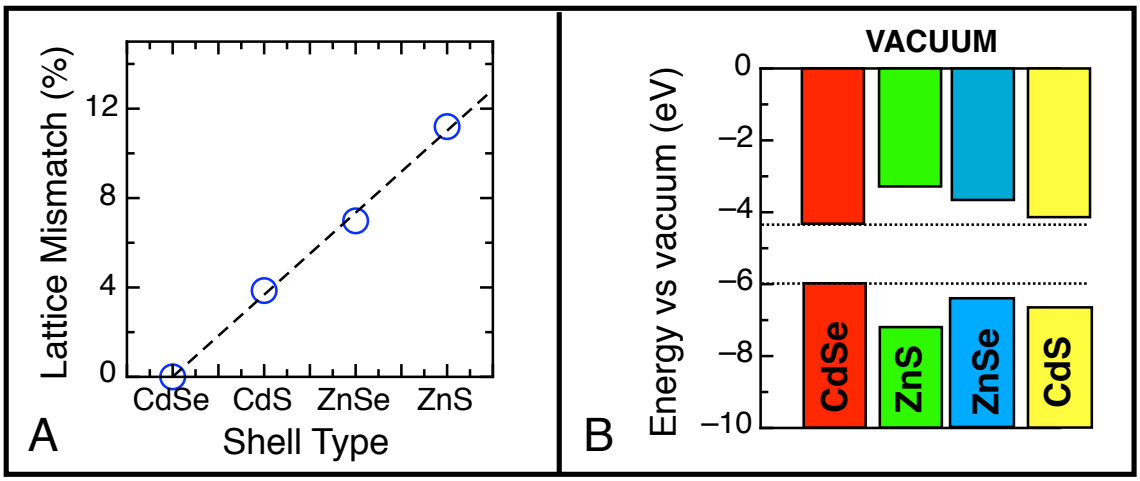

Figure 5.5: **A**; The percent lattice mismatch of different bulk shell types relative to CdSe. **B**; The bulk band offsets of common Type I shell materials, which can be used to coat CdSe.

shell deposition. This maximum is typically observed at lower shell coverage in CdSe/ZnS nanocrystals ($\backsim$1.3 ML, $\backsim$0.40 nm) [35] compared to CdSe/CdS nanocrystals ($\backsim$2.2 ML, $\backsim$0.74 nm) [61], whose lattice mismatch is $\backsim$7% lower. Also, this trend has found to be independent of core size [61]. This suggests that strain induced defects are more prevalent at lower shell coverage in cases where the lattice mismatch between the core and shell are large. It is of importance to note that stopping shell growth at the point where the shell is thin, although ceding highly luminescent particles, results in a lower resistance to adverse environments.

Interfacial strain also manifests itself by increasing the barrier for the nucleation of the shell material at the particle surface. In stark contrast to core growth (where there is zero lattice mismatch), the growth of a shell will tend to increase the surface energy, γ, of the particle, by imparting lattice strain to the crystal. Given that a nanocrystal will strive to minimise its overall free energy, any further increase in γ (beyond the expected increase caused by enlarging the surface area of the crystal) will act as an additional barrier to shell deposition. As such it becomes increasingly difficult to deposit a shell material as the lattice mismatch is increased.

In a similar way, the morphology of the growing nanocrystal is also affected by lattice strain. Given that nanocrystals exhibit multiple crystal facets, each with its own specific surface energy [62], individual facets will possess different growth rates. As the shell becomes thicker, and strain increases, the energy difference between these facets becomes more pronounced, further favouring crystal growth on some faces more than others. The large lattice mismatch ($\backsim$ 12%) between CdSe and ZnS accounts for the broad size distributions and highly faceted morphology commonly observed for CdSe/ZnS particles (see Figure 5.9). On the other hand, thick cadmium sulfide or zinc selenide shells are more routinely grown with tighter size distributions and less faceting compared to CdSe/ZnS, although an increase in aspect ratio is frequently observed ($\backsim$1:1.2). Interestingly, a recent study has suggested that the QY of core/shell nanocrystals may be morphology dependent [63]. In this investigation the authors proposed that slight elongation of the shell on the anion rich $[00\overline{1}]$ face (creating a "bullet" shape shell) resulted in particles with higher QY compared to those with near spherical shells. Therefore, it is of importance to keep in mind that particles whose morphology deviates slightly from spherical may be necessary to realise the highest QY.

From Figures 5.5A and B it can be seen that in CdSe based systems there is a trade off between lattice compatibility and electronic isolation. The small lattice mismatch between CdSe and CdS (c.a 4%) allows for the production of near spherical particles with higher QY compared to ZnS overcoated particles. However, CdSe/CdS core/shells have a low resistance to adverse environments as the electron is only weakly confined to the core (Ref: Section 2.3). Circumventing this apparent bottleneck is achievable if the interface is slowly graded between the two materials. This technique, known as alloying, has only been achieved in CdSe/ZnSe systems [64]. It seems that alloying is possible only if the anions of the core and shell are the same, as this allows efficient diffusion of the smaller cations between tetrahedral interstitial sites. Another method to achieve bright stable structures is to use a core/shell/shell arrangement, where the primary shell is used to grade the lattice parameters and the outer shell provides resistance to the environment through effective electronic isolation of

the core. Examples of such structures are CdSe/CdS/ZnS and CdSe/ZnSe/ZnS [5].

5.3 Optical properties and confinement in Type I CdSe heterostructures

To model the electronic structure of the CdSe core/shell heterostructures, we used an effective mass approximation to describe the electron and hole wavefunctions in a finite spherical potential well, treating the electron and hole separately. The Coulomb interaction between the charge carriers is treated by first-order perturbation theory. To obtain the electron and hole confinement energies we solve simultaneously for the continuity of both the wavefunction (Equation 1) and the corresponding probability currents (Equation 2) at the core/shell interface [35]:

$$R_{1S,CdSe}(k_1 r_1) = R_{1S,shell}(k_2 r_1) \,, \tag{5.1}$$

$$\frac{1}{m^*_{CdSe}} \frac{d}{dr} R_{1S,CdSe}(k_1 r)\big|_{r=r_1} = \frac{1}{m^*_{shell}} \frac{d}{dr} R_{1S,shell}(k_2 r)\big|_{r=r_1} \,, \tag{5.2}$$

where $R_{1S(CdSe)}$ and $R_{1S(shell)}$ represent the radial wavefunctions for the electron and hole in the lowest excited state in either the core or shell respectively. m^* is the effective mass of the charge carriers, and k_1 and k_2 are the wave vectors in the core and shell respectively. To evaluate the wavefunctions we used the following parameters: For CdSe; m^*_e= 0.12, m^*_h= 0.45 [35], for CdS; m^*_e= 0.145, m^*_h= 0.8 [35], for ZnS m^*_e= 0.27, m^*_h= 0.96 [65]. We assigned a potential of zero inside the CdSe core and barrier heights for the electron of 0.2 eV (CdSe-CdS), and 0.68 eV (CdSe-ZnS), and for the hole 0.55 eV (CdSe-CdS) and 1.2 eV (CdSe-ZnS).

The potential barrier for the electron to tunnel into the surrounding matrix was set at 4 eV and for the hole at 10 eV.[§]

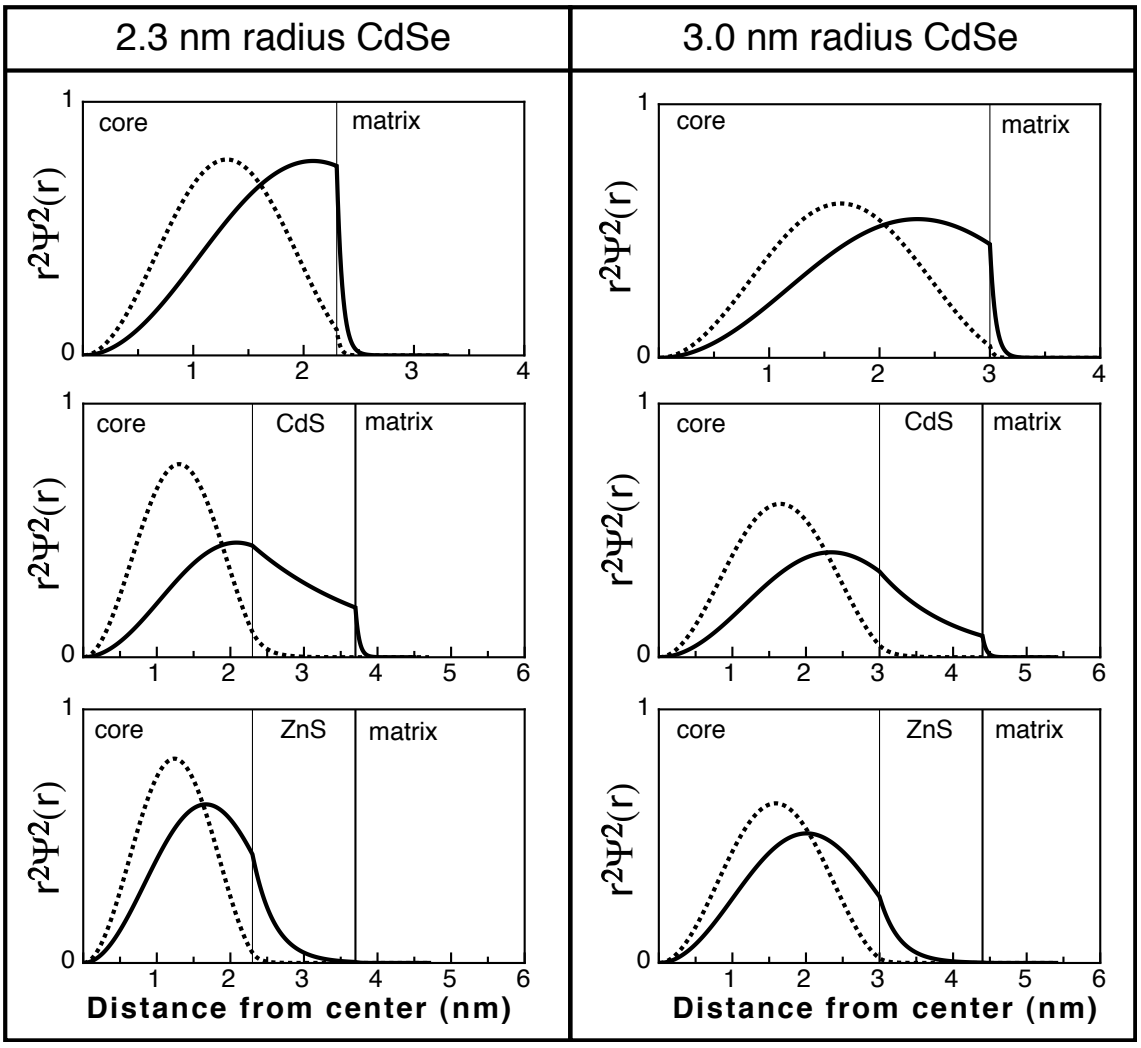

Figure 5.6: Radial probability distributions for the electron (solid line) and hole (dashed line) in CdSe cores with a radius of 2.3 nm (left) and 3.0 nm (right) and for the same cores with a 1.4 nm (c.a 4 monolayers) shell of both CdS and ZnS.

Figure 5.6 displays the radial probability distributions for the electron and hole in CdSe cores with a radius of 2.3 nm and 3.0 nm and with a 1.4 nm (c.a 4 monolayers) shell of both CdS and ZnS. Inspection immediately reveals that in all cases the hole is largely confined to the centre of the particle, whereas the lighter electron is more surface delocalised. The most

[§]The author acknowledges the assistance of D. Gómez with the calculations.

pronounced effect on the radial probabilities is observed upon changing shell types. The small conduction band (CB) offset between CdSe and CdS ($\backsim$200 meV) allows extensive delocalisation of the electron into the shell compared to ZnS where the CB offset is $\backsim$850 meV greater. We also observe that the probability of finding the electron in either the CdS or ZnS shell is sensitive to core size. The higher overall kinetic energy of the exciton in smaller cores leads to increased tunnelling of the carriers into the shell. When decreasing the core radius from 3.0 nm to 2.3 nm the probability of finding the electron in the shell increases significantly, whereas the hole wavefunction remains largely unperturbed.

The delocalisation of the electron into the surrounding shell reduces its kinetic energy. This is manifested as a red-shift of the first excited state transition, observable by monitoring the absorbance spectra during the course of shell growth. As yet, there is no precise link between these red-shifts and the exact amount of shell material deposited; nevertheless absorbance spectroscopy is a useful qualitative tool to monitor shell deposition.

For the production of chemically stable particles it is best to choose a material with the largest barriers for both the electron and the hole, such as ZnS, so as to reduce the probability of either charge carrier escaping to the surface, where it can be scavenged by quenching agents. Cadmium sulfide shells are less capable of confining the electron. CdSe/CdS nanocrystals are therefore intrinsically more susceptible to the local environment, especially when the smallest cores are used, as even with thick shells the electron is still largely surface delocalised. In the case of CdS shells it is also necessary to bear in mind that the energy of the excited state is extremely sensitive to shell thickness. Red-shifts of up to 60 nm have been previously observed for CdSe/CdS preparations [4, 11], making the production of CdSe/CdS core/shell particles with both a thick passivating shell and preservation of the core emission colour impossible to achieve.

The ability of different shells to electronically isolate the core from its environment is best appreciated at the single nanocrystal level. Figure 5.7 shows the representative pho-

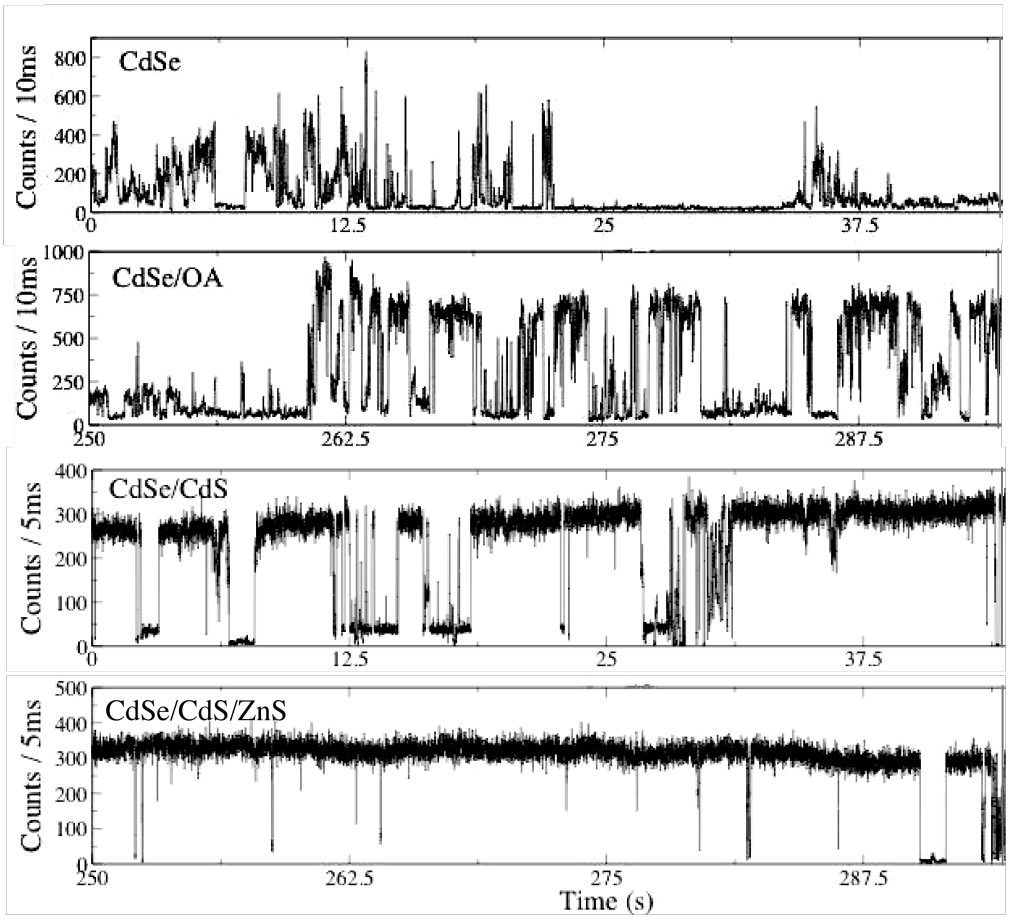

Figure 5.7: Single QD trajectories of CdSe cores and core/shells. From top to bottom; As prepared CdSe cores, octylamine capped cores, CdSe/CdS with a 3.5 ML shell and CdSe/CdS/ZnS with 1 ML of CdS and 2.5 ML of ZnS. We see that by increasing the degree of surface passivation and electronic isolation the time the particle spends not emitting ('off') decreases considerably. In the case of CdSe/CdS/ZnS the particles are almost constantly emitting, with only short interruptions in the photoluminescence.

toluminescence time trajectories (blinking traces) of four single CdSe quantum dots each with different types of surface passivation. We see that as-prepared CdSe cores spend the majority of their time either "off" or in an intermittently luminescent state. After passivation with octylamine, which is known to bind to surface cadmium atoms [2], the quantum dot luminescence improves slightly. The most dramatic change is observed upon deposition of the shell materials. Complete passivation with CdS renders the dot highly luminescent and it exhibits almost binary blinking behaviour. Further increasing the electronic isolation, provided by the ZnS layers, results in a particle that is almost constantly emitting with only short interruptions to the photoluminescence. It is clear from these PL time trajectories that by systematically improving the degree of electronic isolation of the charge carriers in the core, all competing non-radiative processes are increasingly suppressed [52].

5.4 Models on how to grow a defined shell thickness

The ability to synthesise a physically predefined heterostructure (regardless of synthetic method and dimensionality) is firstly reliant upon the ability to precisely calculate the amount of precursor required to produce the desired shell thickness. There are currently two accepted models that can be used to calculate the number of atoms required to generate increasing monolayers of shell. The Concentric Shell Model (CSM) and the Unit Cell Model (UCM). For simplicity in the explanation of these models we will assume the growth of a spherical shell on a spherical core.

In the CSM the amount of shell material required is calculated volumetrically. To begin the calculation, half the c-lattice parameter of the shell material is taken (as one unit cell may be viewed as two single semiconductor layers, one on top of the other). This value is then assumed to be the radial increase that occurs upon the deposition of a single *semiconductor layer*. Consequently, the volumes of the concentric shells can be calculated and

converted through the bulk densities of the shell material into the number of cations and anions required. A common misconception is that the complete deposition of one atom type (either the cation or anion) increases the crystal radius by half the c-lattice parameter. In fact, equimolar amounts of both atom types are needed for the complete growth of a single semiconductor layer. This is highlighted in Figure 5.8 which shows that the deposition of both cadmium and sulfur is necessary to increase the radius of the particle by half the c-lattice parameter. Thus, the growth of a shell six semiconductor monolayers thick requires twelve atomic monolayer injections.

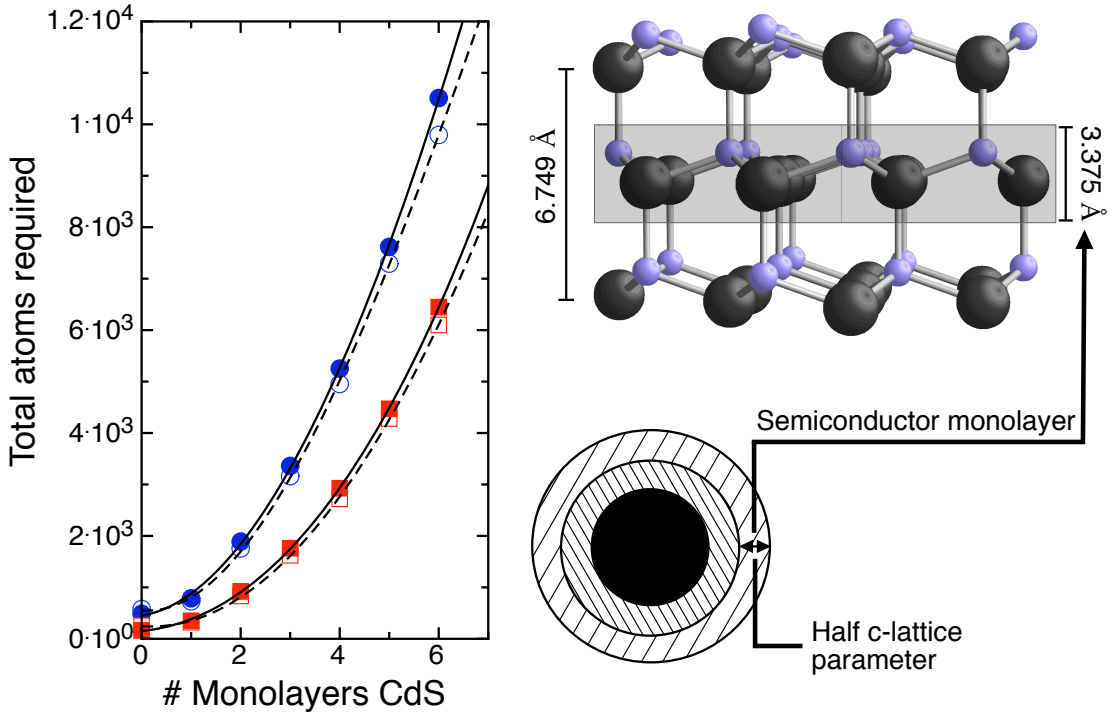

Figure 5.8: Left; Simulation performed using the CSM (solid symbols) and UCM (open symbols) models in the calculation of the total atoms required for the deposition of increasing CdS monolayers on 2.3 *nm* (squares) and 3.8 *nm* (circles) diameter cores. The zero point represents the number of surface atoms calculated using both models (CdSe; a-lattice parameter 4.300 Å, c-lattice parameter 7.020 Å, CdS; 4.135 Åand 6.749 Årespectively). Right; Schematic of concentric shells (dashed areas) around a core nanocrystal (solid circle). Each layer represents one semiconductor monolayer (for CdS this corresponds to 3.375 Å). The enlarged area serves to highlight the bonding inside one semiconductor monolayer.

The UCM, like the CSM, is based on bulk lattice parameters. Computation of the required number of atoms per monolayer can be readily performed with the aid of existing

crystallographic programs [66]. Although these programs are extremely precise for bulk crystals, when modelling curved (highly faceted) crystals, they may eliminate lower coordination number atoms at the surface, slightly reducing the accuracy of their calculations. Figure 5.8 shows the results of calculations performed using both models for the epitaxial growth of CdS onto CdSe. It is seen that at low coverage of CdS the models agree to within a few percent, which increases to $\backsim$10% at shell thicknesses above 3-4 monolayers. This trend is also found to be largely insensitive to the initial core size.

5.5 Evolution of CdSe core/shell synthetic methods

The aim of this section is to place in context the issues involved in the production of core/shell nanocrystals. To achieve this we provide the reader with a critical analysis of the literature, which has evolved over the past 25 years on core/shell synthesis. As the majority of literature on CdSe core/shells has concentrated on Type I structures they will form the basis for this section. Type II structures and anisotropic shells have emerged only in recent times, consequently only the key findings and synthetic advances will be discussed.

5.5.1 Type I heterostructures

The advantages of synthesising particles with a core/shell type structure have been known for some time. As early as 1982 it was observed that adsorbing zinc cations onto sulfur rich surfaces of CdS particles (pseudo ZnS shell) increases the overall luminescence of the as-prepared colloid [67]. More comprehensive studies were later accomplished by Henglein and co-workers who showed that samples of aqueous CdS/$Cd(OH)_2$ could achieve a room temperature QY of 50% and display orders of magnitude more resistance to photo-anodic corrosion compared to bare CdS [68]. In 1990 White *et al* and Brus *et al* were successful in depositing ZnS [69] and ZnSe [70] shells onto CdSe using the inverse micelle method.

Although in these early methods an improvement in QY was demonstrated, the shells were thin and the size dispersions of the resultant particles were relatively poor (exceeding 15%). The production of high quality core/shell nanocrystals in aqueous based media is made difficult by many compounding factors. Firstly, the size distribution of the core sample is often broad due to the low temperatures of nucleation. This broadening culminates in a broad distribution of growth rates, making the production of uniform shells across the entire size distribution difficult to achieve. The low temperatures of reaction also reduce the reactivity of the shell precursors and prevent adequate annealing of lattice imperfections, which unavoidably leads to particles with numerous crystal defects.

The discovery that semiconductor nanocrystals could be produced in high-boiling point, non-polar, coordinating solvents, circumvented many of the problems encountered in aqueous synthesis [71]. This breakthrough also forged a new approach to shell synthesis. In 1996, a paper by Hines and co-workers demonstrated a method to synthesise CdSe core/shells with both a high QY and a tight size distribution [36]. The authors added highly reactive metal and chalcogenide precursors (dimethyl zinc, and bis(trimethylsilyl)-sulfide; (TMSS)) to the as-prepared CdSe cores at c.a 300°C to create a 0.6±0.3 nm ZnS shell with a room temperature QY of 50%. A later publication built on the method outlined by Hines *et al* to produce CdSe/ZnS with thicker shells (c.a 1.5 nm) [35]. Although impressive characterisation was presented, the size distribution of the resultant particles approached 20% with average aspect ratios of around 1.2. These attributes are a consequence of lattice mismatch (Ref: Section 2.4). Subsequent investigations proved that organometallic type precursors could be used to synthesise other kinds of heterostructures. The combination of dimethyl cadmium and TMSS proved effective in preliminary experiments for the generation of highly luminescent CdSe/CdS nanocrystals [72].

At a similar time, other synthetic advances argued for a "one-pot" approach to core/shell synthesis [48], which involves the addition of the shell precursors to the as-prepared cores without intermediate washings. Although providing a relatively simple synthetic route to

core/shell nanocrystals, the quality of the final product is compromised by this type of synthetic method. In a one-pot approach both the composition and tunability of shell thickness are inherently difficult to reproduce as the exact amounts (and reactivity) of the remaining monomers are speculative and will no doubt vary between preparations of different core sizes. Furthermore, due to the presence of unreacted monomer in solution, the production of a composite (alloy) shell cannot be dismissed.

Up to this point published methods for the synthesis of core/shells in non-aqueous media necessitated the use of organometallic precursors. The main drawback of these precursors is their extremely high reactivity. Even with the most optimised ligand chemistry they do not permit a high degree of control over the kinetics of shell deposition. As a consequence the heterostructures produced using these types of precursors typically exhibit thin shells (2-3 ML) [47, 48] and broad size distributions [35, 72]. In order to gain greater control over the synthetic procedure and improve sample quality, organometallics have since been replaced by the use of salt precursors. The wide variety of available metal salts, which are easier to handle, less toxic and more enviromentally friendly than their organometallic counterparts undoubtedly contributed to their immediate success. Preliminary work using salt precursors was accomplished by Mekis and co-workers who showed that cadmium acetate and H_2S could be used in place of dimethylcadmium and TMSS to produce CdSe/CdS core/shells with improved quantum efficiencies [48]. In a later publication Riess and co-workers utilised an all salt method (zinc stearate and trioctylphosphine selenide) for the production of CdSe/ZnSe nanocrystals [49].

In 2003 Li *et al* [4] took a novel approach to the synthesis of core/shell structures. The authors adapted the method of successive ion layer adsorption and reaction (SILAR), used in molecular beam epitaxy to produce thin films, and successfully applied it to colloid synthesis. Using SILAR Li *et al* demonstrated that CdSe/CdS nanocrystals could be synthesised with almost monolayer control of shell thickness. In this method the core crystals were heated to around 240°C, at which time specific amounts of cadmium oleate and a 1-octadecene-sulfur

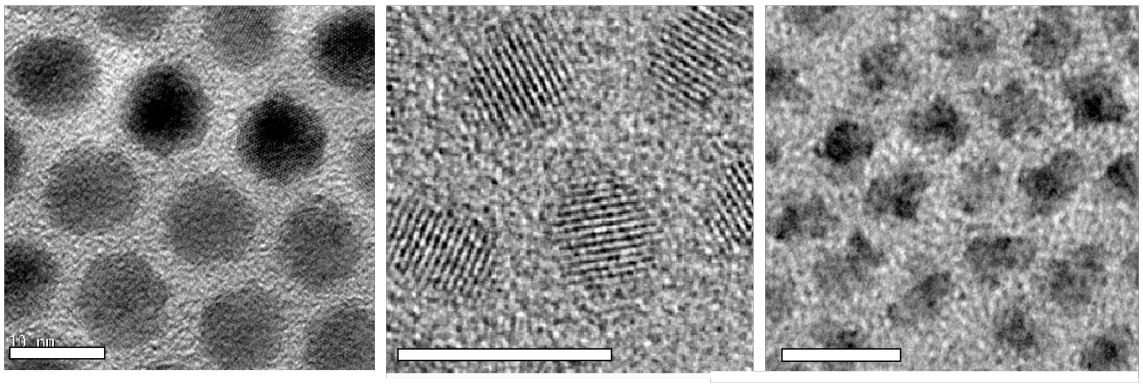

Figure 5.9: From left to right: CdSe/CdS/$Zn_{0.5}Cd_{0.5}S$/ZnS core/multishells (Xie *et al* [11]), scale bar 10 *nm*; CdSe/ZnSe/ZnS (Talapin *et al* [5]), scale bar 9 *nm*; CdSe/ZnS with 6 monolayers ZnS synthesised using the SILAR method (Xie *et al* [11]), scale bar 10 *nm*.

(ODES) complex were injected alternately, allowing each atomic layer of shell material to be deposited separately.

The SILAR method aims to reduce the coexistence of cations and anions of the shell material in solution in order to help suppress homogeneous nucleation. This method also allows the evolution of the absorbance and photoluminescence spectra to be monitored more accurately as the effects of both cation and anion are decoupled. The SILAR process typically generates narrower size distributions compared to other strategies and, as will be discussed, has proved to be a versatile method for the synthesis of a wide range of heterostructures.

Most recently, the synthesis of CdSe core/shells has focused on the production of core/multishell type particles. The synthesis of core/multishell nanocrystals (often termed "graded seals") was first accomplished by Talapin and co-workers [5]. The authors successfully synthesised both CdSe/ZnSe/ZnS and CdSe/CdS/ZnS nanocrystals using organometallic precursors. Comparison of their core/shell/shell particles with single shell CdSe/ZnS revealed that grading the shell type increases both the QY ($\backsim$60-70%) and resistance to oxidation. However, due to their choice of precursor and ligand chemistry the final particles appeared to have thin shells and an elongated morphology (see Figure 5.9). Xie *et al* synthesised CdSe/CdS/$Zn_{0.5}Cd_{0.5}S$/ZnS core/multishell nanocrystals [11]. Using a modifi-

cation of the established SILAR method the authors were able to accurately grow a 2.55 nm spherical shell with multiple gradings to the lattice parameters (see Figure 5.9). The final particles exhibited quantum efficiencies of around 80%. It was concluded that this structural configuration, compared to single shell CdS and ZnS, allows more rigorous processing of the particles with a reduced loss of QY.

5.5.2 Type II heterostructures and anisotropic shells

The production of CdSe core/shells has also been extended to include Type II heterostructures [54, 73]. Examples of such structures include CdSe/ZnTe (electron confinement only) [53] and CdTe/CdSe (hole confinement only) [53]. In Type II structures shell deposition results in extremely large red-shifts of the emission maximum. This may be attributed to indirect recombination, a phenomenon unique to the band structure of Type II core/shells. As a consequence the emission energy can be tuned over a vast range (VIS-NIR) compared to Type I structures. The synthesis of Type II nanocrystals is in its infancy; nonetheless Type II structures show promise in their ability to separate the charge carriers in the excited state. Presumably they will prove valuable in the future as the active material in photoconductive devices [74].

Further expansion in the pool of available CdSe heterostructures has been achieved with the synthesis of anisotropic shells [75–77]. Most notable are the publications by Mokari *et al* and Manna *et al* who accomplished the overcoating of CdSe rods of varying aspect ratios with ZnS [78] and graded seal CdS/ZnS [79] shells respectively. Talapin and co-workers synthesised CdSe/CdS nanocrystals with a spherical CdSe core and a CdS rod shell [75]. By directing the growth of CdS along the $[00\bar{1}]$ facet of the cores the authors were able to generate shells with diameters comparable to the core and aspect ratios as high as 4:1. The QY of the resultant heterostructures ranged between 40-80% depending on the aspect ratio. The particles also displayed length-dependent Stokes shifts and massive extinction coeffi-

cients below 400 nm ($\backsim 10^7$ L $cm^{-1}mol^{-1}$). The synthetic methods outlined here generate particles with both a high QY and polarisable emission.

The growth of anisotropic shells can only be achieved with an excess of one monomer over the other. To achieve anisotropic growth of the CdS shell Talapin *et al* used a Cd:S ratio of between 1:3 and 1:5. Anisotropic shell growth, whether on a spherical or rod shaped core, requires the use of low temperatures (100-150°C). This is due to the thermodynamically unstable nature of both rods and rod shells, which will tend to ripen into spheres at elevated temperatures. The use of organometallic precursors allowed the authors to obtain shell growth below those temperatures that induce ripening. At present no method exists to generate anisotropic structures using salt precursors.

5.6 Concluding remarks

The growth of shells onto semiconductor cores is certainly proving to be useful, not only for the production of bright stable luminophores, but as a means to modify the electronic properties of the core semiconductor nanocrystals. For instance, shells can facilitate charge separation and, if grown anisotropically, may lead to tuneable, polarisable emission. The physical and electronic structure of core/shells is governed by the lattice strain induced by the shell, and by the core and shell band offsets respectively. In the case of CdSe, the trade-off between these phenomena has fuelled the development of complex core/shell/shell structures.

Throughout this chapter it has hopefully become clear that the ligands play a vital role in determining the outcome of the synthetic procedure of shell deposition. Ligand controlled deposition kinetics refine the core/shell synthetic method and produce particles with a more well defined structure. However, at this time there exists no quantitative data linking the physical dimensions of semiconductor core/shell particles to their absorbance spectra. Gen-

erating this link would accelerate future research into core/shell nanocrystals, as it would simplify structural characterisation, circumventing the need for HRTEM. Furthermore, the determination of core size/shell thickness dependent extinction coefficients would provide a means to routinely estimate particle concentrations. These are perhaps the most significant challenges facing those who are interested in providing further insight into the complex properties of semiconductor nanocrystal heterostructures, and for incorporation into future technologies.

Bibliography

[1] J. van Embden, J. Jasieniak, D. Gomez, P. Mulvaney and M. Giersig. Australian Journal of Chemistry **60**, 457 (2007).

[2] C. Bullen and P. Mulvaney. Langmuir **22**, 3007 (2006).

[3] H. Liu, J. S. Owen and A. P. Alivisatos. The Journal of the American Chemical Society **129**, 305 (2007).

[4] J. J. Li, Y. A. Wang, W. Guo, C. Keay Joel, D. Mishima Tetsuya, B. Johnson Matthew and X. Peng. Journal of the American Chemical Society **125**, 12567 (2003).

[5] D. V. Talapin, I. Mekis, S. Goetzinger, A. Kornowski, O. Benson and H. Weller. Journal of Physical Chemistry B **108**, 18826 (2004).

[6] E. Lifshitz, M. Bashouti, V. Kloper, A. Kigel, M. S. Eisen and S. Berger. Nano Letters **3**, 857 (2003).

[7] J. S. Steckel, J. P. Zimmer, S. Coe-Sullivan, N. E. Stott, V. Bulovic and M. G. Bawendi. Angew. Chem. Int. Ed. **43**, 2154 (2004).

[8] L. Fradkin, L. Langof, E. Lifshitz, A. Rogach, N. Gaponik, H. Weller and A. Eychmueller. ChemPhysChem **4**, 1203 (2003).

[9] S. Haubold, M. Haase, A. Kornowski and H. Weller. Chemphyschem **2**, 331 (2001).

[10] Y.-W. Cao and U. Banin. Angewandte Chemie, International Edition **38**, 3692 (1999).

[11] R. Xie, U. Kolb, J. Li, T. Basch and A. Mews. Journal of the American Chemical Society **127**, 7480 (2005).

[12] Z. A. Peng and X. Peng. J. Am. Chem. Soc. **123**, 183 (2001).

[13] L. Qu, Z. A. Peng and X. Peng. Nano Letters **1**, 333 (2001).

[14] C. B. Murray, D. J. Norris and M. G. Bawendi. Journal of the American Chemical Society **115**, 8706 (1993).

[15] D. V. Talapin, A. L. Rogach, I. Mekis, S. Haubold, A. Kornowski, M. Haase and H. Weller. Colloids & Surfaces A Physicochemical & Engineering Aspects—Colloids & Surfaces A: Physicochemical & Engineering Aspects **202**, 145 (2002).

[16] A. Rogach, S. Kershaw, M. Burt, M. Harrison, A. Kornowski, A. Eychmuller and H. Weller. Advanced Materials **11**, 552 (1999).

[17] U. Banin. Nanoparticles 79–107 (2004).

[18] D. Battaglia and X. Peng. Nano Letters **2**, 1027 (2002).

[19] C. B. Murray, S. H. Sun, W. Gaschler, H. Doyle, T. A. Betley and C. R. Kagan. IBM Journal of Research & Development **45**, 47 (2001).

[20] W. W. Yu and X. Peng. Angewandte Chemie, International Edition **41**, 2368 (2002).

[21] L. S. Li, N. Pradhan, Y. Wang and X. Peng. Nano Letters **4**, 2261 (2004).

[22] C. C. Warren and S. Nie. Science **281**, 2016 (1998).

[23] M. Dahan, S. Levi, C. Luccardini, P. Rostaing, B. Riveau and A. Triller. Science **302**, 442 (2003).

[24] M. Bruchez Jr, M. Moronne, P. Gin and P. B. Weiss, S. Alivisatos. Science **281**, 2013 (1998).

[25] A. R. Clapp, I. L. Medintz, J. M. Mauro, B. R. Fisher, M. G. Bawendi and H. Mattoussi. J. Am. Chem. Soc. **126**, 301 (2004).

[26] A. Y. Nazzal, L. Qu, X. Peng and M. Xiao. Nano Letters **3**, 819 (2003).

[27] C. Wang, B. L. Wehrenberg, C. Y. Woo and P. Guyot-Sionnest. The Journal of Physical Chemistry B **108**, 9027 (2004).

[28] R. D. Schaller, M. A. Petruska and V. I. Klimov. J. Phys. Chem. B **107**, 13765 (2003).

[29] R. D. Schaller and V. I. Klimov. Nature 429, 642 (2004). **429**, 642 (2004).

[30] S. Coe, W.-K. Woo, M. Bawendi and V. Bulovic. Nature (London, United Kingdom) **420**, 800 (2002).

[31] J. Zhao, J. Zhang, C. Jiang, J. Bohnenberger, T. Basch and A. Mews. Journal of Applied Physics **96**, 3206 (2004).

[32] A. H. Mueller, M. A. Petruska, M. Achermann, D. J. Werder, E. A. Akhadov, D. D. Koleske, M. A. Hoffbauer and V. I. Klimov. Nano Letters **5**, 1039 (2005).

[33] H. Mattoussi, L. H. Radzilowski, B. O. Dabbousi, E. L. Thomas, M. G. Bawendi and M. F. Rubner. Journal of Applied Physics **83**, 7965 (1998).

[34] R. D. Schaller and V. I. Klimov. Physical Review Letters **92**, 186601/1 (2004).

[35] B. O. Dabbousi, J. Rodriguez-Viejo, F. V. Mikulec, J. R. Heine, H. Mattoussi, R. Ober, K. F. Jensen and M. G. Bawendi. Journal of Physical Chemistry B **101**, 9463 (1997).

[36] M. A. Hines and P. Guyot-Sionnest. Journal of Physical Chemistry **100**, 468 (1996).

[37] N. A. Hill and K. B. Whaley. Journal of Chemical Physics **100**, 2831 (1994).

[38] K. Leung and K. B. Whaley. Journal of Chemical Physics **110**, 11012 (1999).

[39] J. E. B. Katari, V. L. Colvin and A. P. Alivisatos. Journal of Physical Chemistry **98**, 4109 (1994).

[40] J. R. Heath, C. M. Knobler and D. V. Leff. Journal of Physcial Chemistry B **101**, 189 (1997).

[41] J. Aldana, Y. A. Wang and X. Peng. Journal of the American Chemical Society **123**, 8844 (2001).

[42] A. Issac, C. von Borczyskowski and F. Cichos. Physical Review B **71**, 161302(R) (2005).

[43] R. M. Kraus, P. G. Lagoudakis, J. Muller, A. L. Rogach, J. M. Lupton, J. Feldmann, D. V. Talapin and H. Weller. J. Phys. Chem. B **109**, 18214 (2005).

[44] V. Klimov and D. McBranch. Materials Research Society Symposium Proceedings **452**, 317 (1997).

[45] V. I. Klimov. Journal of Physical Chemistry B **104**, 6112 (2000).

[46] X. Chen, Y. Lou and C. Burda. International Journal of Nanotechnology **1**, 105 (2004).

[47] D. V. Talapin, A. L. Rogach, A. Kornowski, M. Haase and H. Weller. Nano Letters **1**, 207 (2001).

[48] I. Mekis, D. V. Talapin, A. Kornowski, M. Haase and H. Weller. J. Phys. Chem. B **107**, 7454 (2003).

[49] P. Reiss, J. Bleuse and A. Pron. Nano Letters **2**, 781 (2002).

[50] A. Y. Nazzal, X. Wang, L. Qu, W. Yu, Y. Wang, X. Peng and M. Xiao. Journal of Physical Chemistry B **108**, 5507 (2004).

[51] M. Nirmal, B. O. Dabbousi, M. G. Bawendi, J. J. Macklin, J. K. Trautman, T. D. Harris and L. E. Brus. Nature **383**, 802 (1996).

[52] D. E. Gomez, J. L. van Embden, J. Jasieniak, T. A. Smith and P. Mulvaney. Small **2**, 204 (2006).

[53] S. Kim, B. Fisher, H.-J. Eisler and M. Bawendi. J. Am. Chem. Soc. **125**, 11466 (2003).

[54] P. T. Chou, C. Y. H. and H. T. Chiu. J. Phys. Chem. B **108**, 10687 (2004).

[55] B. N. Alexey and Y. F. The Journal of Chemical Physics **122**, 104511 (2005).

[56] D. V. Talapin, A. L. Rogach, M. Haase and H. Weller. J. Phys. Chem. B **105**, 12278 (2001).

[57] D. V. Talapin, A. L. Rogach, E. V. Shevchenko, A. Kornowski, M. Haase and H. Weller. J. Am. Chem. Soc. **124**, 5782 (2002).

[58] U. Muinasmaa, P. Burk and J. Pentchuk. International Journal of Quantum Chemistry **62**, 653 (1997).

[59] J. L. van Embden and P. Mulvaney. Langmuir **21**, 10226 (2005).

[60] L. Qu, W. W. Yu and X. Peng. Nano Letters **4**, 465 (2004).

[61] X. G. Peng, M. C. Schlamp, A. V. Kadavanich and A. P. Alivisatos. J. Am. Chem. Soc. **119**, 7019 (1997).

[62] J. Schrier and L. Wang. The Journal of Physical Chemistry B **110**, 11982 (2006).

[63] J. R. McBride, J. Treadway, L. C. Feldman, S. J. Pennycook and S. J. Rosenthal. Nano Letters **6**, 1496 (2006).

[64] X. Zhong, M. Han, Z. Dong, T. J. White and W. Knoll. The Journal of the American Chemical Society **125**, 8589 (2003).

[65] J. Zhu, S. Zhu, Z. Zhu, Y. Kawazoe and T. Yao. Journal of Physics: Condensed Matter **10**, L583 (1998).

[66] D. Palmer. *CrystalMaker Version 6.3.4, CrystalMaker Software Ltd. http://www.crystalmaker.com*, 4 th ed. (2003).

[67] R. Rossetti, J. M. Hull, J. M. Gibson and L. Brus. J. Chem. Phys. **83**, 1406 (1985).

[68] L. Spanhel, M. Haase, H. Weller and A. Henglein. J. Am. Chem. Soc. **109**, 5649 (1987).

[69] C. F. Hoener, K. A. Allan, A. J. Bard, A. Campion, M. A. Fox, T. E. Mallouk, S. E. Webber and J. M. White. Journal of Physical Chemistry **96**, 3812 (1992).

[70] A. R. Kortan, R. Hull, R. L. Opila, M. G. Bawendi, M. L. Steigerwald, P. J. Carroll and L. E. Brus. J. Am. Chem. Soc **112**, 1327 (1990).

[71] C. B. Murray, D. J. Norris and M. G. Bawendi. J. Am. Chem. Soc. **115**, 8706 (1993).

[72] X. Peng, M. C. Schlamp, A. V. Kadavanich and A. P. Alivisatos. Journal of the American Chemical Society **119**, 7019 (1997).

[73] L. P. Balet, S. A. Ivanov, A. Piryatinski, M. Achermann and V. I. Klimov. Nano Letters **4**, 1485 (2004).

[74] C. Chen, C. Cheng, J. Yu, S. Pu, Y. Cheng, P. Chou, Y. Chou and H. Chiu. J. Phys. Chem. B **108**, 10687 (2004).

[75] D. V. Talapin, R. Koeppe, S. Goetzinger, A. Kornowski, J. M. Lupton, A. L. Rogach, O. Benson, J. Feldmann and H. Weller. Nano Letters **3**, 1677 (2003).

[76] D. V. Talapin, E. V. Shevchenko, C. B. Murray, A. Kornowski, S. Foerster and H. Weller. Journal of the American Chemical Society **126**, 12984 (2004).

[77] S. Kudera, L. Carbone, C. Francesca, R. Cingolani, F. Andrea, E. Snoeck, J. Parak, Wolfgang and L. Manna. Nano Letters **5**, 445 (2005).

[78] T. Mokari and U. Banin. Chem. Mater. **15**, 3955 (2003).

[79] L. Manna, E. C. Scher, L.-S. Li and A. P. Alivisatos. J. Am. Chem. Soc. **124**, 7136 (2002).

Chapter 6

Synthesis and Optical properties of CdSe-CdS and CdSe-CdS-ZnS Heterostructure Nanocrystals

The production of core/shell semiconductor nanocrystals is still very much in its infancy, and in fact, most of the current research is fuelled by the desire for a more comprehensive understanding of the quantum size effects in these materials. As research questions become more specific, the necessity to produce structures with well defined dimensionalities becomes more critical. Therefore, achieving greater control over the synthetic procedure of shell deposition is essential not only for the production of more chemically stable luminophores but to provide accurate insights into the complex properties of semiconductor nanocrystal heterostructures. In light of this, the current challenge is to synthesise heterostructures with well defined physical parameters and to characterise these particles by high resolution transmission electron microscopy, with the goal of establishing a clear link between core size, shell type and shell thickness, and the optical properties of core/shells.

6.1 Introduction

In the first part of this chapter a detailed outline of the conditions necessary to achieve high quality CdSe/CdS heterostructures will be presented. This is followed by an exposition of the optical properties of CdSe/CdS structures with varying core sizes and shell thicknesses. The later part of this chapter is dedicated to the synthesis and optical properties of CdSe/CdS/ZnS heterostructures. The advantages and drawbacks of using a wide band gap material as an outer coating are compared and contrasted.

CdSe/CdS Heterostructures

6.2 Experimental Section

6.2.1 Injection solutions

The cadmium stock solutions (0.1 M) were produced by dissolving CdO (0.01 mol, 1.2841 g) in TMPPA (0.04 mol, 11.6 g) and ODE (68.864 g). The solution was heated to 100 °C and degassed for 15 min followed by three pump/purge cycles. The solution was then switched to a nitrogen atmosphere and heated to 300 °C for 1 hr. The solution was then allowed to cool to 100 °C and placed under vacuum for a further 10 min. The solution was then reheated to 300 °C for a further 2 hrs then cooled to room temperature. At this time the solution appeared optically clear. The sulfur stock solution (0.1 M) was prepared by heating sulfur powder in ODE at 180 °C for 2 hrs. Prior to use both of these mixtures were heated to 60 °C.

6.2.2 Monolayer calculations

The spherical concentric shell model (CSM) was employed to calculate the amount of shell precursor necessary for the growth of each monolayer. Hereafter, referral to a monolayer (ML) will be taken to mean the length scale equal to half the c-lattice parameter of the bulk semiconductor, 0.337 nm in the case of CdS.

The first injection consisted of enough cadmium to make the particles Cd-rich, calculated by determining the number of surface selenium atoms (outermost 0.17 nm), and then adding enough cadmium to passivate all these sites. The following injections, beginning with sulfur, consisted of equimolar amounts of Cd and S necessary to grow concentric CdS shells 1 ML in thickness. For example, the amounts of the injection solutions for a hypothetical reaction containing CdSe cores (1 μmol, diameter 3.44 nm) are as follows: To make the particles Cd-rich requires 1.93 mL of Cd stock solution to be injected, followed by 3.61 mL of Cd and S stock solutions for the growth of the first monolayer, 4.89 mL of Cd and S stock solutions for the growth of the second monolayer, then 6.36 mL, 8.02 mL, 9.88 mL and finally 11.94 mL of Cd and S stock solutions for the growth of the third, forth, fifth and sixth MLs respectively.*

The amounts stated above agree to within 6% of those values obtained from simulations of shell growth for a wurtzite CdS shell on a core of the same crystal phase (Ref: Chapter 5). It is of importance to note that using the synthetic method outlined here the complete growth of each semiconductor layer was only observed by introducing 30% excess cadmium monomer. For clarity the volumes of the injection solutions stated above are for a zero excess of cadmium (such that the calculations may be easily reproduced). However, for all the reactions accomplished here the volume of each cadmium injection was increased to achieve a 1.3:1 Cd:S mole ratio. In this way we compensate for the strong solubility of the cadmium monomer in solution, with the extent of shell growth limited by the sulfur content

*This method of shell growth is referred to as the Selective Ion Layer Adsorption and Reaction (SILAR) technique, first implemented in colloidal systems by Peng *et al* [1].

in the growth medium.

6.2.3 Growth temperatures

Table 6.1 lists the optimised reaction temperatures for the growth of CdSe/CdS nanocrystals with various initial CdSe core sizes. For clarity, the size range of the cores is listed in column one, followed by the wavelength range that corresponds to their first absorption maximum in column two. The growth temperatures are listed in columns three and four where Temp.1 indicates the temperature required for the growth of the first 2 MLs and Temp.2 for MLs 3-6.

Table 6.1: Required reaction temperatures for the growth with CdSe/CdS nanocrystals of various core sizes.

Size range (nm)	λ_{max} range (nm)	Temp.1 (°C)	Temp.2 (°C)
2.2-2.7	480-530	200†	230
2.7-3.5	530-570	230	240
3.5-4.6	570-600	235	240
4.6-6.2	600-630	235	245

† The special case of this size range requires that the 2^{nd} ML is grown at 215°C.

6.2.4 Core Preparation

CdSe cores of various sizes were produced using the two acid size control methods outlined in Chapter 3. The as-prepared cores were purified using the method outlined in Chapter 2. After completing several purifications the solution containing the nanocrystals was then bubbled with nitrogen to remove trace amounts of volatile solvents. The resulting dispersion of nanocrystals in pure ODE was then filtered through a 0.22 μm filter and stored in the dark for later use. To determine the core size and concentration an aliquot of the washed cores was dispersed in chloroform and a quantitative absorption spectrum taken. The core

size and concentration was then determined using the calibration curves of Yu *et al* [2].

6.2.5 Core-Shell synthesis

The required amount of cores were added to a three neck round bottom flask along with a mixture of ODE:ODA in a 2.5:1 ratio by weight in order to produce a 40 μM dispersion of nanocrystals in the shell growth solvent. The mixture was then heated to 80 °C under vacuum, pump/purged three times and then further heated to the appropriate shell growth temperature depending on the size of the cores. The calculated amounts of the injection solutions were then added in sequential order beginning with cadmium. Immediately after the injection of any cadmium layer supplements of OA were injected into the reaction mixture in a mole ratio of 20:1 (OA:Cd-Injected). After each injection of monomer the solution was allowed to react for 15 min. Although no major changes to the absorbance spectra were observed after $\backsim$10 min, additional time was given to ensure the complete growth and annealing of each atomic layer. After the growth of each layer a small aliquot was taken for optical measurements. Following the completion of shell growth all crystals were annealed at 200 °C for 1 hr and then cooled to RT. The resulting core/shell nanocrystals were then washed using the same procedure outlined in Chapter 2 for the washing of the core nanocrystals. The final washings consisted of several precipitations from chloroform/methanol. The core/shells were then dispersed in hexane and placed in the dark for storage. It should be noted that in cases where long-term storage of the core/shells was required, they were kept in their original growth solutions.

6.3 Results and Discussion

To precisely determine the effects of core size and shell thickness on the optical properties of the resultant particles, monolayer control of shell thickness must be achieved over a wide range of initial core sizes. In order to realise this goal, we firstly synthesised CdSe cores with mean sizes 2.55, 3.40, 3.84 and 4.68 nm according to the methods outlined in Chapter 3. Next, these cores were overcoated with CdS adhering to the optimised conditions outlined in the Experimental section. For clarity and brevity the four different core sizes under investigation will herein be reffered to as *Samples 1-4*, in order of increasing initial core size.

6.3.1 Electron Microscopy

Figures 6.1 to 6.4 show the HRTEM images and the corresponding histograms obtained for *Samples 1-4* with various CdS shell thicknesses. The HRTEM images correspond to the core CdSe nanocrystals followed by CdSe/CdS with 2 MLs ($\backsim$0.84 nm), 4 MLs ($\backsim$1.52 nm) and 6 MLs ($\backsim$2.19 nm) of CdS shell respectively. Particle sizes were gathered on no less than 150 particles per sample. The recorded sizes were then binned into intervals of 0.1 nm and the resultant histograms fitted to Gaussian distributions using a Levenberg-Marquardt algorithm to extract the mean sizes and standard deviations. For direct comparison, the theoretically predicted mean size of the nanocrystals at each stage during the reaction is plotted alongside its corresponding histogram (dashed line). The error associated with the expected mean size at any point during shell growth is assigned a value of a single lattice plane and is displayed by the shaded areas.[†]

[†]The expected mean size of the CdSe core nanocrystals, based on the calibration curve of Yu *et al*[2], is noted to have an error of approximately one lattice plane. This error will propagate and affect the calculations of later expected particle sizes. Thus we may only *expect* that the mean observed particle size falls within the range of $\sim \pm 0.175$ nm (one c-lattice plane for CdSe) of the calculated expected size.

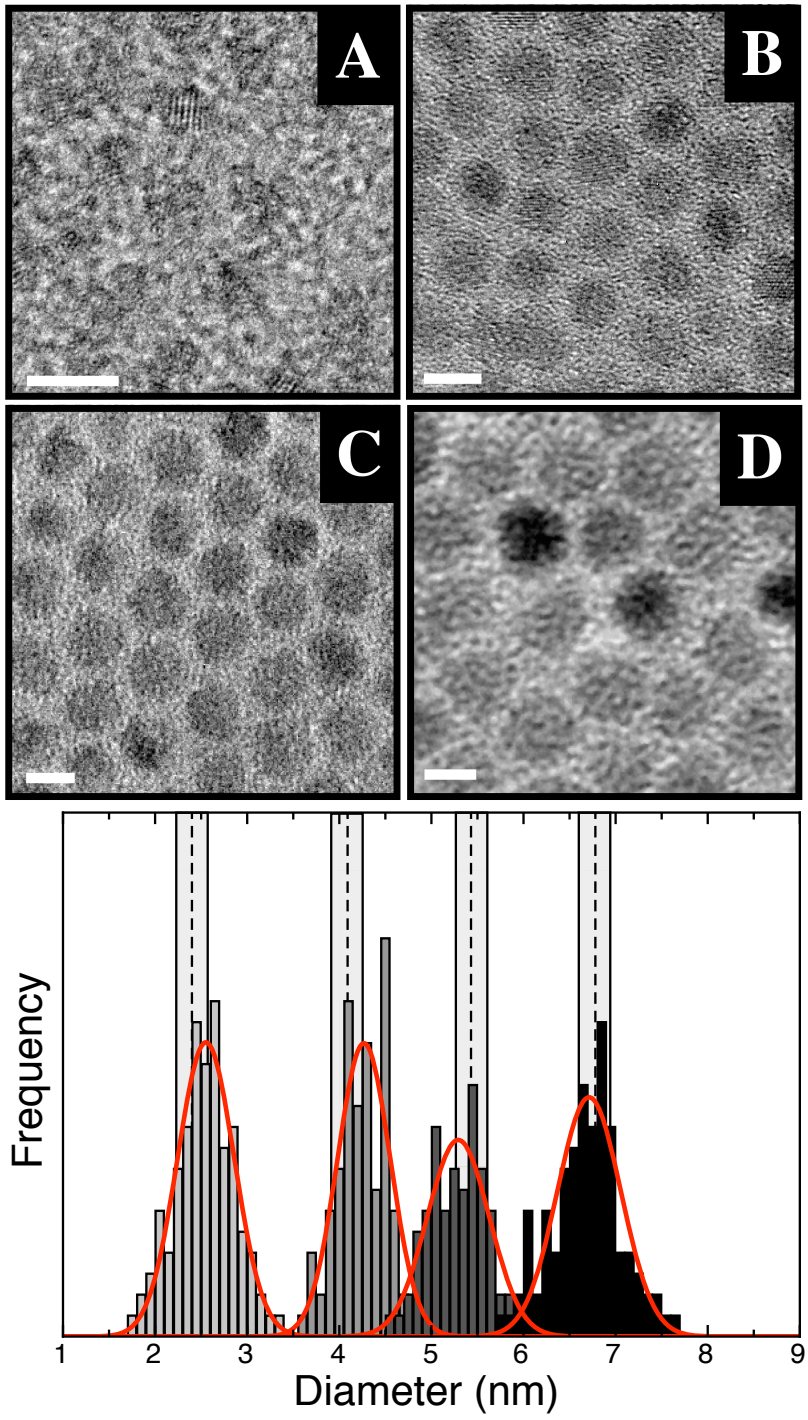

Figure 6.1: **Top**: High resolution transmission electron micrographs of *Sample 1*; **2.55** *nm* core. Scale bar equals 5 *nm*. **(A)** CdSe cores, **(B)** CdSe/CdS with a ∽2 ML CdS shell, **(C)** CdSe/CdS with a ∽4 ML CdS shell, **(D)** CdSe/CdS with a ∽6 ML CdS shell. **Bottom**: Histograms of the measured particle sizes obtained during the course of shell growth. The dashed line indicates the expected size of the nanocrystals, with the grey box outlining the associated error due to the error in the initial core size calibration curve of Yu *et al*[2].

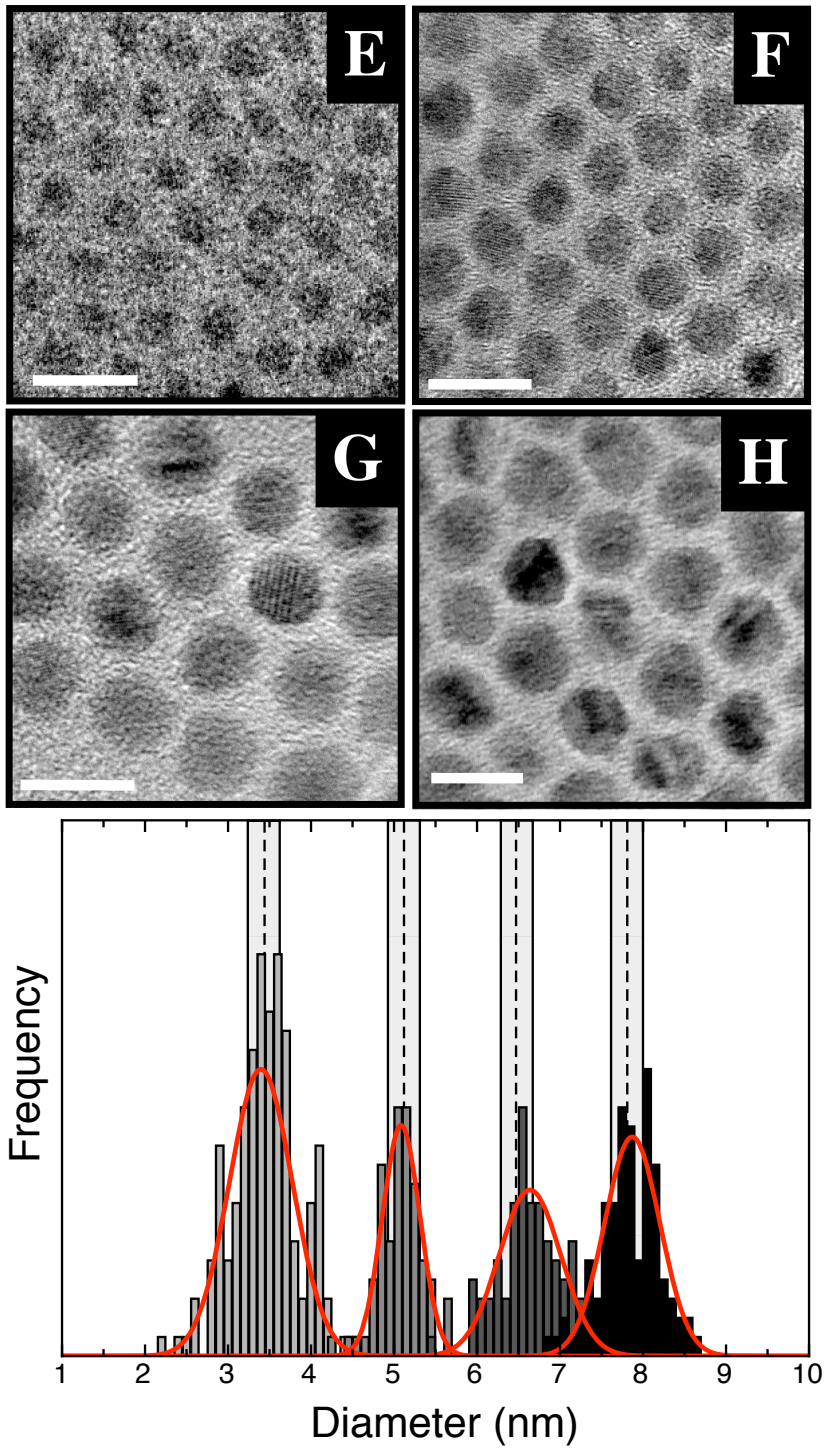

Figure 6.2: **Top**: High resolution transmission electron micrographs of *Sample 2*; **3.40** *nm* core. Scale bar equals 10 *nm*. **(E)** CdSe cores, **(F)** CdSe/CdS with a ∽2 ML CdS shell, **(G)** CdSe/CdS with a ∽4 ML CdS shell, **(H)** CdSe/CdS with a ∽6 ML CdS shell. **Bottom**: Histograms of the measured particle sizes obtained during the course of shell growth. The dashed line indicates the expected size of the nanocrystals, with the grey box outlining the associated error due to the error in the initial core size calibration curve of Yu *et al*[2].

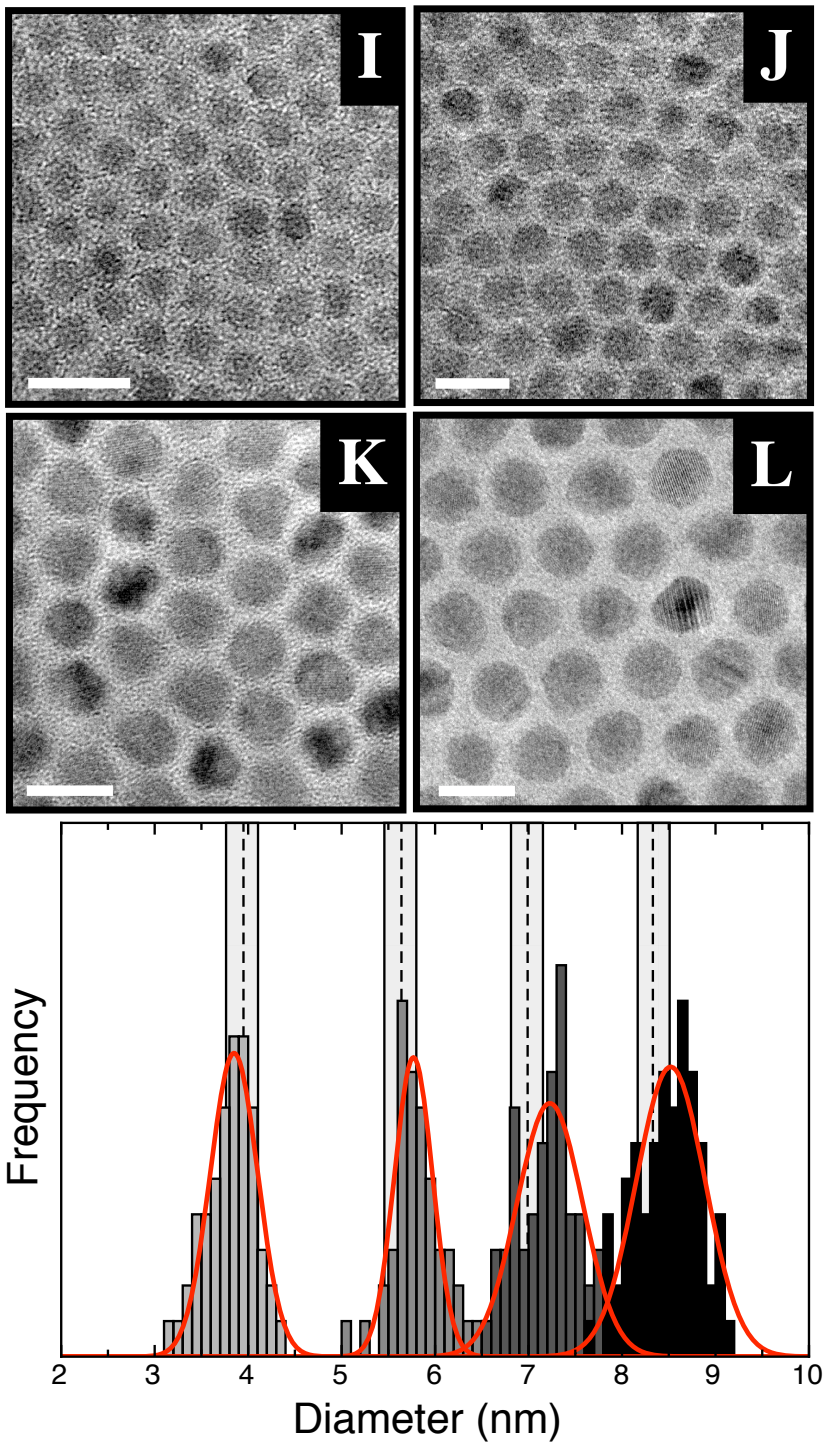

Figure 6.3: **Top**: High resolution transmission electron micrographs of *Sample 3*; **3.84** *nm* core. Scale bar equals 10 *nm*. **(I)** CdSe cores, **(J)** CdSe/CdS with a ∽2 ML CdS shell, **(K)** CdSe/CdS with a ∽4 ML CdS shell, **(L)** CdSe/CdS with a ∽6 ML CdS shell. **Bottom**: Histograms of the measured particle sizes obtained during the course of shell growth. The dashed line indicates the expected size of the nanocrystals, with the grey box outlining the associated error due to the error in the initial core size calibration curve of Yu *et al*[2].

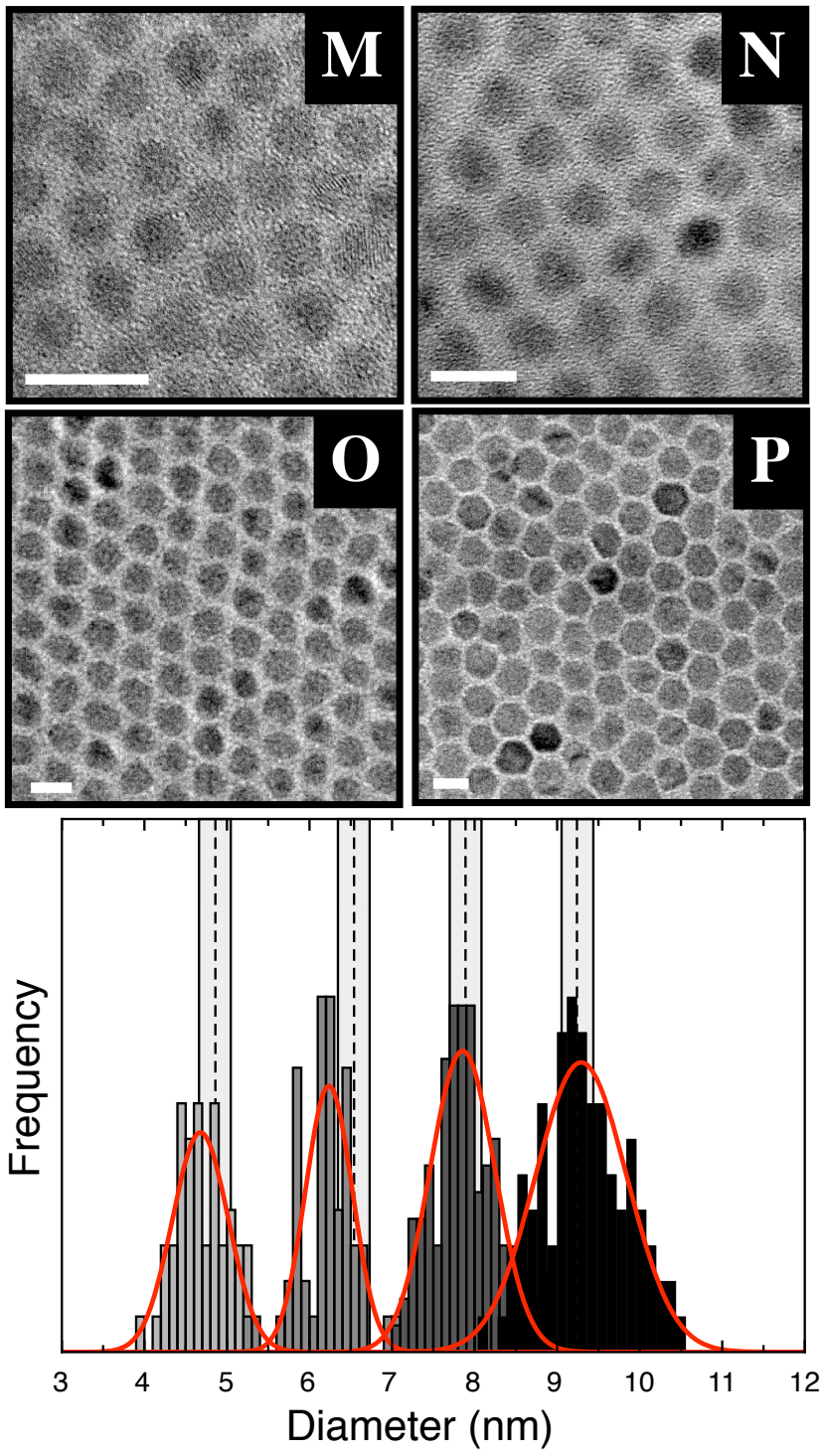

Figure 6.4: **Top**: High resolution transmission electron micrographs of *Sample 4*; **4.68** *nm* core. Scale bar equals 10 *nm*. **(M)** CdSe cores, **(N)** CdSe/CdS with a ∽2 ML CdS shell, **(O)** CdSe/CdS with a ∽4 ML CdS shell, **(P)** CdSe/CdS with a ∽6 ML CdS shell. **Bottom**: Histograms of the measured particle sizes obtained during the course of shell growth. The dashed line indicates the expected size of the nanocrystals, with the grey box outlining the associated error due to the error in the initial core size calibration curve of Yu *et al*[2].

Table 6.2: Statistics obtained from analysis of the histograms corresponding to the particle sizes for *Samples 1-4* at various stages of CdS shell growth

Sample	CdS ML	Measured $\bar{d}_m$ (nm)	Predicted $\bar{d}_p$ (nm)	$(\bar{d}_m$-$\bar{d}_p)$ (nm)
1	0	2.55 ±0.31	2.34	+0.21
1	2	4.27 ±0.29	4.03	+0.24
1	4	5.29 ±0.34	5.38	−0.09
1	6	6.71 ±0.35	6.72	−0.01
2	0	3.40 ±0.38	3.44	−0.04
2	2	5.08 ±0.23	5.12	−0.04
2	4	6.64 ±0.37	6.47	+0.17
2	6	7.87 ±0.33	7.81	+0.06
3	0	3.84 ±0.25	3.95	−0.11
3	2	5.27 ±0.20	5.64	−0.37
3	4	7.23 ±0.35	6.99	+0.24
3	6	8.52 ±0.37	8.33	+0.19
4	0	4.68 ±0.34	4.86	−0.18
4	2	6.24 ±0.28	6.55	−0.31
4	4	7.85 ±0.39	7.89	−0.04
4	6	9.29 ±0.55	9.24	+0.05

Analysis of the HRTEM images in Figures 6.1 to 6.4 reveal that throughout the growth process the nanocrystals maintain their initial spherical morphology except in the later stages of shell growth for core sizes larger than 3.40 nm (Panels L and P), where the nanocrystals begin to adopt a distinct hexagonal shape. Upon inspection of the histograms in these figures it can be seen that in all cases the particle size distribution (PSD) narrows significantly following the growth of the first 2 MLs of CdS. The size distributions then broaden slightly with each additional monolayer. The distributions of the final core/shells with 6 MLs of CdS have FWHM typically around 0.1-0.2 nm greater than those of the original cores. By comparing the peaks of the Gaussian functions (mean nanocrystal sizes; $\bar{d}_m$) to their corresponding predicted sizes ($\bar{d}_p$, dashed lines) it is seen that for all stages during shell growth there is good agreement between these two values. Table 6.2 summarises the statistics obtained from fitting the sizing histograms to Gaussian functions. The data therein show

that during shell growth the largest deviation of the mean value of any PSD from its predicted size was 0.37 nm, with a large majority of the values falling within 0.2 nm. Considering radial shell growth, all measured shell thickness were found to be within 0.19 nm of the mean predicted sizes (dashed lines), well under the thickness of a single CdS ML (0.337 nm). From the results of Table 6.2 it is clear that when adhering to the specific reaction conditions outlined in the Experimental section, and by using two-acids to manipulate the growth kinetics, sub-monolayer control of shell thickness may be achieved across a wide range of initial core sizes.

6.3.2 X-ray and Electron diffraction

To confirm the crystal phase of the CdSe/CdS core/shell nanocrystals both X-ray and electron diffraction were carried out. Figure 6.5 (left) displays four X-ray powder difraction (XRD) patterns. Panel A shows a pattern obtained from 3.40 nm CdSe cores. Consistent with previous results [3], the peak positions agree well with those expected for a bulk wurtzite CdSe crystal. In the upper panel, patterns B-D depict the XRD patterns obtained for small (2.55 nm), intermediate (3.40 nm) and large (4.68 nm) CdSe cores with 6 MLs of CdS shell. Upon growth of the shell the peaks sharpen and shift to approach the predicted values for a bulk wurtzite CdS crystal. Both the sharpening and the shifts are consistent with larger local crystal domains and the large volume of CdS compared to CdSe in the final individual structures respectively [4]. It should be noted that attenuation of the {102} reflection is commonly observed for CdSe and their related heterostructures and arises as a result of zinc blende stacking faults in the {002} direction [4, 5].

Figure 6.5 (right) displays a selected area diffraction pattern taken of CdSe/CdS core/shells with an intermediate core size (3.40 nm) and a 6 ML shell of CdS. The relative ring spacings (d-spacings) were calculated by measuring the distance from the centre point out to the middle of each ring and dividing these values by the distance obtained for the nearest

ring; hkl={100}. These observed (OBS) values are then tabulated along with the simulated (SIM) values based on a bulk wurtzite CdS crystal. The OBS and SIM values for each set of Miller indices (hkl values) agree to within 4.6%, which supports the XRD data and confirms the wurtzite crystal phase of the core/shells. Collectively, the data obtained from X-ray and electron diffraction prove that shell growth proceeds in an epitaxial manner.

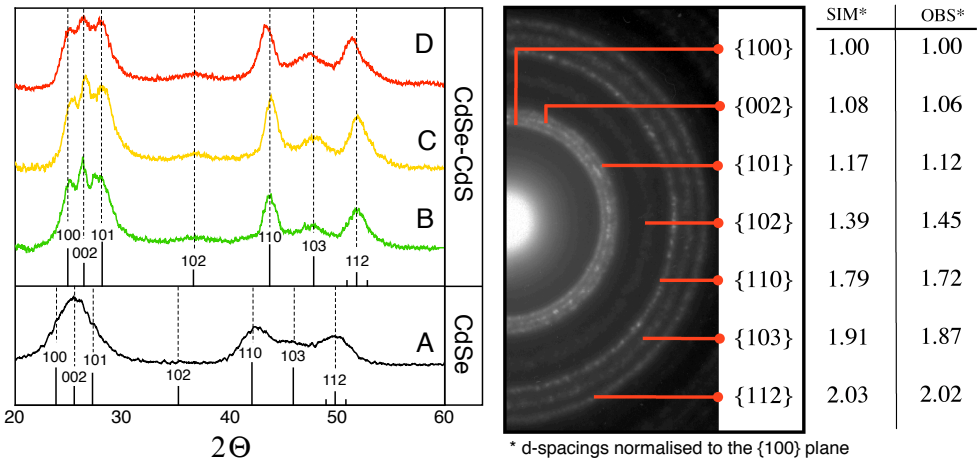

Figure 6.5: Left; Powdered X-ray diffraction patterns of (A) CdSe core, (B)-(D) CdSe/CdS particles with a 6 ML CdS shell with core sizes 2.55 *nm*, 3.40 *nm* and 4.68 *nm* respectively. The theoretically predicted reflections from bulk wurtzite CdSe and CdS are shown in the lower and upper panels respectively. The dotted lines highlight the shift of the reflections to higher angles after shell deposition. Right; Selected area diffraction pattern taken of CdSe/CdS core/shells with an intermediate core size (3.40 nm) and a 6 ML shell of CdS.

6.3.3 Super HRTEM: Structural analysis

Figure 6.6A shows a high resolution transmission electron micrograph of the 2D zone axis of a CdSe/CdS nanocrystal with 6 ML of CdS shell; 10.19 *nm* in diameter. The nanocrystal shown in Panel A clearly exhibits hexagonal morphology as well as hexagonal symmetry on the atomic scale. Panel B shows a magnified area of this nanocrystal highlighting the *a* and *c* lattice planes. Panel C shows a simulation of a pure CdS nanocrystal viewed on the same crystal face shown in A and B. The measured and simulated values for *a*, *c* and

θ are as follows:‡ **Measured**; a= 3.941 Å, c= 6.823 Å, θ=60°. **Simulated**; a= 4.135 Å, c= 6.749 Å, θ=60°. From comparison of these values we determine the view direction to be perpendicular to both the {100} plane (a axis) and {002} plane (c axis). The d-spacings of the CdSe/CdS heterostructure agree well with those values obtained for a bulk wurtzite CdS nanocrystal. However, a slight contraction of the a-lattice parameter ($\backsim$4.7%) and an elongation of the c-lattice parameter ($\backsim$5.3%) is observed. This is perhaps a consequence of the small scale of the crystal relative to a bulk crystal or may be due to the strain imposed on the crystal lattice through the core-to-shell lattice mismatch.

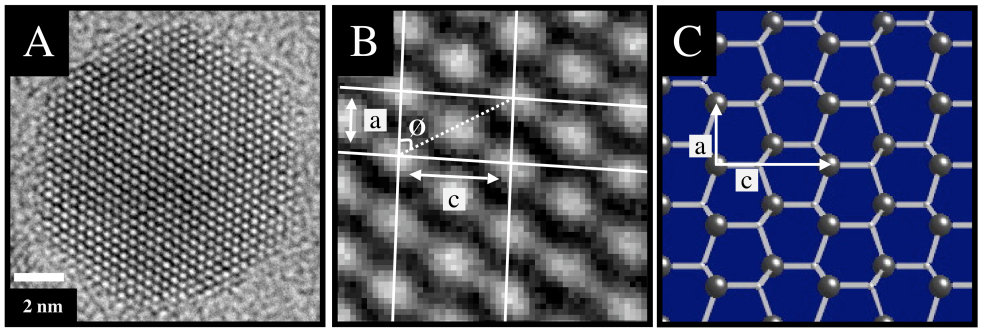

Figure 6.6: **(A)** Super high resolution transmission electron micrograph of the 2D zone axis of a CdSe/CdS nanocrystal with 6 ML of CdS shell; 10.19 *nm* in diameter. Scale bar equals 2 *nm*. **(B)** Magnified area of the nanocrystal highlighting the a and c lattice planes. **(C)** Simulation of a pure CdS nanocrystal viewed on the same crystal face shown in A and B.

6.3.4 Elemental analysis (EDS)

Figure 6.7 shows the results of an elemental analysis performed on a selected area of a few hundred CdSe/CdS nanocrystals with an intermediate core size of 3.40 *nm* and 6 ML of CdS shell (Ref: Figure 6.2 HRTEM image H). The corresponding bar-chart summarises the observed and calculated relative atomic percentages of cadmium, selenium and sulfur present in each heterostructure. The expected and observed percentages agree to within 4.4% for all three elements analysed. The close agreement of these values supports the HRTEM sizing

‡Measured bond distances were obtained by averaging over 20 lattice planes in both directions. Simulated values were obtained from a CdS nanocrystal constructed using bulk CdS lattice parameters and symmetry.

data obtained for both the initial core and final particle sizes. Furthermore, it rules out the possibility that ripening of the CdSe cores has contributed to the observed shell thickness as in such cases it is expected that (on average) higher amounts of selenium would be present in the final core/shell structure.

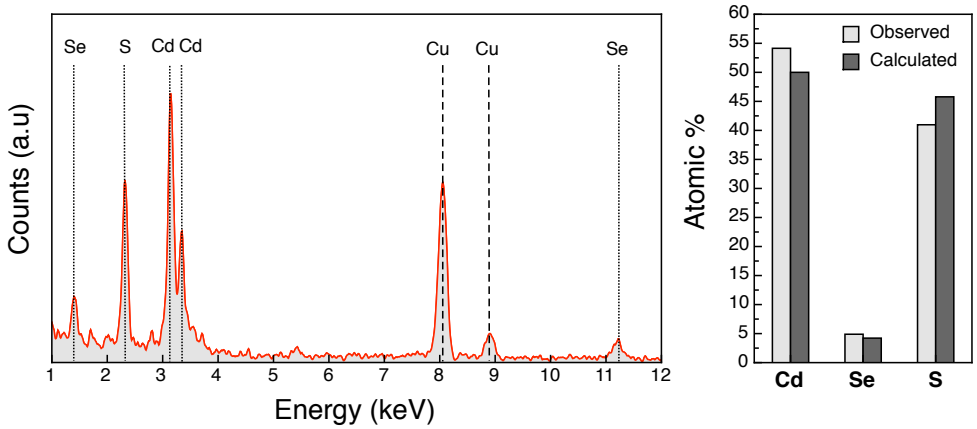

Figure 6.7: Left; EDS spectrum of CdSe/CdS nanocrystals with a core size of 3.4 *nm* and a shell thickness of 6 ML. The peaks due to the copper grid are indicated by the dashed lines. Right; The observed and calculated atomic percentages of Cd, Se and S in the heterostructure.

6.3.5 Ligand chemistry and Reaction Temperature

As previously discussed in Chapter 5, optimising the conditions for shell growth involves systematically altering multiple reaction variables. The growth medium, temperature, precursor type and concentration as well as the type and amount of free ligand all need to be customised to achieve the growth of high quality core/shell nanocrystals. For the purposes of this chapter only the most critical parameters, namely the effects of the ligands and the reaction temperature will be discussed for the specific case of cadmium sulfide shell growth.

Ligand chemistry: The choice of ligand chemistry is perhaps the most vital consideration, because the rate and extent to which monomers are consumed is reaction controlled during shell growth. The role of the ligands is to balance the particle/monomer reactivity in order to avoid the extremes of ripening or homogeneous nucleation.

Early trials using Cd-TMPPA and ODES to controllably grow a CdS shell were unsuccessful. The shell thickness of the resulting core/shells was smaller than predicted and HRTEM investigations revealed that the final particles to be highly faceted.[§] Furthermore, during these preparations homogeneous nuclei would invariably appear after 5-6 atomic monolayers (2-3 MLs CdS) had been injected. The formation of these nuclei is signalled by a PL darkening of the core/shells and the formation of strong absorbance and PL bands centred around 400 nm, consistent with the formation of isolated CdS nanocrystals (Ref: Appendix D). Reactions which included higher concentrations of TMPPA (up to 1 M) in the injection solution proved unable to suppress the formation of these nuclei. Given that we consistently observed homogeneous nucleation (HN) after 5-6 injections of precursor (specifically after the injection of sulfur monomer) we submit that the formation of isolated CdS is a direct consequence of TMPPA binding strongly to the particle surface, inhibiting shell growth and subsequently causing a build-up of unreacted Cd-TMPPA in solution, which may later nucleate in the presence of sulfur.

In efforts to improve shell growth and prevent HN another cadmium precursor, cadmium oleate, was also trialled. It was found that by employing cadmium oleate with OA:Cd ratios above 10:1, thicker shells could be grown with a reduction to the amount of HN. However, HRTEM images of the core/shells grown using this precursor displayed pronounced growth of the shell along the |002| axis when the CdS shell thicknesses exceeded 4 MLs, a result that is consistent with the findings of Li *et al* [1].[¶] A further drawback of employing cadmium oleate is that it must be introduced into the growth medium with a minimum of a ten-fold excess of oleic acid in order to adequately suppress HN. While the introduction of this excess acid was found to have a negligible effect on larger core sizes, it caused the dissolution or ripening of those particles with initial sizes below $sim3\ nm$ (1^{st} Abs max $\backsim$550 nm).

In accordance with the findings presented in Chapter 3, TMPPA was found to slow

[§]HRTEM images of particles synthesised using Cd-TMPPA are provided in Appendix F.
[¶]HRTEM images of particles synthesised using Cd-oleate are provided in Appendix E.

growth, inhibit Ostwald ripening and promote HN, while OA facilitated growth and suppressed HN. The opposing effects of these two ligands were used to manipulate the solubility of the monomer as well as particle reactivity in order to provide an environment that was conducive to growth only. After numerous trials it was found that combining these ligands in a mole ratio of 5:1 (OA:TMPPA) provided the conditions necessary for the growth of highly crystalline spherical shells on core sizes ranging from $\backsim$2.3 nm to $\backsim$6 nm in the absence of either ripening or HN.

Reaction Temperature: The growth rate of a nanocrystal is both size and temperature dependent. Given their small volume and high surface energy, the growth rate of a nanocrystal responds to small changes in reaction temperature. As such, the temperature at which the nanocrystals are overcoated is critical. To impart maximum crystallinity to the growing shell high temperatures are desirable. High temperatures also increase the reactivity of both the particles and the shell precursors (monomers), which favours shell growth and prevents the build up of monomer in solution - a condition that leads to the homogeneous nucleation of the shell material. Conversely, if the temperature is too high Ostwald ripening of the nanocrystals will occur.

In light of this we found it necessary to tailor the reaction temperature to suit different sized nanocrystals. For example, nanocrystals with sizes above $\backsim$3 nm required initial temperatures greater than 230°C for shell growth to occur at appreciable rates. However, for cores with sizes less than $\backsim$2.3 nm it was found that if the initial reaction temperature exceeded 200°C ripening of the cores would occur prior to the first injection of shell precursor. Furthermore, in the case of these small cores, if the initial temperature was much below 200°C, or if the temperature was not suitably raised during the reaction (typically by about 20-30°C above the initial temperature), large amounts of monomer would remain unreacted in solution, and homogeneous nuclei would eventually appear. It should be noted that the appearance of these nuclei could not be avoided by increasing the time given for each ML to react, even for delays of up to 1 hr between subsequent injections. The optimal

reaction temperatures for each core size were those that maintained high conversion rates of monomer into shell material throughout the reaction.

Given that high temperatures and high concentrations of cadmium complexing ligands (especially OA) were required to prevent HN, it was imperative to ensure that ripening did not accompany shell growth. Ripening not only broadens the particle size distribution but, if allowed to continue throughout the reaction also results in changes to the absorbance spectra that are unrelated to shell growth, making those values obtained for the absorbance shifts as a function of shell thickness unreliable. As such, during the course of optimisation several trial experiments were undertaken to make certain that the core nanocrystals were stable at their initial growth temperatures and that any later increase in temperature would not trigger ripening of the core/shell nanocrystals. Taking quantitative absorbance spectra over time allowed the size and size distribution of a nanocrystal population to be monitored. If no changes to the spectra were observed the nanocrystal population was regarded as stable. The results of these experiments indicated that the core nanocrystals could be heated at their initial growth temperature for 20-30 *min* prior to the injection of shell precursor without growth or spectral broadening.[‖] Furthermore, without the usual addition of monomer the core/shell nanocrystals could be heated for a total of 70-80 *min* following the second temperature increase before any spectral changes were seen to occur.

6.3.6 Absorbance shifts

Figures 6.8 to 6.11 display a series of normalised absorbance spectra at different magnifications taken during the growth of a CdS shell on the four samples under investigation. Similar trends are observed for all four samples. We begin by discussing these trends followed by an analysis of those effects specific to each core size. In all four sets of spectra we see that as the CdS shell deposits onto the core a large red-shift of the first excited state occurs. This

[‖] In the cases where CdSe nanocrystals with diameters below $\backsim 2.5$ *nm* were used, spectral changes were commonly observed if the cores were heated at their initial temperature for longer than 10 *min*.

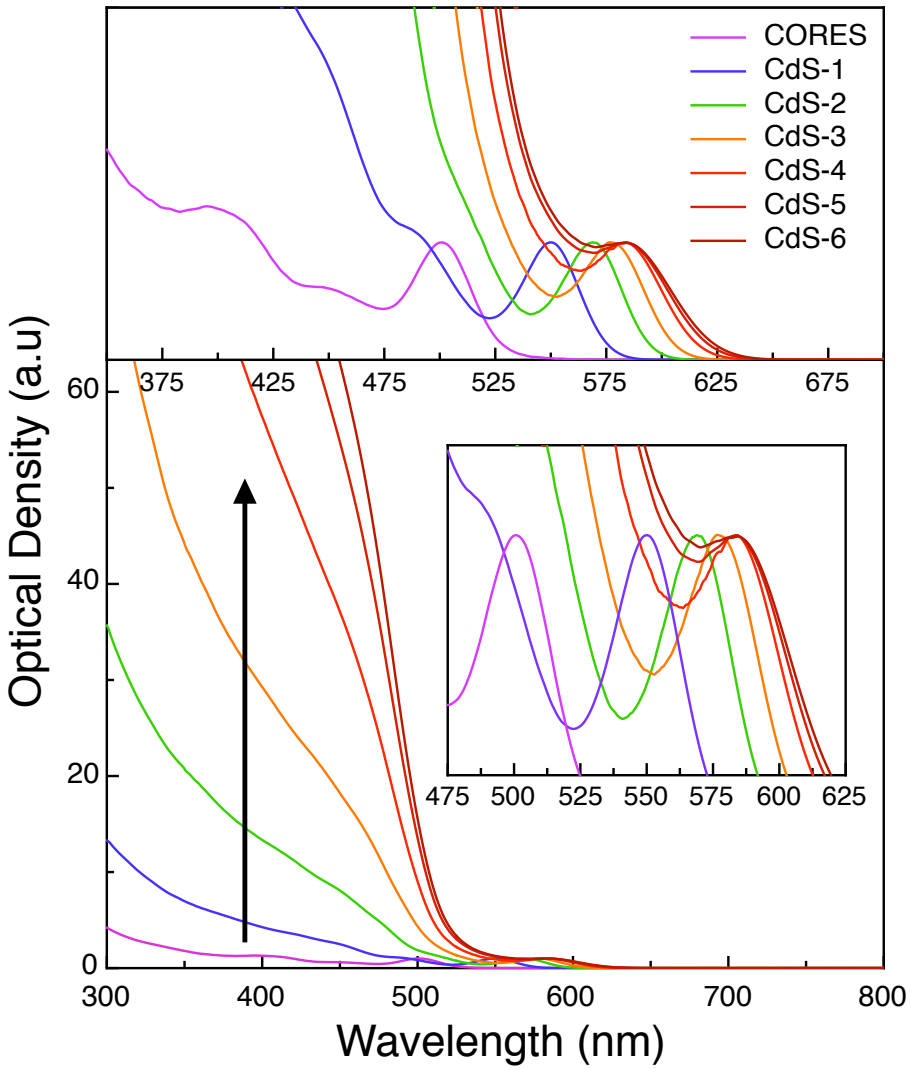

Figure 6.8: Normalised absorbance spectra taken after each monolayer of CdS shell growth on a 2.55 *nm* CdSe core (*Sample 1*). The different magnifications highlight the various spectral changes that occur upon shell deposition.

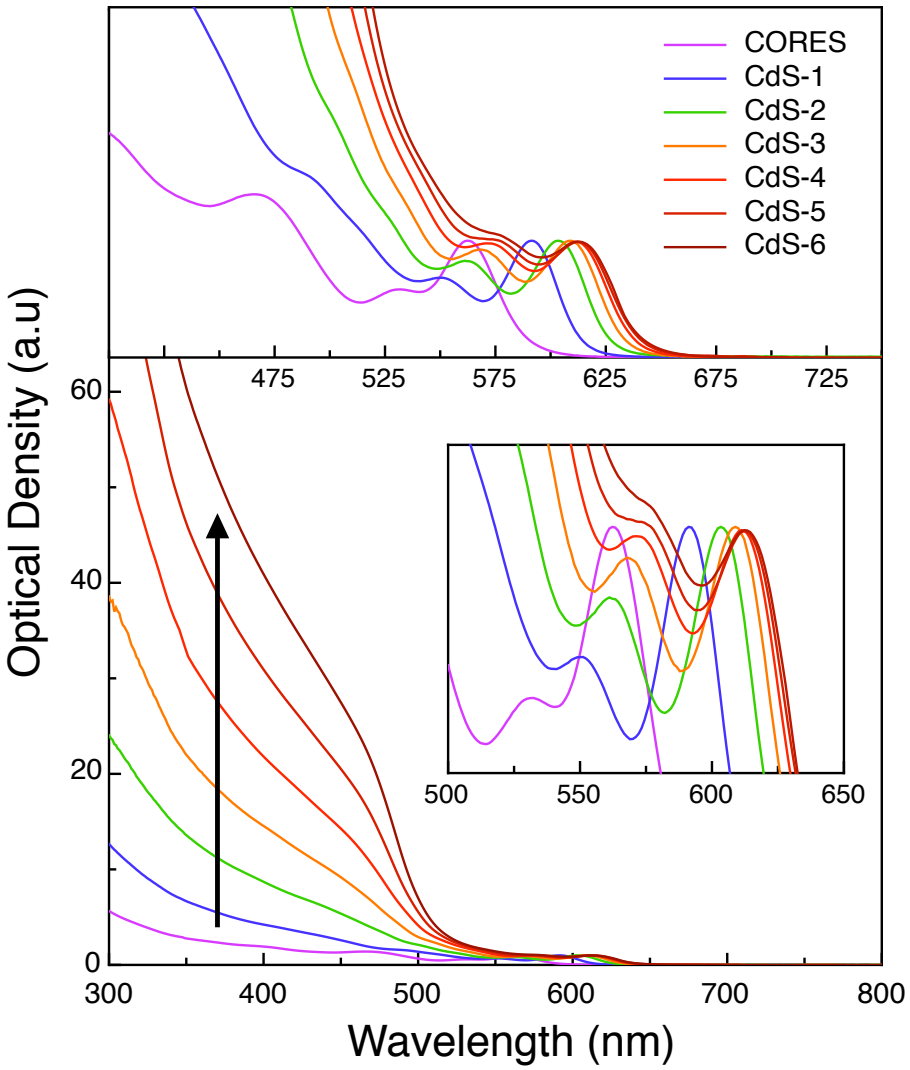

Figure 6.9: Normalised absorbance spectra taken after each monolayer of CdS shell growth on a 3.40 *nm* CdSe core (*Sample 2*). The different magnifications highlight the various spectral changes that occur upon shell deposition.

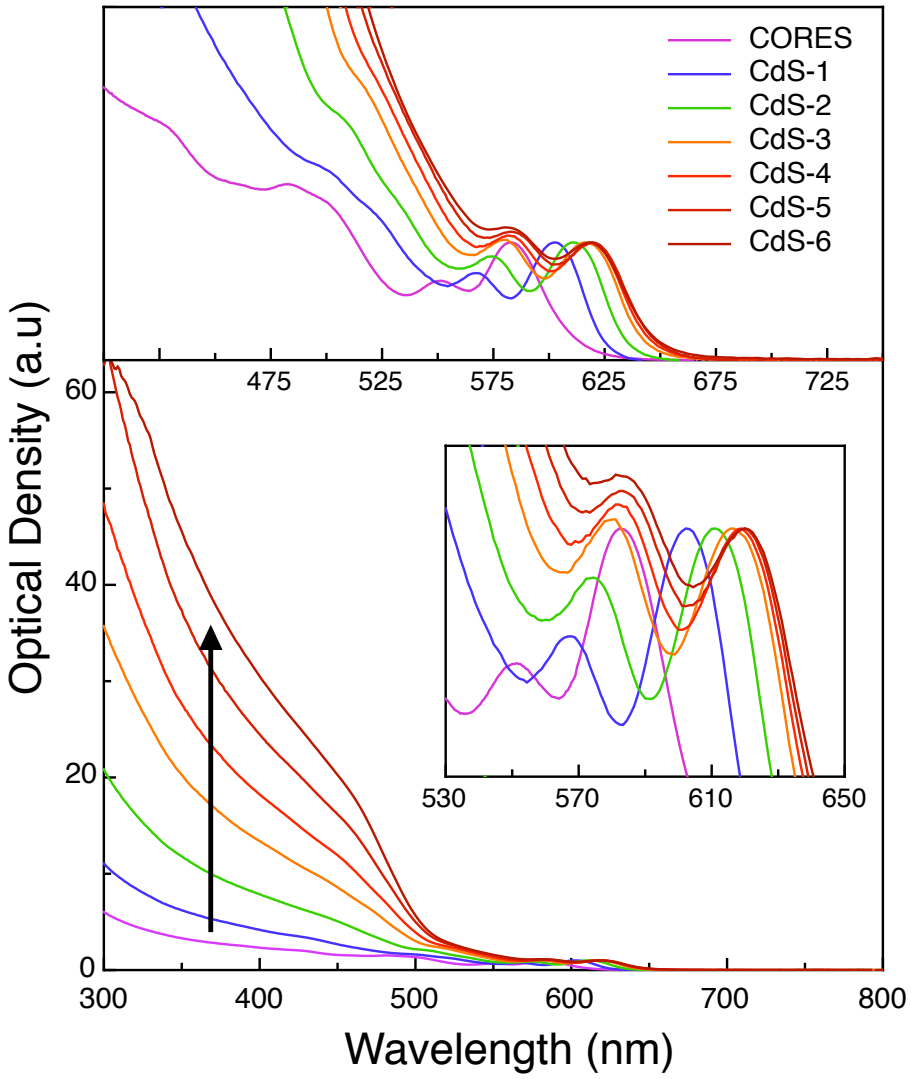

Figure 6.10: Normalised absorbance spectra taken after each monolayer of CdS shell growth on a 3.84 *nm* CdSe core (*Sample 3*). The different magnifications highlight the various spectral changes that occur upon shell deposition.

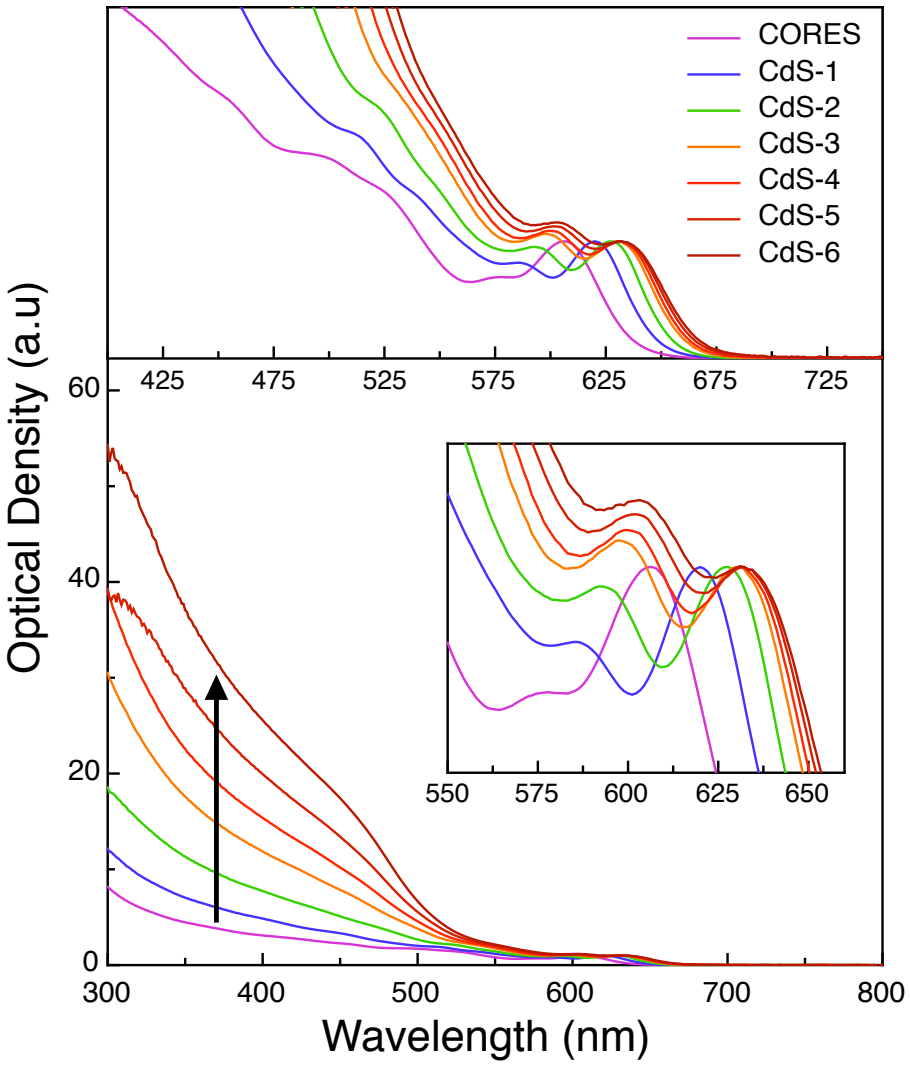

Figure 6.11: Normalised absorbance spectra taken after each monolayer of CdS shell growth on a 4.68 *nm* CdSe core (*Sample 4*). The different magnifications highlight the various spectral changes that occur upon shell deposition.

phenomenon is caused by extensive delocalisation of the electron into the surrounding shell and has been previously observed during CdSe/CdS preparations [1, 6]. Close examination of the lowest energy $1S_{(h)} \leftarrow 1S_{(e)}$ transition with increasing shell thickness reveals that the largest red-shift occurs upon deposition of the first monolayer. The magnitude of the shift then declines for each additional monolayer deposited. As the electron delocalises into the shell its distribution function decays with tunnelling distance. Thus as the shell gets thicker the extent to which the electron may continue to delocalise diminishes. The consequence of this is that the energy of the excited state is most greatly reduced upon the addition of the primary monolayers of shell.

Further inspection of Figures 6.8 to 6.11 reveals that the second excited state transition ($2S_{(h)} \leftarrow 1S_{(e)}$) increases in absorption with respect to the band edge transition. This phenomenon is common to CdSe/CdS preparation regardless of the synthetic method used to generate the shell [1, 6, 7]. The apparent gain in the oscillator strength of this transition is misleading. In fact we expect that all core transitions should decay in strength, given that the overlap of the electron and hole wavefunctions decreases as the shell is grown. To explain this result we may postulate that the oscillator strength of the first excited state decays more rapidly than the second, giving rise to the *appearance* that the $2S_{(h)} \leftarrow 1S_{(e)}$ transition is gaining strength.

Shell deposition also dramatically increases the absorbance below $\backsim 500\ nm$, which is coincident with the onset of the absorption in bulk CdS ($\backsim 512\ nm$). As indicated by the arrows, each additional monolayer of CdS that is deposited systematically increases the magnitude of the absorbance at energies below $\backsim 500\ nm$. The enormity of these absorbance values relative to the band edge absorbance may be attributed to a combination of the increased absorbance cross-section of the resultant nanostructure, the high shell:core volume ratio, and the high extinction value of CdS compared to CdSe. It should be noted that the absorbance from this spectral region is not due to homogeneous nuclei as indicated by HRTEM investigations. We may also rule out the possibility of absorbance from reaction

by-products as no changes in absorbance within this region was observed after purification of the particles.

In-situ absorption measurements: Reaction time scale

Figure 6.12 shows the growth of cadmium and sulfur atomic monolayers at 200°C monitored by an in-situ absorbance probe. 2.5 nm CdSe cores were chosen for this experiment as they exhibit the greatest absorbance shifts upon shell deposition. Furthermore, deposition may be conducted at lower temperatures compared to larger cores, which diminishes the extent of spectral broadening due to phonon coupling [8, 9]. Panel A shows the spectral changes that occur after the injection of cadmium (2^{nd} Cd-injection) into the reaction solution. No spectral changes were observed in the minute following injection (solid line). Between 1 min and 10 min the band-edge transition red-shifted 7 nm and a slight increase in the absorbance at higher energies was observed. Continual monitoring of the spectra up to 30 min revealed only a further 1 nm shift with no other changes to the spectral profile observed.

Panel B shows the spectral changes that occur after the injection of sulfur monomer (2^{nd} S-injection). In sharp contrast to the addition of cadmium monomer, the injection of sulfur immediately results in drastic spectral changes. Between 10 s and 100 s the band edge transition shifted 14 nm. Each red-shift was accompanied by a concomitant increase in absorbance at higher energies. Between 100 s and 30 min no further red-shifts were observed. However, during this time period an increase in the absorbance within the "shell" spectral region was seen, which may be a sign of increased crystallinity within the particle due to annealing of the lattice.

Comparison of Panels A and B reveal important information about the growth of a CdS shell. Firstly, the red-shift that occurs upon the deposition of cadmium is less ($sim40\%$) compared to sulfur. Secondly, the increase in the absorption at higher energies is almost solely a consequence of sulfur deposition. This indicates that a *full* semiconductor monolayer

may not grow unless equimolar anounts of cadmium and sulfur are present. Finally, by comparing the time scale of the two reactions, it is clear that sulfur deposition occurs at a rate almost an order of magnitude faster than cadmium. This infers that the activation barrier to the nucleation of monomer at the surface of the particle is largely dependent upon the strength of the ligand-monomer bond, with sulfur deposition occuring faster due to the absence of strong sulfur binding additives.

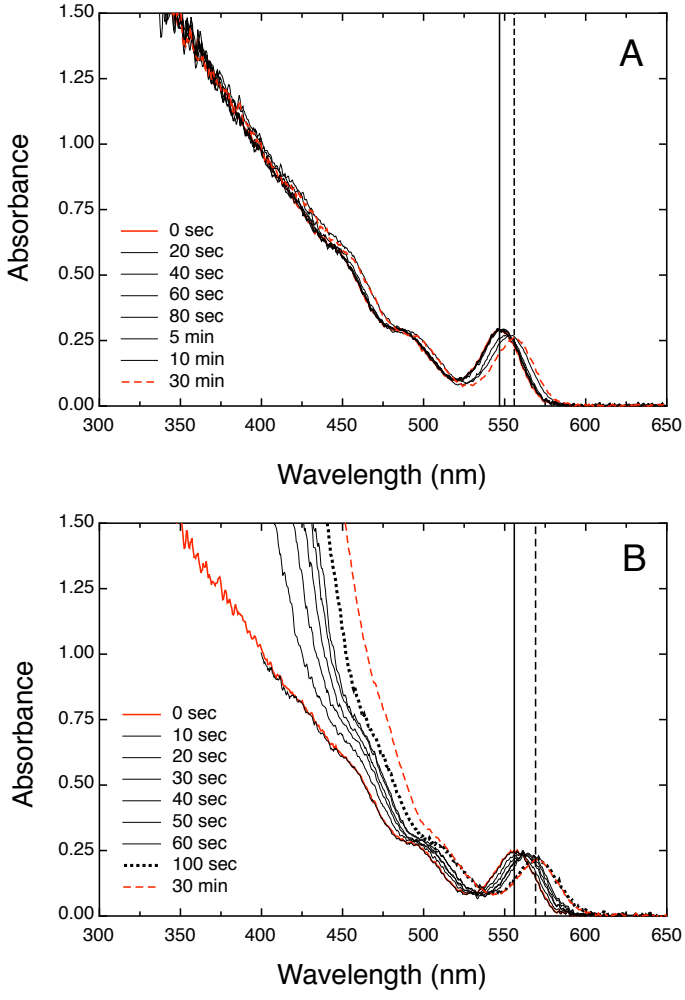

Figure 6.12: In-situ absorbance measurements during CdS shell deposition. Panel **A** shows the changes to the absorbance spectra after the addition of Cd-TMPPA. Panel **B** shows the changes to the absorbance spectra after the addition of ODES.

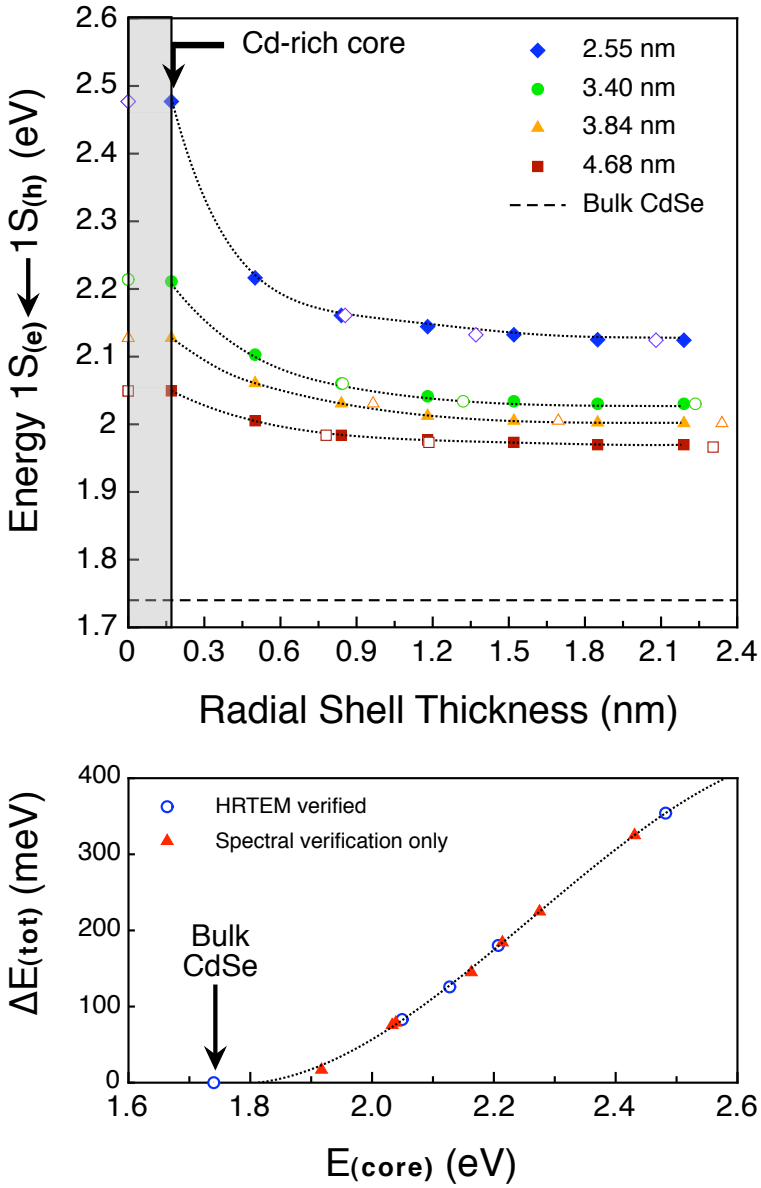

Figure 6.13: **Top**; Energy decays of the first excited state,$1S_{(h)} \leftarrow 1S_{(e)}$, as a function of CdS shell thickness. **Bottom**; Total energy loss after CdS shell growth as a function of the initial core energy.

Transition energy changes

Figure 6.13A shows the energy decay of the first excited state ($1S_{(h)} \leftarrow 1S_{(e)}$) for the four different samples under investigation as a function of CdS shell thickness. The HRTEM verified shell thicknesses (open symbols) are plotted along with the expected shell thicknesses (solid symbols). The dotted lines are fits of the HRTEM verified data to restricted cubic polynomials and act only as a guide to the eye. The area inside the grey box corresponds to the shifts associated with making the particles Cd-rich preceding shell growth (assume $\backsim$0.17 nm increase in radial shell thickness). It was found that the shifts associated with making the particles Cd-rich was not predictable and varied randomly with core size as well as between different batches of cores. Saturating the particle surface with cadmium prior to shell deposition allowed precise measurements of the optical changes as a function of shell thickness to be made beginning from particles with similar surface chemistries. Thus we assume that the first true CdS monolayer is present only after equimolar amounts of cadmium and sulfur have been added, subsequent to saturating the surface with cadmium.

The data of Figure 6.13A reveals two important trends. Firstly, for shell coverages below $\backsim$1.2 nm (3 MLs), the energy loss per nanometre of CdS shell increases dramatically as the initial core size is decreased. As the shell coverage on all samples is further increased the energy decay of the first excited state begins to plateau. At shell coverages between 1.5 nm (4 MLs) and 2.19 nm (6 MLs) the energy loss of all the samples is below $\backsim$8 meV. Secondly, as the initial core size decreases the *total* energy loss (after the growth of a 6 ML shell) increases dramatically. Although the 1^{st} excited state energies of the initial core samples span $\backsim$450 meV, these energies condensed to span a range of only $\backsim$90 meV after 6 ML of CdS shell had been deposited. As a consequence preservation of emission colour in CdSe/CdS heterostructures is impossible to achieve, e.g cores that have initial emission maxima around $\backsim$515 nm shift to $\backsim$590 nm by the termination of shell growth.

Given that the energy losses which occur upon the growth of the 6^{th} ML are less than

$\backsim$3 meV for all samples investigated here, we may assume the energy loss upon continued growth of the shell to be negligible. This allows for the determination of the total energy loss, ΔE_{tot}, as a function of the initial energy of the core. The values obtained are as follows; 344 meV for a 2.55 nm core and 180 meV, 129 meV and 83 meV for 3.40 nm, 3.84 nm and 4.68 nm cores respectively. Figure 6.13B displays a plot of ΔE_{tot} as a function of the initial energy of the core. The open circles are those obtained for the four samples under investigation. The energy for the bulk band gap of CdSe (1.74 eV) is also plotted at ΔE_{tot} = 0 to aid the fitting of the data (indicated by the arrow). This point is reliable given that no further changes to the absorbance spectra of semiconductor nanocrystals are expected once a particle reaches its bulk size. The data fits well to a cubic polynomial between 1.74 and 2.5 eV (dotted line). To verify this fit, ΔE_{tot} for other initial core sizes are also plotted (solid triangles). These points were gathered from syntheses accomplished using the same synthetic method but without verification of shell thickness from HRTEM investigations. It is seen that these values agree well with those predicted from the fit.

6.3.7 Lifetimes and Quantum Yield

Given the large extents to which the wavefunctions delocalise upon shell deposition it is important to establish how well the CdS shell electronically isolates the core from its environment. In order to test this, the lifetimes and QY of the core/shells were measured under various environmental conditions. Aliquots of the washed core/shells (*Samples 1-4* in ODE) were divided into three subsets. To create either *activating* or *quenching* environments, 10 μL of trioctylphosphine (TOP) [10] or octanethiol [10] were added to the samples respectively. As a reference, washed samples in ODE were also included in the analysis. The samples were then heated at 60°C for 6 hrs, then left at room temperature for $\backsim$20 hrs to ensure equilibrium had been established in each of the solutions. At this time aliquots of the samples were diluted with chloroform to obtain an absorbance of 0.1 at 400 nm (ex-

citation wavelength) for the lifetime measurements and 0.05 at the appropriate excitation wavelengths for Rhodamine B and Rhodamine 6G in order to accurately determine the QY of the nanocrystals. The average of these two values were taken to be the QY of the particles.

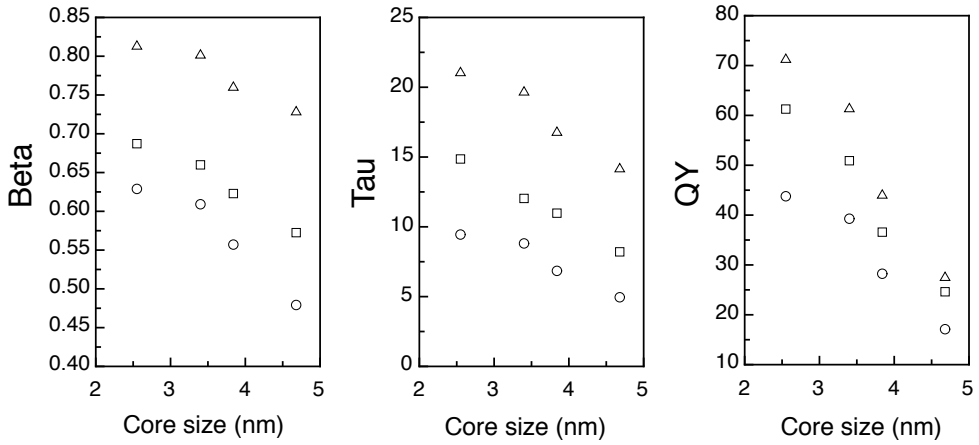

Figure 6.14: Statistics from the stretched exponential fits to lifetime measurements obtained from *Samples 1-4* (6 ML CdS shell) in the as-prepared (squares), trioctylphosphine activated (triangles) and octane thiol quenched (circles) states. The corresponding quantum yields in each of these states are also plotted.

The measured lifetimes were fitted to stretched exponentials of the form $A\exp\left(-t/\bar{\tau}\right)^{\beta}$. These fits yield the average lifetime $\bar{\tau}$, and a beta (β) parameter ranging between 0 and 1. A β value of 1 indicates a single exponential process, with decreasing values indicative of a broader distribution (increased number) of recombination pathways, provided by either defects inside the nanocrystal or by traps at the nanocrystal surface [11].

Figure 6.14 shows plots of the values obtained for β and $\bar{\tau}$ as well as the QY for *Samples 1-4* in the as-prepared (squares), activated (triangles) and quenched (circles) states as a function of initial core size. The first point to note is that the β, $\bar{\tau}$ and QY values obtained for the as-prepared samples decrease as the initial size of the nanocrystal cores increases. In CdSe cores it is commonly observed that the band-edge lifetime increases weakly with core size [12]. This may be attributed to decreased confinement (reduced Coulomb attraction between the charge carriers) within the nanocrystal [13]. Recalling that smaller cores exhibit a greater ΔE_{tot}, we rationalise the observed increase of the lifetime with decreasing initial core

size as more efficient charge separation is achieved when beginning from smaller cores, despite the overall smaller size of the initial nanocrystal. Decreasing β values in larger structures (assuming similar surface chemistries) are typical of an increasing number of surface sites, which may provide alternative recombination pathways. Interestingly the magnitude of the changes to β and $\bar{\tau}$ upon either activation or quenching appear independent of the initial core size. From these data we may conclude that the recombination dynamics remain sensitive to the surface chemistry even though a 6 ML shell of CdS is present. The data obtained for QY as a function of core size reveals that CdSe/CdS nanocrystals synthesised from smaller cores have an increased sensitivity to surface bound adsorbates. This implies that despite the thick potential barrier is created by the 6 ML CdS shell one or both of the charge carriers still has access to the nanocrystal surface.

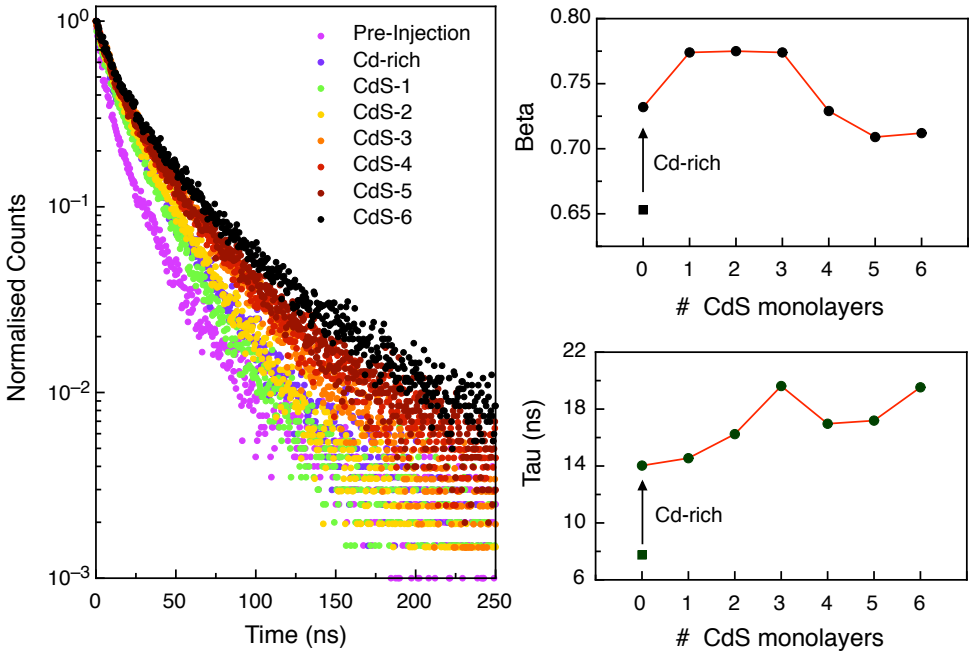

Figure 6.15: (**A**); Lifetime traces as a function of CdS shell growth. (**B**) and (**C**); β and $\bar{\tau}$ values obtained from the stretched exponential fits of these lifetime traces respectively.

To deepen our understanding of these phenomena, the recombination dynamics of the ensemble may be measured as a function of shell thickness. Figure 6.15A shows a series of

lifetime traces taken after each subsequent layer of CdS shell growth on an intermediate size core (3.40 nm). Panels B and C are plots of the β and $\bar{\tau}$ values obtained from fitting the lifetimes. We see that upon making the particles Cd-rich both β and $\bar{\tau}$ increase dramatically. The injection of cadmium saturates the surface selenium atoms. The newly formed Cd-rich surface is subsequently passivated by the cationic ligands present in the growth solvent, resulting in a more favourable surface chemistry for the particle [14]. This result is expected given that there are no anionic surfactants present to passivate surface selenium atoms. Upon deposition of the first ML of CdS shell another sharp increase in β is observed, indicative of epitaxial surface passivation and increased electronic isolation of the core from its environment. Upon continued shell growth an increase in both β and $\bar{\tau}$ was observed until sim3 ML of CdS shell had been deposited, at which point continued shell growth resulted in a decrease in both parameters. The reversal of the initial trends observed for β and $\bar{\tau}$ may be attributed to increased lattice strain within the structure. The induced strain is typically relieved by the creation of defects in the lattice, which act as non-radiative recombination centres for the charge carriers. As the data for the 6^{th} ML was recorded from an aliquot taken at the end of the reaction, the increase in both parameters observed after the deposition of the final monolayer is likely due to the annealing of the nanocrystals *after* the termination of shell growth.

6.3.8 The effect of Chalcogenide complexing agents

The type of ligands employed to shell CdSe nanocrystals must be scrutinised as not all of the ligands that have been previously employed in the synthesis of core/shell heterostructures are viable for the production of thick shells. To reinforce this point we have chosen two of the most commonly used ligands in the production of core/shell nanocrystals, trioctylphosphine (TOP) and oleic acid (OA), in order to contrast their effects on shell growth. TOP is known to bind to chalcogenides, especially those with high electron affinities, such as sulfur, and

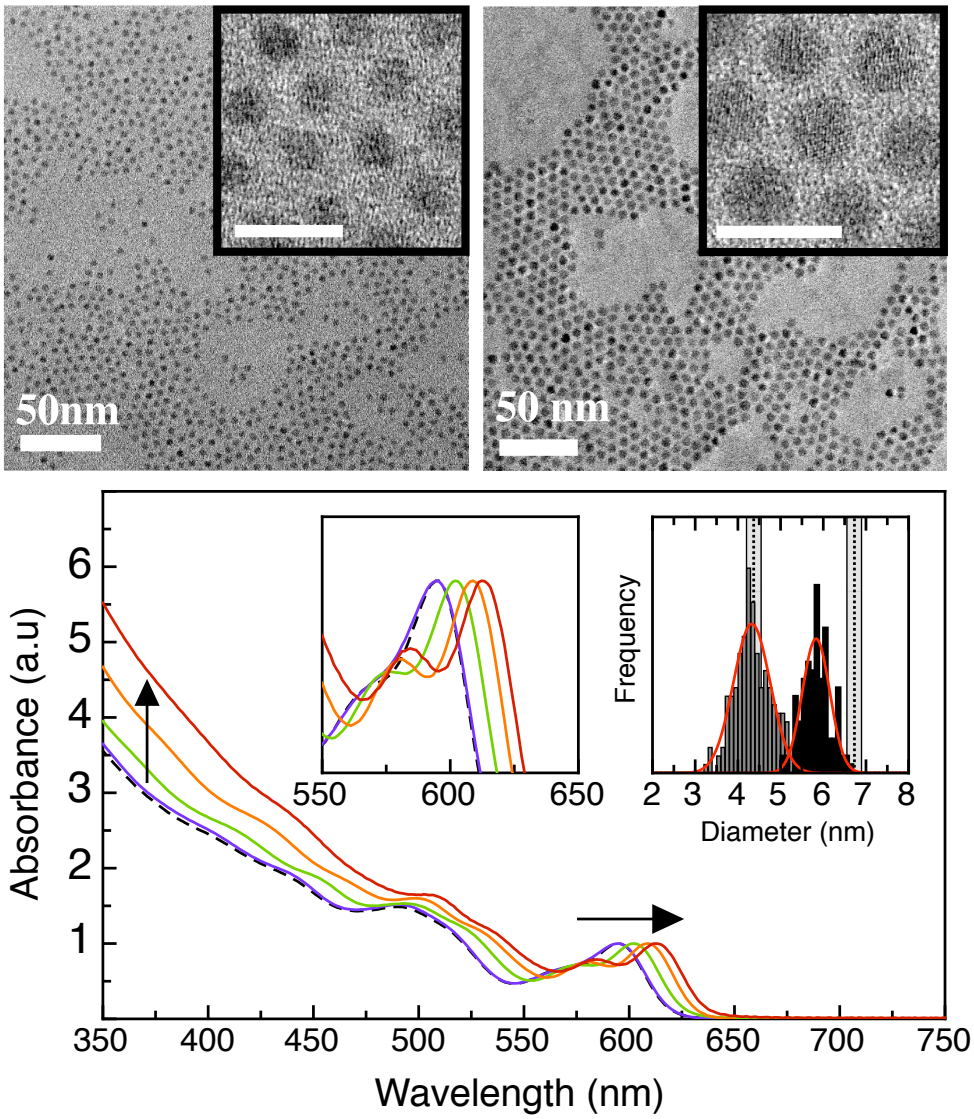

Figure 6.16: Results obtained from shelling CdSe with CdS using a Cd-TMPPA precursor and TOP in the growth medium. The top two panels show the HRTEM images of the particles before (left) and after (right) shell growth. The scale bar for the inset TEM images is 10 *nm*. The panel below displays the absorbance spectra taken during the shelling procedure. The five represented spectra from left to right (or bottom to top) following the arrows are; Preshell (dashed line), cadmium-rich cores, followed by calculated CdS monolayers 1, 2 and 3. The inset highlights the red-shift of the band edge transition during shell deposition. The left inset highlights the red-shift of the band edge transition during shell deposition. The right inset shows the histograms of the particle size before and after shell growth. The calculated mean size, standard deviation and expected size of the particles are; 4.32±0.43 *nm* /4.36 *nm*, 5.83±0.32 /6.71 *nm*.

OA is able to complex metal ions. The choice of these two ligands also allows the effects of increasing either the anion or cation solubility within the solvent to be decoupled and contrasted. Both reactions were accomplished using cores of a similar size and with the exception of the additional ligands, all other reaction conditions were maintained constant. Specifically, in *Reaction 1* supplements of OA were added along with the cadmium injections such that the molar ratio of OA to injected cadmium was 20:1. The results of this experiment are presented in Figures 6.4 Panels M-P and 6.11. In *Reaction 2*, instead of OA 500μL of TOP was added to the growth medium prior to shelling to achieve a ratio of TOP to total *mol* S added of 1.75:1.

We will begin by briefly iterating the outcomes of *Reaction 1*. Using the methods outlined in the Experimental section CdSe/CdS nanocrystals were synthesised whose calculated and measured sizes at all stages during shell growth agreed to within $\backsim$5%. This finding indicates that almost near complete conversion of sulfur monomer to shell is achieved using this synthetic chemistry in the presence of a small excess of cadmium. The photoluminescence FWHM of the final particles was 27 *nm* with a QY of 44%.**

Figure 6.16 displays the data obtained for CdSe/CdS nanocrystals with the presence of TOP in the growth medium. We see from the TEM images that the resultant CdSe/CdS particles are highly spherical and monodisperse. The histograms of the sample before and after shell deposition show a narrowing of the size distribution (from $\pm$0.43 *nm* to $\pm$0.35 *nm*), indicating that, similar to *Reaction 1*, optimal conditions for shell growth are also present in this system. However, the mean observed size of the core/shells was found to be approximately 0.9 *nm* (*sim*1.5 ML) smaller than expected. The reduction in the amount of shell material deposited is reflected in the absorbance spectra taken during shell growth, which show both a smaller red-shift and reduced absorbances below 500 *nm* compared to *Reaction 1*. The photoluminescence FWHM of the final particles was found to be 24 *nm*

**In order to directly compare the QYs of *Reaction 1* and *Reaction 2* the QY stated here is for the nanocrystals in their TOP activated state.

with a QY of 62% relative to Rhodamine B. The higher QY compared to *Reaction 1* may be attributed to the reduced shell thickness.

Given that complete shell growth occurred in *Reaction 1* (where no sulfur binding agent was present) the findings of *Reaction 2* indicate that TOP prevents high conversions of monomer into shell material. The mechanism by which TOP prevents shell growth is most likely to be a combination of strong surface binding, which physically inhibits monomer deposition, and the generation of trioctylphosphine sulfide (TOPS), which lowers the monomer saturation to a level no longer conducive to shell growth. In support of evidence that TOP increases the solubility of sulfur, a recent investigation into the effects of employing TOP in the synthesis of CdSe cores revealed that, even in small quantities, it is able to reduce the kinetics of nucleation [3]. The results outlined therein found that by increasing the amount of TOP in the growth medium, the concentration of nucleated CdSe particles (which is directly related to the monomer saturation) could be systematically decreased.

Contrary to the effect of TOP, large quantities of oleic acid may be used to control shell growth without compromising shell thickness. Clearly, OA solubilises the monomer to some extent, indicated by its ability to prevent homogeneous nucleation. However, unlike TOP, complexation of the monomer by OA results in the formation of a reactive species (cadmium oleate), which is able to continue to liberate free monomer. The precise nature of binding at the surface cadmium sites is speculative, as both TMPPA and OA compete for the same sites. Though it is clear that, unlike TOP, the effect these two molecules exert at the particle surface is complementary to shell growth, and that TMPPA, when used in conjunction with an excess of OA, does not bind surface cadmium atoms strongly enough to preclude shell deposition.

CdSe/CdS/ZnS Multishell Heterostructures

In this section the synthesis of CdSe/CdS/ZnS multishell heterostructures is described. Grading the lattice constant and band offsets produces highly luminescent crystalline structures. Depositing a wide band gap semiconductor such as zinc sulfide onto CdSe/CdS NCs provides structures that are more resistant to adverse environments compared to single shell CdSe/CdS nanocrystals [6, 15]. In such multishell structures the probability of the charge carrier reaching the surface is significantly diminished. As the NCs photoreactivity is reduced by the ZnS shell, CdSe/CdS/ZnS heterostructures are ideal for applications that require harsh processing of the NCs and adverse operating environments.

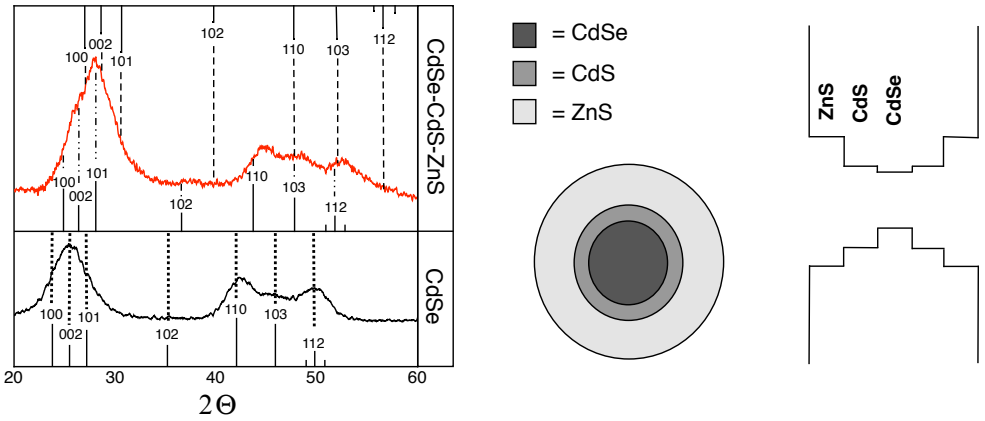

Figure 6.17: Left: XRD of CdSe/CdS/ZnS multishell nanocrystals. Right: Schematic of the core/shell structure and bulk band offsets of the three composite materials.

To synthesise the multi-shell (graded seal) NCs the core NCs were dispersed in an ODA:ODE mixture as outlined for the synthesis of CdSe/CdS heterostructures. The first layer consisted of enough cadmium to make the NCs Cd-rich, with the usual injection of a 20 fold excess of oleic acid. The first CdS layer was grown in the same manner as outlined in the Experimental section of this chapter. The deposition of ZnS was accomplished using Zn-TMPPA[††] and ODES. Every zinc injection was supplemented with a 0.5:1 mole ratio of tributylphosphite (TBPh) to sulfur (appropriate to that ZnS monolayer). TBPh acts to suppress homogeneous nucleation and ensure uniform shell deposition in much the same way

[††]This precursor was made as per the synthesis of Cd-TMPPA by replacing CdO with zinc acetate dihydrate.

as oleic acid. TBPhS is more reactive than TOPS as the oxygen groups intermediate between the phosphorus and the alkyl chains withdraw electron density from the phosphorus moiety making it less nucleophilic. As a consequence (unlike TOP) it does not bind the sulfur atom strongly enough to preclude shell deposition. All other conditions such as temperature, ML reaction times etc. were the same as those outlined for the synthesis of CdSe/CdS heterostructures with various core sizes.

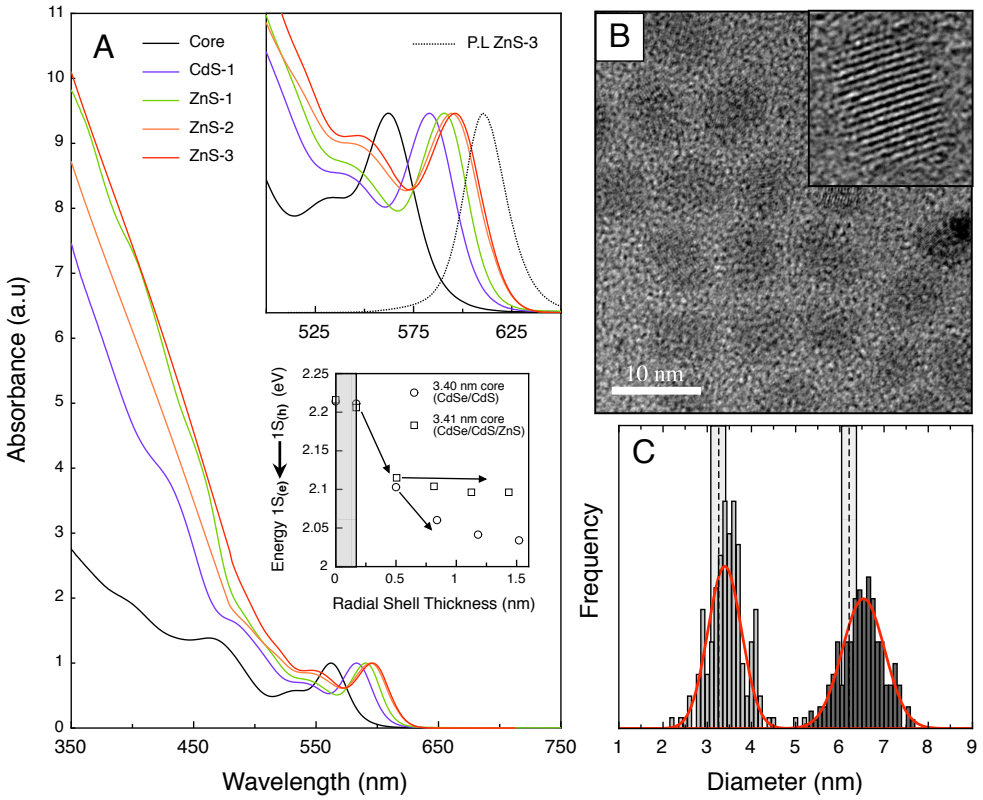

Figure 6.18: **(A)** Absorbance spectra as a function of shell thickness for shell deposition onto 3.26 *nm* CdSe cores. The lower inset highlights the ability of a ZnS shell to confine the charge carriers compared to CdS shell. **(B)** HRTEM image of CdSe/CdS/ZnS heterostructures with 3.26 *nm* CdSe cores, 1 ML of CdS and 3 ML of ZnS. **(C)** Histograms of the initial cores and the final multishell heterostructures with measured and predicted diameters of 3.41 ±0.36 *nm*, 3.26 *nm* and 6.55 ±0.58 *nm*, 6.21 *nm* respectively.

Figure 6.17 (left) shows the XRD of a sample of CdSe/CdS/ZnS core/shells with an initial core diameter of 3.26 *nm*. An XRD of similar size cores is shown for reference (bottom panel). Those reflections resulting from bulk wurtzite CdSe (dotted lines), ZnS (short dashed lines) and CdS (dot-dash lines) are also shown. Analysis of the XRD spectrum from the

core/shells reveals a general shift of all reflections to higher angles and a broadening of the peaks compared to the core NC spectrum. The resultant core/shell XRD pattern appears as a convolution of those reflections arrising from CdSe, CdS and ZnS, with the largest contribution coming from the ZnS shell. Figure 6.17 confirms the wurtzite phase of both CdS and ZnS shells indicating that shell growth was epitaxial. Figure 6.17 (right) shows a schematic of the core multishell structure as well as the bulk band alignments in the prepared heterostructures. It can be quickly seen that ZnS imparts a significant potential barrier to both the electron and hole.

Figure 6.18 shows a series of absorbance spectra taken after the deposition of each subsequent monolayer of shell on a 3.26 nm core. As expected the deposition of the first CdS layer results in a large red-shift of the first excitonic transition and a significant increase in the absorbance at wavelengths below 500 nm. Epitaxial growth of ZnS further red-shifts the first absorbance transition. However, due to the large conduction band offset between CdS and ZnS the lowest energy transition loses only a further 14 meV compared to 70 meV for the same number of MLs on a similar core size (see lower inset). From the upper inset it can be seen that the first transition remains narrow throughout the shelling process, indicative of favourable growth conditions. Panel B shows the HRTEM image of the final CdSe/CdS/ZnS heterostructure NCs. Inspection of Panel B reveals that the NCs are both crystalline and monodisperse. However, unlike the highly spherical NCs obtained after CdS deposition, CdSe/CdS/ZnS NCs were found to have average aspect ratios of sim1.2. This arises due to pronounced growth along the |002| axis as a consequence of the lattice mismatch between CdS and ZnS [16]. Panel C shows the histograms of the NCs before and after shell deposition. Reasonable agreement between the expected and observed sizes is seen, with the final NCs only 0.32 nm larger than predicted. It should also be noted that the final size distribution is slightly broader than the original cores.

To gather information about the effect of the ZnS shell on the energies of the first excitonic transition CdSe/CdS/ZnS heterostructures with several different core sizes ranging

from 2.45-5.61 nm were synthesised.[‡‡] Figure 6.19 shows a plot of the energy of the first transition as a function of shell thickness for all the core sizes investigated. As seen for the CdSe/CdS heterostructures the greatest energy losses are seen upon deposition of the first ML with greater decreases evident for smaller initial core sizes. For initial core sizes larger than $sim3$ nm the deposition of 3 MLs of ZnS resulted in almost no further shifting of the band edge transition. Interestingly, for core sizes below $sim3$ nm the energy of the first excited state continues to decline upon ZnS shell growth. The large observed energy losses upon the deposition of the first 2 ML of ZnS in these samples indicates that the electron has a significant probability of tunnelling deep into the ZnS layers ($\backsim$ 0.6 nm) despite the approximated 0.9 eV potential barrier generated by the shell. The energy losses in all samples upon deposition of the third ZnS ML were less than 3 meV. Thus we may infer that (within experimental error) complete confinement of the charge carriers is reached in such structures when a $sim1$ ML of CdS and 3 MLs of ZnS shell has been deposited. Notably, it required a full 6 MLs of CdS to be deposited before complete confinement was observed in pure CdSe/CdS heterostructures.

The ability of the shell to insulate the core from its local environment may be tested by photoluminescence spectroscopy through the use of quenching agents that adsorb to the NC surface. Any detected drop in PL upon addition of the quencher is a direct consequence of charge tunnelling through the shell. As such the extent of quenching directly reflects the efficiency of the shell to confine the charge carriers. Figure 6.20 shows the PL traces of CdSe/CdS core/shells with 6 MLs of CdS and CdSe/CdS/ZnS core/shell/shell NCs with 1 ML of CdS and 3 ML of ZnS on similar core sizes before and after the addition of thiophenol. A time period of $sim4$ hrs was allowed for the PL to stabilise. It was found that the integrated PL from CdSe/CdS core/shells decreased by 36.4% after the addition of thiophenol while the PL from CdSe/CdS/ZnS multishell heterostructures decreased by only

[‡‡]The data for 3.26 nm cores is shown in Figure 6.18. The absorbance spectra as a function of shell thickness for the other core sizes may be found in Appendix G.

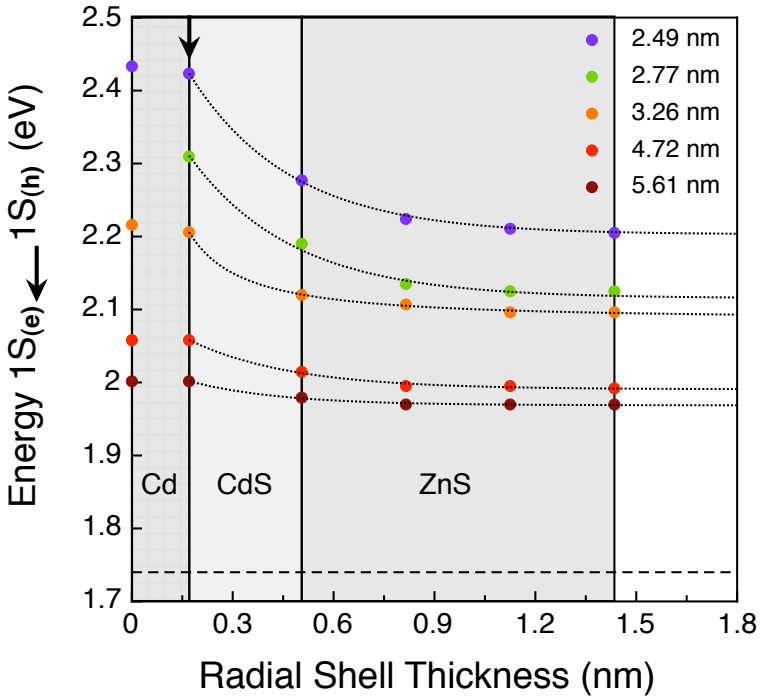

Figure 6.19: Energy of the first excited state as a function of radial shell thickness for five different initial CdSe core sizes ranging from 2.49 *nm* to 5.61 *nm*. The arrow indicates Cd-rich cores, the light shaded area represents 1 ML of CdS shell and the darker shaded area 3 MLs of ZnS. For reference the band gap energy of bulk CdSe is also plotted (dashed line). The important feature to note is that the energy loss of the first excited state diminishes with increasing shell thickness and increasing initial core size.

4.9%. The high degree of resistance to quenching observed for the multishell heterostructures makes them more suitable for applications that require modifications of the NC surface (with unfavourable ligands), harsh processing of the NCs or adverse operating environments.

6.4 Concluding Remarks

Monolayer control of shell thickness during the synthesis of CdSe/CdS heterostructures has been demonstrated. Accurate data on a wide range of core sizes with various shell thicknesses has been obtained. This data allows for the (approximate) determination of shell thickness from a simple absorbance spectra, circumventing the need for HRTEM. Furthermore, this data provides a valuable platform from which quantum mechanical models of the excited

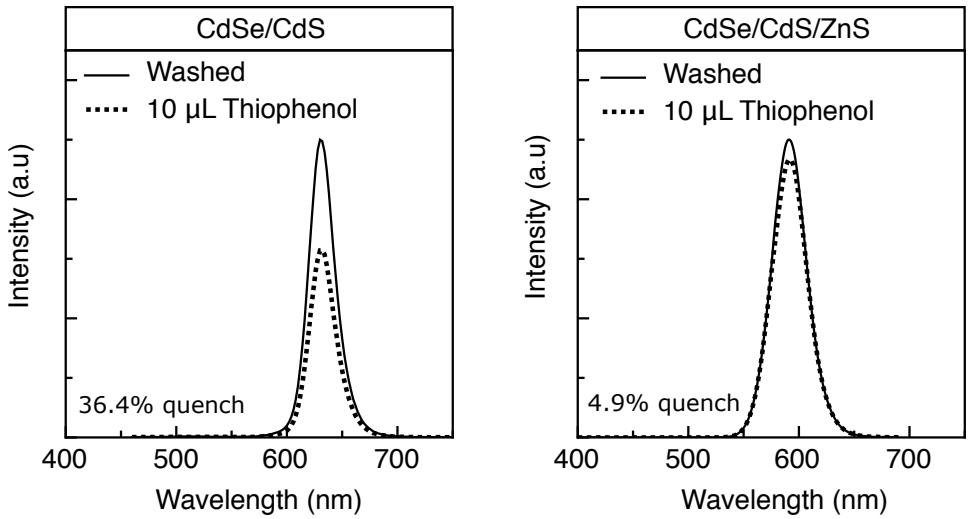

Figure 6.20: PL spectra of CdSe/CdS (left) and CdSe/CdS/ZnS (right) heterostructure nanocrystals both before and after the addition of 10 μL of thiophenol. It can be seen that the CdSe/CdS/ZnS multishell arcitecture provides greater resistance to quencing of the PL compared to single shell CdSe/CdS structures.

states in CdSe/CdS semiconductor nanocrystal heterostructures may be developed. The methods to synthesise CdSe/CdS/ZnS core multishell have also been presented. It was found that such structures resulted in highly luminescent NCs with greater preservation of the core emission colour compared to CdSe/CdS heterostructures. In addition, multishell NCs were found to be more resistant to quenching agents compared to those NCs with only a CdS shell. However, while spherical NCs are obtained in CdSe/CdS structures, CdSe/CdS/ZnS structures were found to have average aspect ratios of $sim1.2$, which may be attributed to lattice strain across the core/shell/shell interfaces. Interestingly, comparison of CdSe/CdS (6 ML) and CdSe/CdS/ZnS (4 ML) revealed vast differences in PL stability despite the fact that the first exciton transition in both structures lost little to no energy upon deposition of the final ML (indicative of complete carrier confinement). As such the link between complete confinement and PL stability should be treated with caution.

Bibliography

[1] J. J. Li, Y. A. Wang, W. Guo, C. Keay Joel, D. Mishima Tetsuya, B. Johnson Matthew and X. Peng. Journal of the American Chemical Society **125**, 12567 (2003).

[2] W. W. Yu, L. Qu, W. Guo and X. Peng. Chemistry of Materials **16**, 560 (2004).

[3] J. Jasieniak, C. Bullen, J. L. van Embden and P. Mulvaney. The Journal of Physical Chemistry B **109**, 20665 (2005).

[4] C. B. Murray, D. J. Norris and M. G. Bawendi. J. Am. Chem. Soc. **115**, 8706 (1993).

[5] B. O. Dabbousi, J. Rodriguez-Viejo, F. V. Mikulec, J. R. Heine, H. Mattoussi, R. Ober, K. F. Jensen and M. G. Bawendi. Journal of Physical Chemistry B **101**, 9463 (1997).

[6] R. Xie, U. Kolb, J. Li, T. Basch and A. Mews. Journal of the American Chemical Society **127**, 7480 (2005).

[7] X. Peng, M. C. Schlamp, A. V. Kadavanich and A. P. Alivisatos. Journal of the American Chemical Society **119**, 7019 (1997).

[8] L. Qu, W. W. Yu and X. Peng. Nano Letters **4**, 465 (2004).

[9] V. Klimov, P. H. Bolivar and H. Kurz. Physical Review B: Condensed Matter **52**, 4728 (1995).

[10] C. Bullen and P. Mulvaney. Langmuir **22**, 3007 (2006).

[11] D. E. Gomez, J. L. van Embden, J. Jasieniak, T. A. Smith and P. Mulvaney. Small **2**, 204 (2006).

[12] G. Schlegel, J. Bohnenberger, I. Potapova and A. Mews. Physical review Letters **88**, 137401 (2002).

[13] A. L. Efros and M. Rosen. Proceedings - Electrochemical Society **98-19**, 177 (1999).

[14] J. Jasieniak and P. Mulvaney. J. Am. Chem. Soc. **129**, 2841 (2007).

[15] D. V. Talapin, I. Mekis, S. Goetzinger, A. Kornowski, O. Benson and H. Weller. Journal of Physical Chemistry B **108**, 18826 (2004).

[16] J. R. McBride, T. C. Kippeny, S. J. Pennycook and S. J. Rosenthal. Nano Letters **4**, 1279 (2004).

Chapter 7

Concluding Remarks and Outlook

This thesis has shown, both experimentally and numerically that the nucleation and growth of semiconductor nanocrystals is an intricate process. Positive outcomes from synthetic procedures may only be realised when the governing kinetics are strictly controlled at every moment of the reaction. Experimental evidence presented in this thesis has shown that nanocrystal evolution can be broken up into three regimes; (i) Nucleation, (ii) Early time ripening (ETR) and (iii) Slow growth. Notably each of these regimes strongly overlaps, with each regime defined only by the observation of the dominant process. Through the judicious use of oleic acid and bis-(2,4,4-trimethylpentyl)phosphinic acid both nucleation and ripening can be controlled systematically, enabling the isolation of high yields of CdSe nanocrystals with predictable sizes. Furthermore, it has been shown that early time ripening determines the overall survival probability of the nuclei and the resultant longer-term growth behaviour. It has also become apparent that two ligands may have remarkably different effects on the nucleation and growth of CdSe, despite the fact that both are basically anionic surfactants, which complex cadmium ions. Further Developments in the field of synthetic colloid chemistry on the nanoscale requires that the chemistry of the ligands used to modify the relevant kinetic processes are better understood. As multiple ligands are almost always used to control particle nucleation and growth, many side reactions (between the ligands) in the solvent

are likely. These side reactions may produce species that directly affect the course of particle evolution. In addition, the formation of semiconductor nanocrystals likely involves several redox processes. To date, few investigations have directly tackled the issues of ligand-ligand interactions. Similarly, current research into semiconductor nanocrystal synthesis suffers from a lack of detailed knowledge on the inorganic mechanisms of how the cation (metal) and anion (chalcogen) react. Such studies would provide valuable insight into the complex chemistry, which occurs throughout the synthetic process. In addition to gaining deeper insight into the underlying chemistry of nanocrystal formation, efforts into improving the synthesis of nanocrystals via non-injection methods would constitute a valuable contribution to the field. Such methods would allow for the reliable synthesis of large quantities of colloidal nanocrystals, and subsequently aid their incorporation into future technologies.

From the simulations performed on NC nucleation and growth it may be concluded that the evolution of NC in the liquid-phase proceeds via highly reaction limited kinetics. This finding is consistent with the experimental results presented in Chapter 3, which showed NC nucleation and growth to be extremely sensitive to the nature and concentration of the adsorbates in solution. The simulations outlined in this thesis were able to successfully replicate the three main aspects of NC evolution observed experimentally. Firstly, the long nucleation time (up to 30 seconds). Secondly, the strong overlap between nucleation, growth and coarsening at early reaction times and finally the presence of a meta-stable (quasi-equilibrium) state, which exists prior to the classical Ostwald ripening of the ensemble.

It has also become clear that ligands play a vital role in determining the outcome of the synthetic procedure of shell deposition. Through tuning the solubility of the monomer as well as the particle reactivity CdSe/CdS heterostructure nanocrystals have been synthesised with monolayer control of shell thickness in the absence of either homogeneous nucleation or Ostwald ripening. A strong link between the physical dimensions of CdSe/CdS core/shell nanocrystals and their absorbance spectra has been established. Accurate data on a wide range of CdSe core sizes with various CdS shell thicknesses has been reported. This data

provides a valuable platform from which quantum mechanical models of the excited states in CdSe/CdS semiconductor nanocrystal heterostructures may be developed. The methods to synthesise CdSe/CdS/ZnS core multishell have also been presented. These multishell nanocrystals were found to exhibit higher quantum yields and increased resistance to quenching agents compared to CdSe/CdS nanocrystals. Given the ability to systematically alter the optical properties of core/shell nanocrystals by changing either the core or shell type, crystal morphology, shell thickness, or core dimensions etc. the synthesis of more complex structures and geometeries are to be expected in the near future.

Appendix A

Temperature profiles

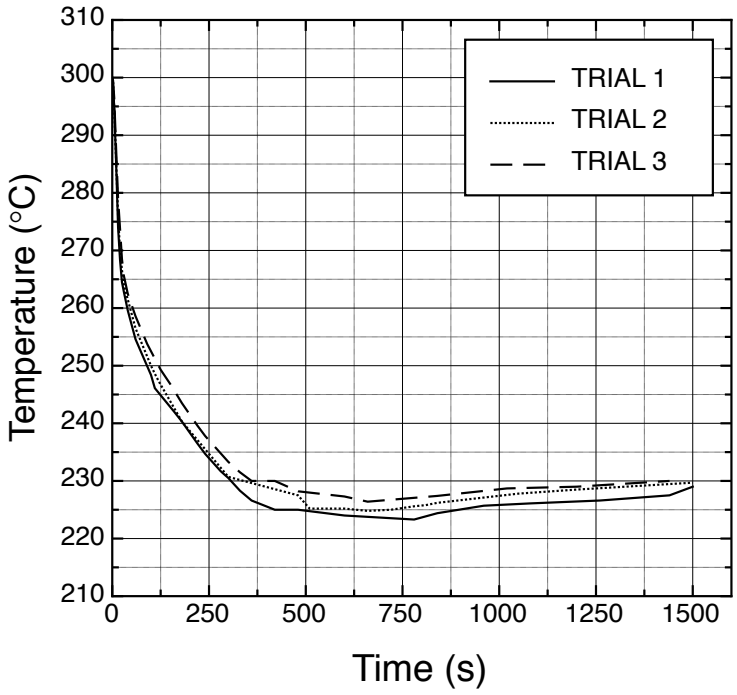

Figure A.1: Temperature profiles for three randomly selected reactions. The temperature variation between reactions is negligible within the first minute of reaction and is maintained to ± 2°C thereafter. All reactions are seen to assume their growth temperatures (230 °C) within 800 s.

Appendix B

Photoluminescence spectra 1

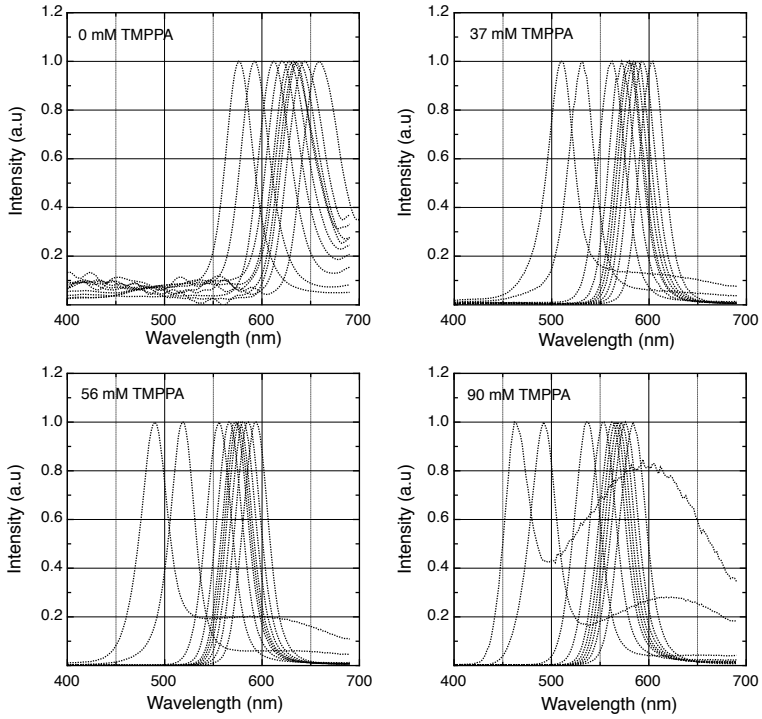

Figure B.1: Photoluminescence spectra for reactions conducted using [TMPPA] of 0 mM, 37 mM, 56 mM and 90 mM.

Appendix C

Photoluminescence spectra 2

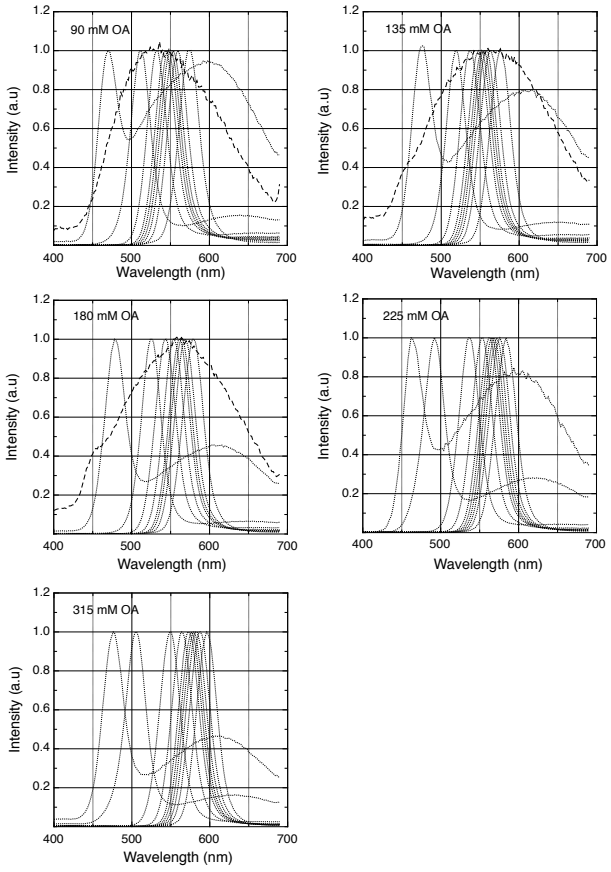

Figure C.1: Photoluminescence spectra for reactions conducted using [OA] of 90 mM, 135 mM, 180 mM, 225 mM and 315 mM.

Appendix D

Homogeneous nuclei

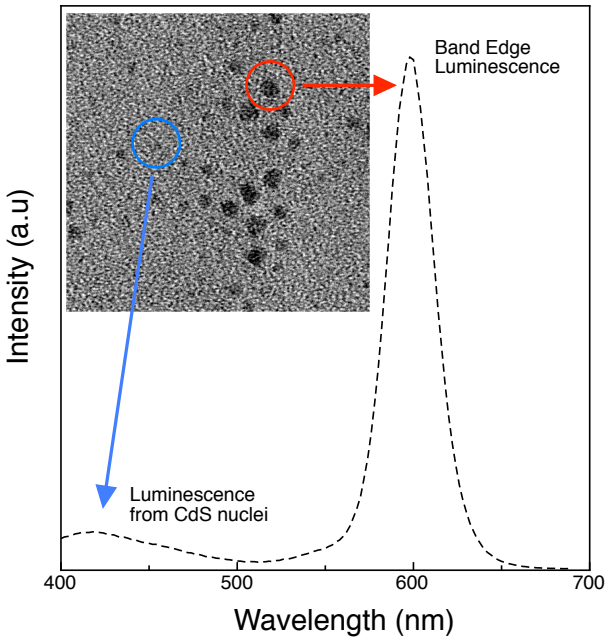

Figure D.1: Photoluminescence spectra and the corresponding HRTEM image taken after the amount equivalent to grow a CdS shell 3 ML thick had been injected. In the TEM image we can see both the CdSe/CdS particles (red circle) and the isolated CdS nanocrystals (blue circle). The emission from the CdS nanocrystals is broad, spanning from $\backsim$350 nm to $\backsim$500 nm, consistent with CdS nanocrystals approximately 3.2 nm in diameter. It should be noted that prior to the injection of "sulphur-3" the region of the P.L spectra between 350 nm and 500 nm was featureless.

Appendix E

HRTEM CdSe/CdS: Cadmium oleate and ODES precursors

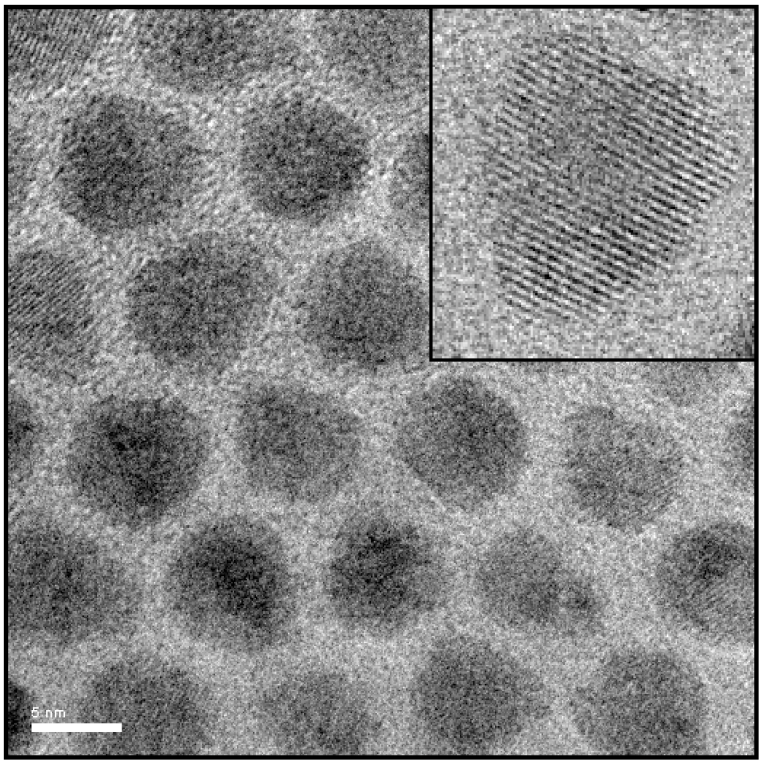

Figure E.1: HRTEM of CdSe/CdS nanocrystals with a 6 ML CdS shell grown using cadmium oleate and ODES as the shell precursors. Employing these precursors typically resulted in particles whose morphology was slightly elongated.

Appendix F

TEM CdSe/CdS: Cadmium-TMPPA and ODES precursors

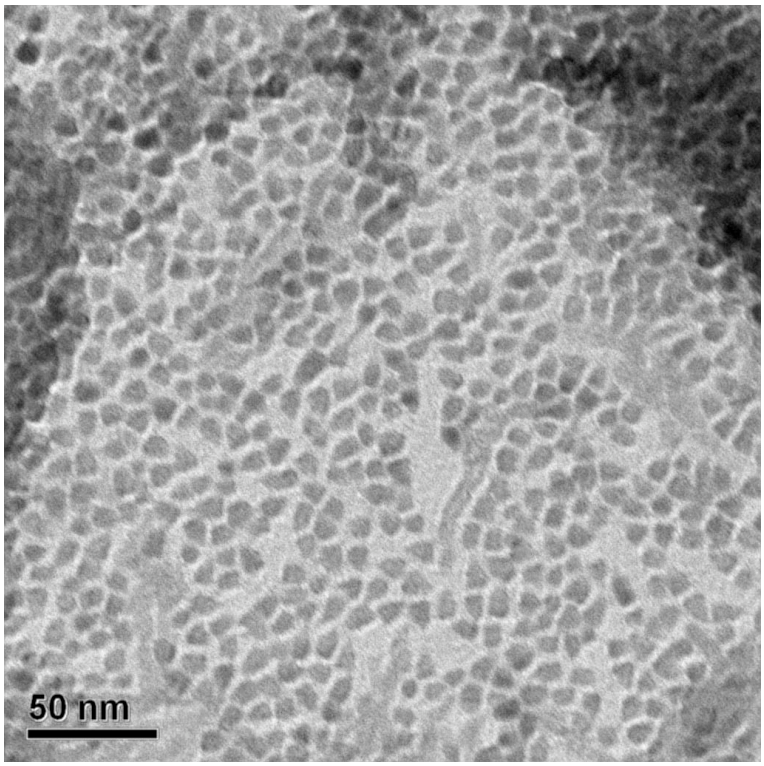

Figure F.1: TEM of CdSe/CdS nanocrystals grown using cadmium-TMPPA and ODES as the shell precursors in the absence of oleic acid. Employing these precursors typically resulted in particles whose morphology was highly faceted.

Appendix G

Absorbance spectra of CdSe/CdS/ZnS NCs

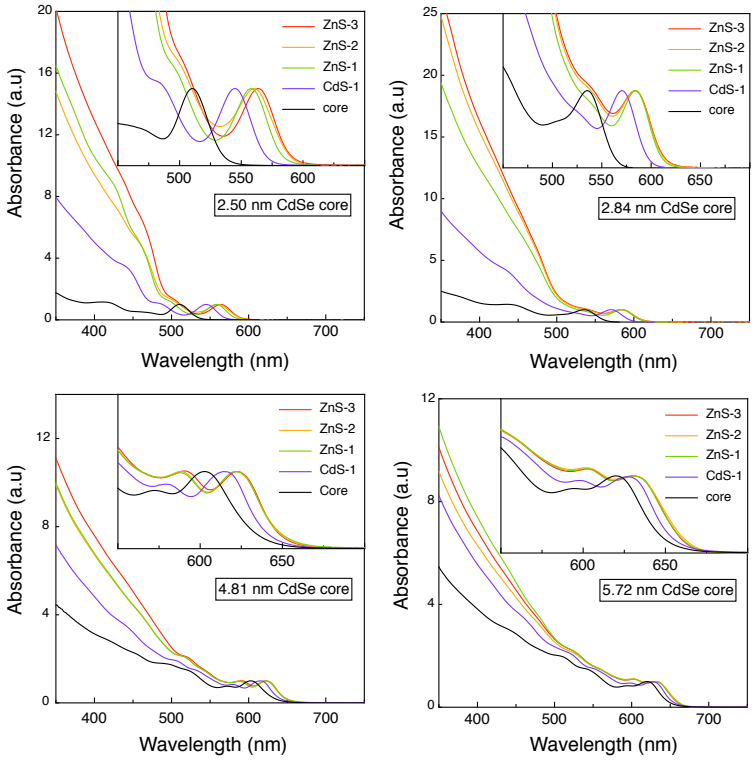

Figure G.1: Absorbance spectra as a function of shell thickness for CdSe/CdS/ZnS heterostructures with several different core sizes ranging from 2.45-5.61 nm.

Appendix H

NC Growth via Syringe Injection

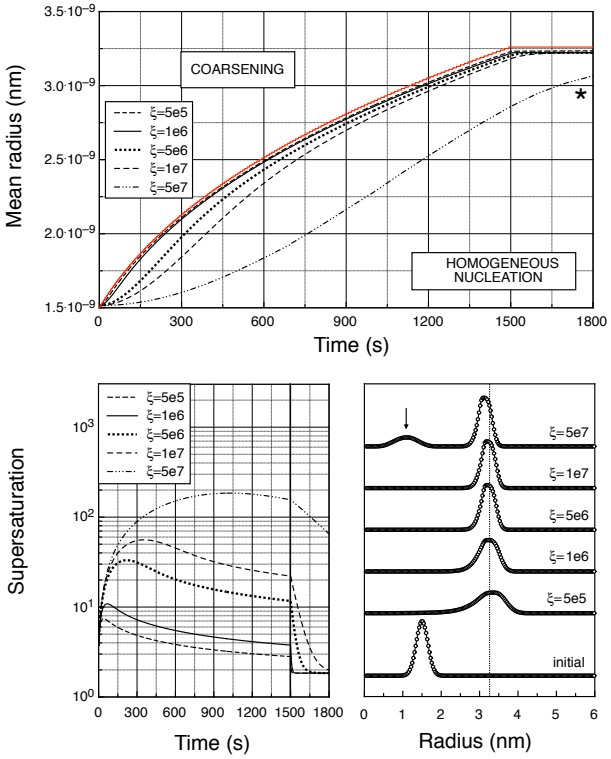

Figure H.1: The above figure displays NC Growth via Syringe Injection. Clockwise from the top: Mean radius as a function of time in reactions with ξ in the range 5×10^5 to 5×10^7. The thick red line indicates the expected NC sizes after each injection of monomer assuming instantaneous growth. The final distributions at $t = 1800s$ for each of the simulations performed. Supersaturation profiles throughout the reaction. Importantly, the syringe pump is terminated at $t = 1500s$.